Power Stabilization of High Power Lasers for Second Generation Gravitational Wave Detectors

Dipl.-Ing. Frank Seifert

geboren am 19.06.1977 in Berlin

2010

Abstract

Ultra-stable light sources are needed for many high-precision experiments, such as interferometric gravitational wave detectors. The goal of these detectors is to detect gravitational waves of astrophysical and cosmological origin incident on the Earth. The existence of gravitational waves is one of the most prominent of Einstein's predictions that has not yet been directly verified. The first direct detection of gravitational waves will open a new window to the Universe and has been a strong source of motivation in the development and construction of instruments with exceptional sensitivity. One of the fundamental sensitivity limits of interferometric gravitational wave detectors comes from the power fluctuations of the laser light. Hence interferometric gravitational wave detectors, especially second and third generation instruments, call for ultra-stable lasers and very stringent requirements on technical power noise must be satisfied.

The scope of this thesis is the power stabilization of solid-state laser systems and experimental investigations of the limits of existing stabilization experiments. A large number of noise sources can affect the performance of a power stabilization control loop. A knowledge of the individual noise sources and their coupling mechanisms is of utmost importance for the design of shot-noise limited laser sources. The design and development of a laser power stabilization for gravitational wave detectors and other experiments which require a shot-noise limited light source is presented. The susceptibility of photodiode-based detector systems are characterized to determine at which level the different noise sources become important. A set of independent experiments was performed to quantify the limiting noise contributions to the stabilization experiments performed in this thesis. Based on this knowledge, our experiment was optimized and a previously unattained power stability could be demonstrated.

In addition to the fundamental investigations on the power stabilization schemes, a detailed control scheme for the stabilization of the 200 W laser system of the Advanced LIGO gravitational wave detectors was designed and tested. The full characterization of a 200 W prototype laser system which was required for the control loop design as well as first results of the power stabilization are presented.

Keywords: solid-state laser, power stabilization, shot-noise limit, gravitational wave detector

Kurzzusammenfassung

Für viele Präzisionsexperimente, wie z.B. interferometrische Gravitationswellendetektoren, werden ultra-stabile Lichtquellen benötigt. Das Ziel dieser Detektoren ist der Nachweis von Gravitationswellen astrophysikalischen und kosmologischen Ursprungs auf der Erde. Die Existenz von Gravitationswellen ist eine der bedeutendsten Vorhersagen Einsteins, die bisher nicht direkt bewiesen werden konnte. Der erste direkte Nachweis von Gravitationswellen wird ein neues Beobachtungsfenster zum Universum öffnen und war die treibende Kraft für die Entwicklung und Konstruktion von Experimenten mit außerordentlicher Empfindlichkeit. Eine der fundamentalen Grenzen der Empfindlichkeit von interferometrischen Gravitationswellendetektoren sind Leistungsfluktuationen des verwendeten Laserlichts. Daher werden ultra-stabile Laser für interferometrische Gravitationswellendetektoren benötigt, insbesondere für Detektoren der zweiten und dritten Generation, und sehr hohe Anforderungen bezüglich des technischen Leistungsrauschens müssen erfüllt werden.

Diese Arbeit umfasst die Leistungsstabilisierung von Festkörperlasern und experimentelle Untersuchungen der Grenzen von existierenden Experimenten zur Leistungsstabilisierung von Lasern. Eine Großzahl von Rauschquellen kann die Leistungsfähigkeit von Regelungsystemen zur Leistungsstabilisierung beeinflussen. Die genaue Kenntnis der individuellen Rauschquellen und deren Kopplungsmechanismen ist insbesondere für das Design von schrotrauschbegrenzten Laserquellen von entscheidender Bedeutung. Der Entwurf und die Entwicklung einer Laser-Leistungsstabilisierung für den Einsatz in Gravitationswellendetektoren und anderen Experimenten, die eine schrotrauschbegrenzte Lichtquelle benötigen, wird vorgestellt. Die Empfindlichkeit von Detektionssystemen, basierend auf Fotodioden, wurde charakterisiert, um die Signifikanz der verschiedenen Rauschquellen zu ermitteln. In dieser Arbeit wurden eine Reihe von unabhängigen Experimenten zur quantitativen Analyse der limitierenden Rauschbeiträge durchgeführt. Die vorliegenden Experimente wurden anhand dieser Erkenntnisse optimiert, so daß eine bis dahin unerreichte Leistungsstabilität gezeigt werden konnte.

Neben den elementaren Untersuchungen an Experimenten zur Leistungsstabilisierung wurde ein detailliertes Stabilisierungsschema des 200 W Lasersystems für die Advanced LIGO Gravitationswellendetektoren entwickelt und getestet. Die vollständige Charakterisierung eines Prototyps des 200 W Lasersystems, erforderlich für die Entwicklung des Stabilisierungskonzeptes, sowie erste Ergebnisse der Leistungsstabilisierung werden vorgestellt.

Stichworte: Festkörperlaser, Leistungsstabilisierung, Schrotrauschlimit, Gravitationswellendetektor

Contents

List of Figures

List of Tables

Glossary

List of Abbreviations

AC	alternating current
ADC	analog-to-digital converter
Advanced LIGO	2nd generation LIGO gravitational wave detector
Advanced VIRGO	2nd generation VIRGO gravitational wave detector
AEI	Albert-Einstein-Institute
AOM	acousto-optical modulator
AR	anti reflective
BS	non-polarizing beam splitter
CCD	charge-coupled device
CLIO	Cryogenic Laser Interferometer Observatory
CMRR	common-mode rejection ratio
DAC	digital-to-analog converter
DC	direct current
DUT	device under test
DWS	differential wavefront sensing
EMF	electromotive force
Enhanced LIGO	upgraded LIGO gravitational wave detector
EMI	electromagnetic interference
EOM	electro-optic modulator
EPICS	Experimental Physics and Industrial Control System
EtherCAT	Ethernet for Control Automation Technology
FBG	fiber-bragg-grating
FFT	fast Fourier transform
FI	Faraday isolator
FSR	free spectral range
FWHM	full width at half maximum
G-R	generation-recombination
GaN	gallium nitride
Ge	germanium
GEO 600	British-German gravitational wave detector
GEO-HF	upgraded British-German gravitational wave detector
GPD	Germanium Power Devices
GR	General Relativity
GW	gravitational wave
GWD	gravitational wave detector
HEPA	high efficiency particulate airfilter
HP-PMC	high-power pre-modecleaner
HPD	high-power photodetector

HR	high reflective
HV	high voltage
HWP	half-wave plate
IAD	ion-assisted deposition
IBS	ion-beam sputtering
IFO	interferometer
IL	in-loop
IL-PD	in-loop photodetector
InGaAs	indium gallium arsenide
InP	indium phosphide
IO	input optics
IR	infrared
LCGT	large-scale cryogenic gravitational wave telescope
LED	light-emitting diode
LFN	low-frequency noise
LIGO	laser interferometer gravitational wave observatory
LISA	laser interferometer space antenna
LISO	**LI**near **S**imulation and **O**ptimization of electronic circuits, written by Gerhard Heinzel
LO	local oscillator
LSD	linear spectral density
LZH	Laser Zentrum Hannover
M	mirror
MI	Michelson interferometer
NEP	noise equivalent power
Nd:YAG	neodymium doped yttrium aluminum garnet
Nd:YVO$_4$	neodymium doped yttrium vanadate
NI	noise-index (resistor current noise)
NPRO	non-planar ring-oscillator
NTC	negative temperature coefficient
OOL	out-of-loop
OOL-PD	out-of-loop photodetector
PBS	polarizing beam splitter
PC	personal computer
PD	photodetector
PDH	Pound-Drever-Hall
PMC	pre-modecleaner
PSD	power spectral density
PSL	pre-stabilized laser
PZT	piezoelectric transducer
QPD	quadrant photodetector
QR	quartz rotator
QWP	quarter-wave plate
REO	Research Electro-Optics Inc.

RF	radio frequency
RIN	relative intensity noise
RPN	relative power noise
RTLinux	real-time Linux
Si	silicon
SiC	silicon carbide
SMD	surface mount device
SNL	shot-noise limit
SNR	signal-to-noise ratio
TAMA300	Japanese gravitational wave detector
TEC	thermoelectric cooler
TEM	transversal electromagnetic wave
TF	transfer function
TIA	transimpedance amplifier
ULE™	ultra-low expansion titanium silicate glass (Corning)
USB	universal serial bus
VCO	voltage-controlled oscillator
VIRGO	French-Italian gravitational wave detector
VIRGO+	upgraded French-Italian gravitational wave detector

List of Symbols

(a) Roman Letters

$a(f)$	beam pointing PSD
A	open-loop gain
c	speed of light in vacuum
e	elementary charge
f	frequency
f_c	corner frequency
$\mathcal{F}$	finesse
$\mathcal{F}_\mathrm{p}$	finesse for p-polarized light
$\mathcal{F}_\mathrm{s}$	finesse for s-polarized light
G	gain
h	Planck's constant
h_MI	Michelson interferometer strain sensitivity
I	electric current
I_F	forward current
I_d	dark current
$I_\mathrm{d,diffusion}$	dark current resulting from diffusion
$I_\mathrm{d,g-r}$	dark current resulting from generation and recombination
$I_\mathrm{d,surface}$	dark current resulting from surface leakage
$I_\mathrm{d,tunnel}$	dark current resulting from tunneling
I_ph	photocurrent

I_s	saturation current
k_B	Boltzmann's constant
K	diode forward voltage temperature coefficient
$K_S(x,y)$	linear coupling coefficient
L	length
m	mass
N	number
P	power
R	ohmic resistance
R_sh	shunt resistance
R_th	thermal resistance
$\mathcal{R}$	responsivity
$\mathcal{R}(x,y)$	local responsivity
$S(x,y)$	position-dependent sensitivity
$S_0 = S(x_0,y_0)$	sensitivity at operating point (x_0,y_0)
$t_{...}$	time
T	temperature
T_J	junction temperature
T_s	transmission for s-polarized light
T_p	transmission for p-polarized light
$\overline{v^2}$	mean-square noise voltage
V	voltage
V_J	junction voltage
x, y, z	rectangular coordinates
Z	impedance

(b) Greek Letters

α_H	Hooge's parameter
δl	length difference
$\delta\Phi$	phase change
Δf	frequency difference
$\Delta\nu$	linewidth
ϵ	fraction
η	quantum efficiency
λ	wavelength
μ	mobility
ν	frequency (light)
$\sigma(x,y)$	relative local responsivity
τ	time constant or time interval
ω	beam radius
ω_0	cavity waist radius

Introduction

The existence of gravitational waves is predicted by Albert Einstein's Theory of General Relativity (GR), published in 1916 [42]. Einstein expanded his Special Theory to include the effect of gravitation on the shape of space and the flow of time and proposed that matter causes changes in the curvature of space-time. Gravitational waves are emitted when masses are accelerated and propagate outward from their source at the speed of light, analogous to Maxwell's prediction that electromagnetic radiation is emitted by accelerated charged particles. The effect of a gravitational wave (GW) can be understood as a weak perturbation of the metric of space-time, changing the distances between freely falling objects by an amount proportional to the gravitational wave strength. Because space-time acts as an extraordinarily stiff medium, the effect of gravitational waves is expected to be extraordinarily small and so gravitational waves were considered an interesting, but purely theoretical subject for a long time.

In 1974, Hulse and Taylor discovered the pulsar PSR 1913+16 and measured the orbital decay of the double neutron-star pulsar. They observed that the rate at which the decay occurs is consistent with the loss of energy via gravitational waves, as predicted by Einstein's theory. For this discovery, they were awarded the 1993 Nobel Prize in Physics. The Hulse-Taylor observations are very important but they are only an indirect evidence for gravitational waves. To date, a direct detection of gravitational waves has not been made.

During the past decades, experimental research in the area of gravitational waves has become a very active field with many new experimental and theoretical developments. Direct detection of gravitational waves is currently one of the most interesting challenges in physics. Gravitational waves provide unique information about the motion of the matter in the Universe. Many of these waves should travel through the Universe, originating from the Big Bang, supernova explosions, rotating neutron stars, inspiraling binary systems, black holes or other objects. The direct observation of gravitational waves would provide information that is inaccessible to electromagnetic observations, but direct detection requires the construction of extremely sensitive detectors and could help to solve the large open problems in astrophysics and cosmology.

1.1 Gravitational wave detectors

The great challenge of the direct observation of a gravitational wave from astrophysical sources is the extraordinarily small effect the waves would produce on a gravitational wave detector (GWD). Recent decades have seen the invention of two main types of GWDs: resonant mass and interferometric detectors.

Resonant mass detectors: The first type of GWDs were large cylindrical masses (up to several tons) of aluminum and other materials with a high mechanical quality factor Q, based on the idea of Weber [173]. A gravitational wave acts like a force across a rigid object, so that it will be alternately stretched and compressed. The incoming gravitational wave excites

the vibrational modes of the cylinder. The small linewidth of the high-Q oscillator limits their sensitivity to a bandwidth of a few Hz around the center frequency of the fundamental mode. As the minimum detectable energy is determined by the effective temperature, resonant bar detectors are operated at cryogenic temperatures [28]. Resonant bar detectors have been operating for many years. At present, new resonant mass geometries like e.g. resonant spheres [33] are under investigation.

Laser-interferometric gravitational wave detectors: Laser interferometers are ideally suited to measure small changes in distances between macroscopic objects and hence the influence of passing gravitational waves on the distance between test masses. The major advantage of laser interferometers compared to resonant mass detectors is the broad detection bandwidth. All interferometric GWDs built so far use Michelson-type interferometers with long arms to detect small motions of suspended test masses induced by gravitational waves, as illustrated in Figure 1.1 [8, 73].

$t = 0$ $t = 1/4\,\tau$ $t = 1/2\,\tau$ $t = 3/4\,\tau$
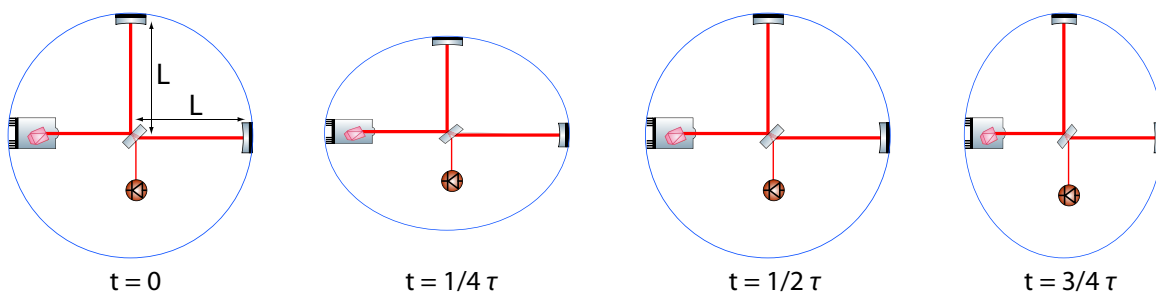
Figure 1.1: Schematic diagrams of a Michelson interferometer to detect gravitational waves. A gravitational wave passing the interferometer (here perpendicular to the interferometer plane) alternately stretches one arm and compresses the other arm. Changes in the arm length difference can be detected at the output using a photodetector. (τ is the period of the gravitational wave)

The incident light to the Michelson interferometer (MI) is split into two beams of equal power. Each of these beams travels along one arm before being reflected by an end mirror. The reflected light from the mirrors in the two arms is recombined at the beam splitter. The interference of the two light fields results in a light power that can be detected by a photodetector at the output port of the interferometer. When a gravitational wave passes the interferometer, it stretches one arm and compresses the other arm. Thus, changes in the relative displacement causes a dynamic interference pattern at the output port which can be detected as a power modulation by the photodetector. In practice the length of both arms are adjusted such that the light returning from the two arms is always 180° out of phase and so the light interferes destructively at the interferometer output such that the output is dark (also called *dark fringe*). This allows a null measurement which is less sensitive to power fluctuations [136].

The so-called *strain sensitivity* h_{MI} of a Michelson interferometer for changes in arm length difference δl induced by a gravitational wave passing the detector is determined by three major parameters, the arm length L, the amount of light stored in the arms P and the wavelength of the light λ:

$$h_{\mathrm{MI}} \equiv \frac{2\delta l}{L} \propto \frac{\lambda}{L\sqrt{P}} \qquad (1.1)$$

The sensitivity can be improved by increasing the length L or power P or a reduction of the wavelength λ. The length of terrestrial Michelson interferometer GWDs varies from several hundred meters up to some kilometers and is limited by geographical and cost factors. All present day interferometric GWDs operate at a wavelength of 1064 nm.

In practice, two major techniques are used to increase the circulating light. The first technique is to configure the arms as Fabry-Perot cavities which are adjusted to resonance and so the amount of light stored in the arms is increased. The second technique is called "power recycling" [12, 38]. For an interferometer operated at its dark fringe operation point, the light goes back to the laser. By placing a mirror between the laser and the beam splitter, the light coming back towards the laser is reflected back to the input port of the interferometer and an optical resonator is formed. Using this technique a power in the interferometer arms in the kilowatt range can be built up with only a few watts of injected laser power.

The sensitivity can be improved further by optimizing the gravitational wave signal storage time. By using another mirror at the output of the interferometer, the signal sidebands induced by a gravitational wave are sent back into the interferometer. The mirror is tuned such that these sidebands are resonant in the interferometer and thereby further increased. This technique is called "signal recycling" [109].

At present, six large laser interferometric gravitational wave detectors are in operation, TAMA300 [7], GEO600 [9], VIRGO [43] and three LIGO detectors [2]. All these detectors require a cw laser of unprecedented stability and high output power.

The first generation of GWDs have reached an enormous level of sensitivity very close to their target design sensitivities. In the past few years, GEO600 has been operated together with the other detectors in an international network of interferometers searching for gravitational waves. First data runs have been performed, but so far no gravitational waves have been observed. However, with the data taken and analyzed during these data runs, new upper limits for event rates and the amount of radiation from astrophysical sources have been obtained.

Currently the so-called "second generation" ground-based GWDs are being designed and research and development on even higher generation detectors has already begun. Before these new detectors become operational ($\sim$2014), some minor enhancements to the existing interferometers will be implemented to improve their sensitivity by about a factor of two [102]. These detectors will be GEO-HF [10], Virgo+ [155] and Enhanced-LIGO [4, 5].

Second generation detectors such as Advanced LIGO [6, 49], Advanced VIRGO [153, 154] and LCGT [93, 116] will be one order of magnitude more sensitive than current detectors, and will require many of the techniques that have been developed over the past decades.

1.2 Noise sources in interferometric gravitational wave detectors

The current generation of interferometers are designed to have a strain sensitivity of about $10^{-21}/\sqrt{\text{Hz}}$ corresponding to a change in arm length of 10^{-18} m/$\sqrt{\text{Hz}}$ for a 1 km long interferometer. Hence the noise requirements for all noise sources that might change the relative positions of the interferometer's mirrors are very stringent. There are several noise sources that limit the sensitivity of ground-based laser interferometric gravitational wave detectors. A short overview of some of the most important and interesting noise sources is given below, which are comprehensively described in [3, 8, 30, 73, 130, 136]. More detailed information can be found in the references given in the relevant places.

Seismic noise: Seismic noise is any kind of ground motion or external mechanical vibration that may lead to displacements of the mirrors. This displacement can be many orders of

magnitude larger than the expected GW signal and cannot be distinguished from a signal caused by a GW. Hence a complex isolation system using a combination of active controls, e.g. hydraulic or piezo-electric actuators and passive isolation, using damping materials and multi-stage pendulum suspensions, are required to filter the seismic noise.

Gravity gradient noise: Fluctuating local gravitational gradients set a limit to the interferometer sensitivity at low frequencies. This environmental noise comes from clouds, atmospheric pressure changes, seismic density waves and ocean waves, but also from human activities at the detector site [74, 156]. Gravity gradient noise becomes dominant at low frequencies and is the primary reason why the detection of gravitational waves in the frequency band below 1 Hz must be done in space, e.g. by the LISA Project [100].

Thermal noise: Thermal noise results from the thermal energy of the atoms and molecules in a system. Today's interferometers are operated at room temperature and thermal noise in the optics and their suspension is a major contributor to the overall performance of a detector [15, 17, 18, 31, 62, 98, 101].

Frequency noise: If the interferometer arms are exactly equal in length, the interferometer output is insensitive to fluctuations of the laser frequency. In practice however, the effective lengths of the arms are slightly different (a couple of centimeters to allow Schnupp modulation [109]) and so a frequency fluctuation causes (due to unequal transit time in the arms) a phase difference $\delta\Phi$ of the interfering beams [145, 146]. This phase change cannot be distinguished from a real change in arm length due to a GW. For current GWDs, the achievable frequency stability is good enough not to limit the overall detector sensitivity.

Scattered light: Scattered light is generated by reflections of a beam on an optical component with a rough surface. A typical rms roughness of a super-polished optical surface of the optics used in GWDs is better than 1 Å. The optical components scatter a small amount of the coherent light over wide angles. Because the optics must be located in a high vacuum system, the scattered light is (often) reflected or scattered many times until reaching another (or the same) optical component in the system. During the interaction with other surfaces on its travel throughout the system, the scattered light acquires a phase modulation determined by the relative movement of the structures passed during travel. When interacting with one of the original beams, this phase modulation results in a noise contribution to the main beam which can be significant [168].

Quantum noise: Quantum noise of the electro-magnetic field is one of the major noise sources, which arises from the quantum nature of the light. Two ways of how quantum noise affects the measurement are important: *photoelectron shot noise* and *radiation-pressure noise* [136].

A limitation to the sensitivity of the optical readout scheme is set by shot noise in the detected photocurrent at the output of the interferometer. If the laser has no technical power noise, the photons arrive randomly at the photodetector, which generates random fluctuations of the light power and thereby apparent fluctuations in the path difference of the arms.

Quantum radiation-pressure noise originates from statistical fluctuations of the optical power (shot noise) in the interferometer. The impact of photons on the suspended mirrors and beam splitter transfer a small amount of momentum to the optics, thereby causing displacement noise and thus differential arm-length fluctuations that are indistinguishable from gravitational-wave signals at the output of the interferometer.

Due to the different power scaling of radiation-pressure noise and the shot noise contribution in the interferometer readout, a compromise regarding the light power has to be made in

order to minimize the uncorrelated sum of both effects. The combination of shot noise and radiation-pressure noise sets a limit on the detector sensitivity known as the standard quantum limit (SQL). For very high powers as in second generation detectors it is expected, that radiation-pressure noise will limit the sensitivity at lower frequencies.

Technical power noise: One very important noise source for laser interferometers are fluctuations of the power of the laser light [66, 134, 144–146]. Technical power fluctuations can be caused by mechanisms related to the laser system itself, fluctuations of the alignment of the interferometer and other technical noise sources. Laser power noise can cause noise in the readout scheme of the interferometer in various ways, which can be divided into two main categories.

First, fluctuations of the laser light directly couple into the output port of the interferometer, e.g. due to deviation from the ideal dark-fringe operation point. As described above the length of both arms of the interferometer are adjusted such that the output of the interferometer is close to a minimum in the output light. If operated exactly at the dark fringe, then in principle it would be insensitive to power fluctuations. However in practice there will be small deviations from the null position causing some sensitivity to laser power fluctuations.

Second, fluctuating light power causes fluctuations in the mirror positions inside the interferometer due to technical radiation-pressure fluctuations. Even though the beam splitter ideally causes the technical power fluctuations injected into the two interferometer arms to be equal, an asymmetry within the arms can cause a differential arm length change induced by laser power fluctuations, which will be detected at the interferometer output. This becomes increasingly important as the effective laser power will be increased for future detectors. In the case of the Advanced LIGO detector the power stabilization requirement for the laser is set by the radiation-pressure effects in the interferometer arms which are expected to show an asymmetry of about 1%.

1.3 Outline of the thesis

To achieve the sensitivity goals for the second generation of laser interferometric GWDs such as Advanced LIGO, the reduction of laser power fluctuations is very important. Hence the general objective of this thesis is to demonstrate the power stabilization of a Nd:YAG laser system to the power stability required for the Advanced LIGO interferometers. Several power stabilization experiments have been performed in the past (e.g. [1, 110, 117, 128, 129, 185]), but none could demonstrate the high stability required. All those experiments were limited by one or more unknown noise sources, especially at low frequencies. Only little information on these limiting noise sources was available so far. Therefore we set up power stabilization experiments of different Nd:YAG laser systems to first reproduce and then improve the published results. During the course of these experiments the main noise sources could be identified and further dedicated experiments were set up to gain a better understanding on the underlying processes. Based on this knowledge, a stabilization concept for the Advanced LIGO laser system was developed. The structure of this thesis follows a logical order to provide the understanding of the basic principles of power stabilization followed by the description of the different experiments and noise investigations and their results.

Chapter 2 will give a short introduction in laser power stabilization, describing some major sources of laser power fluctuations of diode-pumped solid-state lasers and will introduce the principle of power stabilization. Different control loop designs and also the limitations of the stabilization will be discussed.

In Chapter 3, two power stabilization experiments with different laser systems and optical setups will be explained in detail. These experiments were essential for the identification and reduction of individual noise sources limiting former stabilization experiments. In a stabilization experiment of the GEO600-type laser system, the optical setup and the sensing electronics were iteratively optimized to improve the stability very close to the design requirements of Advanced LIGO.

Chapter 4 will focus on the identification and quantification of noise sources that limit the current power fluctuation measurements. Special attention will be given to noise at low frequencies. A selection of the most important noise sources contributing to the sensing noise of the experiments performed in Chapter 3 will be presented.

Chapter 5 will give an overview on the planned stabilization scheme for the Advanced LIGO laser system. The individual parts of the laser system will be introduced and the proposed scheme of the power stabilization loop will be explained. Because the complete 200W Advanced LIGO laser system is not available yet, the stabilization of the 35 W front-end laser of this system was set up and will be described in order to demonstrate the stabilization concept. The system characterization, power actuator identification, loop design and also results of the achieved power stability will be presented.

In Chapter 6 a comprehensive summary of the conclusions to be drawn from this thesis is given.

The thesis provides a number of appendices, which have been separated from the text so as not to disrupt the main line of thought with technical or measurement details. References to these appendices are given in the text.

Laser power stabilization - An introduction

This thesis deals with the design and development of a laser power stabilization for gravitational wave detectors and other experiments which require a shot-noise limited laser source. In order to set the context for this thesis, a brief introduction to the origin and reduction of laser power noise and related information is given. Concepts of an active stabilization loop as well as the limits of such a power stabilization scheme are discussed.

2.1 Sources of laser power noise

The output of a free oscillating laser will fluctuate in power, polarization, frequency, etc. Power fluctuations of the laser light can be caused by many things, both internal and external to the laser source. Power fluctuations inside a laser result from several parameters of the laser itself or its pump source, which can be partly technical noise sources and partly quantum noise [60, 61, 123]. Typical quantum-noise effects associated with the gain medium of the laser and losses inside the laser resonator are spontaneous emission of excited atoms, ions or molecules in the lasing medium and shot-noise. Technical noise sources inside the laser can be:
- intra-cavity photon-number fluctuations introduced by the pump source (pump noise);
- beam-pointing, e.g. due to vibrations of resonator mirrors;
- thermal fluctuations in the gain medium;
- cavity length fluctuations (frequency noise);
- fluctuations in the wavelength of the pump photons;

and other phenomena.

Power fluctuations external to the laser are mostly caused by technical noise sources. Many environmental factors can affect the beam and lead to power fluctuations, e.g dust particles falling through the beam path or vibrations of mechanical parts, temperature changes and air currents, which lead to fluctuations in the index of refraction, can produce beam jitter. This again can change the coupling efficiency at the input to optical resonators, partially clip the beam at apertures or lead to a movement of the beam over the surface of a detector with spatial variations of its sensitivity. But also other laser beam observables, such as frequency and polarization, can cause power fluctuations since e.g. the reflectivity of beam splitters and mirrors are a function of the wavelength and polarization of the incoming beam. All these phenomena result in a fluctuation in the measured power and complicate the task of laser stabilization.

The optical power P of a laser over time is considered to be

$$P(t) = \overline{P} + \delta P(t) \tag{2.1}$$

The relative power fluctuations can then be defined as the fluctuation of the power divided by the mean power ($\delta P/\overline{P}$). In the context of optical power fluctuations of a laser, it is common

to define the relative intensity noise (RIN)[1] or relative power noise (RPN), which is the power noise normalized to the average power level

$$RPN(f) = \frac{\delta P(f)}{\overline{P}} \qquad \text{in units of } \frac{1}{\sqrt{\text{Hz}}} \qquad (2.2)$$

where $\delta P(f)$ is the linear spectral density of power fluctuations at a given Fourier frequency, and $\overline{P}$ is the time-averaged power.

In most cases, the lowest possible power noise level for a laser beam is defined by its shot-noise level. Shot noise describes random fluctuations of discrete signal carriers like electrons or photons. In quantum optics, shot noise is caused by the Poisson distribution of photons in the light beam. Since the Poisson distribution approaches a Gaussian distribution for large numbers, the amplitude distribution of shot noise can be modeled by a Gaussian or Normal distribution for large numbers of photons.

The power spectral density of the optical power P_{opt} in the case of shot noise is

$$S_{\text{P,sn}}(f) = h\nu \, P_{\text{opt}}, \qquad (2.3)$$

which is proportional to the average power of light with frequency ν.

The shot noise in a photodetector results from the quantum nature of the light detected and hence the charge carriers generated. For a photodetector without internal gain the photocurrent i_{ph} can be calculated as

$$i_{\text{ph}} = P_{\text{opt}} \frac{\eta \, e}{h \, \nu} \qquad (2.4)$$

$$= P_{\text{opt}} \, \mathcal{R} \qquad (2.5)$$

where $\mathcal{R}$ is the responsivity of the detector in amperes per watt calculated from the quantum efficiency η. Assuming the light detected by the photodetector to be shot-noise limited, we have the following power spectral density for the shot noise of a photodetector that receives the optical power P_{opt}

$$S_{\text{i,ph}}(f) = 2e \, i_{\text{ph}} \, \Delta f \qquad (2.6)$$

$$= 2e \, P_{\text{opt}} \frac{\eta \, e}{h \, \nu} \, \Delta f \qquad (2.7)$$

The shot-noise current is proportional to the square root of the noise bandwidth Δf which means that it has constant noise power per Hertz of bandwidth. Thus the noise power is independent of frequency so that it has a flat power distribution (so-called *white noise*).

Most of the technical noise mechanisms are too small at high frequencies to affect the overall performance of the laser system. At high frequencies, well above the relaxation-oscillation frequency, the shot-noise level is approached by many laser systems. This is also true for free-running solid-state laser systems, such as the diode-pumped Nd:YAG lasers used in this work. One might expect that the amount of RPN of a laser will remain constant when the beam is subject to linear attenuation. This is not true, however, if the RPN is limited by shot-noise.

---

[1]Laser power fluctuations are often referred to as intensity noise, but is mostly measured and presented in units of power. Therefore, the term *power noise* seems to be more appropriate.

2.2 Laser power stabilization

As lasers exhibit power noise from various origins, several different techniques can be used to suppress this noise. In order to stabilize the output power of a laser system, passive or active stabilization schemes can be used. Passive power stabilization of laser systems can be done by means of optical feedback inside the laser system, nonlinear absorption, filtering of technical noise e.g. using low-pass filters in the supply electronics, or other techniques. Passive stabilization is often simpler and more reliable compared to active stabilization schemes, but often does not provide the required noise reduction. Hence active stabilization schemes are often used and most of them use negative-feedback schemes that use active feedback applied on a control parameter for the power of the laser system.

In principle, power stabilization can be achieved by controlling the optical loss or gain in the laser system. A stabilization scheme using an active negative-feedback loop is shown schematically in Figure 2.1.
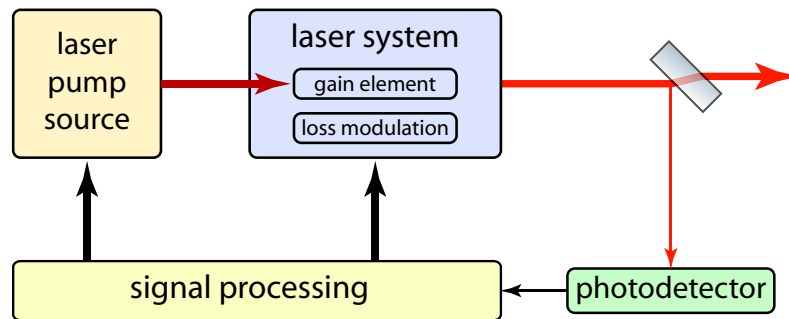
Figure 2.1: Laser stabilization scheme using an active negative-feedback loop.

A fraction of the main beam is split off and detected by a photodetector. The signal obtained is processed and used to control the output power of the laser system by either changing the optical loss or gain in the laser system [23, 115, 118, 182, 183]. In diode-pumped solid-state laser systems effective stabilization can be achieved by modulation of the pump-diode power [1, 110, 117, 128, 129, 185]. An alternative method comprises application of feedback to an intracavity or extracavity modulator, e.g. electro-optic or acousto-optic modulators, which introduce controlled losses to the laser system [126, 158].

The choice among these modulation-techniques used is often influenced by the intended bandwidth, reliability or costs. In most cases an analog control loop is used instead of digital control loops because a very high loop-bandwidth is required. Parasitic coupling of noise from one laser observable into another further complicates the task of laser power stabilization.

2.2.1 Stabilization loop concepts

Different topologies for the design of a power stabilization loop can be used and hence a short introduction into the different power stabilization loop configurations used in this thesis is given below.

AC-coupled feedback loop

The first topology based on closed-loop feedback with vanishing low-frequency gain only compensates for fluctuations in the frequency-band of interest by negative AC-coupled feedback. In power stabilization loops with very high gain requirements ($\gg 100\,\text{dB}$) this topology leads

to problems in the implementation of an analog controller. Even tiny offsets at the input stage of the controller would saturate the output due to the high gain. This requires a careful design of the individual gain and filter stages in the controller and to decouple them from each other at low frequencies. This can be achieved e.g. by either AC-coupling of the individual stages or internal feedback using integrating stages. With this configuration, a stabilization of the mean power is not possible.

DC-coupled feedback loop

In experiments where an absolute stabilization of the output power is required, a DC-coupled feedback has to be implemented. In the case of a DC-coupled loop scheme, the output power of the laser system is measured and compared with a reference value. The controller then takes the difference between the reference and the signal obtained from the laser system to change the input to the power actuator of the laser system under control. Thus in case of a DC-coupled loop with sufficient loop gain[2], the performance of the laser system is defined by the stability and noise of the reference and in consequence also limited by it.

In order to overcome the limitation set by the reference, additional gain can be implemented in the sensor using appropriate filters and sufficient gain in the frequency-band of interest. As an alternative, a combination of the DC-coupled loop and an additional, AC-coupled path injected into the error-point of the control loop can be used. As before, the output of the laser system is measured and the obtained signal is compared with the reference value. Now, in addition, the original signal from the detector is filtered, amplified and then added to the difference of the photodetector signal and the reference signal. Thus with the new loop-shape, the gain in the additional path greatly reduces the importance of the stability of the reference used.

2.2.2 Stabilization limit

The fundamental sensitivity limit in a traditional power-noise detection and stabilization scheme usually refers to the minimum level of quantum noise which couples into the measurement without the use of squeezed-states of light [19, 172]. This limit is given by the shot noise of the detected optical power, the so-called *shot-noise limit* (SNL), and represents the classical lower bound for power noise measurements.

Typically, photodiodes are used to measure the optical power of the beam by converting it into a photocurrent. The linear spectral density of the relative power noise of the SNL (in units of $1/\sqrt{\text{Hz}}$) is given by

$$RPN_{\text{sn}} \quad = \quad \sqrt{\frac{2\,h\,\nu}{P_{\text{opt}}}} = \sqrt{\frac{2\,h\,c}{\lambda\,P_{\text{opt}}}} \tag{2.8}$$

$$= \quad \sqrt{\frac{2e}{P_{\text{opt}}\,\mathcal{R}}} \tag{2.9}$$

where e is the electron charge, $\mathcal{R}$ the photodetector responsivity in amperes/watt calculated from the quantum efficiency η, and P_{opt} the detected optical power. The SNL for different power detection levels of a light source with $\lambda = 1064\,\text{nm}$ is illustrated in Figure 2.2.

The shot noise contribution is proportional to $1/\sqrt{P_{\text{opt}}}$ and so the sensitivity of a detection scales with the square-root of the power. To improve the sensitivity of the power-noise detection,

---

[2]the gain inside the detector for power-sensing is small compared to the loop gain
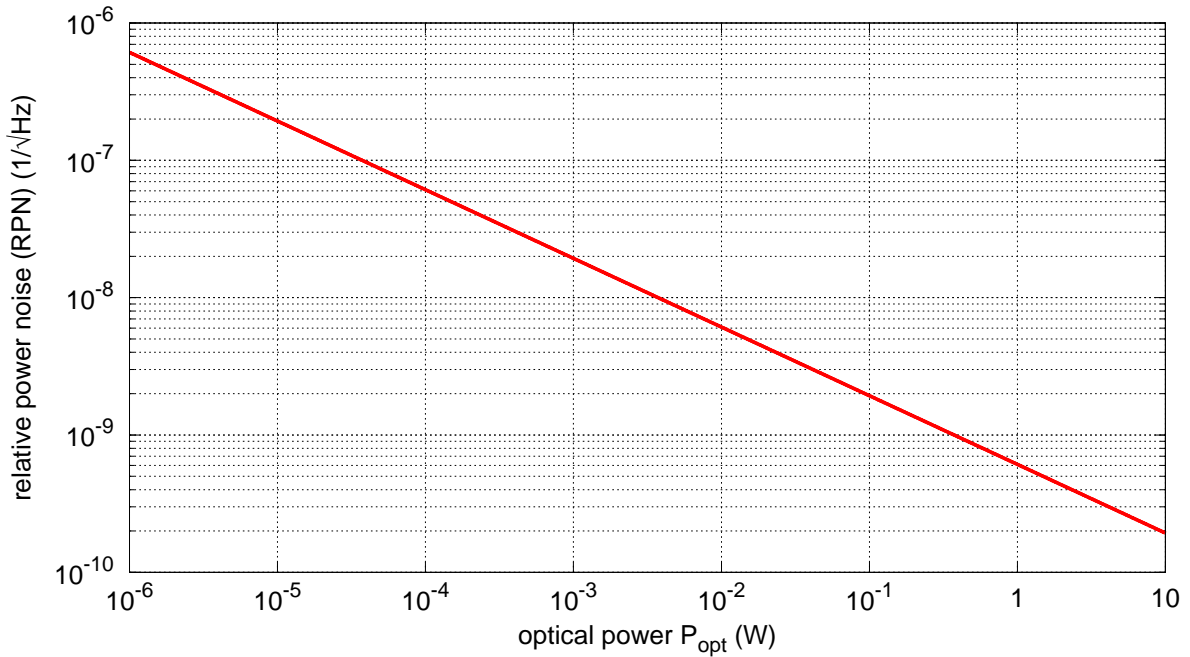
Figure 2.2: Shot-noise limit (SNL) for power fluctuation detection.

the detected optical power and therefore the photocurrent in the photodiode must be increased. To measure RPN down to the SNL, the full optical power needs to be detected, i.e. the measurement cannot be done on an attenuated beam. Otherwise, the optical attenuation adds additional quantum noise (the finite quantum efficiency of the detector has the same kind of effect). At high power levels, this causes problems with photodiode saturation (or even damage) and the dynamic range of the readout electronics. If the full optical power is too high for a single detector, a possible method is to use beam splitters for distributing the power on several photodetectors, and to combine the photocurrents [78].

In order to clarify the importance of the shot-noise limit in the power stabilization of a laser system, a basic stabilization scheme is shown schematically in Figure 2.3.
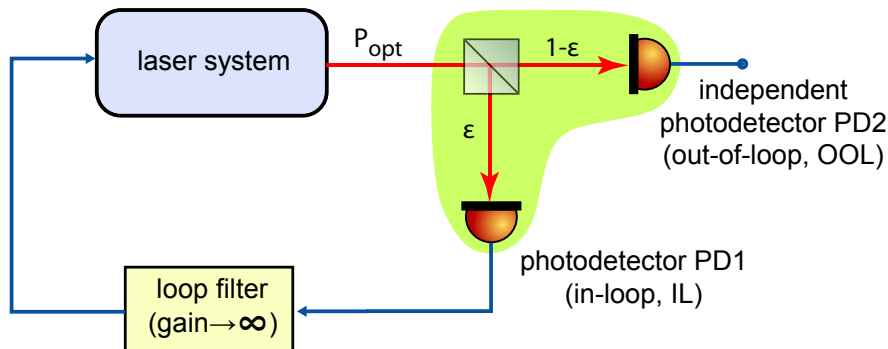
Figure 2.3: Shot-noise limitation in an active negative-feedback loop.

It is assumed that the photodetectors PD 1 and PD 2 have no electronic noise and the loop gain is sufficiently high to suppress all technical noise of the laser system. In the following

the terms *in-loop* and *out-of-loop* describe measurement points that contain signals which are internal or external to the causal signal flow of the given control loop respectively.

A beam splitter taps off a fraction ϵ of the input beam P_{opt} to the in-loop detector PD 1 having a quantum efficiency η_1. The photocurrent of the detector PD 1 can be calculated to be $i_{\text{pd1}} = P_{\text{opt}}\,\epsilon\,\frac{\eta_1 e}{h\nu}$. The photocurrent of the detector PD 2 which detects the fraction $1 - \epsilon$ is $i_{\text{pd2}} = P_{\text{opt}}\,(1 - \epsilon)\,\frac{\eta_2 e}{h\nu}$, respectively. The relative shot-noise of the photocurrent for each detector can then be calculated to

$$RPN_{\text{PD1,sn}} = \sqrt{\frac{2e}{P_{\text{opt}}\,\epsilon\,\frac{\eta_1 e}{h\nu}}} = \sqrt{\frac{2e}{i_{\text{pd1}}}} \qquad \text{for PD 1} \qquad (2.10)$$

$$RPN_{\text{PD2,sn}} = \sqrt{\frac{2e}{P_{\text{opt}}\,(1 - \epsilon)\,\frac{\eta_2 e}{h\nu}}} = \sqrt{\frac{2e}{i_{\text{pd2}}}} \qquad \text{for PD 2} \qquad (2.11)$$

For very high loop-gain of the servo (gain $\to \infty$), the noise of the in-loop photodetector PD 1 is imprinted on the laser light and hence defined by the shot-noise limit of the detected power $\epsilon\,P_{\text{opt}}$ using PD 1. The second, independent photodetector PD 2 detects the power $(1 - \epsilon)\,P_{\text{opt}}$. With an active power stabilization loop with high gain, the noise of the in-loop detector PD 1 defines the noise property of the laser system. Thus the out-of-loop photodetector PD 2 also detects fluctuations measured by PD 1 and imprinted onto the light by the control loop. In addition, the independent detector has its own noise contribution given by the shot-noise of the amount of light detected by itself. Since there should be no correlation, summing the noise from the two photodetectors in quadrature gives the minimum measurement noise. To illustrate this, Figure 2.4 shows the limitation of the power stabilization scheme given in Figure 2.3 for different beam splitter ratios ϵ assuming a quantum efficiency $\eta_1 = \eta_2 = 1$ for both detectors.
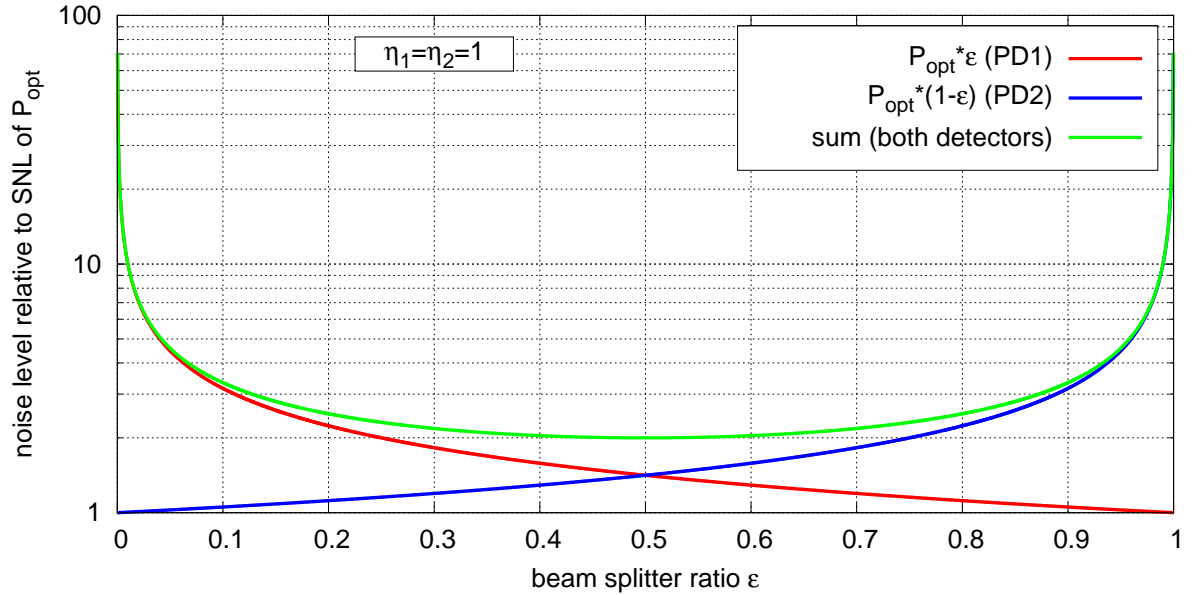
Figure 2.4: Power stabilization measurement-limitation by shot-noise contribution.

The optimum performance is achieved when the detected power by both detectors is equal ($\epsilon = (1 - \epsilon) \Rightarrow \epsilon = 0.5$). In the case of equal detected power the measured out-of-loop noise level is $3\,\mathrm{dB}$ or a factor of $\sqrt{2}$ above the shot-noise level of one detector.

Often the measurements performed with an independent sensor do not show the results expected from theoretical considerations. This is often referred to as *in/out-of-loop problem* and plays an important role in noise measurements. Let's assume an ideal system with a beam splitter having a splitting ratio $\epsilon = 0.5$. A noise contribution to the laser beam outside the green-shaded area shown in Figure 2.3 can be detected with both detectors and the control loop suppresses it on both detectors. Noise sources within the green-shaded area, which are different for both detectors, cause different noise contributions on the two detectors. For example, high electronic noise of the OOL detector would be visible in the independent measurement, but would not be seen on the laser beam. On the other hand electronic noise in the in-loop detector would be imprinted on the light with the opposite sign, which will be also detected by the independent OOL detector. In that case one could erroneously assume that the loop gain is not high enough to suppress all the technical noise of the laser. This has to be kept in mind when interpreting measurements of any control loop in the following.

Power stabilization experiment

Next generation GWDs like the Advanced LIGO detector [6] will be more sensitive to laser power fluctuations since they require very high circulating power. The required relative power noise performance of the laser for the Advanced LIGO detector is shown in Figure 3.1 [180].
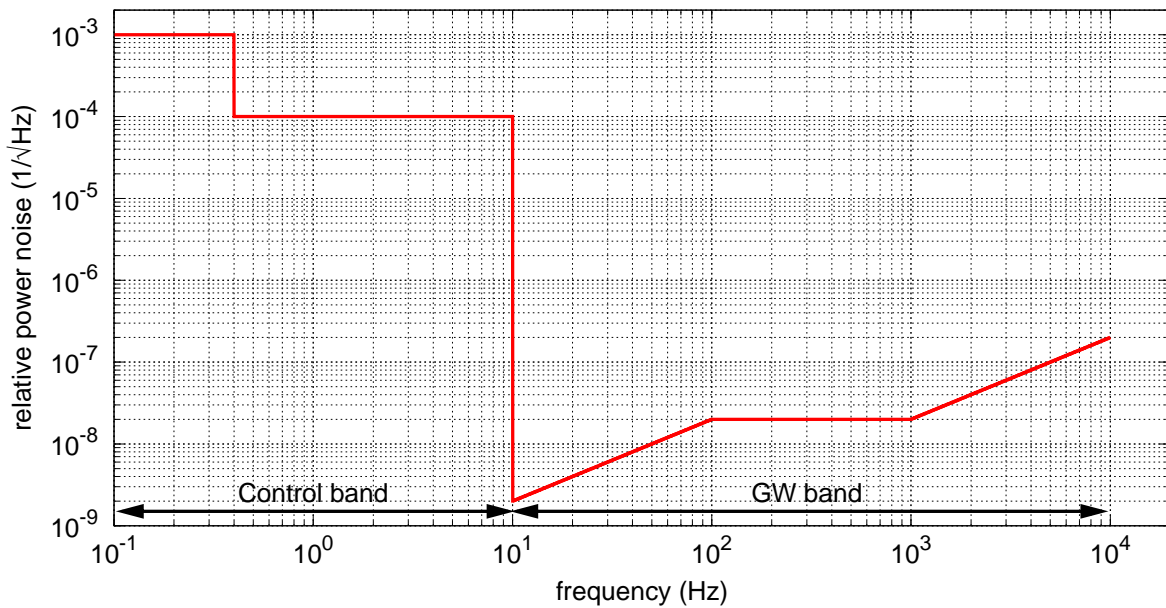
Figure 3.1: Advanced LIGO relative power noise requirements (plotted as the linear spectral density over the signal frequency).

For frequencies up to 10 Hz, the so-called "control band", the requirements on the power stability are not very stringent. Within the highly-sensitive observation band of the GW detector, the "gravitational wave band" (GW band), the requirements are much more stringent. The most demanding laser power noise requirement for Advanced LIGO is $2 \times 10^{-9} / \sqrt{\text{Hz}}$ at 10 Hz.

Several previous laser power stabilization experiments [1, 11, 114, 117, 128] have shown that power stabilization is exceedingly difficult at low frequencies and the stringent power stabilization specifications for the Advanced LIGO detector have not been demonstrated yet.

This chapter presents the power stabilization experiments of diode-pumped solid-state laser systems and addresses the challenge of approaching the shot-noise limited performance required for future GWDs. The main objective of the experiments described below was the stabilization of a solid-state laser system to the stability required for the Advanced LIGO detector and to investigate thoroughly noise sources which have limited power stabilization experiments so

far. Previous experiments showed that the key to a high power stability is the detection of the power fluctuations. Hence attention is focused on the development of improved detection schemes and low-noise control loop electronics.

Section 3.1 deals with the development and test of an improved power stabilization scheme for a GEO600-type high-power laser system [184]. To improve the understanding of the limitations in those setups, an optimized stabilization experiment was designed. A detailed description of this experiment, the optimizations made and its results are presented in Section 3.2. Section 3.3 summarizes the results achieved with the new experiment compared to previous ones.

3.1 12 W-laser stabilization experiment

Previous power stabilization experiments in our institute have used a GEO600-type injection-locked 12 W laser system [67, 121]. This type of system is well understood and reliable and has been operated in GEO600 for many years. Even though this laser system exhibits good noise characteristics, active stabilization of the laser is necessary to achieve the required stability levels. Therefore an identical second system was used to develop and test an improved detection scheme for the power fluctuation measurement and power stabilization experiment.

3.1.1 The GEO600-type injection-locked 12 W laser system

Achieving high output power with single-mode, single-frequency emission using only one laser is difficult. To obtain a high-stability laser system with high output power, two or more independent laser oscillators can be phase-locked. This technique is called "injection locking", because the output of the laser oscillator with higher stability, called *master laser*, is injected into the laser oscillator with less stability, the so-called *slave laser*. If the frequency difference between master and slave laser is within the so-called locking-range, the free-running oscillation of the slave laser is suppressed and the slave-laser frequency is determined by the master laser. Often a control loop is necessary to ensure that the frequency-difference is kept small enough to stay within the locking-range. Details of this technique are extensively explained elsewhere [24, 142, 150, 184]. The GEO600-type 12 W laser system uses this technique to lock a high-power slave laser with lower stability performance to a highly stable master laser. Figure 3.2 shows a schematic of the complete injection-locked 12 W laser system.

The master laser used is a commercially available, diode-pumped monolithic non-planar ring-oscillator (NPRO) Nd:YAG laser (InnoLight *Mephisto*™ 800). For fundamentals of operation refer to [83, 113]. The laser crystal acts as the laser medium and laser resonator simultaneously. This monolithic design leads to a very high intrinsic frequency-stability of the NPRO. A total pump power of 2 W leads to a nominal output power $P_{\mathrm{OUT}} = 800\,\mathrm{mW}$ of laser emission at 1064 nm. The very high beam quality of the emitted light ($M^2 < 1.1$) is obtained by mode-selective pumping of the laser crystal [48]. Unidirectional lasing is achieved by placing a strong permanent magnet beneath the NPRO crystal which causes unequal gains for the two propagation directions by means of the Faraday effect.

In general, the frequency of NPROs can be controlled by changing the laser crystal temperature [85], by using a piezo-electric transducer (PZT) glued on the laser crystal [84] and by changing the pump diode current [177]. The NPRO has a "noise eater" option to reduce the relative power noise at the relaxation oscillation frequency (at approx. 500 kHz). Although NPROs achieve shot-noise limited performance at MHz frequencies, the laser is dominated by technical noise at the frequency range interesting for GWDs.

The slave laser is a quasi-monolithic end-pumped Nd:YAG laser in a planar bowtie-configuration. It was designed and built at Laser Zentrum Hannover (LZH) for the GEO600
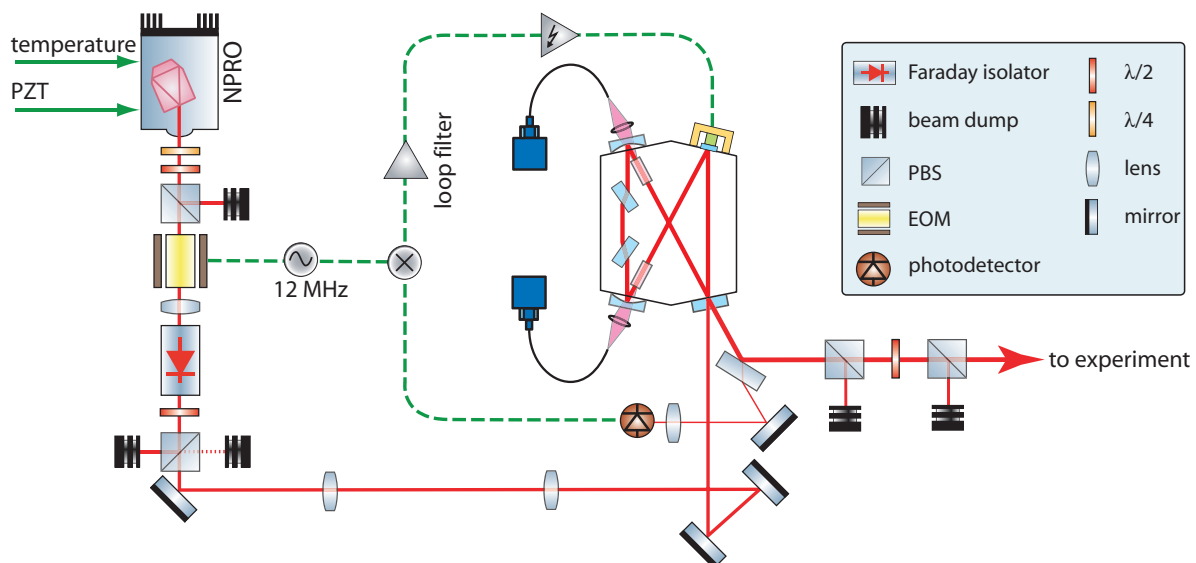
Figure 3.2: Schematic of the injection-locked 12 W laser system: The high-power slave oscillator is phase-locked to the master laser (NPRO) using the Pound-Drever-Hall (PDH) technique [39, 184].

gravitational wave detector [184]. The spacer of the laser resonator is made of Invar, an nickel steel alloy with a very low coefficient of thermal expansion. Invar has a fractional change in length per degree of temperature change of α=0.8 ppm/K, which is more than a factor of ten less compared to typical metals like steel or aluminum. The laser resonator is formed by two curved pump-mirrors and two flat mirrors. The resonator mirrors are glued to the Invar spacer by epoxy glue. This quasi-monolithic design results in a small sensitivity to environmental influences and hence a higher intrinsic frequency stability.

The slave laser is pumped by two temperature-controlled fiber-coupled laser-diode arrays (Jenoptik, model JOLD-30-CPXF-1L). Each of these laser diode arrays nominally emits 30 W at 808 nm. For their use in the slave laser the output power is reduced to 17 W each. By reducing the power, the lifetime of the laser diodes is significantly increased. With the total pump power of 34 W the slave laser emits around 12 W of output power at 1064 nm. To ensure that the output polarization of the laser is mainly in one plane (parallel to the table surface, p-polarization), two quartz Brewster plates are located in the beam path between the two curved mirrors. They introduce a round-trip loss of 42% for the s-polarization [184].

The slave laser cavity optical round-trip length is $L_{\mathrm{res,12W}} \approx 550$mm and hence the free spectral range (FSR) of the slave is calculated to be $\nu_{\mathrm{FSR,12W}} = c/L_{\mathrm{res}} \approx 540$ MHz. A PZT glued to one of the flat resonator mirrors acts as an actuator for the slave laser cavity length. The dynamic range of the PZT is more than 2 µm and is therefore sufficient to scan over more than four FSRs. The tuning bandwidth is limited by several resonances of the PZT above 55 kHz.

A MgO:LiNbO$_3$ electro-optic modulator (EOM) (New Focus, model 4003) resonant at 12 MHz provides the phase-modulation sidebands for injection-locking of the slave-laser on the NPRO beam. A single-stage Faraday isolator (FI)(LINOS Photonics, FR1060/8) placed behind the EOM protects the EOM and the master laser from laser light that comes from the 12 W laser oscillator towards the master laser. Because the slave laser cavity is completely

symmetric for both directions, the free-running oscillator direction switches with a typical frequency of 10 kHz.

The NPRO beam is mode-matched to the eigenmode of the slave laser resonator. Optimal mode matching is very important to obtain a stable injection-lock of the system. The two lasers are locked by using the Pound-Drever-Hall (PDH) technique [14, 39]. The NPRO beam partly enters the slave laser cavity through the output port and partly interferes with the high-power beam leaving the resonator at the output port. The signal obtained by a photodetector resonant at 12 MHz in transmission of the first steering mirror behind the slave laser cavity is demodulated and one obtains an error-signal for the injection-locking of the slave laser. The error-signal is used to generate a feedback signal by means of the injection-locking controller, which is amplified by a high-voltage (HV) amplifier before it is fed back to the PZT of slave laser cavity. The feedback loop keeps the frequency difference between the master laser and the slave laser cavity resonance within the so-called locking range to ensure a stable locked system. The locking-range of the 12 W laser system is approximately $\omega_{lock} = 2.6$ MHz depending on the linewidth of the slave-laser cavity and P_{master}/P_{slave} the ratio of optical power of the master laser to slave laser.

3.1.2 Optical setup of the 12 W-laser power stabilization experiment

The principle of the power stabilization experiments using the injection-locked 12 W laser system is illustrated in Figure 3.3.
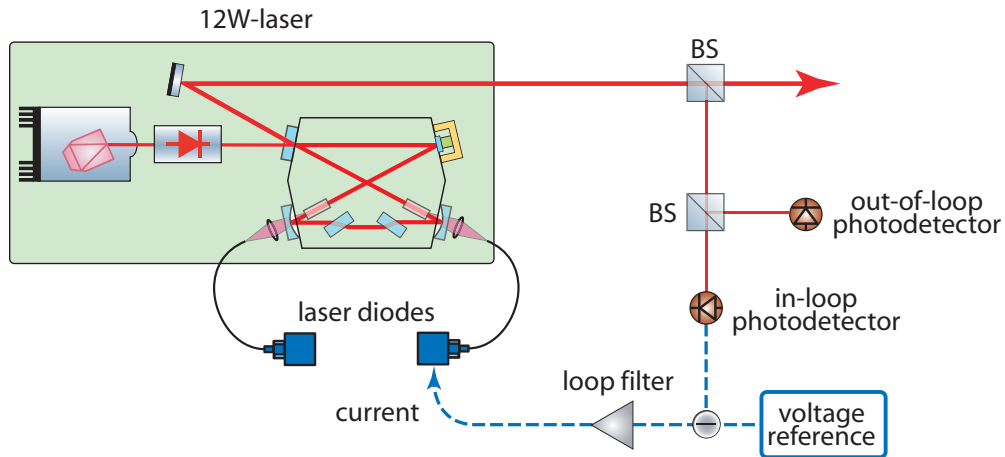
Figure 3.3: Principle of the 12 W-laser power stabilization setup.

A small fraction of the 12 W beam is split in two equal parts using a non-polarizing beam splitter and is detected by two photodetectors. The control signal for the power stabilization comes from the first photodetector, the in-loop detector (IL-PD). The second photodetector, the out-of-loop detector (OOL-PD), is used as an independent sensor. A DC-coupled loop design (see Section 2.2.1) is used in which the signal of the in-loop detector is compared to a very stable low-noise voltage reference. The difference is then processed by several filter stages to correct the output power by changing the drive current of the slave laser pump diodes.

Early experimental layouts used very elementary setups for the power noise sensing [138]. Using polarization optics, a small fraction ($\approx 1\%$) of the main laser beam (10.4 W) was taken and split at a 90:10 non-polarizing beam splitter. The smaller fraction was used for beam-pointing measurements with a silicon quadrant-photodetector (QPD). The remaining part of

the light was split in two equal parts by a 50:50 non-polarizing beam splitter. Each part was then detected using a custom designed InGaAs-photodetector suitable for high optical power. One result of these experiments is shown in Figure 3.4 as an example.
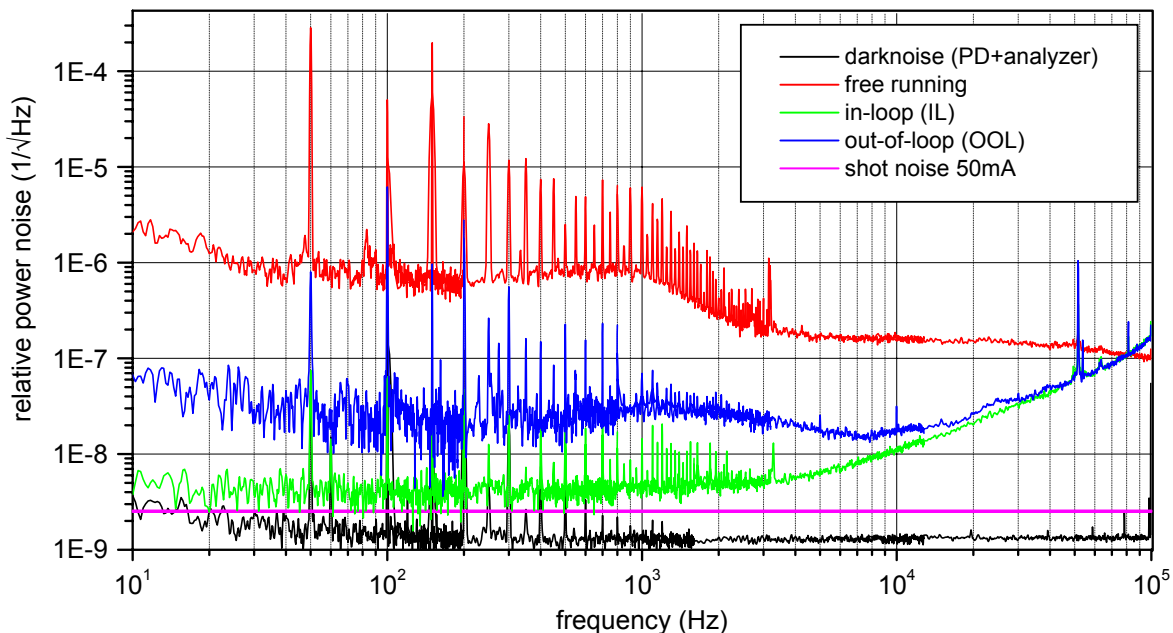
Figure 3.4: Results of the 12 W-laser power stabilization experiment performed in [138].

The in-loop (IL) detector shows nearly shot-noise together with electronic noise or loop-gain limited performance, while the out-of-loop (OOL) measurement is dominated by excess noise across the complete frequency range. In those experiments, beam pointing seemed to be a general problem, because generation of air-fluctuations on the optical table caused the out-of-loop noise level to increase significantly.

Since beam pointing seemed to be one major noise contributor in previous experiments, an improved detection-scheme for the power fluctuation measurement was set up. An outline of this new experimental setup is shown in Figure 3.5. The complete detection including an optical ring-resonator was placed in a vacuum tank to minimize the influence of air-currents. The ring-cavity, also known as a *pre-modecleaner* (PMC) [161] is a three-mirror Fabry-Perot ring-cavity with a fixed spacer and a round-trip length of $L_{\mathrm{res,PMC}}$=420 mm. It can be used to improve the properties of the laser beam [114, 179] and was initially foreseen to filter the laser technical RPN excess at RF-frequencies and to provide a $\mathrm{TEM_{00}}$ mode downstream of the PMC. It acts also as a spatial mode filter that reduces laser beam geometry fluctuations and beam pointing of the incoming laser beam [94]. A schematic of the pre-modecleaner used in this experiment is displayed in Figure 3.6.

The input and output mirrors M1 and M2 are flat and have an equal power transmissivity of T_{p}=1.5 % for p-polarization and T_{s}=700 ppm for s-polarization. The end mirror M3 has a radius of curvature of rc=-1 m and a transmissivity of T_{c}=30 ppm for both polarizations.

The resonator is almost impedance-matched, as the input and the output coupler mirrors were coated in the same coating run and the transmission of the curved mirror is very small compared to the transmissivity of the input and the output coupler. To ensure a high rigidity of the PMC all three mirrors are glued onto a fused silica spacer. To control the length of
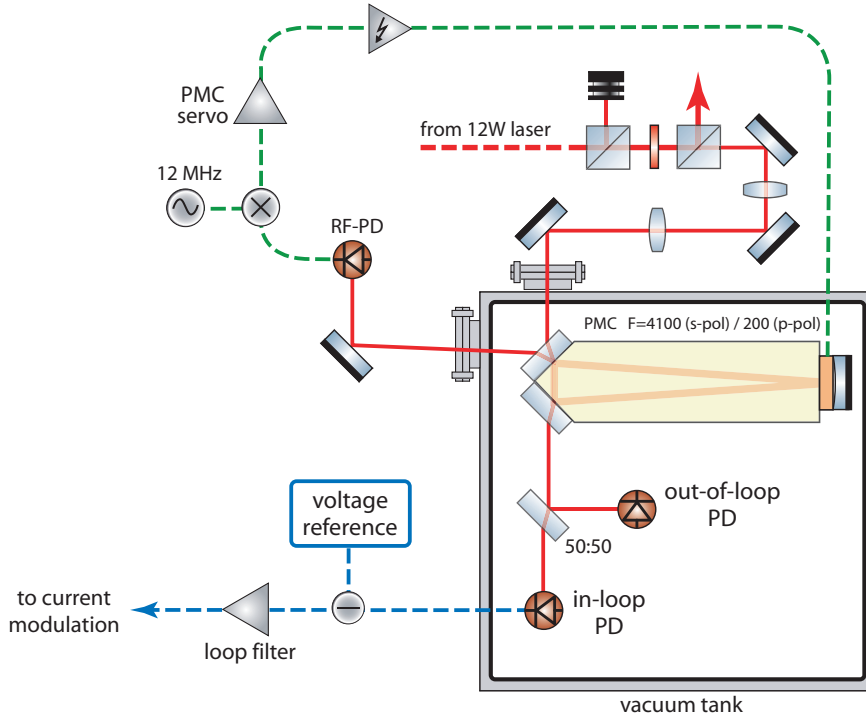
Figure 3.5: Improved 12 W-laser power stabilization scheme placed in a sealed tank.
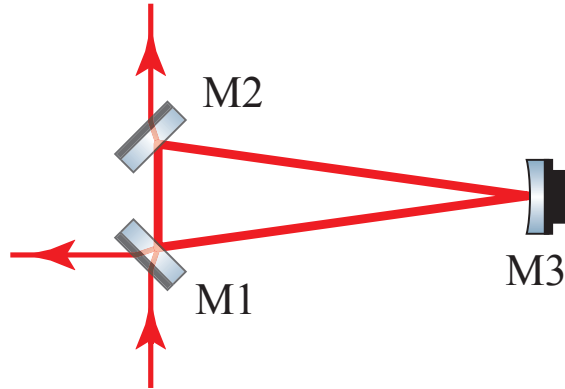
Figure 3.6: Schematic of the triangular Fabry-Perot filter-cavity, the so-called *pre-modecleaner* (PMC).

the PMC and thereby change the resonance frequency of the cavity modes, a piezoelectric transducer (PZT) is glued between the curved mirror M3 and the spacer. The upper frequency limit for this PZT-actuator is $\approx 13\,\mathrm{kHz}$, set by the first mechanical resonance. The beam waist position of the cavity's fundamental eigenmode is between the two flat mirrors and has a radius of $\omega_0 \approx 372\,\mathrm{\mu m}$.

Because of the polarization-dependent reflectivity of the mirrors M1 and M2, the finesse of the PMC depends on the polarization of the input light. The finesse in s-polarization is $\mathcal{F}_{\mathrm{s}} \approx 4100$ and in p-polarization $\mathcal{F}_{\mathrm{p}} \approx 200$. The free spectral range of the PMC can

be calculated to be $\nu_{\mathrm{FSR,PMC}} \approx 714\,\mathrm{MHz}$. The linewidth $\triangle\nu$ (full width at half maximum (FWHM)) of the PMC is calculated to be $3.57\,\mathrm{MHz}$ in p- and $174\,\mathrm{kHz}$ in s-polarization.

The PMC has some properties which are helpful for the power stabilization experiment. First, the PMC acts as a low pass filter for power fluctuations of the incoming laser beam. The transfer function of a modecleaner is shown in Figure 3.7.
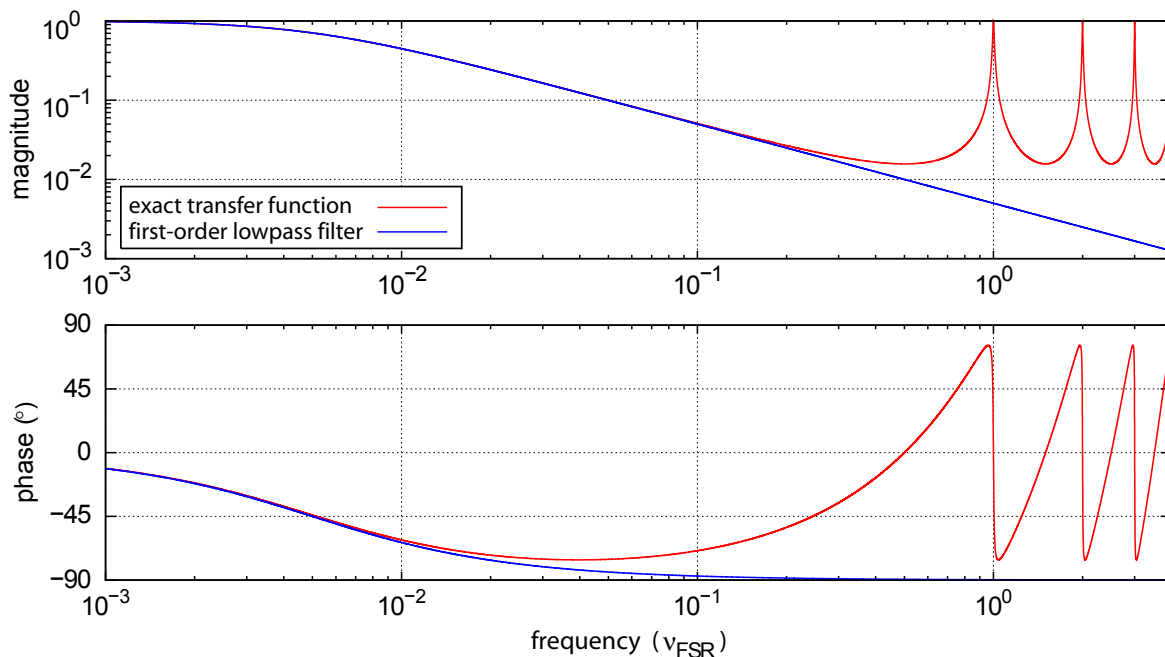
Figure 3.7: Calculated transfer function of a PMC with a finesse $\mathcal{F}{=}100$.

For Fourier frequencies $f \ll \nu_{\mathrm{FSR}}$ the response of the PMC can be approximated by a first-order low-pass filter. The corner-frequency can be calculated to

$$f_0 \approx \frac{\nu_{\mathrm{FSR}}}{2 \cdot \mathcal{F}} = \frac{\triangle\nu}{2}, \tag{3.1}$$

where $\mathcal{F}$ is the finesse of the cavity. The PMC has a 3-dB corner-frequency $f_0{=}87\,\mathrm{kHz}$ for the high-finesse mode and $1.79\,\mathrm{MHz}$ for the low-finesse mode respectively. This largely reduces the technical noise of the laser at higher frequencies, but has no effect in the frequency-region of interest for this experiment.

The second improvement due to the PMC is the filtering of beam pointing and beam-geometry fluctuations. Beam pointing and beam-geometry fluctuations of the laser beam at the input of the PMC can be described by higher-order modes of the eigenmode-basis of the PMC. During normal operation the length-control scheme keeps the TEM_{00}-mode resonant in the PMC. As the resonance-frequencies of $\mathrm{TEM}_{\mathrm{lm}}$ resonator eigenmodes are generally different, the higher-order modes are not resonant and will be suppressed. A more detailed description of this topic can be found in [94].

Lastly, the phase shift in a Fabry-Perot ring-cavity with an odd number of round-trip reflections depends on the polarization of the light, which leads to different resonance-frequencies for s- and p-polarized light. Therefore, a PMC stabilized such that one polarization is resonant, acts as a polarizer with a high extinction-ratio [135]. With the finesse $\mathcal{F}$ and the free spectral

range ν_{FSR} of the PMC, the power transmission through the PMC, locked at resonance, is given by

$$G(\triangle f) = \frac{1}{1 + \left(\frac{2\mathcal{F}}{\pi}\right)^2 \sin^2\left(\frac{\pi\triangle f}{\nu_{\text{FSR}}}\right)}, \tag{3.2}$$

where $\triangle f$ is the frequency-detuning from resonance. For a triangular cavity, like the PMC, locked to the TEM_{00}-mode in one polarization, the TEM_{00}-mode of the other polarization is resonant half a free-spectral range away. If the PMC is locked at resonance for s-polarization, the calculated transmission for p-polarized light is 42 dB (68 dB vice versa). In this experiment, beam splitters and photodiodes behind the PMC are slightly polarization sensitive. Hence an extra attenuation of the wrong polarization and especially of polarization-fluctuations by the PMC reduces the coupling of polarization-fluctuations into an unequal sensing of the IL and OOL photodetector.

The PMC was locked by means of the Pound-Drever-Hall technique to the laser. In front of the PMC the beam passes two lenses to match its transversal mode shape to the eigenmode of the PMC. A half-wave plate can be used to select one of the two orthogonal polarization modes of the PMC. The PMC is typically operated in s-polarization because this maximizes the filtering effect for laser power fluctuations, beam-geometry fluctuations and beam pointing of the incoming laser beam. This is very important because previous investigations have shown that the responsivity of the photodiodes varies across their surfaces [119, 138] , so that variations in the beam position or size on the photodiodes lead to variations in the photocurrent [94]. A more detailed analysis on this will be given in Section 4.3.

The incoming beam enters the vacuum tank through an AR-coated wedged window, is reflected at the PMC and exits the vacuum tank again through another window. The reflected beam passes a half-wave plate and a polarizing beam splitter to attenuate it to a lower power level which is detected with a photodetector resonant at 12 MHz. The phase-modulation sidebands to lock the PMC are the same as those used for injection-locking of the 12 W laser system. The obtained error-signal for the PMC length-control is amplified and fed back to the PZT of the PMC.

For the power noise detection, thermo-electrically cooled 2 mm InGaAs photodiodes made by Hamamatsu (model G5832-12 [56]) are used in a special transimpedance configuration, which enables both low-noise and high-current operation. The key to this design is the combination of an ultra-low-noise amplifier as the input stage with a high-current output amplifier within the feedback loop of the transimpedance amplifier (TIA). The total input noise of this configuration is defined by the input amplifier, as long as the open-loop gain is large enough to suppress the noise of the output amplifier.

A reverse bias of 8 V was chosen as a trade off between the heat dissipation in the photodiode and a linear operating range. The bias voltage also decreases the parasitic capacitance associated with the photodiode and therefore increases the bandwidth of the photodetector. The transimpedance gain was set to $R_{\text{TIA}}{=}100\,\Omega$, which gives a good signal-to-noise ratio (SNR) for the photodetector supplied with $\pm15\,\text{V}$ and $\approx 100\,\text{mA}$ of maximum photocurrent. In this configuration the complete photodetector showed a linear behavior up to 140 mW of optical power, which is shown in Figure 3.8. The measured responsivity was $\mathcal{R}{=}0.74\,\text{A/W}$, which corresponds to a quantum efficiency of $\approx 86\,\%$. The maximum optical power was limited by the long-term cooling capability of the built-in thermoelectric cooler (TEC).

For the power stabilization experiments two identical photodetectors were used, one for the stabilization itself (in-loop, IL) and the other for an independent measurement (out-of-loop,
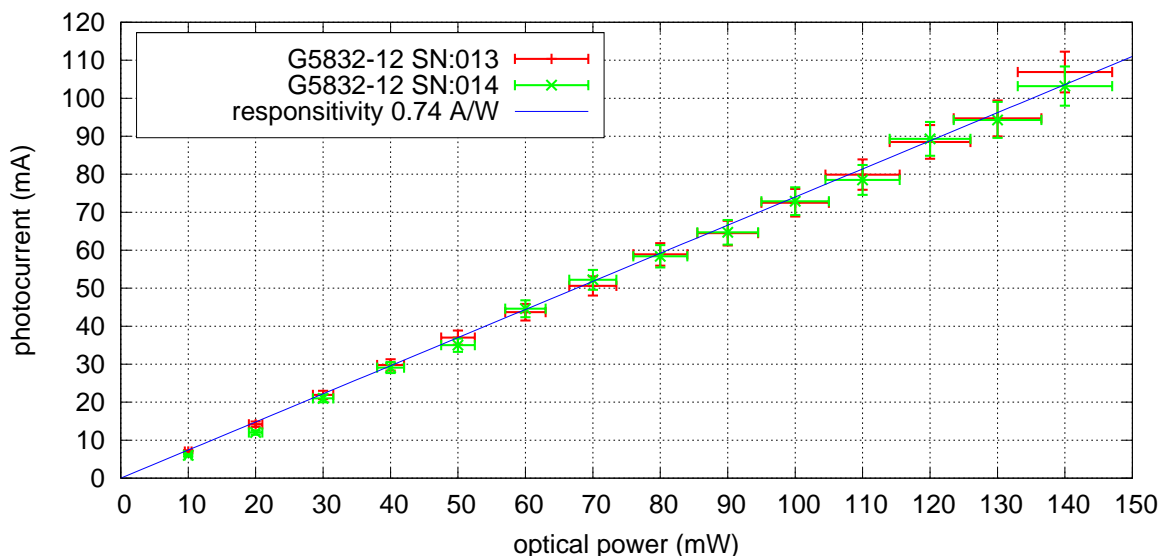
Figure 3.8: Hamamatsu G5832-12 InGaAs photodetector P-I curve.

OOL). For this experiment the light level incident on each photodetector was approximately 65 mW and was thus in the linear regime of the detector.

3.1.3 Laser and power actuator characterization

In order to set up the power stabilization loop, the system was characterized first. A typical noise spectrum of the free-running laser system measured in front of and behind the PMC is shown in Figure 3.9. The entire noise spectrum of the free-running laser system before the PMC is dominated by resonator internal noise of unknown origin. It is not dominated by pump power fluctuations, because reducing the pump power fluctuations by passive filtering or active stabilization does not reduce the total noise of the laser system. At the PMC, beam pointing and beam-geometry fluctuations are converted into power fluctuations. This increases the noise level at low frequencies behind it. The requirements for the Advanced LIGO detector are plotted for comparison.

In order to be able to suppress the free-running power fluctuations of the laser system, the dynamic range of the actuator has to be sufficient. Several previous power stabilization experiments have used the pump-current of the laser as the power actuator. This is a very easy and effective way to modulate the output power of a laser over a large range without the need of additional optical components in the beam-path. Thus the current of the laser diodes of the slave-laser has been chosen as the power actuator for the injection-locked laser system.

The laser diodes were supplied by low-noise, switching power-supplies (Delta Elektronika, SM 15-100). These power-supplies have an analog control-input to adjust the output current. The transfer function measured from this control-input to output current has a bandwidth of a couple of hundred hertz only (see Figure 3.10). As a direct modulation of the pump current via the control input of the power-supplies is too slow for the power stabilization loop, a current bypass is used. Figure 3.11 shows the principle of the current bypass.

The current bypass is a voltage-controlled current sink, which basically consists of a power-MOSFET with a shunt resistor in series connected to the anode and cathode of the laser diode in parallel. The gate of the MOSFET is driven by an operation amplifier (opamp) which
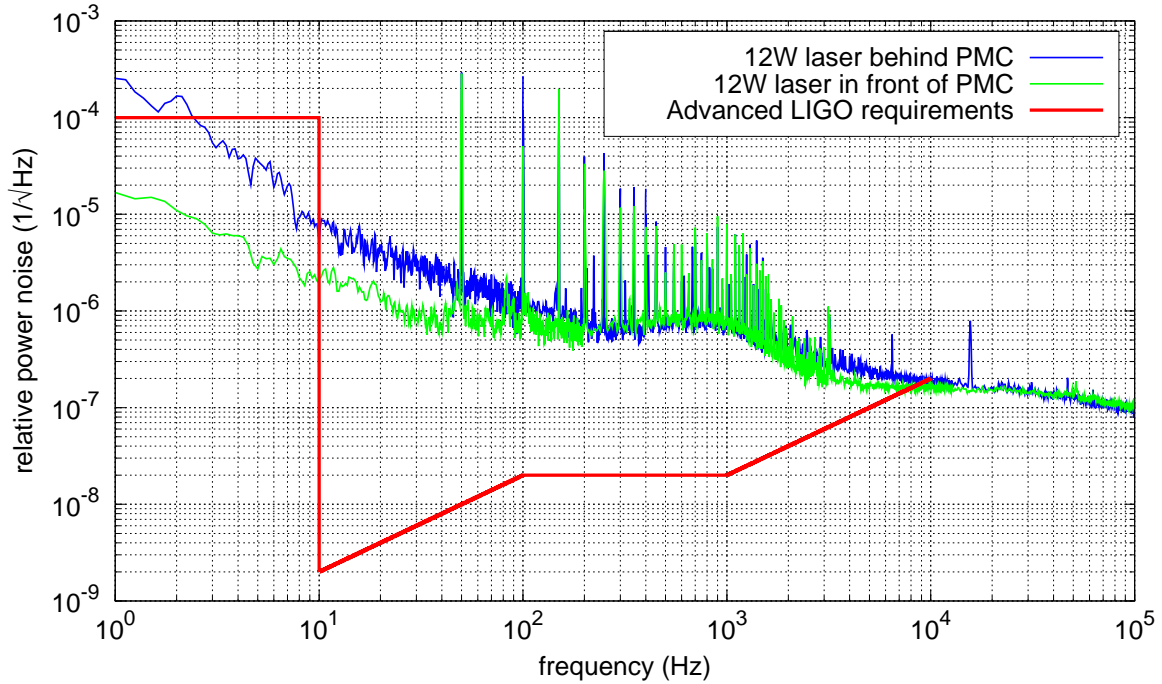
Figure 3.9: Power fluctuation spectra of the free-running 12 W injection-locked laser
system measured in front of and behind the PMC.

receives a feedback from the shunt resistor. The control-signal is fed to the input of this opamp.
The amount of current bypassed is then proportional to the voltage applied to the opamp. As
the circuit can only subtract current from the laser diode, an offset voltage is applied to the
control-input to allow a positive and negative modulation with the actuator.

An existing design has been improved and optimized to achieve a higher current modulation
capability while having a high modulation bandwidth in order to achieve a high loop gain of
the power stabilization . The new current shunt can sink up to 2 A which is limited by the
maximum power dissipation of the shunt resistor used. A fuse limits the maximum current
drawn by the shunt to protect the circuit. Either a ground-referred or a differential input
can be selected by using an internal switch. Also a low-noise voltage reference to apply the
offset to the input is implemented. Figure 3.12 shows the measured transfer function from
input-signal to current-modulation of the current shunt.

The modulation bandwidth depends slightly on the current drawn and is a couple of hundreds
of kilohertz which is sufficient for the planned stabilization. The response of the laser diodes
by actuating the current is flat up several megahertz. The laser dynamics however determines
the useful bandwidth of this actuator due to a transfer function pole at a frequency that
corresponds to the inverse of the effective lifetime of the upper laser level. The calculation
of the transfer function of the pump to output power modulation of an injection-locked laser
system is explained in [60, 184]. The response of the slave-laser output power to variation
of the pump power is shown in Figure 3.13. The measured modulation transfer function of
the slave-laser exhibits one pole at 45 kHz which is independent from the laser diode used for
modulation.
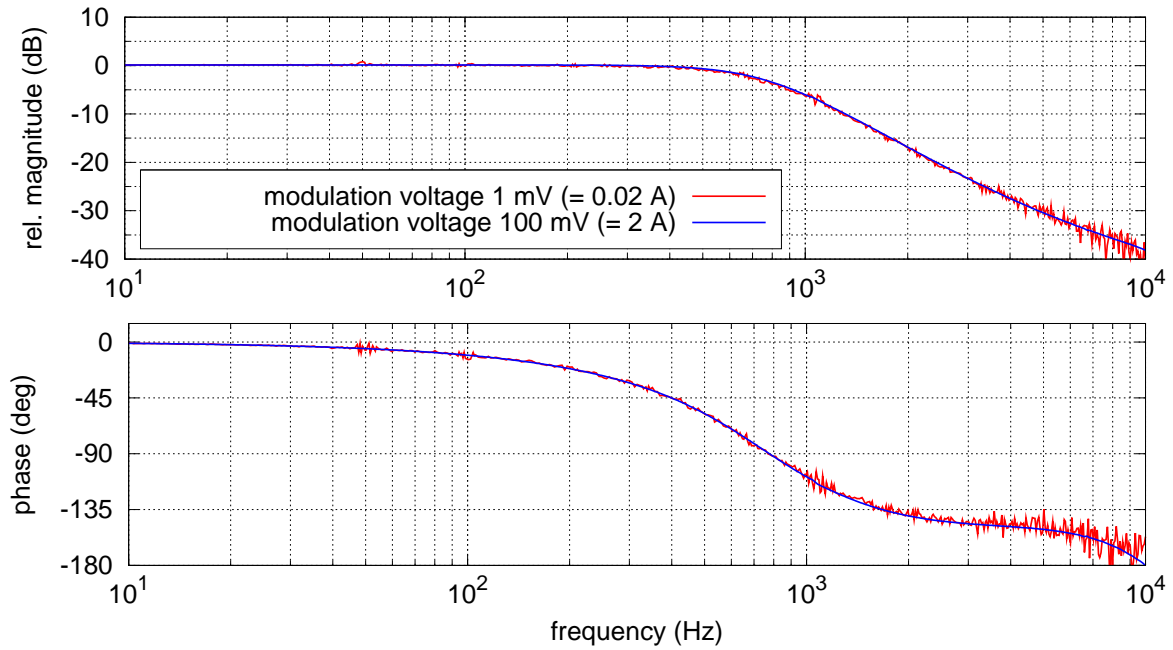
Figure 3.10: Transfer function of the laser power-supply via the analog control-input.
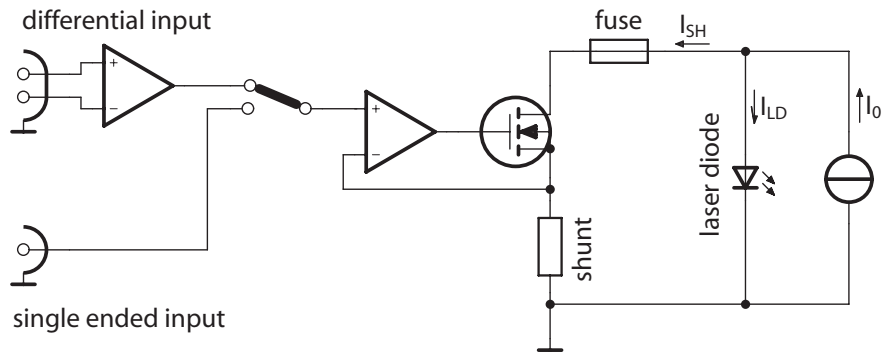
Figure 3.11: Principle schematic of the voltage-controlled current sink.

Finally, the frequency response of the entire actuator chain from the input of the current shunt to the high-power photodetectors downstream of the PMC has been measured and is illustrated in Figure 3.14. The measured overall response is dominated by the pole of the slave laser at 45 kHz and the filter cavity of 87 kHz in the high-finesse mode. Equation 3.3 describes the response of the plant $G_P(s)$, including the actuator, laser and the PMC, calibrated to one Watt of output power per volt of control signal $\left(G_P = P_{opt}/U_{mod} \quad [G_P] = \frac{W}{V} \right)$.

$$G_P(s) = \frac{0.16}{\left(1 + \frac{s}{2\cdot\pi\cdot45\,\text{kHz}}\right)\cdot\left(1 + \frac{s}{2\cdot\pi\cdot87\,\text{kHz}}\right)} \tag{3.3}$$
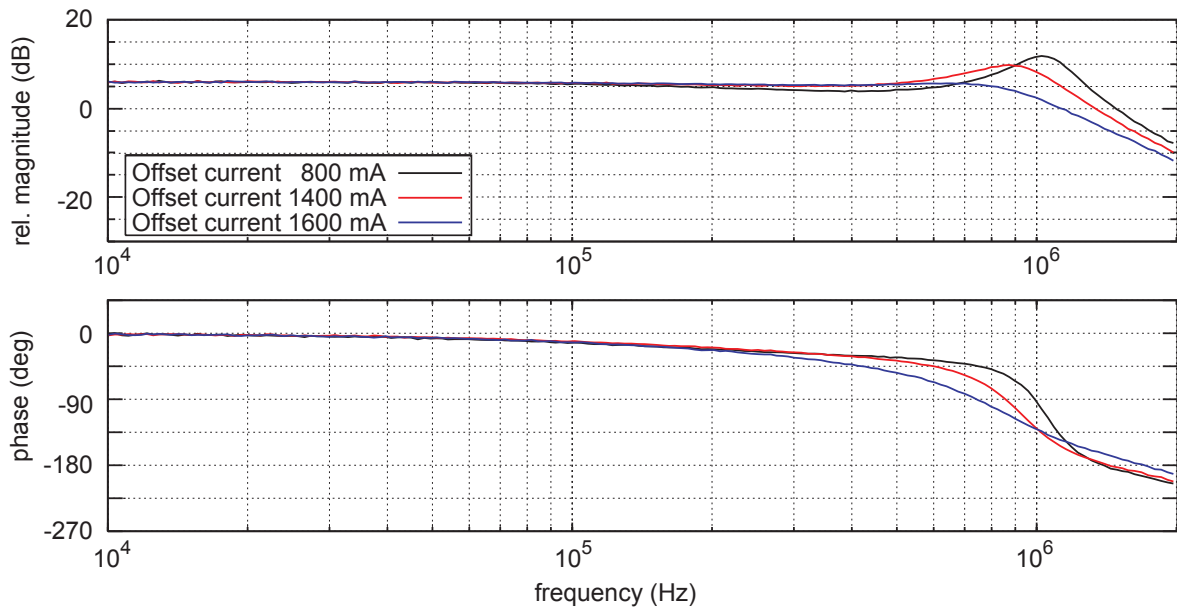
Figure 3.12: Transfer function from input-signal to current-modulation of the current shunt.
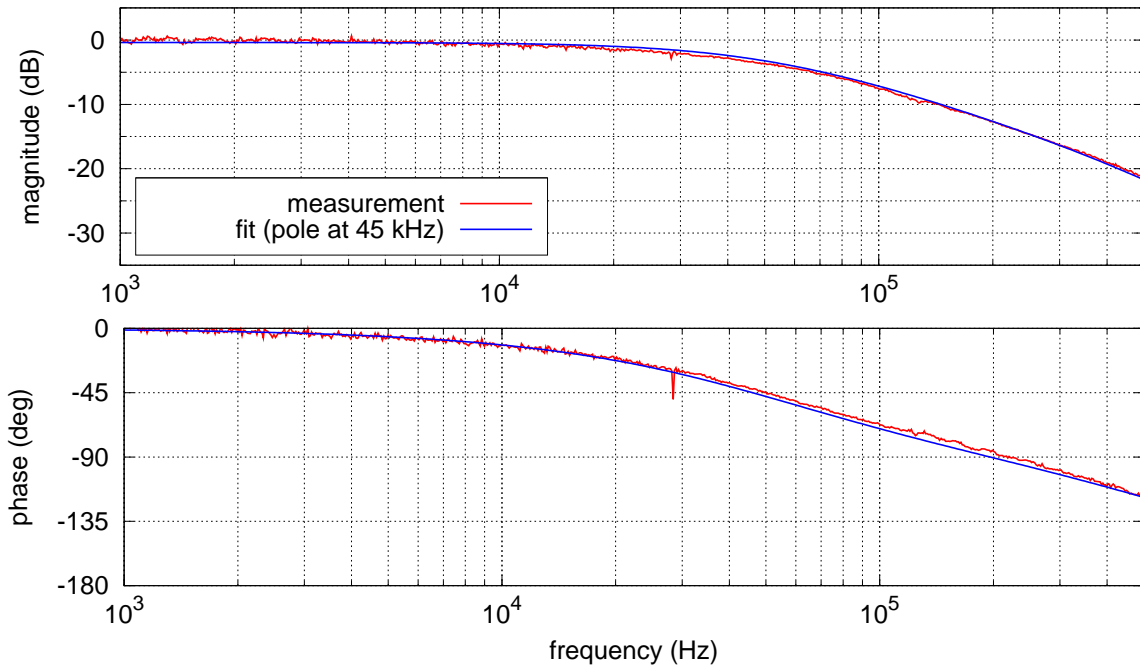
Figure 3.13: Transfer function of the slave-laser output power by variation of the pump power (in $W_{1064\,nm}/W_{808\,nm}$).
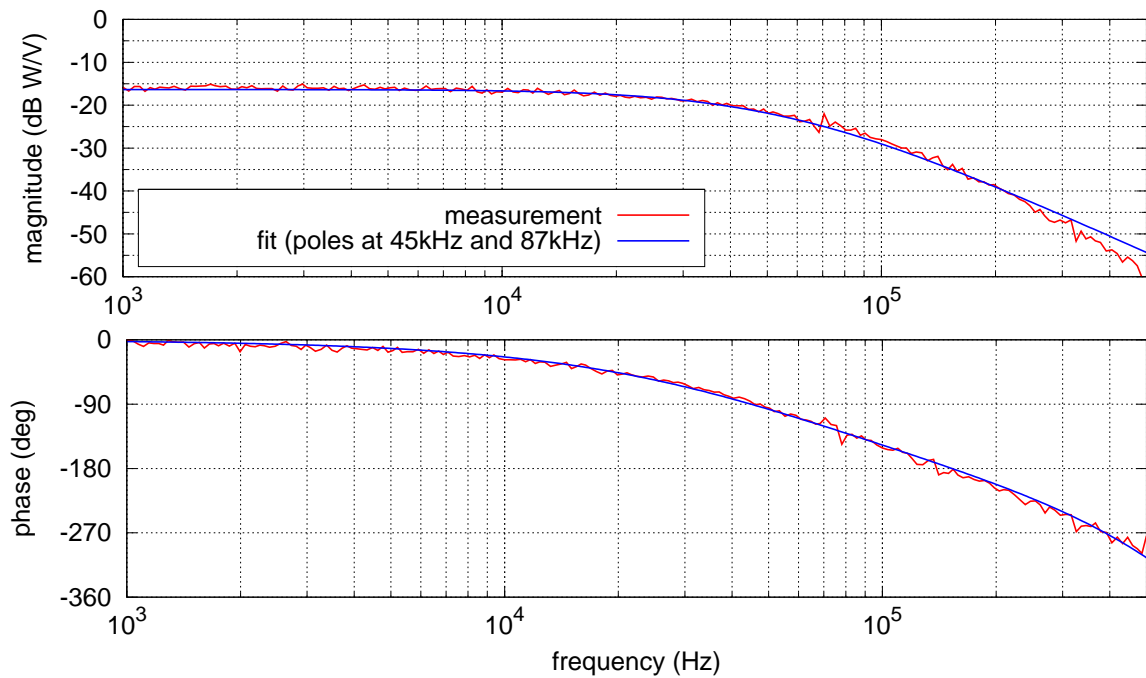
Figure 3.14: Transfer function measured from the input of the current shunt of the 12 W-laser to the high-power photodetectors behind the filter cavity.

3.1.4 Power stabilization loop design

With the knowledge of the frequency response of the system shown in Figure 3.14 one can design the required controller-response. For the power stabilization a DC-coupled loop design was chosen. The block diagram of the stabilization loop is illustrated in Figure 3.15.
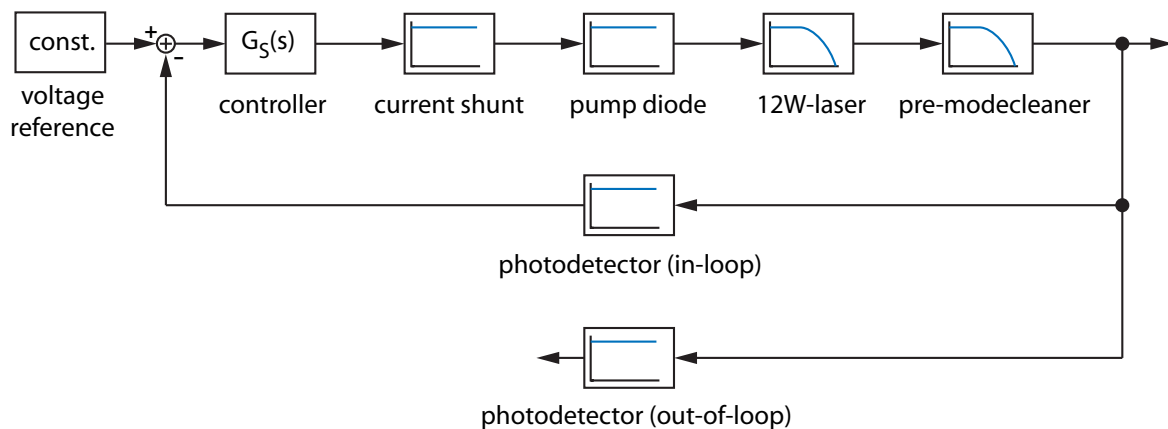
Figure 3.15: Block diagram of the power stabilization loop for the 12 W laser system.

The signal obtained from the in-loop photodetector is compared with a highly-stable voltage reference. The difference is amplified by the power stabilization controller and fed back to the current shunt connected to one of the two pump-diodes of the slave-laser. The response of the plant G_P has to be taken into account for the loop design. The selection and filtering of the

voltage reference and the description of the power stabilization controller itself will be given in the following sections.

Voltage reference for DC-stabilization

Since the minimum noise level achievable with a DC-coupled loop is limited by the stability of the voltage reference used, some investigations on the performance and on the filtering of available voltage references were performed. The better the voltage reference, the better the achieved in-loop performance and hopefully also the out-of-loop performance. There are many factors to be considered when selecting the optimum reference. Typical specifications of some selected voltage references are listed in Table 3.1. It covers all of the important parameters for the stabilization: reference output voltage, line regulation, stability, and noise.

type	voltage V_{out} (V)	line regulation LR (ppm/V)	temperature coefficient TempCo (ppm/K)	output voltage noise	
				$V_{\text{n,pp}}$ (µV$_{\text{pp}}$) $0.1\,\text{Hz} \leq \text{f} \leq 10\,\text{Hz}$	v_{n} (nV/$\sqrt{\text{Hz}}$) f=1 kHz
AD586	5	20	2–25	4	100
AD587	10	10	5–20	4	100
LT1021-5	5	2	2–3	3	75
LT1021-7	7	1	2–3	4	90
LT1021-10	10	0.5	2–5	6	125
LT1027	5	3	1–3	3	65
LT1236-5	5	2	2–10	3	75
LT1236-10	10	0.5	2–10	6	125
MAX6250	5	2	1–2.5	3	80
MAX6350	5	2	0.5–1	3	80

Table 3.1: Specifications of selected voltage references. Vendors: AD=Analog Devices[1], LT=Linear Technologies[2] and MAX=Maxim Integrated Products[3]

First, the absolute value of the *reference-voltage* V_{out} is relevant. It defines the relative noise of the reference by dividing the noise by the output voltage level. This relative noise of the reference is very important for the design because it determines the minimum relative noise level of the laser system which can be achieved. A higher reference-voltage level also reduces the impact of other electronic noise sources when compared with the signal from the photodetector.

Line regulation (LR) is the capability to maintain a constant output voltage level despite changes in the supply voltage level. It is expressed as change in the output voltage relative to the change in the supply voltage. For low-noise references this is very important, because even small changes in the supply voltage affect the output signal of the reference. The relatively high noise of a standard voltage regulator should not affect the noise performance of the voltage reference.

In addition the temperature induced drift of the reference voltage has to be small. The *temperature coefficient* (TempCo) of the reference output voltage specified in ppm/°C is more important for long-term stability. Changes in temperature of the electronic assembly

---

[1]http://www.analog.com
[2]http://www.linear.com
[3]http://www.maxim-ic.com

can be rather high over a couple of hours or days if not actively stabilized. The long-term stability of the laser power has to be in the order of 1% per day. With a typical temperature coefficient of 10 ppm/K the induced relative change of 10^{-5}/K in laser output power is negligible. Nevertheless one has to watch out for temperature fluctuations due to air currents at a couple of hertz. Hence adequate thermal shielding is recommended.

The most important parameter is the *voltage noise* at the reference output. The $1/f$-component is usually specified in μV_{pp} over a 0.1 Hz to 10 Hz bandwidth ($V_{n,pp}$). The output voltage noise spectral densities v_n at 1 kHz are given too. All voltage references have too high output noise to serve as a reference for the laser power stabilization without further reduction of the output noise level.

One could stack multiple voltage references in series to reduce their noise. The references' DC outputs add linearly, their uncorrelated internal noise sources add geometrically. For example, adding four equal 2.5 V voltage references in series one obtains a 10 V reference, but the noise only doubles. The problem here is that the noise of voltage references often does not scale with the output voltage. For example the 5 V voltage references AD586 and LT1021-5 do not have half the output noise of their 10 V equivalent AD587 or LT1021-10. The low voltage output references often offer little less output noise as their high voltage equivalent.

In theory, adding a low-pass filter to a reference's output reduces noise. In practice, a low-pass RC-filter for suppression of noise frequencies below 10 Hz requires large values of series resistance and shunt capacitance. Unfortunately, a high-value series resistor introduces resistance errors and thermal noise, and a shunt capacitor's leakage resistance forms an unpredictable and unstable shunt path. Together, the two components form a noisy and highly temperature-dependent voltage divider that directly affects the reference's accuracy and long-term stability. Nevertheless, filtering is the only way to reduce the noise level to the requirements of the power stabilization.

Unfortunately, for a low-pass filter with low corner frequency one cannot use ceramic capacitors because of their piezoelectric behavior and poor volumetric efficiency. Tantalum or aluminum-electrolytic capacitors have a considerable leakage current which is moreover a function of their operating voltage and temperature. Electric double-layer capacitors, also known as supercapacitors or ultracapacitors, are electrochemical capacitors that have high energy density compared to commonly used capacitors. They offer a capacitance of several farads, an improvement of several orders of magnitude in capacitance compared to conventional capacitors of the same geometrical size. The problem of leakage current is the same as for conventional tantalum or electrolytic capacitors. The internal series resistance (ESR) is also comparable to classic capacitors which are not trimmed to be low ESR types. The internal series resistance limits the factor of suppression in a classical low-pass RC filter. The capacitor-leakage current introduces high noise at low frequencies.

Foil capacitors are the best choice to design the lowpass filter for the DC-reference. They offer good volumetric efficiency, low leakage currents and are less sensitive to their operating voltage and temperature compared to tantalum or electrolytic capacitors. We used metalized polyethylene-terephthalate (PET) film capacitors (WIMA, MKS2 and MKS4) which are available up to 220 µF. Several distributors have values up to 33 µF typically in stock.

Figure 3.16 shows the implemented filter structure, an active second-order Sallen-Key low-pass filter. The opamp provides buffering between the filter stage and the load connected to it, so that the filter stage can be designed independently of the other control loop electronics. The filter has been optimized for both high noise-suppression for the voltage reference and low additional noise. The values of the resistors R1 and R2 for the filter are chosen to 100 kΩ,
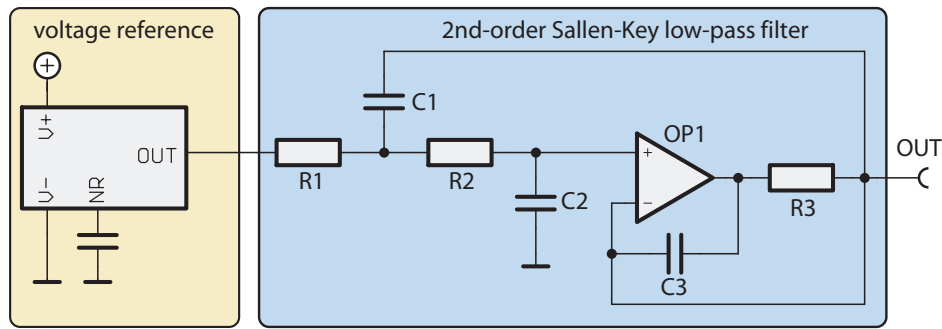
Figure 3.16: Filter structure of the implemented filter for the DC voltage-reference.

which offers a very low corner frequency of the filter with small values for the filter capacitors. For the capacitors C1 and C2, $4.7\,\mu\text{F}$ or $33\,\mu\text{F}$ foil capacitors are used. The corner frequency is defined by the RC-product of the resistors R1/R2 and the capacitors C1/C2 and can be calculated to $48\,\text{mHz}$ for the $33\,\mu\text{F}$ capacitors and to $338\,\text{mHz}$ for $4.7\,\mu\text{F}$. With OP1 being a low-noise operational amplifier (e.g. AD797 or LT1028) this gives a good filtering by minimized overall noise of the filter circuit. Resistor R3 improves the stability with capacitive loads, C3 adds a zero in the feedback counteracting the pole formed by the load capacitance with R3. The total input noise of the filter at low frequencies is dominated by the input current noise and at higher frequencies by the input voltage noise of the opamp used.

LISO[4], a program for linear simulation and optimization of analog electronic circuits written by Gerhard Heinzel, was used for numerical simulation of the filter circuit. The simulation of the filter circuit with different voltage reference levels showed that with a $5\,\text{V}$ reference, the relative noise level of $2\times10^{-9}/\sqrt{\text{Hz}}$ at $10\,\text{Hz}$ cannot be achieved. The best noise performance of the voltage reference including the filter is achieved using a reference with $10\,\text{V}$ output voltage. Three different voltage-references were tested: AD587, LT1021-10 and LT1236-10. The AD587 gives the lowest relative noise of the references and is thus used for all experiments. The measured and simulated performance of the voltage reference with and without filter circuit is shown in Figure 3.17. With the relative voltage noise of the filtered $10\,\text{V}$ reference using $4.7\,\mu\text{F}$ or smaller, the goal of a total stability of $2\times10^{-9}/\sqrt{\text{Hz}}$ at $10\,\text{Hz}$ is not achievable so capacitors with $\text{C}>4.7\mu\text{F}$ have to be used. Using a filter with $33\,\mu\text{F}$ the DC-reference is not the limiting part anymore.

Power stabilization controller design

The structure of the power stabilization controller is shown in Figure 3.18. The voltage reference was filtered by the second-order low-pass filter described above. The signal from the in-loop photodetector (w) was first buffered by either a single-ended or differential input amplifier. Both, self-made and commercial differential amplifiers were tested. As the signal from the detector is DC-coupled and has a level around $10\,\text{V}$ for best signal-to-noise ratio, only a gain of $0\,\text{dB}$ could be used. In the low-gain regime the self-made differential amplifier performs much better than the integrated circuits one can buy, because all commercial amplifiers offer either high gain or poor noise performance at low frequencies (e.g. SSM2141 or SSM2143 typ. $> 20\,\text{nV}/\sqrt{\text{Hz}}$ at $10\,\text{Hz}$).

---

[4]ftp://ftp.rzg.mpg.de/pub/grav/ghh/liso/
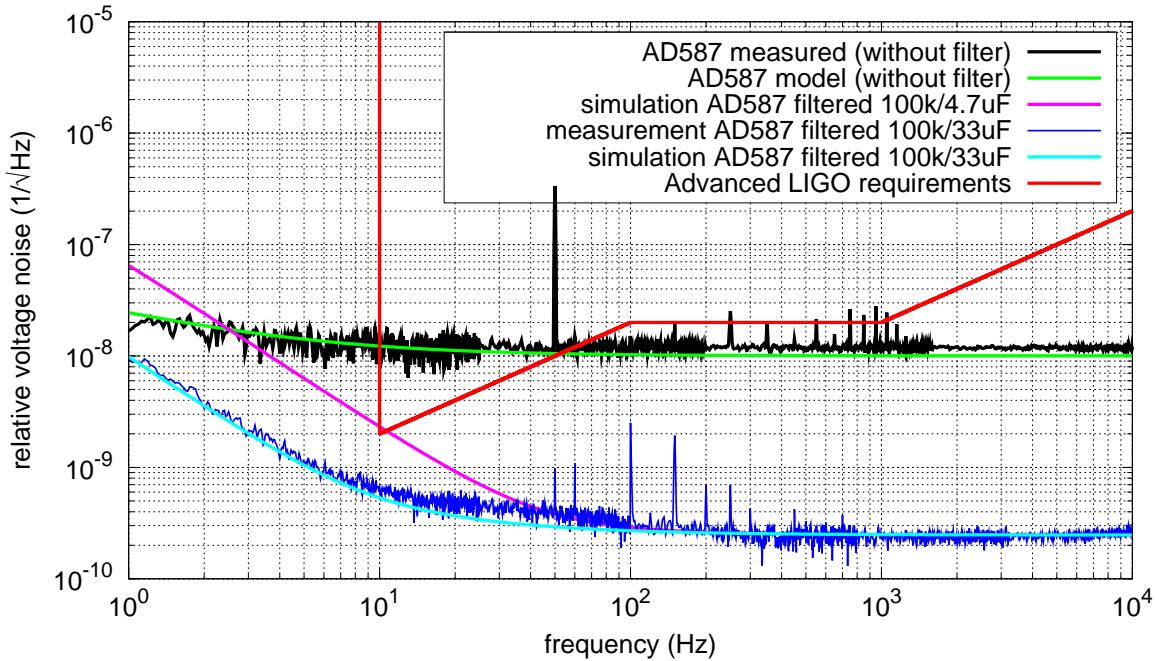
Figure 3.17: Results of the second-order low-pass filtered voltage reference.
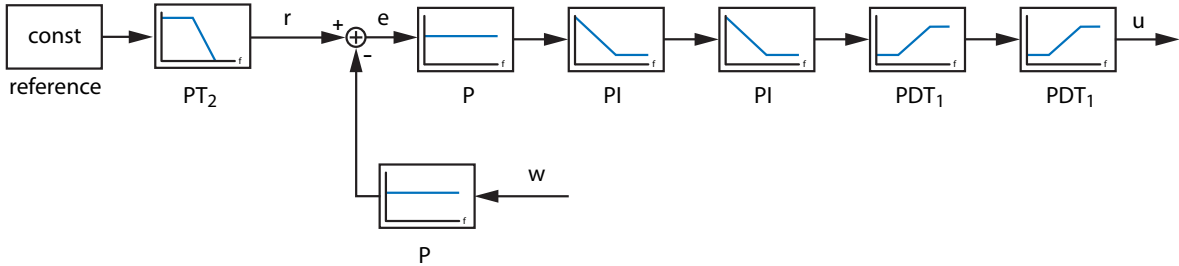
Figure 3.18: Block diagram of the power stabilization controller for the stabilization of the 12 W laser system.

For buffering in a single-ended scheme several circuits were tested. Either a single low-noise operational amplifier (e.g. AD797, LT1028, LT1115) or a combination of one of these op-amps with a buffer-opamp in the feedback-path (to increase the maximum output current capability) was used. The buffer stage for the photodetector signal was necessary as not all photodetectors tested in the stabilization setup could provide the amount of current needed by the subtraction circuit. The relative stringent noise requirement forces the subtraction circuitry to be a low-impedance design to reduce the thermal noise of the input stage. For subtraction a low-noise opamp was used in the inverting amplifier configuration. Different opamps were tested and the values of the resistors used were matched to the input noise of each model to optimize the overall noise performance. The gain of the subtraction stage was set to be about ten. Thus the input noise of the following stages is almost negligible.

Other subtracting circuits have been tested, e.g. using a classical differential amplifier with high gain for low-noise operation (e.g. INA103, A=100: $3.5\,\mathrm{nV}/\sqrt{\mathrm{Hz}}$ at $10\,\mathrm{Hz}$). Here the input impedance is much higher and almost no input current is necessary. Therefore the additional

buffer at the input can be eliminated. It turned out that the input voltage is very close to the maximum common mode range and the speed of these amplifiers dropped to a level where the phase lag affects the achievable total loop bandwidth. Hence the classical subtraction circuit without the additional buffer circuit was used.

By subtracting the photodetector signal from the reference one obtains the error-signal (e), which was first amplified by an adjustable proportional gain stage. The signal was then amplified by two integrators, increasing the gain for frequencies below 10 Hz to more than 100 dB. Both integrators could be switched on or off independently from each other using analog switches. By switching it off, the gain of each stage was limited to a factor of ten at low frequencies to avoid saturation effects in the startup behavior of the control loop.

Two differentiators were used to compensate for the two poles of the laser system (slave-laser and PMC) and to increase the loop bandwidth. The corner frequency of each stage could be adjusted by a potentiometer to fit exactly the pole to be compensated. Each differentiator could be turned on or off by switches. Typically only one differentiator was used (for the slave-laser), and the uncompensated low-pass was used to provide a $1/f$-slope at the unity-gain frequency.

The control signal (u) was then injected into the current shunt to adjust the pump current and therefore the output power of the laser system. The measured open-loop gain of the power stabilization controller is illustrated in Figure 3.19.
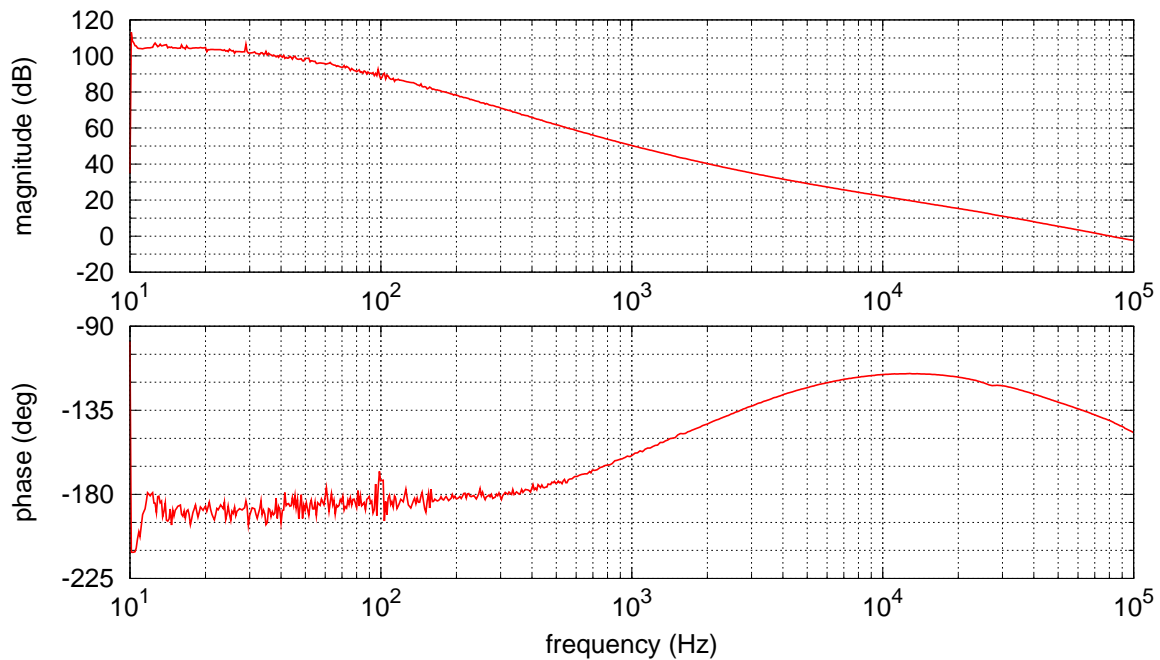
Figure 3.19: Measured open-loop gain response of the power stabilization loop for the 12 W laser system with reduced gain.

For this measurement the bandwidth was reduced to have a high phase margin. After optimization of the loop, the integrator was tuned to higher frequencies to achieve more gain at low frequencies for the price of less phase-margin while accepting a "servo bump" at high frequencies (see results in Figure 3.20). At low frequencies the measurement is limited by the dynamic range of the measurement equipment.

The whole controller was housed in a metal 19"-6 HU plug-in unit for proper electromagnetic shielding. It turned out that this also reduced thermoelectric noise from air flow due to internal natural convection when mounted horizontally instead of vertically.

As the photodetectors were only equipped with single-ended outputs, coaxial cables were used for wiring. The interfacing between the controller and the current modulation was also connected using single-ended coaxial cables. This is much easier to handle in the lab environment as all the measurement equipment used has single-ended and ground referred inputs.

As an electrical supply, linear regulated power supplies with additional regulation and filtering inside the controller-box were used.

3.1.5 Experimental results

Figure 3.20 shows the final results for the improved power stabilization scheme of the injection-locked 12 W laser system compared to the previous one. The new measurements were either performed in the vacuum enclosure in air or at a reduced pressure (<1 mbar). Thereby only a small reduction of mechanical resonances stimulated by acoustics could be observed.
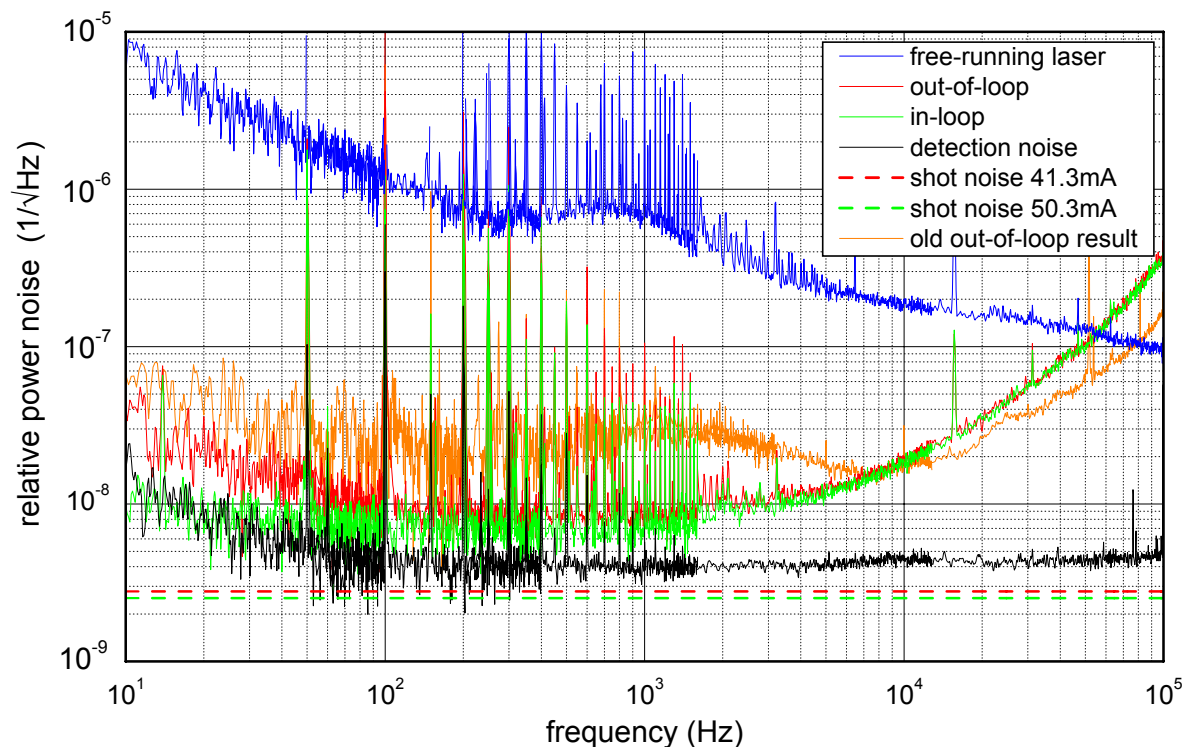
Figure 3.20: Final 12 W injection-locked laser power stabilization results.

The photocurrent of the photodetectors was $i_{\mathrm{ph,IL}}$=50.3 mA for the in-loop detector and $i_{\mathrm{ph,OOL}}$=41.3 mA for the out-of-loop detector respectively. The independent shot-noise level of the photodetectors can be calculated to be $\approx 2.5 \times 10^{-9}/\sqrt{\mathrm{Hz}}$ for the in-loop detector and $\approx 2.8 \times 10^{-9}/\sqrt{\mathrm{Hz}}$ for the out-of-loop detector respectively. Both levels are below the so-called *detection noise*. The detection noise is the combined dark noise of a photodetector and the input noise of the FFT analyzer (Stanford Research, SR785). In this case it was dominated by the analyzer noise. The measurement noise is only a factor of two to three below the measured

out-of-loop power noise level and already limits the in-loop measurement at low frequencies. All peaks in the spectra are line harmonics, mechanical resonances or switching power supply disturbances of the measurement equipment distributed over the setup (e.g. oscilloscopes, network analyzers, power meters or video screens).

The loop was optimized to achieve very high gain at low frequencies. This reduces the phase margin at high frequencies and so the "servo bump" arises. Hence the "stabilized" noise level exceeds the free-running non-stabilized noise level for Fourier frequencies higher than 55 kHz. Down to a hundred Hertz the in-loop and out-of-loop noise level are comparable. In the mid-frequency range, the achieved out-of-loop performance is limited by either loop gain at high frequencies or the in-loop noise level at lower frequencies. Below a hundred Hertz, the out-of-loop performance is dominated by some excess noise. For low frequencies the in-loop measurement is limited by the measurement equipment, in the mid-frequency range by the noise level of the input stage of the power stabilization controller and for frequencies higher than 1 kHz by insufficient loop gain.

It could be observed that using the pump-light of the high-power oscillator as the power actuator not only changed the output power; by directly affecting the laser mode in the laser resonator, it also changes other laser parameters like its frequency, beam pointing and beam size. Furthermore it could be demonstrated that actuating the PZT of the slave resonator couples into the power stabilization loop. Since all loops are nested it is hard to decouple the power stabilization experiment from the laser system itself.

The reduction of beam pointing by the filter cavity and the vacuum enclosure led to better power stability in the mid-frequency range, which was the frequency band dominated by acoustic noise so far. Compared to the old results (from [138]), the out-of-loop stability could be increased by a factor of two to three in the mid-frequency range before being the same below 10 Hz. Thus pointing cannot explain the excess noise at 10 Hz, the Fourier frequency with the most demanding stability requirement for Advanced LIGO.

The excess noise can be caused for example by a noise source that arises in the photodetectors and is not observable in the dark noise, a source in the power stabilization controller input-stage which cannot be seen in the electronic noise or a source which couples uncorrelated into the optical detection scheme.

In order to clarify the origin of this source of excess noise, a new experiment has been set up, which will be described in the next section.

3.2 Optimized stabilization experiment

The optimization of the stabilization experiment using the injection-locked laser system showed an improvement in the out-of-loop performance. Nevertheless the Advanced LIGO requirements on the power stability are well below the achieved level. In order to achieve the stringent requirements for Advanced LIGO and to investigate the coupling of different parameters thoroughly, a more simple system and a different power actuator with reduced cross-coupling have been chosen. This section deals with the detailed description of this new experimental setup.

3.2.1 Optical setup

An outline of the experimental layout used in the further optimized power stabilization experiment is shown in Figure 3.21.

The new optical setup can be divided into three major parts: ① The first part includes the laser source with the RF phase-modulation for locking cavities using the Pound-Drever-Hall
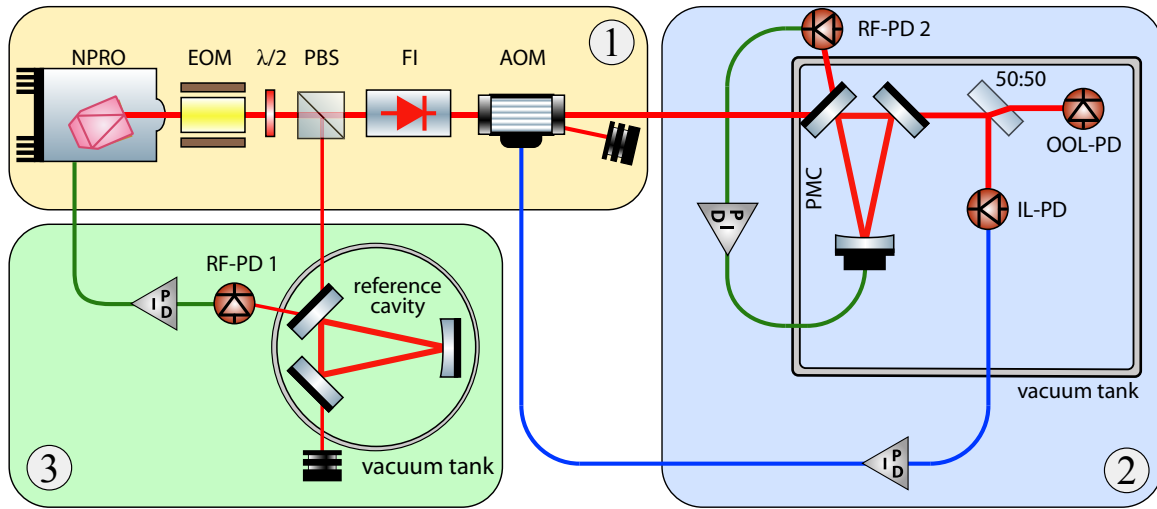
Figure 3.21: Outline of the further optimized power stabilization setup. The experiment can be divided into three sections: ① laser source with phase modulation and amplitude modulator, ② the power fluctuation detection part and ③ an additional frequency stabilization.

technique and the amplitude modulator for power actuation; ② The second part contains the power fluctuation detection including the filter cavity placed in a vacuum tank; ③ The third part includes an additional frequency stabilization using a high-finesse Fabry-Perot ring-cavity (*reference-cavity*) in high vacuum to examine the sensitivity to laser frequency noise. The individual parts of the further optimized power stabilization experiment are described in more detail below.

Laser preparation and power modulation

The laser used for this experiment is an NPRO similar to the master laser for the injection-locked system described in Section 3.1.1. The optical setup of the laser with the RF phase-modulation and the amplitude modulator is illustrated in Figure 3.22.

An EOM (New Focus, model 4003) resonant at 12 MHz provides phase-modulation sidebands for the locking of the filter cavity and the high-finesse reference-cavity. A single-stage Faraday isolator (FI)(LINOS Photonics, FR1060/8) placed behind the EOM protects the EOM and the master laser from laser light reflected back from the experiment toward the laser. A half-wave plate at the output in conjunction with a PBS was used to split the beam. Most of the light was used for the power stabilization experiment and a small fraction for the additional frequency stabilization with the reference-cavity.

The main beam was focused into an acousto-optic modulator (AOM) which was used as the power actuator. The AOM was chosen to provide an actuator which is independent of the laser system used. The intensity of light diffracted depends on the acoustic power being proportional to the power of the radio-frequency (RF) signal applied to the AOM. Changing the RF power for the AOM not only changes the amount of diffracted light, but also introduces beam pointing due to the RF-power absorbed in the crystal [50]. A test of different AOMs showed that with a carefully selected AOM the change in beam geometry and pointing of the beam is very small. It can be much smaller than the pointing introduced by an equivalent
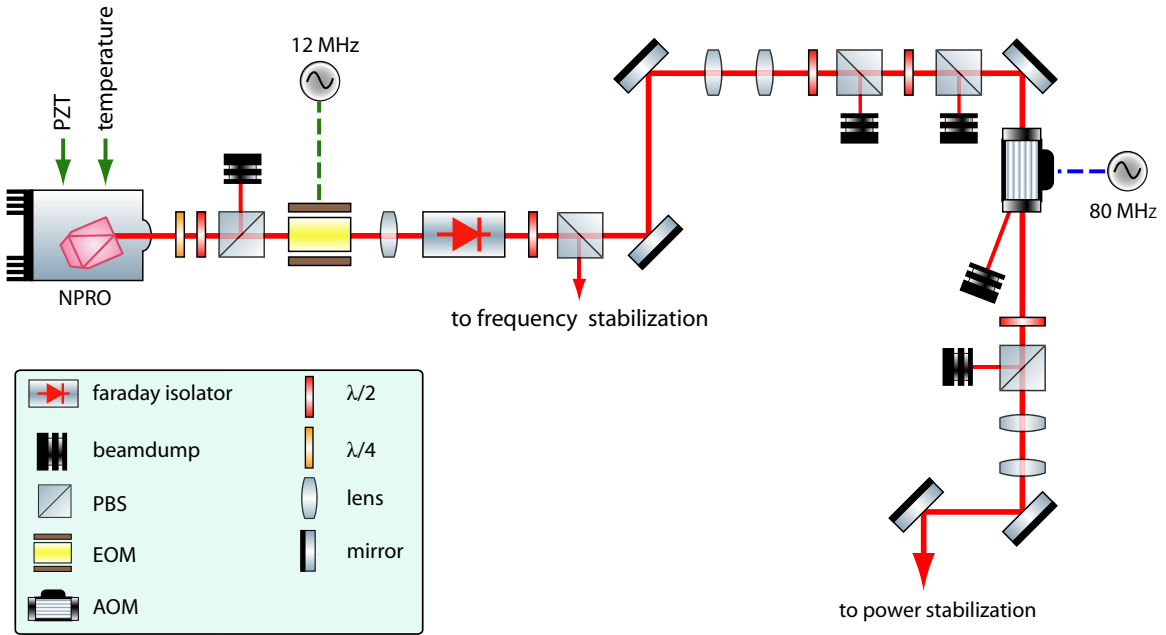
Figure 3.22: Laser preparation and power modulation for the improved power stabilization experiment.

direct modulation of the NPRO or injection-locked laser system via the pump diodes. The undeflected (0-order) transmitted beam then passed very high polarization-extinction-ratio (PER) (PER $> 10^{-6}$) Glan-laser polarizers (Leysop Ltd) to ensure a highly linear-polarized beam entering the vacuum chamber to be detected.

Power fluctuation detection

The main part of the experiment is the power fluctuation detection shown in Figure 3.23. All components of the detection system including an optical ring-resonator were placed in a sealed tank to minimize the influence of air-currents. The same filter-cavity (PMC) as already used in the improved power stabilization setup of the 12 W-laser was used again. The PMC was locked by means of the Pound-Drever-Hall technique to the laser and provides a clean TEM_{00}-mode to the detection part downstream of the cavity.

In front of the PMC two lenses were used to match the mode shape of the beam to the eigenmode of the PMC. A half-wave plate in conjunction with a rotatable polarizing beam splitter with a high extinction ratio was used to select one of the two orthogonal polarization modes of the PMC. It could be observed that the half-wave plate not only rotates the polarization of the incoming beam, but also introduces a very small elliptical polarization. This effect largely depends on the vendor of the half-wave plate. The additional polarizing beam splitter filters the beam again and ensures a high extinction ratio of the incoming laser beam.

Again, the PMC was typically operated in s-polarization to maximize the filtering effect of the incoming laser beam. The incoming beam enters the vacuum tank through an AR-coated wedged window. A fraction of the beam reflected at the PMC exits the vacuum tank again through another window. This beam passes some half-wave plates and polarizing beam splitters
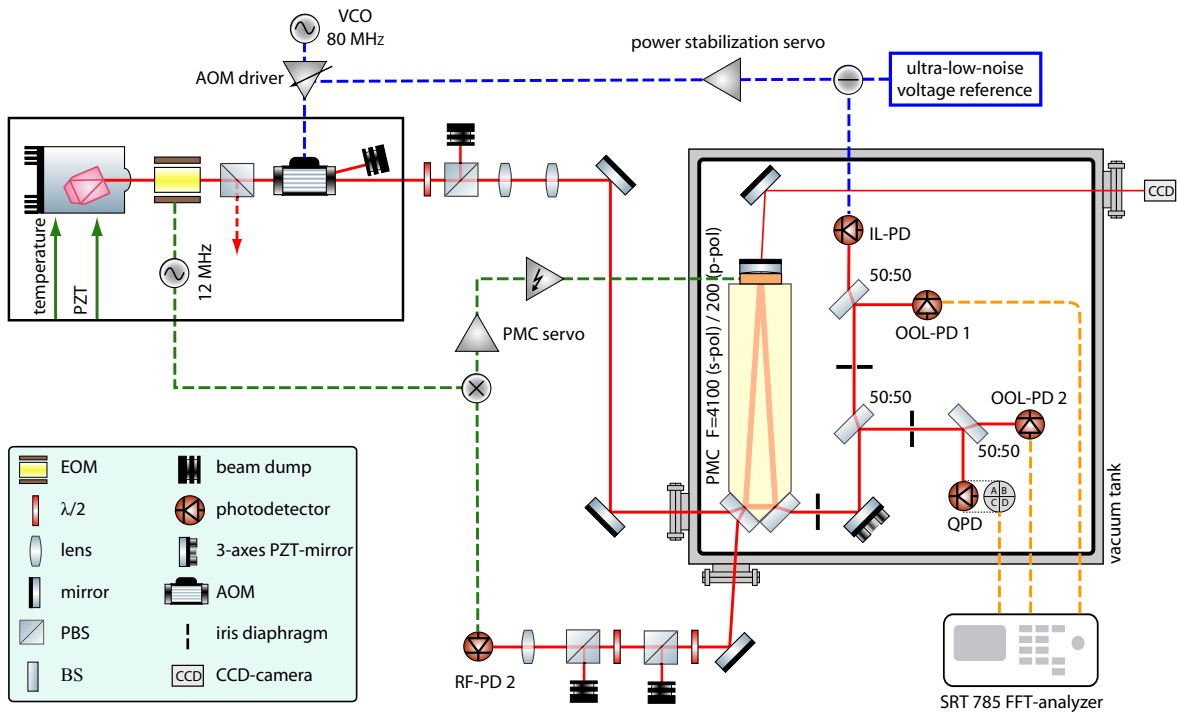
Figure 3.23: Schematic of the power fluctuation detection part of the improved power stabilization experiment.

to attenuate it to a lower power level which is detected with a photodetector resonant at 12 MHz. The obtained error-signal is used to generate a feedback signal processed by the length control servo, which is amplified by a high-voltage (HV) amplifier before it is fed back to the PZT of the PMC.

In order to investigate the coupling between beam-pointing and apparent power fluctuations on the photodiodes, a multi-axes piezoelectric mirror (Physik Instrumente (PI), S-311.10) was placed in the beam after the PMC. The tilt-angle range is $\approx 600\,\mu\text{rad}$ for each axis with a bandwidth of $\approx 6.1\,\text{kHz}$. A commercial 3-axis piezo controller (Thorlabs, MDT 693) is used to drive the multi-axis PZT-mirror. The reflected beam is split via non-polarizing beam splitters into four beams of identical power which are aligned with similar optical path length onto photodetectors. A quadrant photodetector (QPD, Centronic QD50) is used to measure the pointing of the laser beam at the output of the PMC.

In previous setups, the individual components were clamped to the optical table using conventional mechanic parts with significant relative motion of the individual parts. Since variations in the position of the beam on the photodiodes lead to variations in the photocurrent, resulting in increased noise, the complete new detection setup including the optical resonator is mounted via solid bases on a 2 cm thick aluminum baseplate. This ensures a highly rigid detection bench and the relative motion of the individual components is minimized.

For the power noise detection several different photodetectors have been tested. Because of the strong coupling of beam pointing with the spatial non-uniformity of the photodiode, new mechanical photodetector designs were tested. The photodiodes are mounted in 2-axis XY-translation stages with high-precision micrometer screws, to adjust the photodiode relative to the beam. The diodes were cooled using a TEC, either included in the diode package

(Hamamatsu, G8605 [56]) or mounted externally (Perkin Elmer, C30642G [119]). It turned out that for the latter design, the heat transfer away from the photodiode is very difficult, especially if used in vacuum. The heat transfer through the adjustable mechanics of the translation stage was small as was the radiation via the surface of the diode mount. The temperature of the mount was about 50°C for long-term operation of the photodetectors. Thus the same TEC-cooled 2 mm InGaAs-photodiodes from Hamamatsu as already described in Section 3.1.2 were used for the measurements of the new stabilization experiment presented in Section 3.2.4.

Since the photodiodes have to be properly adjusted relative to the incoming laser beam in order to reduce the influence of beam pointing on the photodiodes, a mirror in front of each detector was used to optimize the beam position on the photodiode. For this optimization we applied a controlled pointing with the 3-axis piezo and minimized the RPN by aligning the beam. A reduction of the coupling by more than two orders of magnitude was observed. The light level incident on each of the photodetectors was approximately 110 mW which corresponds to a photocurrent of approximately 80 mA. Again two identical photodetectors were used, one for the stabilization itself (in-loop) and the other for an independent measurement (out-of-loop). Figure 3.24 shows a photograph of the detection setup.
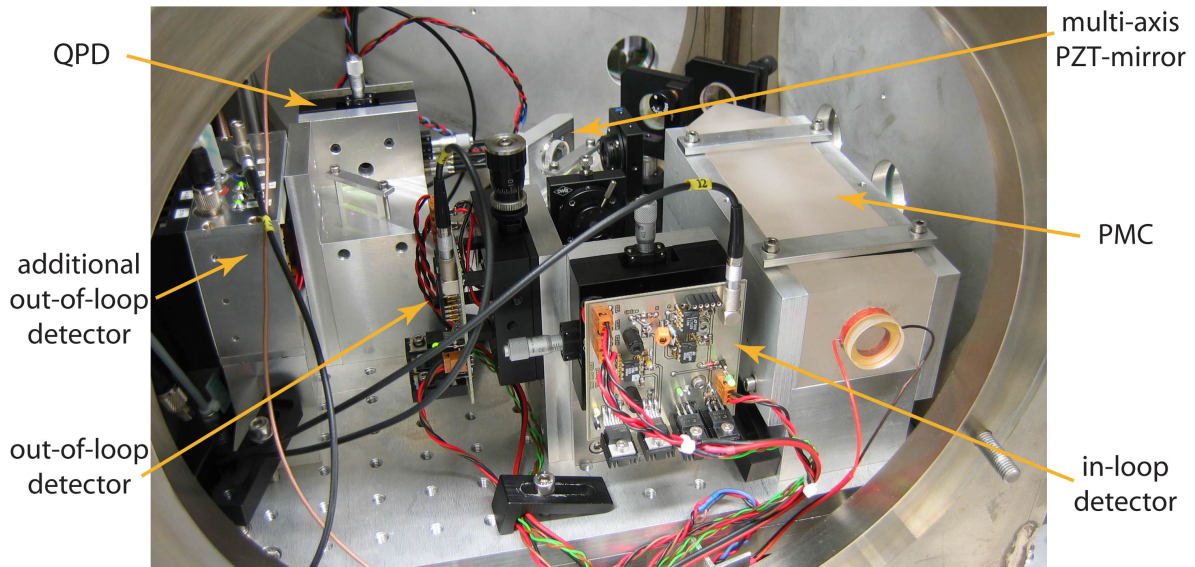
Figure 3.24: Photograph of the detection part of the improved power stabilization experiment.

Frequency stabilization

To improve the frequency stability of the NPRO, a high-finesse ($\mathcal{F}$=58000 (s-pol)) Fabry-Perot triangular ring-resonator, a so-called *reference-cavity* was used. Fundamental research demonstrated that the used NPRO laser has a much lower frequency noise if locked to this reference-cavity [21]. The reference-cavity was fabricated by Research Electro-Optics Inc. (REO). The spacer and the mirrors are made from ultra-low expansion titanium silicate glass (ULE™). The mirrors are optically contacted to the spacer and the cavity was placed in ultra-high vacuum.

To determine the influence of frequency noise on the power stabilization, the frequency stability of the laser was improved by locking it to this reference-cavity using a standard

Pound-Drever-Hall scheme. The NPRO provides two inputs to match the frequency of the laser with the resonance-frequency of the reference-cavity. Therefore the control signal is split into two signals. For fast frequency actuation the signal is amplified by a high-voltage amplifier before it feeds back to the PZT of the NPRO. To ensure long term stability, the low frequency part is fed back via an additional integrator to the temperature-controller of the NPRO crystal. The cross-over frequency is below $100\,\text{mHz}$. The experimental layout of the frequency stabilization is depicted in Figure 3.25.
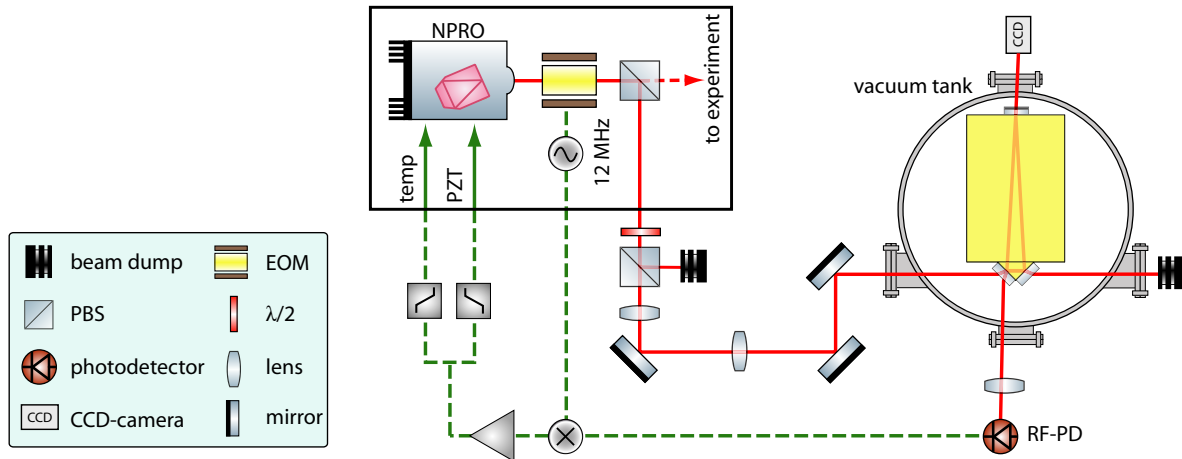
Figure 3.25: Frequency stabilization of the NPRO with a high-finesse ULE™ reference-cavity in ultra-high vacuum.

3.2.2 Power stabilization loop design

In order to reach the required stability at low frequencies high electronic gain is needed. High gain AC-coupled control loops can have difficulties with the control of DC offsets and drift causing saturation. A DC-coupled control loop ensures the long term robustness of the loop but is limited by the noise-level of the DC reference. In order to overcome the limitation set by the reference while ensuring a good long term robustness of the stabilization loop, a combination of the basic DC-coupled loop and an additional, AC-coupled path injected into the error-point of the control loop can be used (see Section 2.2.1). This design was chosen for the new power stabilization loop. Starting with a detailed analysis of the laser system performance and the power actuator, the design of the control loop for the power stabilization of the NPRO will be described below.

Laser and power actuator characterization

In order to develop the power stabilization controller a detailed characterization of the laser system performance and of the power actuator is necessary. Knowledge of the laser system's free-running power noise is important to design the control loop. Figure 3.26 shows the measurement of the free-running power noise after the PMC.

Pointing due to air fluctuations and the relative motion of optical components in front of the PMC is converted into power fluctuations behind the PMC and therefore raises the power noise level at low frequencies behind it. The AOM together with its driver were characterized with regard to the dynamic range and its transfer function, in order to determine the loop gain and corner frequency of the power stabilization controller.
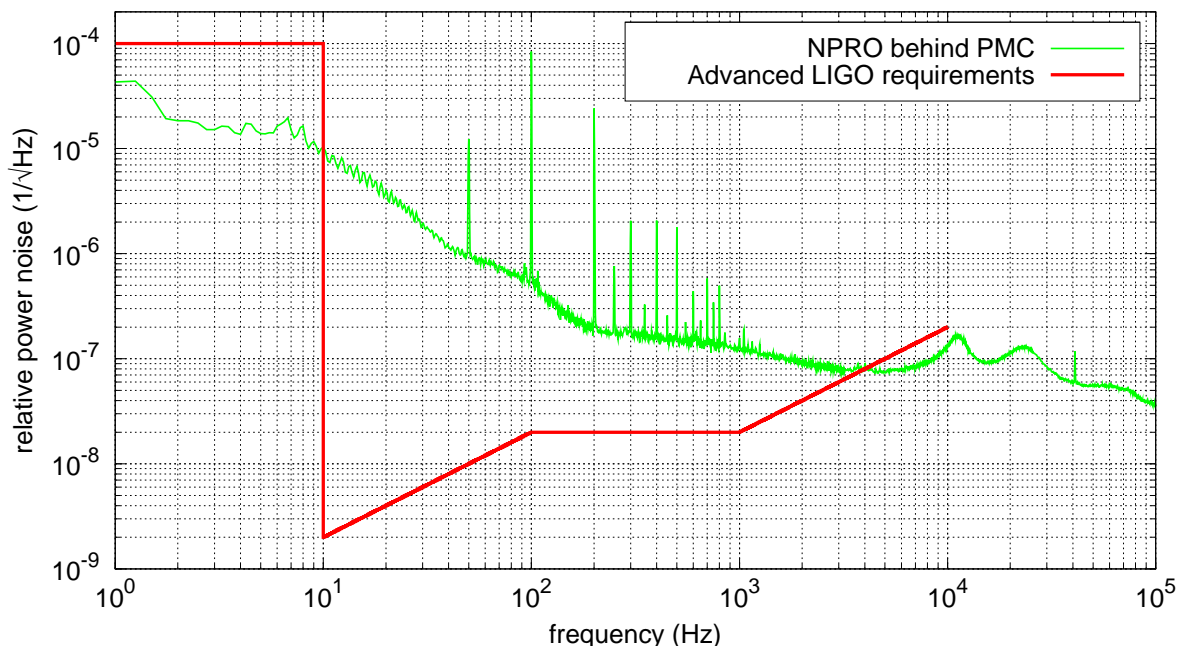
Figure 3.26: Free-running power noise of the NPRO behind the PMC.

The AOM-crystal is driven by a fixed-frequency RF-oscillator (80 MHz) amplified by an amplitude-controlled power-amplifier (Landwehr Electronic, Q-Switch Driver A 274-18). The driver used was principally chosen because of its high amplitude modulation bandwidth. In order to achieve high loop gain at frequencies up to one hundred kilohertz, the AOM driver must have a bandwidth of the order of hundreds of kilohertz. Conventional drivers used so far in our institute have only a bandwidth of some tens of kilohertz. The RF output power is 5 W maximum. The output power was limited to 2 W maximum so as not to exceed the maximum permissible power for the AOM. Figure 3.27 shows the RF output power of the AOM driver depending on the power control input signal.

The output power P_{RF} has a quadratic response as the relation between the input control voltage and the output voltage of the driver is linear. The transfer function of the driver/AOM-unit was measured for several different output power-levels with two different AOMs. The first AOM was from Crystal Technology, model 3110-125, the second from Isomet, model 1205C-2. Both are AR-coated for 1064 nm. The AOM from Crystal Technology is originally designed for a center frequency of 110 MHz but has been operated at 80 MHz with the disadvantage of some higher return loss and consequently smaller diffraction efficiency. Figure 3.28 shows the transfer function measured for both AOMs using the same driver.

Since changes of the transfer function on output power are tiny for both AOMs, only one graph for each AOM is shown. The amplitude response is flat up to 1 MHz. However the Isomet AOM shows a phase lag of 45° at 125 kHz and the Crystal Technology AOM at 450 kHz. This phase lag is introduced by the speed of the acoustic wave inside the AOM-crystal. The Crystal Technology AOM uses TeO_2 with an acoustic velocity of 4.2 mm/µs instead of $PbMoO_4$ with a velocity of 3.63 mm/µs as used by the Isomet AOM. As this delay is a material constant, the phase lag can only be reduced by a reduction of the distance the acoustic wave has to travel before interacting with the beam. This can be achieved by aligning the beam close to
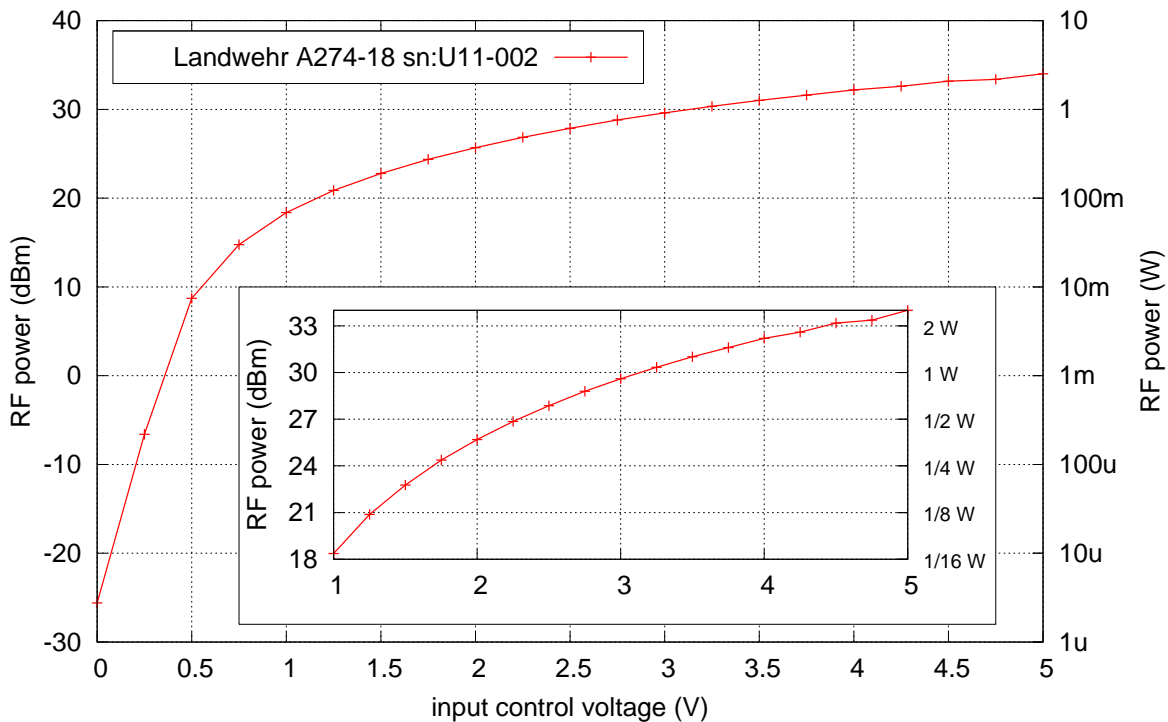
Figure 3.27: RF output power of the 80 MHz AOM driver (Landwehr Electronic, model A 274-18) depending on the power control input signal.

the side of the crystal where the acoustic wave is produced. This causes a small change in the delay but increases the risk of optical damage if adjusted too close to the edge of the free aperture of the crystal. Because of the lower phase lag, the AOM from Crystal technology was chosen as the power actuator.

Controller design

In the previous sections all necessary parts required for the design of the control loop have been quantified. A block diagram of the new power stabilization controller is shown in Figure 3.29. As before, the in-loop photodetector signal was compared to an ultra-stable low-pass filtered voltage reference (see Section 3.1.4). In this new controller design, the voltage reference was RF-shielded as well as acoustically and thermally insulated to further improve the noise performance at low frequencies.

In order to find the optimum way for the signal transmission from the photodetector to the controller, five different input stages on the controller board, single ended with and without buffer as well as differential, could be tested and compared. In order to overcome the noise limitations set by this reference, the input signal from the photodetector was also amplified in the frequency band with the largest stability requirements (10 Hz–100 Hz). The amplified signal was then added to the original photodetector signal together with the inverted reference signal. The lower corner frequency of the band pass was 0.3 Hz and the upper 330 Hz. The maximum gain in the pass band was 45 dB. The complete input stages including the subtraction and band pass filter were RF-shielded and acoustically and thermally insulated.
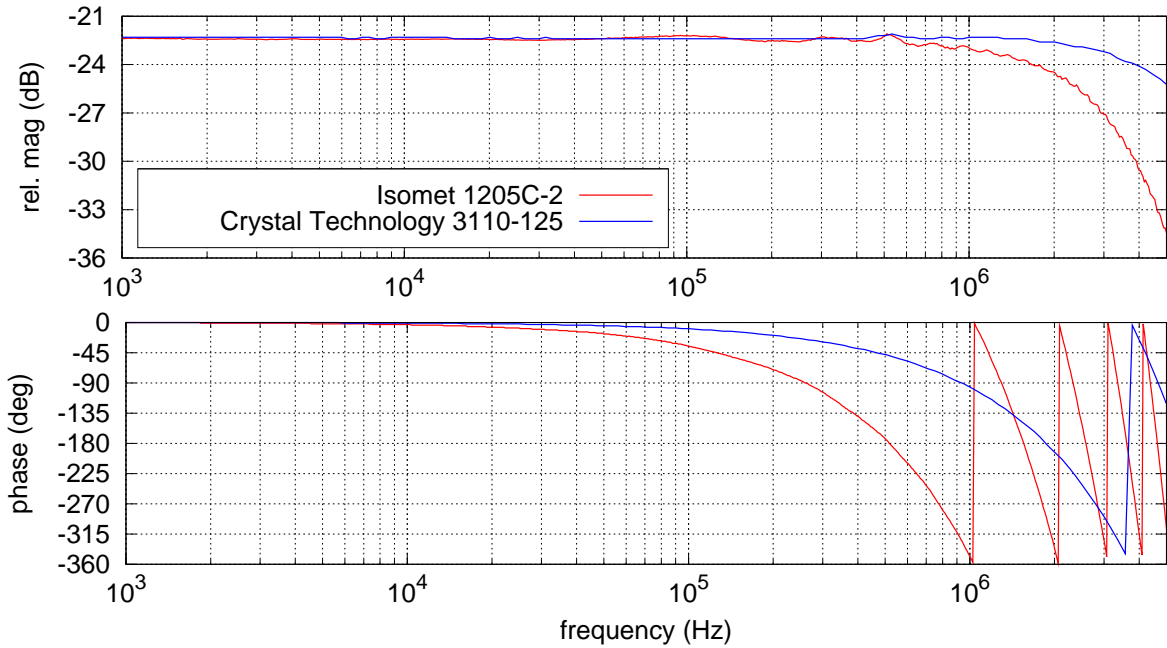
Figure 3.28: Measured transfer function of two AOMs tested as the power actuator using the same AOM driver for both measurements.
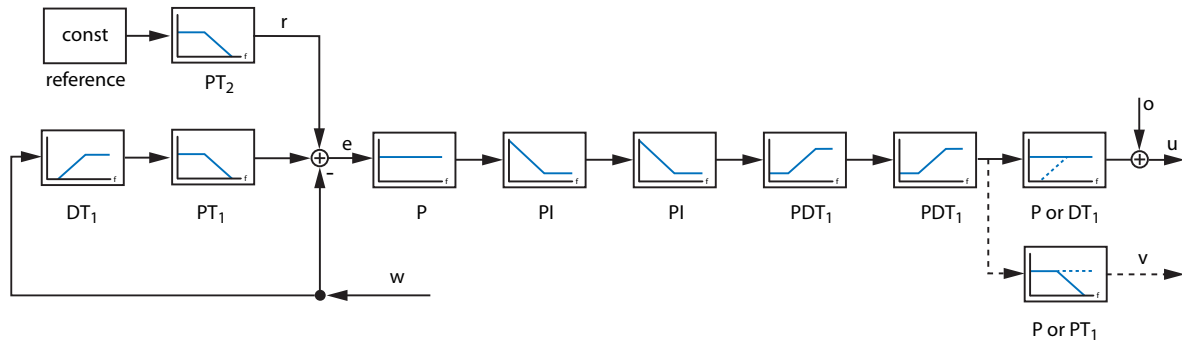
Figure 3.29: Block diagram of the improved power stabilization controller.

The loop design chosen for the new loop has two advantages. On the one hand the photodiode signal is still compared to an ultra-stable reference at DC to ensure a good long-term performance of the power stabilization loop. Also saturation of individual stages caused by the high gain in the controller can be avoided. On the other hand, the additional band-pass-filtered and amplified signal that is added into the error point increases the pass-band fluctuations in the photodetector signal with respect to the noise of the voltage reference. This additional band-pass gain for the photodetector signal could have been implemented inside the detector as well. Implementing it in the controller input-stage as an optional feedback path allows a more detailed analysis of the reference-noise coupling and makes the photodetectors less complex. A disadvantage of this strategy is that the signal is so small on the path from the photodetector to the controller such that EMI-noise coupling into this path might become more relevant.

By subtracting the photodetector signal (w) from the reference (r) with or without the additional path, one obtains the error-signal (e), which is first amplified by an adjustable proportional gain stage. Two following integrator stages increase the gain at low frequencies to more than 100 dB. Both integrators could be switched on or off independently from each other by analog switches. In the off-state, the gain of each stage was limited to a factor of ten at low frequencies to avoid saturation before the control loop is closed and to investigate the noise performance at low frequencies as a function of loop gain.

As explained in Section 3.2.1, the corner-frequency of the filter-cavity at 87 kHz has to be taken into account in the design of the power stabilization controller. A differentiator is used to compensate for this pole in the control loop's plant and to increase the unity-gain frequency. The corner frequency could be adjusted by a potentiometer to match exactly to the pole to be compensated.

Two filter stages individually configured could be used to switch the output signal of the controller to different actuators, e.g. the current modulation input of the NPRO or the AOM. For the stabilization experiment only one path (u) was used. In different experiments, the other path (v) was used too.

The input impedance of the AOM driver used for first tests was 50 Ω (AA Optolectronic, model AA.80.B46), so an additional high-current output buffer had to be used to drive the input even at high voltage levels (maximum 5 V input≙100 mA). The new, faster Landwehr driver described earlier has an input impedance of 600 Ω (see Section 3.2.2) and did not need this extra driver. As the zero-order beam of the AOM is used, it can only "subtract" light. Thus an offset (o) has to be added to the driver to convert the AOM to a bipolar power actuator. This offset could be adjusted inside the controller electronics. The output signal (u) was injected into RF driver for the AOM to adjust the output power of the laser system. The measured open-loop gain of the power stabilization controller without the additional AC-path is illustrated in Figure 3.30.

The control loop was designed to have an upper unity-gain point beyond 100 kHz to achieve high gain in the acoustic region and very high gain at low frequencies. The unity-gain frequency could be set as high as 300 kHz with reduced performance at high frequencies. The gain at frequencies below 200 Hz was at least 100 dB and around 160 dB at 10 Hz, which in the absence of additional noise sources is more than sufficient to reduce the technical laser power fluctuations to the shot-noise level of the sensing photodetectors or their electronic noise. The experimental results will be presented in Section 3.2.4.

3.2.3 Low-noise pre-amplifiers

With the new control loop design, the electronic noise of individual parts like the voltage reference or the input stage could be reduced to a level that the input noise of the measurement equipment like FFT-analyzers and oscilloscopes was too high. This section describes the design of low-noise pre-amplifiers (preamps) placed between the device under test and the diagnostic equipment. Except for the input-noise voltage, the amplifier requirements are not particularly demanding. Since the output impedance of the devices to be characterized is low, the input impedance of most amplifier circuits is acceptable. A frequency range from a few hundred millihertz to more than 100 kHz is adequate and the output load is usually a high impedance spectrum analyzer or oscilloscope.

The amplifiers can be of two general types: DC-coupled and AC-coupled. The major disadvantage of DC-coupled amplifiers is that their gain limits the amount of permissible DC input voltage. AC-coupled circuits do not suffer from this disadvantage, but the AC-coupled
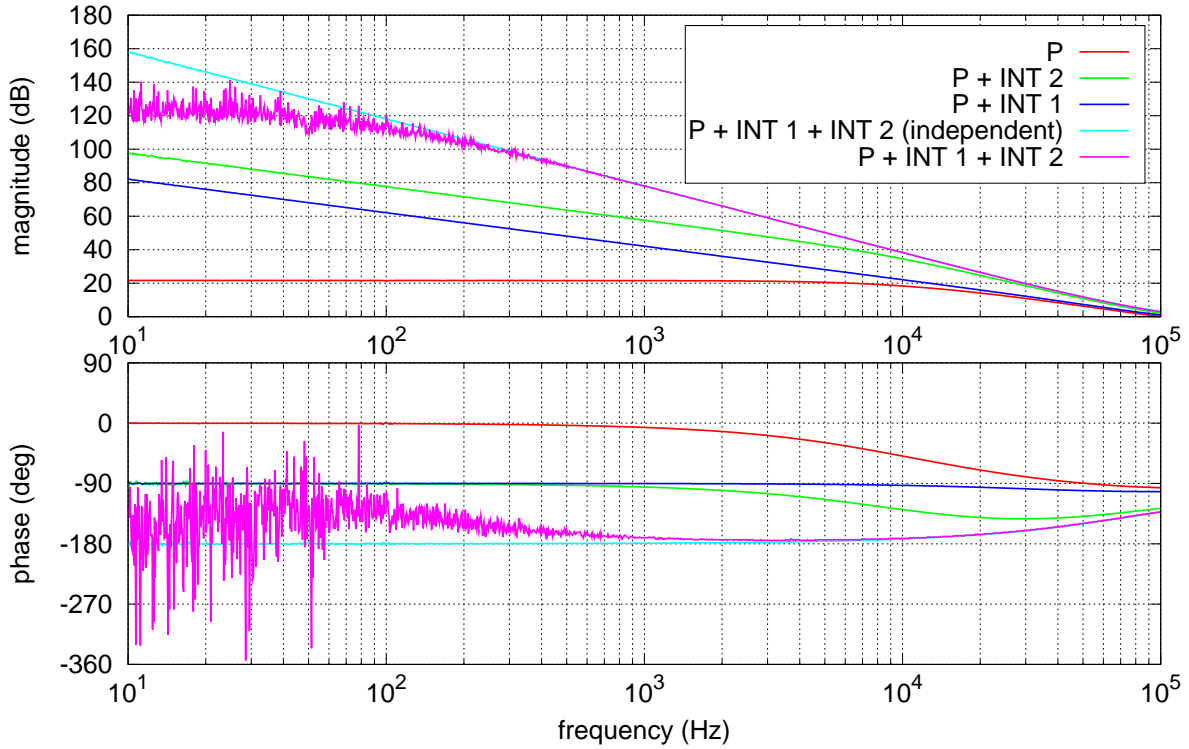
Figure 3.30: Measured open-loop gain of the power stabilization loop with different stages switched on and off.

circuits are typically difficult to build for very low corner frequencies. Since typical signals in our experiments have a high DC-voltage, AC-coupled designs were used in most cases. To measure electronic noise of sub-assemblies, e.g. the dark noise of photodetectors, DC-coupled designs will also work and can be used to measure down to very low frequencies.

Current technology offers two types of low-noise amplifier devices, the junction field-effect transistor (JFET) and the bipolar transistor (BJT), either as a standalone component or as a part of a ready-to-use amplifier. Since the JFET devices offer only low input current noise, the BJT was used, which has lower input voltage noise. Several bipolar opamps are available with very low input noise at low frequencies down to $1\,\mathrm{nV}/\sqrt{\mathrm{Hz}}$ or even a bit below (e.g. AD797, LT1028/LT1128). Pre-amplifiers built from any of these parts will perform well in most applications. As these opamps are already used in the photodetector circuits and the noise level which should be measured is quite low, even lower input noise would be preferable.

Four different preamp designs have been tested. One design uses a single op-amp as the input amplifier stage, another a couple of them in parallel to reduce the input noise. The other two designs are based on a discrete input stage of matched transistor pairs in a differential amplifier configuration. Here PNP and NPN transistors were compared. The two amplifiers with a discrete input stage are DC-coupled and the two others AC-coupled using different techniques. The two discrete amplifiers had a total gain of $60\,\mathrm{dB}$ ($G = 1000$), one design $40\,\mathrm{dB}$ ($G = 100$) and the other $54\,\mathrm{dB}$ ($G \approx 500$), which reflects a compromise between low input noise and high bandwidth. A block diagram of both AC-coupled designs is illustrated in Figure 3.31.

(a) Passive AC-coupled pre-ampflifier (b) Active AC-coupled pre-ampflifier
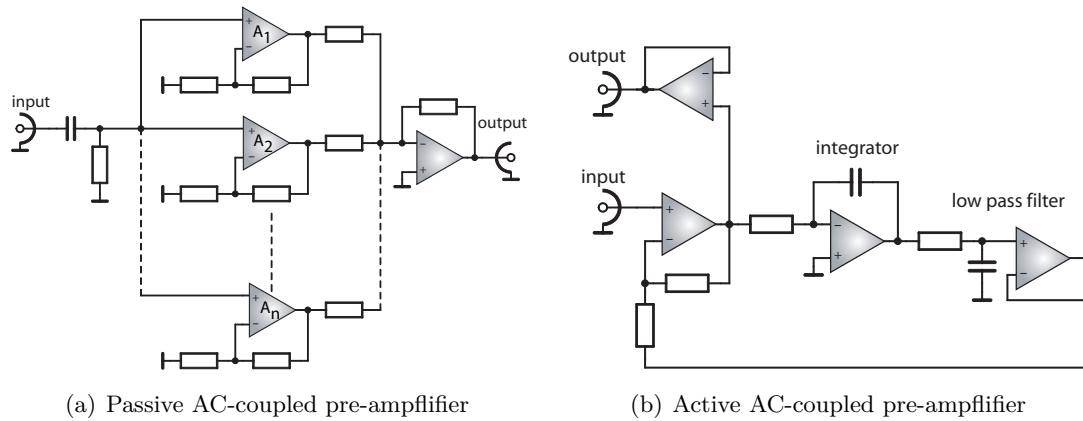
Figure 3.31: Block diagram of two AC-coupled pre-amplifier designs.

The first AC-coupled design shown in Figure 3.31(a) uses a passive first-order high-pass filter followed by a low-noise amplifier. The low-noise amplifier consists of multiple identical amplifiers in parallel ($A_1 \ldots A_n$) followed by an adder which sums up the signals from all these amplifiers. The basic design idea was taken from the datasheet of the LT1028. Because the input noise of the individual amplifiers is uncorrelated, paralleling amplifiers reduces the overall input noise by the square-root of the number of individual amplifiers. In this design, four identical input amplifiers (LT1028) were implemented to reduce the input noise by a factor of two. The total gain of 54 dB was distributed to the amplifier stages (34 dB) and the adder (20 dB) to achieve a higher bandwidth. The corner frequency of the high-pass filter was set to 146 mHz using low leakage current, high-capacity bipolar electrolytic capacitors ($4{\times}820\,\mu$F).

In the second AC-coupled design (Figure 3.31(b)), the AC-coupling is done by a slow feedback loop from the output to the input stage. The total gain of 40 dB was implemented in the first stage using a low-noise operational amplifier (AD797). The amplified output is then fed into an integrator stage followed by a low-pass filter to reduce the additional noise caused by the integrator stage. This filtered signal is then fed into the first stage. As a result the DC and low frequency part of the signal is compensated by the integrator and the output signal is high-pass filtered. In this design the corner frequency was set to 100 mHz. An additional buffer at the output decouples the load from the input stage.

The scheme of the discrete designs was inspired by the "super low-noise amplifier" proposed in the data sheet of the low-noise matched transistor pairs MAT02/MAT03 and SSM2210/SSM2220 from Analog Devices. By using three matched pairs in parallel, a further reduction of amplifier noise is attained. Since we assume equal noise contributions from each transistor, the total output noise is $\sqrt{3}$ smaller than a single transistor's input noise. For the final amplifier design the cheaper SSM2210/SSM2220 matched pairs were used. The collector current of each transistor was set to $I_C = 1\,$mA to achieve very low-noise. The closed-loop gain was set to $A \approx 1000$.

Air currents cause small temperature changes that can appear as noise at the output, especially at low frequencies. To eliminate this noise source, all amplifiers were assembled in aluminum boxes to achieve a thermal coupling to the environment with a suitable low time constant and to reduce the influence of convection currents.

The input noise of the FFT-analyzer (Stanford Research, SR785) in its most sensitive operation-mode and the input noise of the preamp designs is shown in Figure 3.32.
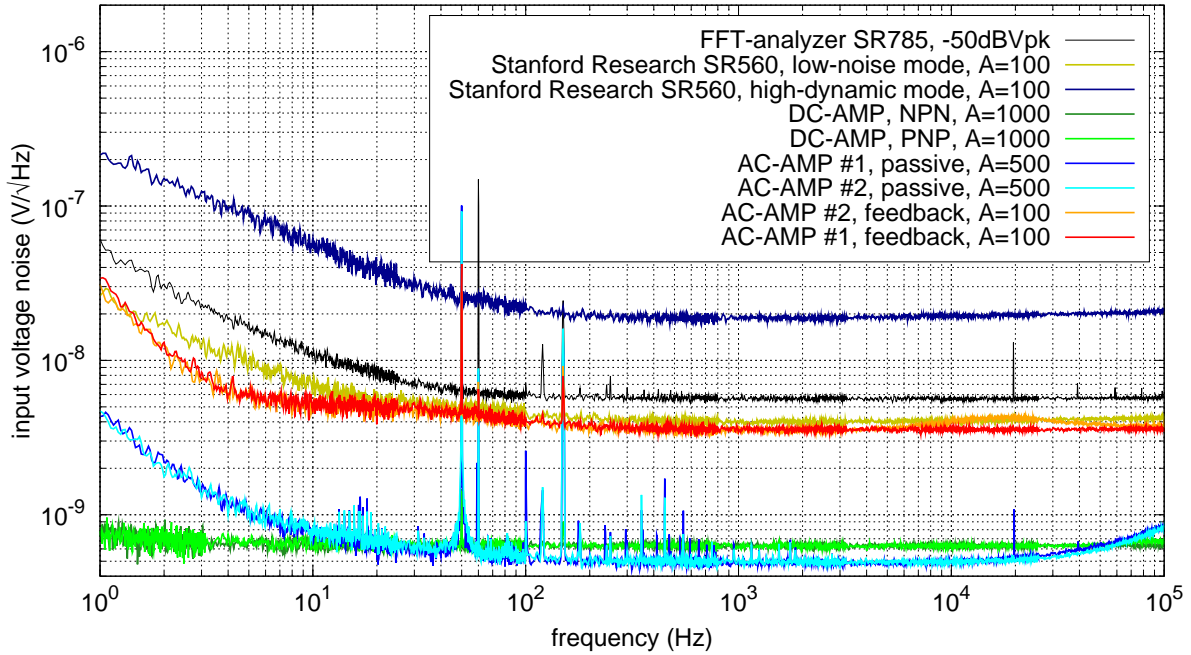
Figure 3.32: Comparison of input noise of different preamps and the FFT-analyzer in its most sensitive input configuration (-50dBVpk).

A commercial pre-amplifier (Stanford Research, SR560) operated with a gain of A=100 is plotted for comparison. The preamps were battery-powered to avoid ground loops since the inputs are single-ended. Nevertheless one can see the electromagnetic interference of the surrounding equipment in the electronic workshop. The input noise of all self-made designs is below the input noise of the Stanford FFT-analyzer. The preamp design with active feedback is slightly better than the commercial amplifier in the low-noise operation mode. The passive AC-coupled amplifier design having a gain of A=500 has lower input noise, but suffers from higher input leakage current at high DC-levels. The matched transistor pairs show much lower noise than the operational amplifier designs.

For a low corner frequency high capacitance values are needed in the passive AC-coupled design when using moderate resistance values. This can cause measurement errors due to leakage currents of the large input capacitors. Thus the preamp with internal feedback loop was used for the final measurement setup, although the noise performance of this design is the worst. Nevertheless, if the DC input-level of the photodetector signal is above a few volts, the relative noise is below the required $2 \times 10^{-9}/\sqrt{\text{Hz}}$. The discrete preamp design based on NPN transistors was used for electronic noise characterization whenever possible.

3.2.4 Experimental results

The final performance of the system is shown in Figure 3.33. All experiments were performed in low vacuum (pressure <1 mbar). The detection noise is dominated by the combined dark noise of the photodetectors and the noise of the self-made battery-powered pre-amplifier. The dark noise is comfortably far below the measured out-of-loop intensity noise level. The photocurrent

of the photodetectors is $i_{\text{ph,IL}}=78\,\text{mA}$ for the in-loop detector and $i_{\text{ph,OOL}}=79.6\,\text{mA}$ for the out-of-loop detector respectively. The shot noise for each photodetector is $\approx 2 \times 10^{-9}/\sqrt{\text{Hz}}$. For low frequencies the in-loop measurement is limited by the detection noise level, in the mid-frequency range by the noise level of the voltage reference and for frequencies higher than $3\,\text{kHz}$ by the loop gain.
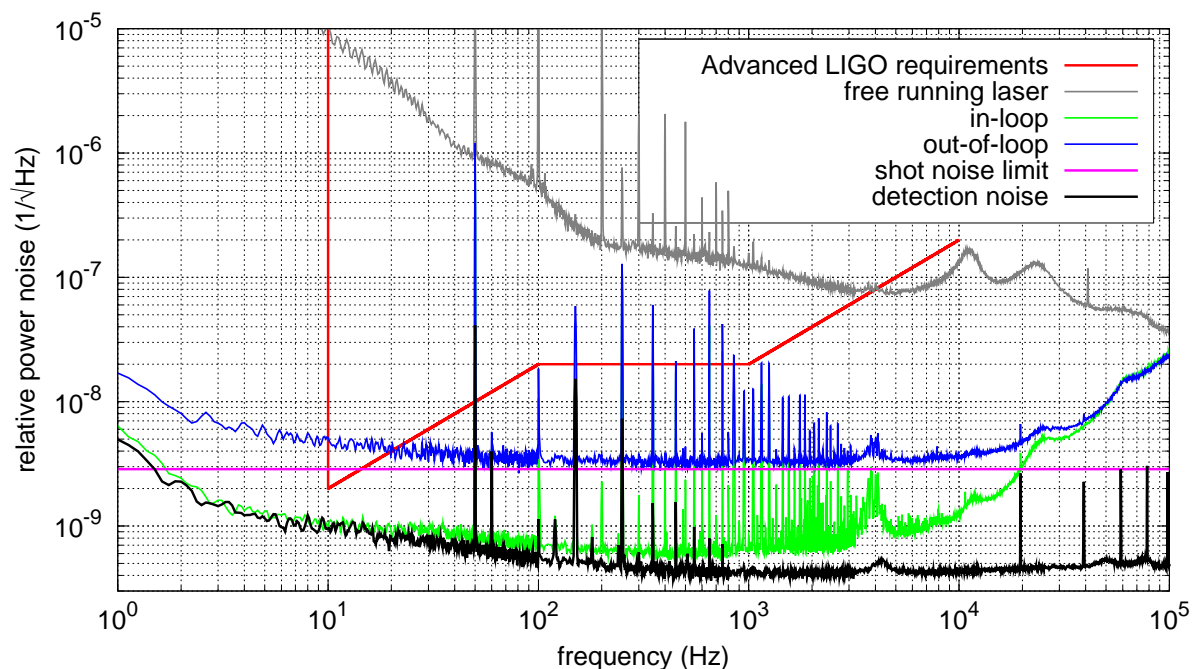
Figure 3.33: Final performance of the new power stabilization experiment.

The out-of-loop measurement is fundamentally limited by the uncorrelated sum of the shot noise on the in-loop and out-of-loop detector. Summing the shot noise from both photodetectors in quadrature gives a minimum for the out-of-loop measurement noise of $2.8 \times 10^{-9}/\sqrt{\text{Hz}}$. In addition, the noise of the voltage reference used to set the operation point of the control loop and the input noise of the controller is imprinted on the light. The out-of-loop measurement of $3.5 \times 10^{-9}/\sqrt{\text{Hz}}$ for $\approx 100\,\text{Hz}$ up to a few kHz indicates that a technical noise source in addition to the reference and input noise of the controller contaminates the in-loop measurement and is imprinted on the light by the control loop or adds excess noise in the out-of-loop measurement. Most probably a combination of both effects describes the measurement best.

For Fourier frequencies below $100\,\text{Hz}$ the residual out-of-loop noise was higher which can not be explained so far. At the lowest frequency of interest for ground-based gravitational wave detectors like Advanced LIGO ($10\,\text{Hz}$) the noise increased to $5 \times 10^{-9}/\sqrt{\text{Hz}}$. For frequencies above $10\,\text{kHz}$ the performance of the stabilization loop is limited by the loop gain. The appearance of peaks in the spectra due to line harmonics or switching power supplies could be reduced compared to previous experiments. Most of the electromagnetic interference is already present in the dark noise with battery-supplied equipment (except the FFT analyzer) and thus a measurement limitation and not a principal problem of the stabilization.

3.3 Summary

In conclusion, a power stabilization of a Nd:YAG laser of $5 \times 10^{-9}/\sqrt{\text{Hz}}$ at $10\,\text{Hz}$ has been achieved, which is very close to the requirements for the Advanced LIGO gravitational wave detector. The final results shown in Figure 3.33 represent, to the best of our knowledge, the lowest RPN levels published so far in this field. For the optimized system the limitation of the in-loop performance is known. For low frequencies it is limited by the detection noise level, in the mid-frequency range by the noise level of the voltage reference and for high frequencies by the gain of the stabilization loop.

With the optimized stabilization setup, the discrepancy between the in-loop and out-of-loop performance could be reduced compared to the measurements using the more complex injection-locked laser system described in Section 3.1.5, but is still observable at low frequencies. As explained in Section 2.2.2, the limiting noise source must be at or after the beam splitter, where in and out-of-loop beams are generated, detected and processed.

A large number of possible noise sources were identified and characterized in order to explain the difference between the in-loop and the independent out-of-loop performance. Here laser parameters like frequency, polarization and beam geometry and pointing, as well as environmental parameters like temperature or humidity could introduce uncorrelated noise. Iterative optimization of the detection scheme reduced the influence of these effects to a minimum.

Various electronic noise sources were characterized. It could be observed that the residual noise level at low frequencies is highly sensitive to small leakage currents caused by ground loops. After careful optimization of the electronics and cabling, a higher noise level at lower frequencies was still observed. Slew-rate limits of the amplification stages or electronic down-conversion due to electromagnetic interference were ruled out by adding large calibration peaks to the system. Other electronic noise like microphonic noise or thermoelectric noise (thermal EMF) were observed, but could be reduced to very low levels which do not affect the overall performance. Also detailed studies on excess noise in active and passive electronic components, including low-frequency noise in the photodiodes were performed. A detailed study and projection of different noise sources will be given in the next chapter.

Limitations to sensitivity: Noise sources

A large number of noise sources can affect the performance of a power stabilization control loop. Several important noise sources were identified and characterized during the stabilization experiments conducted in this work (see Chapter 3). More detailed noise investigations have been performed in order to improve future power stabilization setups.

Generally one can distinguish between two types of noise sources. The first can be described as a cross coupling of fluctuations in secondary variables like wavelength, polarization, beam pointing, beam geometry, temperature, acoustics, EM-fields or others into power noise which becomes relevant in case the associated coupling coefficient is different for the in-loop and out-of-loop path. Secondly independent noise sources in optical or electro-optical components which depend on the absolute power only, e.g. thermal noise, $1/f$-noise in photodiodes, etc. can differ between the in-loop and out-of-loop path. In the former case a reduction of the source or changing of the coupling should help. In the latter case the origin of the noise has to be found and must be eliminated as much as fundamental physically processes allow.

Apart from the power stabilization servo electronics, possible objects / components of the power stabilization setup which can be different for the two beam paths are:
- the power beam splitter
- the optical path between beam splitter and photodiodes
- the photodetectors (photodiodes and readout electronics)
- the measurement equipment (spectrum analyzer, preamp).

In this chapter, a more quantitative evaluation of important noise sources by means of specifically designed experiments is given.

As the out-of-loop noise performance shows typical $1/f$-noise characteristics, low-frequency excess noise is considered to be one of the dominant effects. Section 4.1 deals with the measurement of low-frequency noise in photodiodes. Following on in Section 4.2 the low-frequency noise of a large variety of resistors is investigated. Another noise source that was investigated is the influence of position-dependent photodiode efficiencies in conjunction with beam pointing, which is presented in Section 4.3. In Section 4.4 measurements of temperature fluctuations have been used to estimate their effect on the power stability. Temperature dependencies of photodiode efficiency and the temperature dependency of splitting ratio of the beam splitter used to sample a fraction of the beam for the in-loop and out-of-loop detectors were found to be important. Subsequently, in Sections 4.5 and 4.6, the influence of the bias voltage in photodetector circuits and spurious signals outside the measurement and stabilization bandwidth, so called "out-of-band noise", has been investigated. The influence of scattered light and polarization fluctuations of the laser beam are discussed in Sections 4.7 and 4.8 respectively. Finally, Section 4.9 addresses laser frequency noise, which can be converted into power noise, e.g. due to wavelength-dependent response of the photodiodes or the splitting-ratio of the power beam splitters. At the end of this Chapter in Section 4.10, the contribution of the individual noise sources to the overall limitation of a power stabilization loop are discussed.

4.1 Low-frequency noise in junction photodiodes

The key component for optical light detection are semiconductor photodetectors. In this section low-frequency noise in junction semiconductor detectors (photodiodes) is discussed. Photodetectors with high quantum efficiency and appropriate electronic circuitry are required for obtaining shot-noise sensitivity of power noise measurements. GWDs are currently operating at 1064 nm wavelength. Three materials are commonly used for this wavelength: Silicon (Si), Germanium (Ge) and Indium-Gallium-Arsenide (InGaAs).

Silicon has a cutoff wavelength of 1050 nm–1100 nm, depending on the manufacturing process. Since the cutoff is very close to the operating wavelength of currently operating GWDs, the quantum efficiency is very poor and the thermal coefficient of the quantum efficiency is fairly large, up to several percent per Kelvin. Therefore it is not the best choice for high sensitivity measurements at this specific wavelength.

Germanium is a bulk material and the InGaAs-composition can be grown lattice matched on indium-phosphide (InP) substrates. The cutoff wavelength of germanium and of standard lattice matched $InP/In_{0.53}Ga_{0.47}As$ is around 1.7 μm. The quantum efficiency is therefore much higher compared to silicon. Lattice mismatch introduces dislocation-induced junction leakage which causes high dark current and reduced quantum efficiency. Furthermore dislocations can be electrically active as generation-recombination centers which produce excess low-frequency noise as explained in Appendix A.1. However, as quantum efficiency is much higher for InGaAs photodiodes in general and dark current much less compared to germanium, these devices are preferred for power stabilization experiments in the near infrared regime.

A large number of investigations on the origin and behavior of low-frequency noise in junction photodetectors have been performed over the past decades and various different results can be found in the literature, e.g. [77, 81, 91, 92, 124, 131, 132]. Some of them take into account the influence of light exposure on the low-frequency noise [20, 25, 65, 68, 79, 87, 103, 176]. Unfortunately the majority of those investigations have been performed for other materials or configurations different from the typical large-area InGaAs photodiodes used in our experiments.

Thus, several investigations to quantify the low-frequency noise under reverse bias conditions and illumination similar to the application conditions have been performed for this work. The experiments and their results are presented in the following sections. All measured noise spectra are plotted as linear spectral densities and thus $1/f$-noise appears with a $1/\sqrt{f}$ slope but will be still called $1/f$-noise.

4.1.1 Photodiode dark current

For a reverse biased photodiode as used in most photodetectors, it is important to minimize the device dark current in order to achieve a high signal-to-noise ratio. The dark current of a photodiode is the leakage current that flows when the photodiode is in the dark and a reverse bias voltage is applied across the junction. Dark current is always specified at a specific value of applied bias voltage. The general equation for the I-V characteristics of a photodiode with a saturation current I_s is given by

$$I = I_s \left[\exp\left(\frac{eV}{k_B T} \right) - 1 \right] - I_{ph} \tag{4.1}$$

where I_{ph} is the photocurrent, V the applied voltage and T the absolute temperature. For a reverse-biased photodiode ($V < 0$) in the dark ($I_{ph} = 0$), the diode current is determined by

the junction leakage current of the photodiode. Different current conduction mechanisms can contribute to dark current I_d of a photodiode:

$$I_d = I_{d,g-r} + I_{d,diffusion} + I_{d,surface} + I_{d,tunnel} \tag{4.2}$$

where $I_{d,g-r}$ results from charge generation and recombination, $I_{d,diffusion}$ from diffusion, $I_{d,surface}$ from surface leakage, and $I_{d,tunnel}$ from tunneling of electrons via the junction. As the individual components of the dark current have different origins, their individual contribution to the overall noise performance is very complex and will not be treated here.

In general, the low-frequency noise of photodiodes is dominated by generation and recombination of carriers in the diode and by trapping and releasing of charge in the bulk or at surface states at the top and bottom contacts [22, 36, 45, 124, 125]. The general behavior of generation-recombination (G-R) or trapping processes is explained in Appendix A.1. Typically two models, those by McWhorter or Hooge can be used to mathematically describe the excess noise in photodiodes (see Appendix A.3). However, both models are not based on real physical mechanisms and parameters. Further more Hooge's relation is hard to apply in the case of reversed biased photodiodes since the number of free carriers in the diodes is unknown. Therefore no precise mathematical model of the noise level has been realized and only a quantitative comparison of the noise exhibited by the tested devices at relevant Fourier frequencies has been carried out.

In photodiodes, the temperature dependence of the dark current is very important. The dark current dependence on temperature variation arises from thermally excited electron-hole pairs. The dark current increases with increasing temperature. The rule of thumb is that the dark current will approximately double for every 8 to 10 K increase in ambient temperature. This is equivalent to a reduction of the shunt resistance R_{sh} of a photodiode. However, specific diode types can vary considerably from this relationship.

In this work, the dark noise exhibited by several large area InGaAs photodiodes has been characterized. Typically the dark noise of a complete photodetector circuit is measured at a fixed bias voltage and room temperature. This noise is often assumed to be a non-changing device parameter that defines the detection noise for the experiment. However, for photodetectors designed for high optical powers the thermal load of the diode changes dramatically and thus also the temperature of the photodiode. As the dark current is a function of temperature, the low-frequency noise changes with temperature, too. This could explain the low-frequency noise behavior of the out-of-loop noise in the power stabilization experiments. In addition, the amount of excess noise exhibited by devices can be used as a non-destructive analysis to predict their reliability [76, 80, 89].

In order to evaluate the fraction of the overall $1/f$-noise of a typical photodetector circuit under illumination, the $1/f$-behavior of the current noise for different bias voltage levels in dark condition has been measured first. In addition the typical temperature increase of the photodiodes in high-power detectors was evaluated.

The noise spectra were measured using a variable gain low-noise current amplifier (FEMTO Messtechnik, DLCPA-200), a D/A-converter (National Instruments, USB-6009) to generate a variable bias voltage and an FFT analyzer (Stanford Research, SR785). The current range and the input sensitivity could be changed by varying the gain of the amplifier to meet the needs of various measurement conditions. The photodiode under test was mounted upside down in a metal mount to avoid any illumination. The amplifier and the diode mount was mounted in a box made of aluminum to shield the setup against air currents and to ensure dark operation.

The diode mount could be temperature controlled using a TEC and a temperature controller (Team Wavelength, LFI 3751) in order to determine the temperature dependence of the dark current-noise spectra. The bias voltage was filtered by a 2nd-order low-pass filter identical to the one described in Section 3.1.4. The complete noise characterization was conducted using a computer running a LabVIEW® program, in order to perform an automated measurement sequence.

Selected results of the noise characterization of devices with an active area of 2 mm are shown in Figure 4.1. The noise spectra are given for a typical bias voltage of 5 V measured at room temperature, including two different germanium devices for comparison.
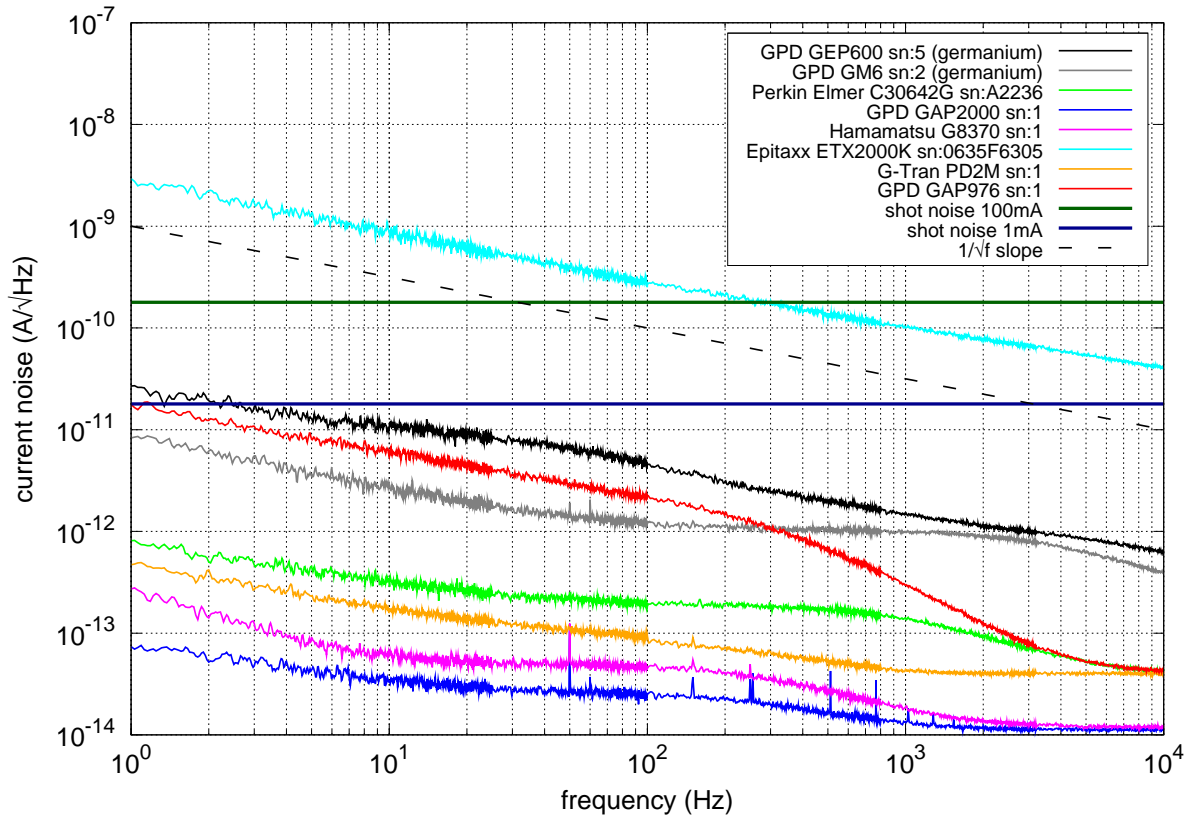
Figure 4.1: Comparison of low-frequency noise of selected InGaAs and Ge photodiodes with an active area of 2 mm (bias voltage 5 V, T=293 K).

All devices showed $1/f$-noise at low frequencies and except for two devices the noise shape changed with increasing frequency. The absolute level of the dark noise exhibited by the characterized devices varies by more than four orders of magnitude. In general, it is observed that photodiodes with low dark current and a low bias voltage dependence of the dark current also exhibit low $1/f$-noise. The best devices offer very low dark current below the sensitivity of the measurement setup used. Furthermore it is observed that devices with very high dark current also exhibit high $1/f$-noise.

For typical power stabilization experiments a shot-noise limited performance for 1 mA to 100 mA is intended. The corresponding linear spectral density for the shot noise of 1 mA of photocurrent is $18\,\mathrm{pA}/\sqrt{\mathrm{Hz}}$ and $180\,\mathrm{pA}/\sqrt{\mathrm{Hz}}$ for 100 mA respectively. Thus the Epitaxx

(ETX 2000K) cannot be used and also the "GAP976" from GPD is very close to the target design sensitivity at low frequencies.

To operate the photodiode in the linear regime when illuminated with high optical power, the bias voltage has to be increased, often to levels higher than the maximum value specified by the manufacturer. Hence it is very important to characterize all devices in order to determine how the noise level changes with the applied bias. Dark-current noise spectra for several devices were measured for different bias voltage levels at room temperature. Typical results for two different photodiodes with medium dark noise are shown in Figure 4.2. The general behavior of these devices is representative for InGaAs photodiodes. In particular for all measured devices, the excess noise level scales with the applied bias voltage.

Two general forms of the excess noise could be observed. The device from Epitaxx shown in Figure 4.2(a) shows almost perfect $1/f$-noise over the entire frequency band from 1 Hz to 10 kHz. Below a bias of 4 V a strong dependence of the dark noise on the bias voltage was observed. The noise seems to approach an upper limit which is about four orders of magnitude higher compared to small values. In contrast, the dark noise of the photodiode from GPD shown in Figure 4.2(b) increases only about two orders of magnitude for the same voltage span. For reverse biases up to 3.5 V, the observed noise also has a $1/f$-shape. For higher voltages, the characteristics change to typical low-frequency noise due to generation-recombination or trapping processes, which results in a noise shape that can described by superposition of Lorentzian spectra.

For both devices, the measured noise increases rapidly from the point where the dark current also increases very rapidly with the reverse bias voltage applied. However, the total amount of dark current measured for both devices is almost the same, whereas the excess noise dependence on bias voltage for these devices varies strongly.

In order to determine how the measured low-frequency noise scales with the dark current, the linear spectral density for Fourier frequencies 1 Hz, 10 Hz, 100 Hz and 1 kHz were taken from the measurements and plotted as a function of dark current. As an example, the results from the measurements shown in Figure 4.2 are given in Figure 4.3.

Regardless of the shape and absolute level of the dark noise exhibited by the characterized devices, the linear spectral density for all tested Fourier frequencies increases steadily with the measured dark current. Similar results can be found in literature [152]. Thus a pre-selection process in terms of high shunt resistance which is equal to low dark current is recommended if a photodiode for low-noise measurements is needed.

To investigate the current noise dependence on temperature, the temperature increase of the photodiode when illuminated has to be determined. To measure the actual temperature of a photodiode under high illumination, two different methods were used and compared. First the actual temperature of an illuminated photodiode was measured using an infrared micro-bolometer array, also known as a thermal imaging camera. The camera measures the infrared emission in the wavelength range from 8–14 µm. Thus the glass window of the photodiode had to be removed in order to be able to measure the chip temperature. The illumination with the laser wavelength of 1064 nm, well outside the measurement range of the bolometer, does not disturb the infrared measurement. The results are shown in Figure 4.4.

The temperature increase of the chip was measured for an InGaAs diode from Perkin Elmer (model C30642G). A bias voltage of 7 V was used and a responsivity of 0.77 A/W was measured for this specific device, which gives a maximum power dissipation in the photodiode of 0.83 W. The maximum increase in temperature of the surface is about 11.5 K for ≈ 100 mA of photocurrent.
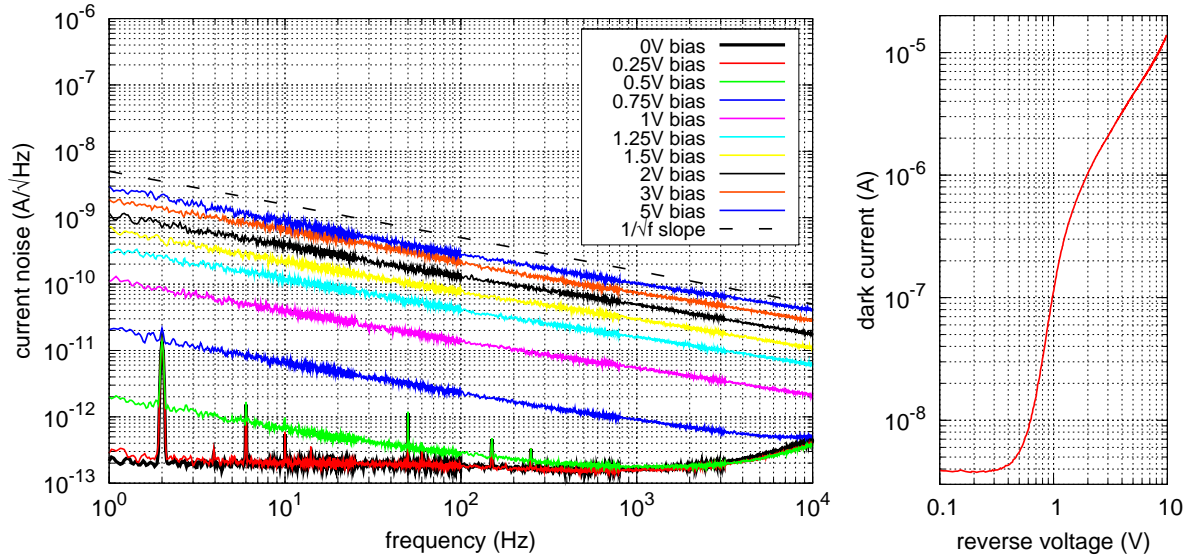
(a) Epitaxx ETX 2000K T5 sn:0635F6305
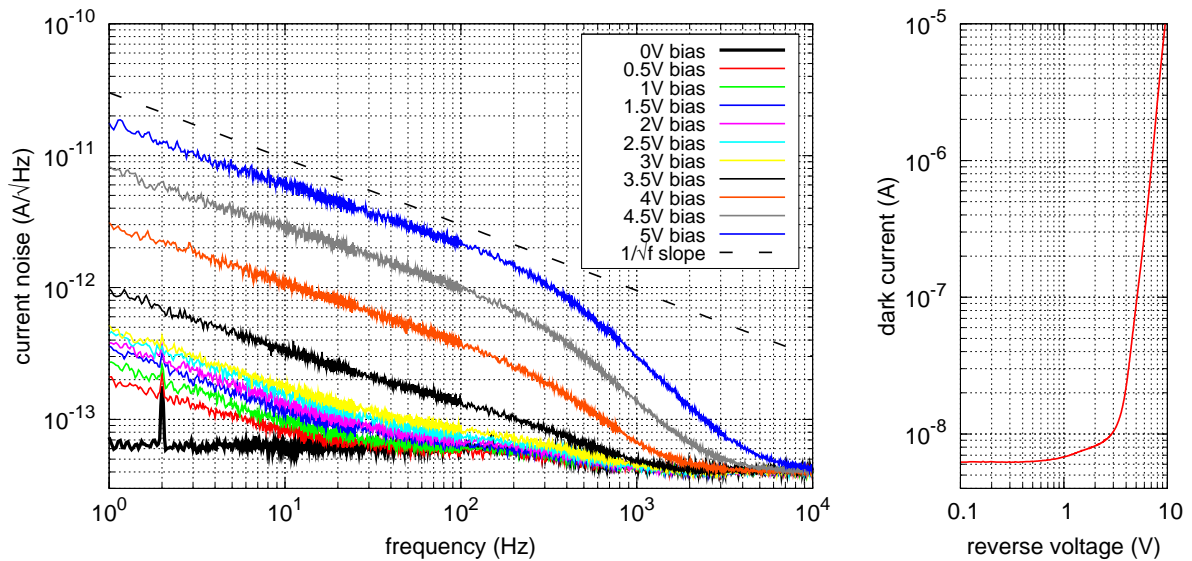
(b) Germanium Power Devices (GPD) GAP 976 sn:1

Figure 4.2: Typical dark current noise spectra of two different 2 mm diameter InGaAs photodiodes for different bias voltage levels at room temperature. Also shown: dark current versus reverse bias voltage for each device.

(a) Epitaxx ETX 2000K T5 sn:0635F6305   (b) Germanium Power Devices GAP 976 sn:1
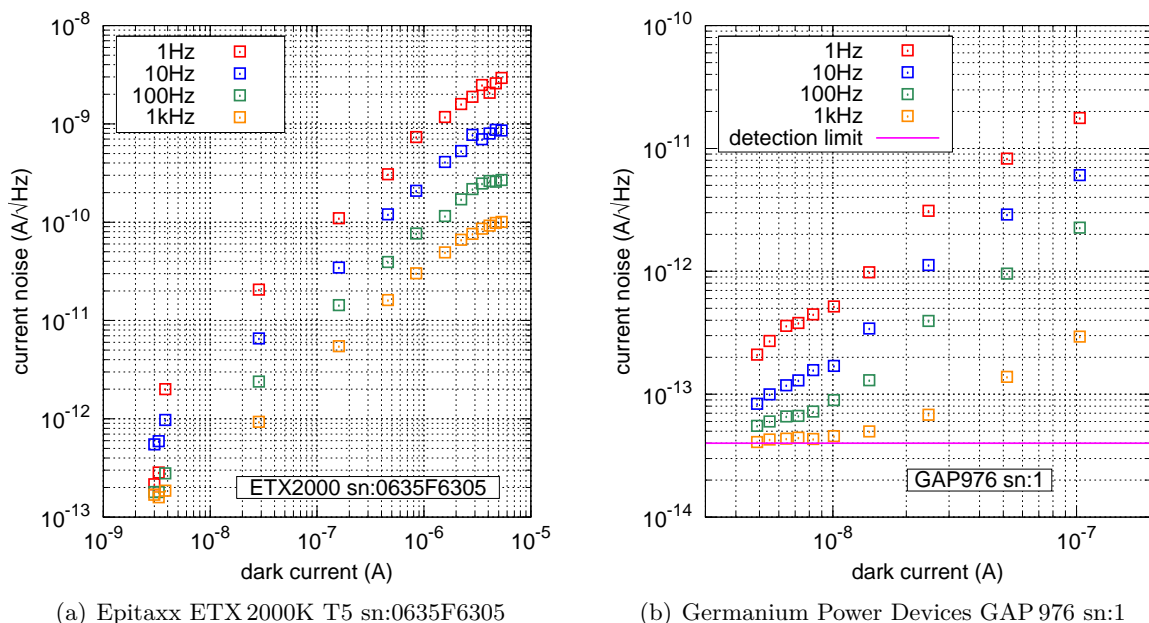
Figure 4.3: Noise in InGaAs photodiodes as a function of measured dark current for Fourier frequencies 1 Hz, 10 Hz, 100 Hz and 1 kHz derived from the measurements shown in Figure 4.2.

The biggest inaccuracy for this temperature measurement is the unknown emission coefficient of the chip material. For the measurement in Figure 4.4(a) without any power dissipation, the temperature of the diode and its mount is the same, but the measured absolute difference is about a couple of Kelvin. The emission coefficient was adjusted such that the absolute value of the chip without any power dissipation was correct.

In order to validate the data obtained from the bolometer measurement, a second, completely different temperature measurement technique was used. A simple semiconductor junction makes an excellent temperature sensor. At low values of forward current I_F, the junction voltage V_J is nearly linear to the junction temperature T_J. Thus a change in junction temperature δT_J produces a corresponding change in forward voltage δV_J as

$$\delta V_J = K \times \delta T_J \tag{4.3}$$

with $K = \frac{\delta V_J}{dT}$ the temperature coefficient of the diode forward voltage. As already mentioned one has to use a low forward current in order to be in the linear regime. Thus one has to switch very quickly between the typical operation point (under illumination) and the temperature measurement setup for the junction temperature using the same device. The experimental setup is shown in Figure 4.5.

The device under test (DUT) is illuminated using a probe beam with appropriate power. The probe beam was generated using an fiber coupled laser and an AOM (Crystal Technology, 3080-194) in the first diffraction order. A small fraction of this probe beam was monitored by a fast photodetector (PD1). The rise time of the AOM including the driver (Landwehr Electronic, A274-18) was <70 ns. Hence the beam can be rapidly switched on and off compared to the expected thermal time constants in the DUT.

(a) $P_{\text{opt}} = 0\,\text{mW}$

(b) $P_{\text{opt}} = 65\,\text{mW}$

(c) $P_{\text{opt}} = 105\,\text{mW}$
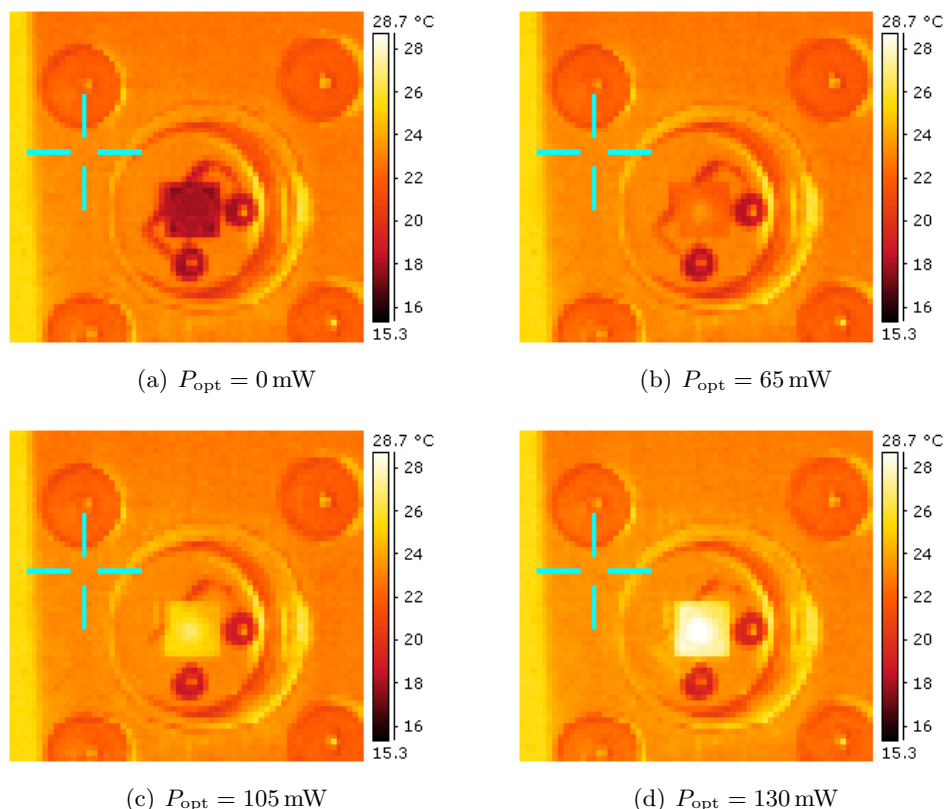
(d) $P_{\text{opt}} = 130\,\text{mW}$

Figure 4.4: Chip temperature measurement of an illuminated photodiode using a thermal imaging camera: (a) P_{opt}=0 mW; (b) P_{opt}=65 mW; (c) P_{opt}=105 mW; (d) P_{opt}=130 mW.

The DUT was illuminated over 2 minutes to ensure a steady state of the diode chip temperature. The light was then switched off and the DUT was switched to low constant current operation using a current regulating diode (J505, 1 mA). The forward voltage drop of the DUT, the power monitoring signal and the switching signal was recorded using a fast oscilloscope (Agilent, 54621A) with 4 MB of deep memory to obtain a high resolution time signal.

This setup has been used to characterize 13 different models of large area InGaAs photodiodes. Due to the large amount of data obtained, only the results for the specific device will be given here. More details and all results can be found in Appendix B.

Using the junction voltage measurement technique, the junction-to-case thermal resistance of the photodiode "C30642G" could be measured to be $R_{\text{th,C30642G}}$=15.2 K/W. This corresponds roughly to a temperature rise of 12.6 K for 130 mW of optical power and a typical bias voltage of 7 V.

In comparison, the two methods show almost the same result. The infrared imaging camera using an infrared micro-bolometer array is not as sensitive and accurate as the direct measurement via the junction-temperature measurement technique using the forward voltage. Nevertheless both techniques are very powerful. The bolometer measurement can be performed very quickly while a special setup is necessary to use the more accurate junction-temperature
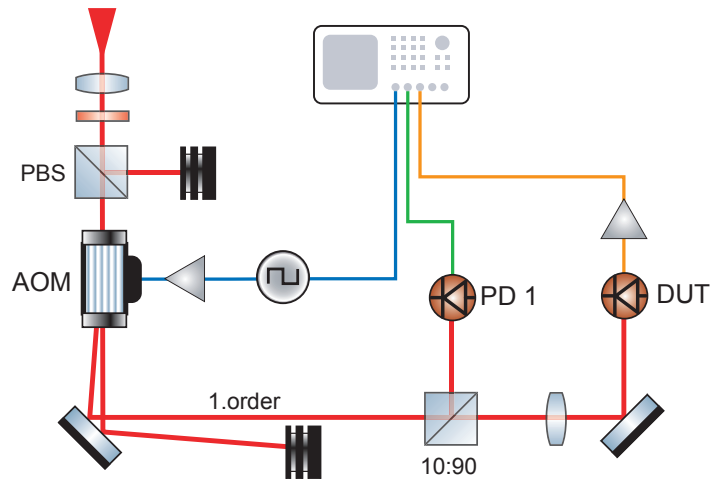
Figure 4.5: Experimental setup for thermal impedance measurements of photodiodes.

measurement technique with high resolution, which can be used to build a detailed thermal model of the individual device.

As the change in temperature when illuminated is only around $10\,\mathrm{K}$, according to the rule of thumb, the increase in dark current will be approximately a factor of two higher. In order to demonstrate the increase in low-frequency excess noise is due to the increase in dark current caused by higher chip temperatures, the $1/f$-noise was measured as a function of temperature of the device. Since the noise level for this specific device was very low, the bias voltage was increased to about $10\,\mathrm{V}$. Figure 4.6 shows an example of the temperature characteristics of the dark noise of a typical photodiode.
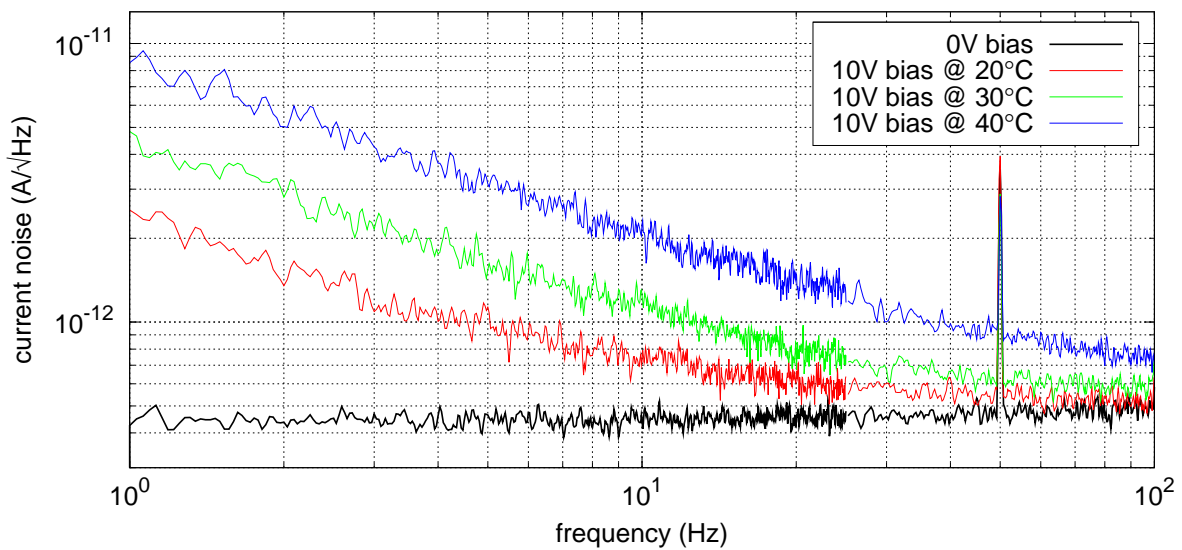
Figure 4.6: Low-frequency noise in a photodiode as a function of junction temperature.

For the tested device, the dark current as well as the absolute noise level approximately doubles every 10 K. To assess the relevance of this effect the absolute noise level has to be compared to the fundamental shot noise. The linear spectral density of shot noise of 100 mA of photocurrent is 180 pA/$\sqrt{\text{Hz}}$. Even with a 20 K increase in temperature the shot-noise level is a factor of 20 above the dark noise at 1 Hz. The dark noise of photodiodes used in the power stabilization experiment show even less noise as the example devices shown above. Thus the increase in dark noise due to a temperature change can not explain the limitation observed in the power stabilization experiments.

4.1.2 White light source measurements

To directly measure low-frequency excess noise in photodiodes and photodetectors under illumination, an ultra-stable light source is essential. In order to even demonstrate if a shot-noise-limited detection is possible, the source has to be shot-noise limited. Generally lasers exhibit large excess noise at low frequencies and it is very difficult to reduce their noise to the shot-noise limit of high power levels by means of active feedback.

LED sources are intrinsically less noisy than lasers. Nevertheless there are several noise sources in LED's including shot, generation-recombination, $1/f$, and random-telegraph noise [133]. Generation-recombination and $1/f$-noises are dominant at low frequencies and are usually caused by defect levels and/or tail states located in different parts of the device. At higher frequencies classical shot noise dominates. Although the quantum efficiency of LEDs is typically not as high as that of lasers, today modern high-power LEDs are available in the infrared region, e.g. for infrared illumination for surveillance systems. The total radiant flux of these devices can exceed 500 mW from a point-like emitting area and are hence ideally suited for a high-power photodiode measurement setup.

In the past, thermal light sources like tungsten-halogen lamps have been used as low-noise light sources. Generally conventional thermal light sources are assumed to be shot-noise-limited. Tungsten-halogen lamps have the virtue that the thermal inertia of the coiled-coil filament behaves as a low-pass filter to suppress noise of the power supply. The tungsten-halogen lamp and the LED can both be operated with a battery-powered source providing very high stability. In the following, the performance and noise qualities of a tungsten-halogen lamp with a thermal spectrum and a high-power infrared LED under the more realistic conditions of a critical optical experiment are compared.

The experimental arrangement is based on a light source and the photodiode or detector under test. Two different light sources were tested, a 100 W tungsten-halogen lamp (Osram, Xenophot 64625) and a high-power infrared LED (Osram, Golden Dragon IR-LED 940 nm). Both devices were supplied by lead acid batteries providing a very high amplitude stable constant voltage.

The tungsten-halogen lamp is typically at a temperature of approximately 2800 K. The black-body radiation spectrum is given by Planck's law:

$$I(\lambda) = \frac{2\,h\,c^2}{\lambda^5} \frac{1}{\exp\left(h\,c/\lambda\,k_{\mathrm{B}}\,T\right) - 1},\tag{4.4}$$

where T is the temperature of the black body, h is the Planck's constant, and k_{B} is the Boltzmann's constant. At 2800 K, the maximum of the black body radiation spectrum is at $\lambda = 1035$ nm. The drawback of a thermal light source such as a tungsten-halogen lamp is its low brightness. Its spectrum is very broad and a lot of light beyond the spectral sensitivity of

InGaAs photodiodes is emitted. In order to reduce unwanted effects caused by light beyond the spectral sensitivity of the detector, the spectral bandwidth of the illumination was limited using a bandpass filter combined with a heat filter, placed in the light path, between the bulb and the detector. The bandpass filter was a dielectric 45° high reflective mirror with a center wavelength of λ_c=1064 nm having a bandwidth of approximately 100 nm. The visible spectrum was filtered using a dielectric coated cold light reflector (Linos Photonics, KS 93/45°). A high-pass filter (Schott, RG850, 3 mm thick) directly in front of the detector under test ensures that no visible light e.g. ambient light in the lab interferes with the measurement.

The LED was operated in constant current mode using wire wound resistors, which offer very low excess noise (please refer to Section 4.2). The high-power LED (Osram, Golden Dragon Hi Power IR LED 940 nm) was driven at the specified current of 1 A. As the power LED has to dissipate high power from a small package, the LED was soldered to a special aluminum-based PCB with a board thickness of 1 mm which acts as a heat spreader. The PCB was then mounted to a large heat sink.

Figure 4.7 depicts the direct comparison between the noise from the tungsten-halogen bulb and that from the LED, recorded with the same detector.
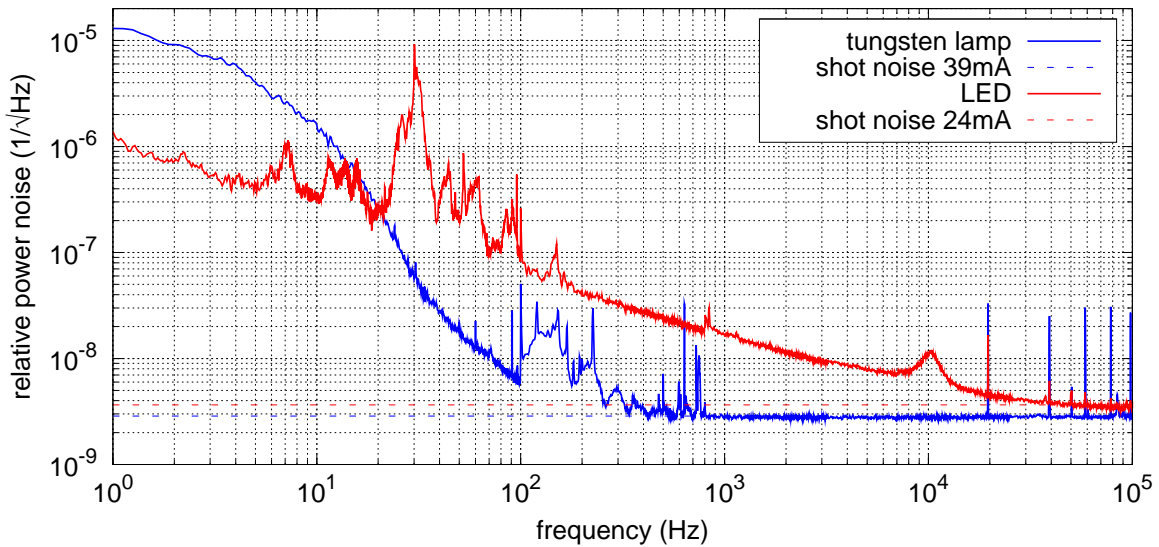
Figure 4.7: Comparison between the intrinsic noise of a tungsten-halogen lamp and a high-power infrared LED.

The shot-noise level was calculated from the mean detector photocurrent I_{DC}. Both light sources show markedly unstable low-frequency behavior. The noise exhibited by the high-power LED used is higher than that of the filament lamp and is only shot-noise limited above 50 kHz. Using the tungsten lamp, shot-noise limited measurements can be performed for Fourier frequencies above 800 Hz. Further mechanical improvement of the setup would reduce acoustic coupling and reduce the lower frequency limit to about 400 Hz. The large increase in the observed noise for the tungsten lamp below 100 Hz might be due to convection caused by the high power dissipation in the setup. In early measurements using both sources, technical noise from linear regulated power supplies could be observed in the emitted light. Therefore the measurements were conducted using lead-acid batteries.

In conclusion, the experiment could demonstrate that shot-noise dominates for both light sources at high frequencies. For lower frequencies, power noise exhibited by the high-power LED is much higher than by a tungsten-halogen bulb. Even more stable thermal sources can be anticipated by further reduction of technical noise in the acoustic region and at low frequencies, e.g by using a source less sensitive to acoustics such as silicon carbide (SiC) thermal infrared radiators (so-called Globars). Also conducting the experiment in a sealed chamber or maybe in vacuum could improve the performance at low frequencies. However, both sources available for this work are not suitable to measure low-frequency excess noise in photodiodes under high illumination and a different measurement technique had to be used.

4.1.3 Balanced-detection experiment

A common configuration for low-noise power measurements is that of a balanced homodyne detector, containing two photodetectors, where a beam splitter sends equal parts of the optical power to each detector, and the sum or the difference of the photocurrents are obtained electronically. Using a balanced homodyne detector, both the laser power noise level and the SNL can be measured. The sum of the photocurrents is the same as for using all light on a single detector. Theoretically, subtracting the individual currents in a balanced-detection scheme should show shot-noise limited performance, even when the laser light used is dominated by technical noise. If the light is split equally on both detectors, the technical noise of the laser would be the same and thus eliminated when subtracted. Figure 4.8 shows the principle schematic of such a balanced receiver.
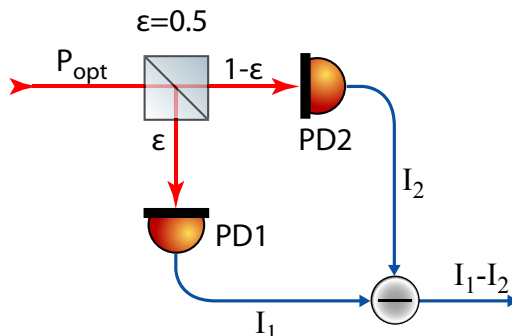
Figure 4.8: Schematic diagram of a balanced detector comprising a 50:50 beam splitter and a balanced detector pair.

The optical power P_{opt} is split equal onto a pair of photodetectors (PD 1 and PD 2) using a 50:50 beam splitter ($\epsilon = 0.5$). The noise reduction for correlated, technical noise on both detectors can be quantified by a common mode rejection ratio [35]

$$\text{CMRR} = -20 \log_{10} \left| \frac{I_2 - I_1}{(I_2 + I_1)/2} \right|^2 \tag{4.5}$$

where I_1 and I_2 are the photocurrents from the two photodiodes. Since the available laser systems have high technical noise level at low frequencies, a high CMRR is required in order to suppress technical noise of the laser. In order to achieve a high common mode rejection, the balancing has to be very good, either by selection of the photodiodes for equal quantum efficiency or adjusting the splitting ratio of the beam splitter. Since all on both photodiodes

correlated fluctuations will be suppressed, uncorrelated noise sources, e.g. scattered light or intrinsic noise in the photodiodes (e.g. $1/f$-noise) will show up in the difference of the two photocurrents. Only if no uncorrelated noise sources exist to a precision set by the technical noise of the laser and the CMRR, the observable noise level will be shot-noise limited to $I_1 + I_2$ equivalent photocurrent.

The big advantage of a balanced-detection scheme conducted within the same optical setup as for the power stabilization experiments is that both, the physical properties of both devices and conditions specific to the experimental setup, like scattered light, will be identical. Hence the observed noise level of the balanced detection experiment equals the minimum achievable noise level for a power stabilization experiment loop. It is hard to distinguish between low-frequency noise in photodiodes and scattered light as both show up in the same style. Scattered light from external sources like lenses and mirrors can be reduced to a certain point, but even when using high quality optical components, scattering can not be excluded completely.

In order to examine the low-frequency detection limit, two different experimental setups for a balanced-detection scheme were used. The first setup was constructed in the same vacuum chamber as used for the power stabilization experiment. Also the laser, the filtering cavity and the PZT to introduce pointing were used. In order to investigate the influence of the beam splitter, the beam path to the photodiodes and of scattered light in the tank, a fiber based experiment was performed with a second setup. The two experiments and their results will be presented in the following section.

Experimental setup

The first experiment is almost identical to the power stabilization experiment already described in Section 3.2. Hence the optical setup (see Figure 4.9) will be described only briefly.
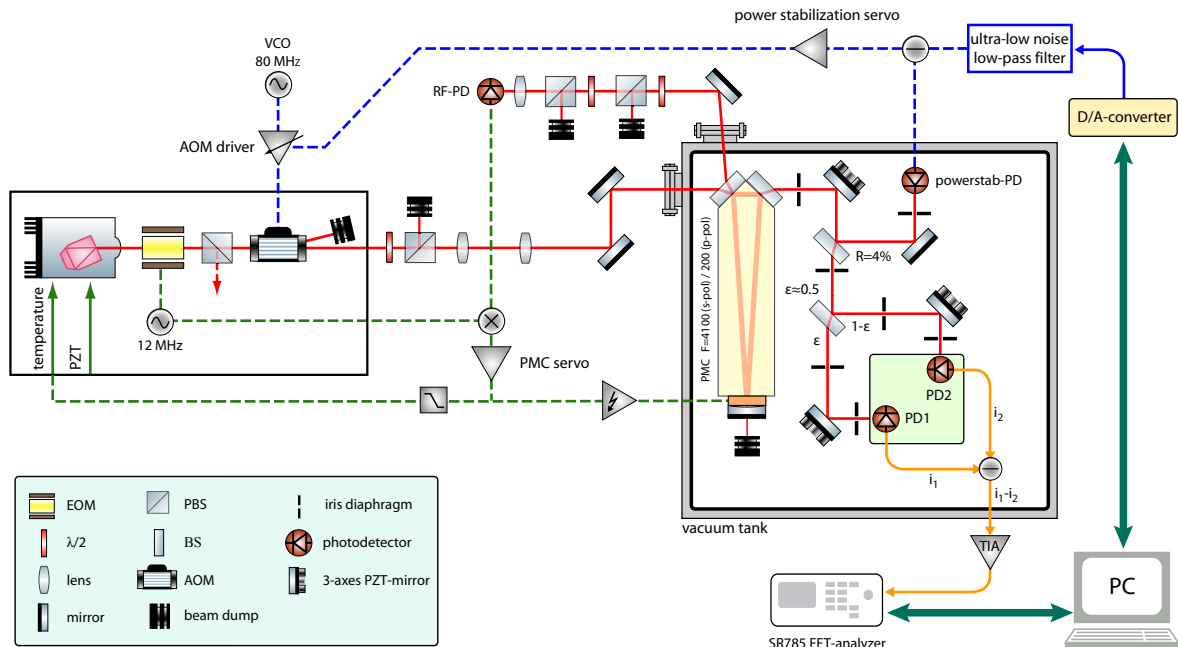
Figure 4.9: Schematic diagram of the free-space balanced-detection setup.

The main part of the experiment, the complete detection including an optical ring resonator, was placed again in a vacuum tank to minimize the influence of air-currents. The filter cavity

used in both power stabilization experiments was replaced by a new cavity with a higher finesse ($\mathcal{F}_\mathcal{S}$=10400, formerly 4100). The spacer was made of aluminum instead of fused silica, which reduces scattered light transmitted through the spacer generated inside the cavity at the mirrors. The higher finesse improves the reduction of laser beam geometry fluctuations and beam pointing of the incoming laser beam. The PMC was locked by the Pound-Drever-Hall technique to the laser and provides a TEM$_{00}$ mode to the detection part downstream of the cavity. As ambient temperature fluctuations cause large length fluctuations of the PMC due to the thermal expansion of the new aluminum spacer, additional feedback to the thermal actuator of the NPRO was used to ensure locking over several hours.

Downstream of the PMC, a partial reflective mirror was used to split off about 4% of the main beam which is detected by a photodetector for power stabilization of the filtered beam. The obtained signal was fed back to an AOM in front of the PMC. By changing the DC-setpoint of the power stabilization loop, the power for the photodiodes in the balanced configuration could be adjusted over a wide range (80%). The optical radiation with adjustable power was split into two nearly equal beams with fraction ϵ and $1 - \epsilon$ respectively using a non-polarizing beam splitter and was detected by the two photodiodes in the balanced configuration. The photocurrents produced by the two photodiodes, I_1, and I_2, are directly subtracted before being processed. The difference, $I_1 - I_2$ of both current signals is amplified using a transimpedance amplifier with $R_{\mathrm{TIA}} = 1\,\mathrm{k\Omega}$, and the noise power analyzed with a spectrum analyzer. Differences in the optical power or photodiode efficiencies were compensated by slightly changes of the angle of incidence on the beam splitter. Also changing the polarization behind the PMC using a waveplate was tested but its influence on the noise at low frequencies, e.g. due to temperature fluctuations of the waveplate, has not been determined.

To reduce the effect of temperature fluctuations on the detection, both photodiodes were mounted on the same, large heat sink made of aluminum. As the measurements were conducted in vacuum, a heat transfer was possible only via conduction and radiation (which can be neglected as surrounding parts are on same temperature). In order to investigate the coupling between beam pointing and apparent power fluctuations, three multi-axes piezoelectric mirrors (Physik Instrumente (PI), S-311.10) were placed directly downstream of the PMC and in front of each photodiode of the balanced detector. The two piezoelectric mirrors in front of the photodiodes were mounted on conventional mirror mounts. By applying a signal to the individual axes of the PZT and measuring the response in each photodetector signal, the beam on each photodiode could be aligned independently of the point of minimum sensitivity to pointing. The deflection angle was $\approx 600\,\mathrm{\mu rad}$ for each axis with a bandwidth of $\approx 6\,\mathrm{kHz}$.

Wherever possible super-polished substrates with low-loss coatings were used in order to achieve a minimum of scattered light. As scattered light was found to be an important source of low-frequency noise, several apertures made of infrared absorbing glass (Schott, BG39) with a small center bore were used. They were placed after each optical component to block as much scattered light or ghost beams generated by them as possible. The transmitted beam of the PMC was blocked as well. Figure 4.10 shows a photograph of the balanced-detection experimental setup.

In order to investigate the influence of the beam splitter and scattered light in the tank on the observed $1/f$-noise, a fiber based experiment was performed in which the beam splitter was replaced by a fiber coupled version. The stabilized beam after the PMC was injected into the input of the fiber beam splitter and both outputs were connected to a self-made fiber-coupled photodiode each, using the same photodiodes as for the free-space setup. In the following discussion the results for both experiments will be given.
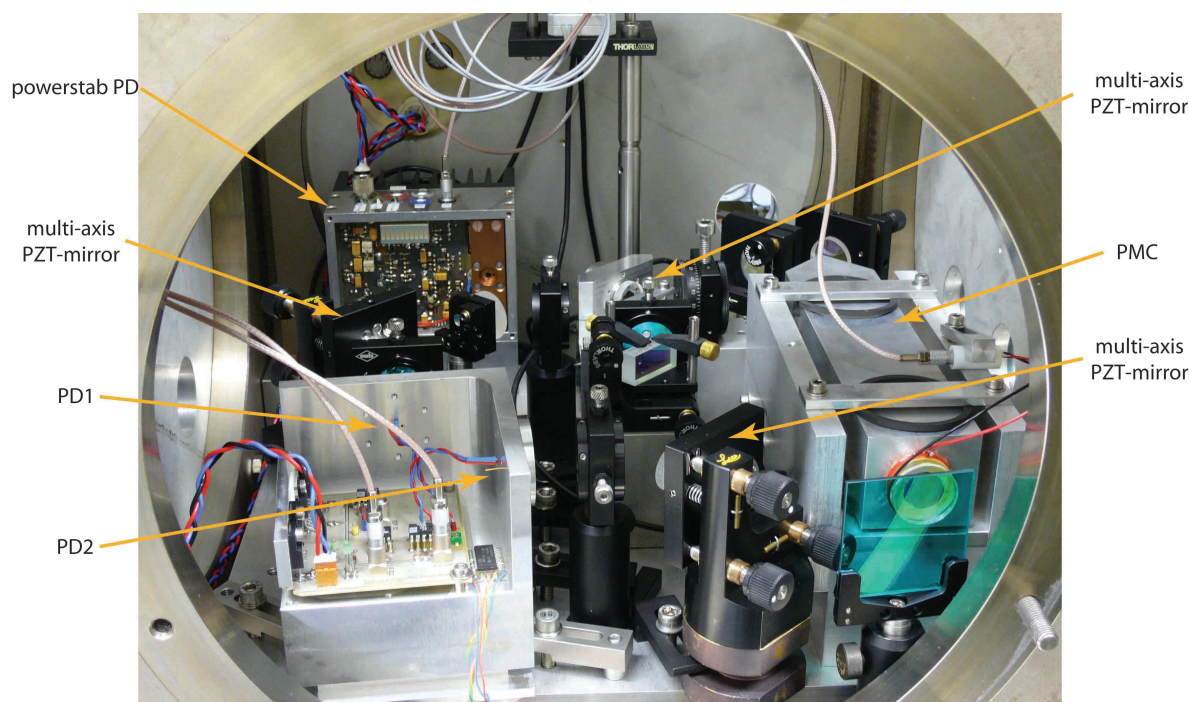
Figure 4.10: Photograph of the balanced-detection experimental setup.

Results

Two photodiodes from the same batch were used as pairs for the balanced receiver. Important conditions for each set of measurements are given on top of each graph. The upper photocurrent level was limited by the optical power available, not by the devices. Five different types have been compared. In the prototyping phase cheap silicon diodes without window and devices made from germanium have been used. As an example, the results for the germanium photodiodes are depicted in Figure 4.11.

Examples for relative power noise spectra obtained for different power (photocurrent) levels on both detectors is shown in Figure 4.11(a). The dashed lines correspond to the calculated equivalent relative noise level for the shot noise of the photocurrent. Independent of the photocurrent, the noise spectra are dominated by low-frequency excess noise over the entire frequency band of the measurement setup.

A better comparison of the observed noise level is achieved by a direct comparison of the observed noise level for different Fourier frequencies for the individual measurements plotted versus the photocurrent of the devices. Figure 4.11(b) shows the graph for a large number of measurements for the germanium photodiode. As already seen in the noise spectra, all measurements are dominated by excess noise up to 10 kHz, independent of the photocurrent. For 10 Hz the observed level is more than one order of magnitude higher than the theoretical shot-noise limit. Using these photodiodes, a shot-noise limited performance for several tens of mA of photocurrent is not possible below 100 kHz, a much worse performance compared with the results achieved in the power stabilization experiment before using InGaAs photodiodes. The observed poor performance of these germanium devices might be due to intrinsic material issues. But these devices were also not optimized for 1064 nm and hence a large amount

(a) Noise spectra

(b) Noise-level versus photocurrent

Figure 4.11: Balanced-detection results for germanium photodiodes from GPD (GEP600 [54]): 4.11(a) examples for relative power noise spectra obtained for different power levels; 4.11(b) comparison of observed noise levels for different Fourier frequencies plotted versus photocurrent.

of the incoming light is reflected and scattered throughout the vacuum chamber where the experiments were conducted.

For final measurements with respect to a shot-noise limited power stabilization at 1064 nm, InGaAs photodiodes from different vendors have been compared. Results for two different types from different vendors are given in Figures 4.12 and 4.13.

The measurements for the InGaAs devices show much less low-frequency excess noise. For Fourier frequencies down to about 100 Hz the measurements are shot-noise limited independent from the detected photocurrent up to about 55 mA. Higher photocurrents could not be achieved due to lack of laser power. For Fourier frequencies <100 Hz excess noise starts to become dominant. The shape of the low-frequency noise changes at lower frequencies. Here two different (but unknown) noise mechanisms seem to appear. Between 1 Hz and 10 Hz the slope is almost linear. Between 10 Hz and 100 Hz it is also linear but with a different slope.

For both devices, the noise level obtained at 1 Hz and 10 Hz starts to decrease like the theoretical shot-noise limit with increasing photocurrent, but the curve for 10 Hz seems to level off for higher photocurrents, while the noise level at 1 Hz is still decreasing. It is also expected that the noise level at 1 Hz levels off at even higher photocurrents as already indicated by the GAP2000-device. This seems to indicate that one of the two noise sources is proportional to and one is independent of the light power.

In order to investigate environmental influences, several measurements were performed while varying the pressure inside the vacuum tank, the temperature of the photodiodes from 20°C to

(a) Noise spectra

(b) Noise-level versus photocurrent
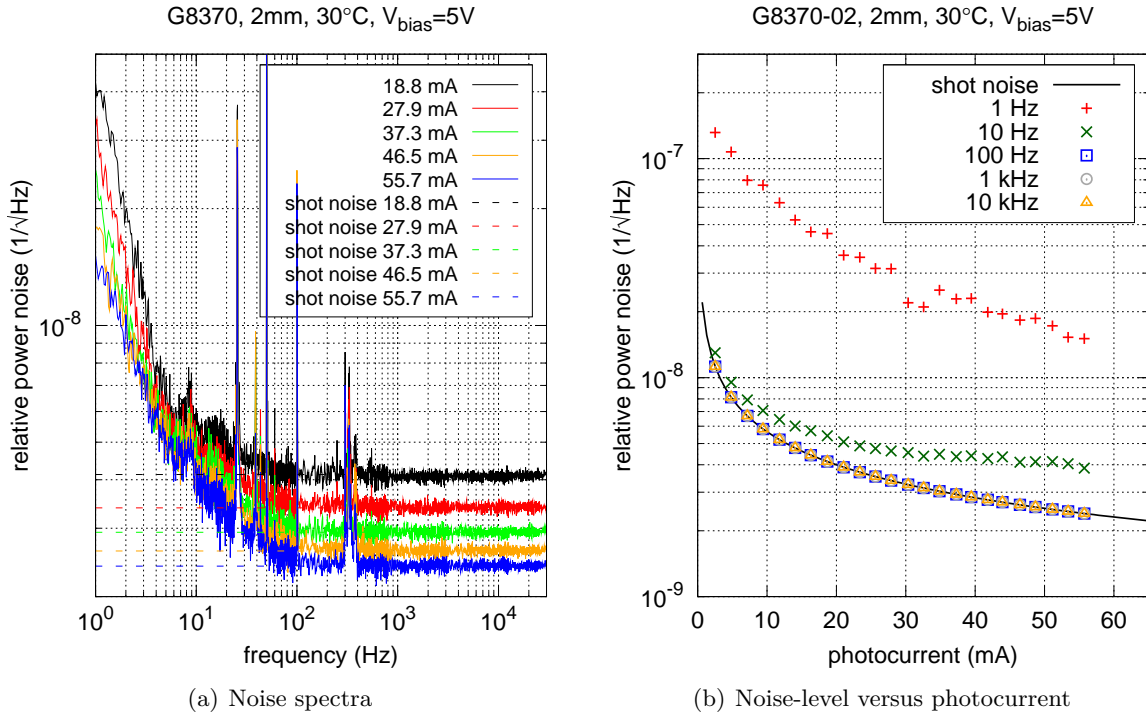
Figure 4.12: Balanced-detection results for InGaAs photodiodes from Hamamatsu (G8370-02 [57]): 4.12(a) examples for relative power noise spectra obtained for different power levels; 4.12(b) comparison of observed noise levels for different Fourier frequencies plotted versus photocurrent.

70°C and also the influence of the reverse bias voltage from 5 V to 10 V has been examined. All these measurements showed that the low-frequency excess noise observed in the devices studied in this work does not depend on these parameters.

As mentioned in the previous section, the free-space beam splitter was replaced by a fiber coupled version in order to investigate the influence of the beam splitter and scattered light in the tank. Each output of the fiber beam splitter were connected to a custom-made fiber-coupled photodiode, using the same photodiodes (Hamamatsu, G8370-02) as already used in the free-space setup. The results for the fiber-based experiment are given in Figure 4.14.

It could be observed that some light was transferred from the core into the cladding of the fiber at the junction of the two fibers from which the beam splitter is made off. In order to strip off the light in the cladding, two 40 m-long polarization-maintaining single-mode fibers (Nufern, PM980), bent in a kidney-shaped manner, were connected between each output of the beam splitter and the photodetector. The fiber-based setup shows much higher low-frequency noise using identical photodiodes than the free-space setup. Without the long cleaning-fiber, the noise level was even about two orders of magnitude higher. Hence for photodiode characterization, the fiber-based setup as implemented is not suitable.

The balanced-detection measurements showed that low-frequency excess noise already dominates the performance at low frequencies when using two bare photodiodes without noisy readout electronics or a control loop. This detection limit cannot be bettered by a power

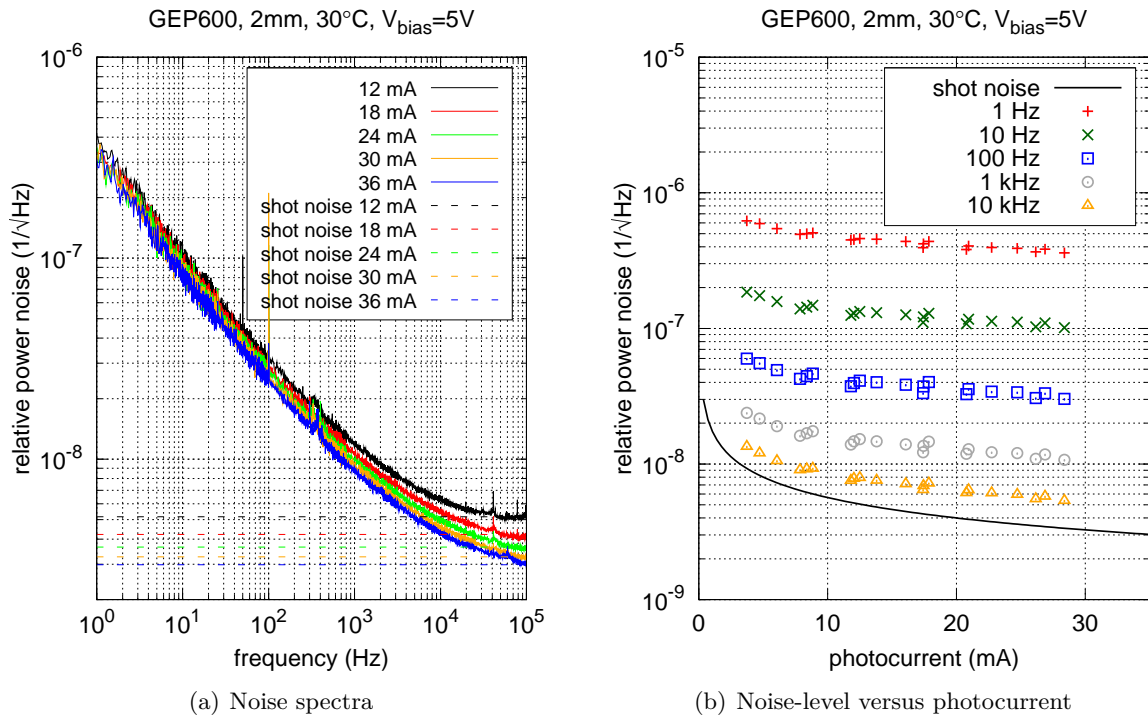(a) Noise spectra

(b) Noise-level versus photocurrent
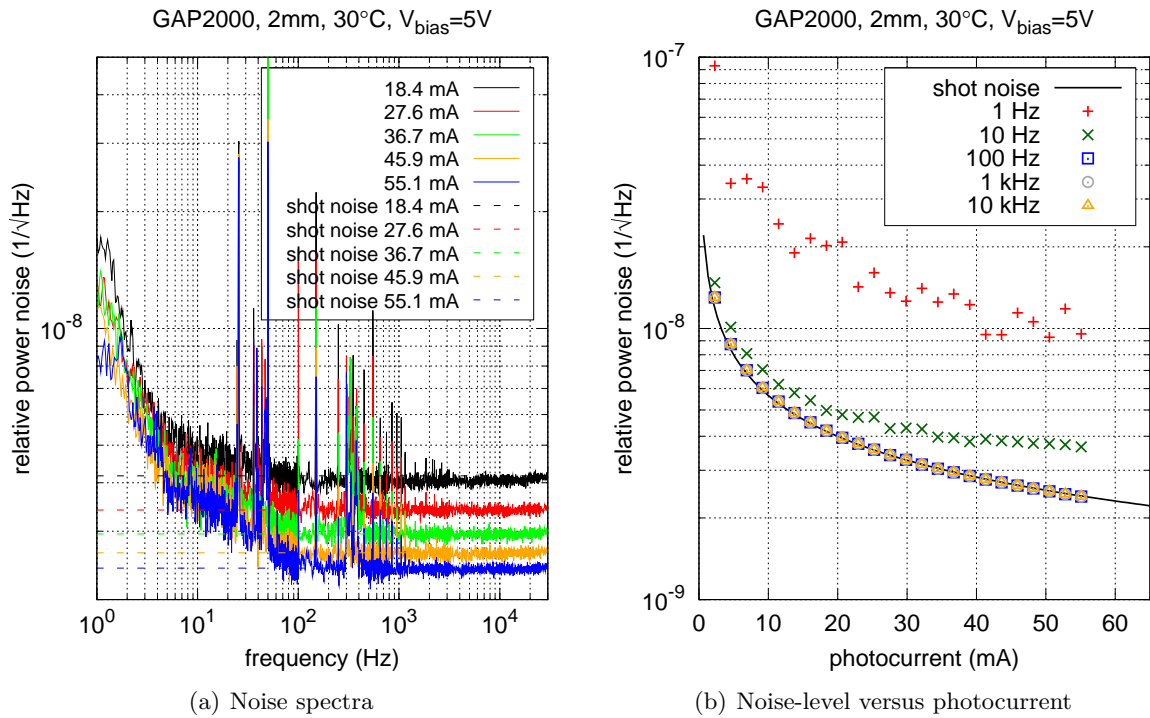
Figure 4.13: Balanced-detection results for InGaAs photodiodes from GPD (GAP2000 [53]): 4.13(a) examples for relative power noise spectra obtained for different power levels; 4.13(b) comparison of observed noise levels for different Fourier frequencies plotted versus photocurrent.

stabilization loop when using one of these diodes as the in-loop detector. Hence the best performance of a power stabilization loop that can be achieved can be easily determined and optimized when simply using both detectors in the balanced scheme.

The origin of the observed low-frequency noise could not be determined. As the relative noise level seems to level off for high photocurrents, both intrinsic noise in the photodiode and scattered light may explain the performance. Here more detailed investigations are necessary. As an intrinsic noise source would be independent for multiple devices, operating several devices in parallel would lower this limitation by the square-root of the number of devices used.

The observed level at 10 Hz for the devices made from InGaAs can explain the limit of the best results of the power stabilization experiment described in Section 3.2.4. In order to overcome this limitation set by the photodiodes used so far, further characterization of more photodiodes is necessary for the pre-selection of suitable photodiodes.

4.2 Resistor current noise

Excess low-frequency fluctuations are observed in many devices and materials [70, 163, 164] that carry a current. Because most materials and devices usually show a very low noise-level, the noise is hard to measure. Several different methods of measuring the excess noise in conducting materials have been discussed in literature [34]. Some techniques have in common that they focus on the phase sensitive readout of a standard, center-tapped Wheatstone
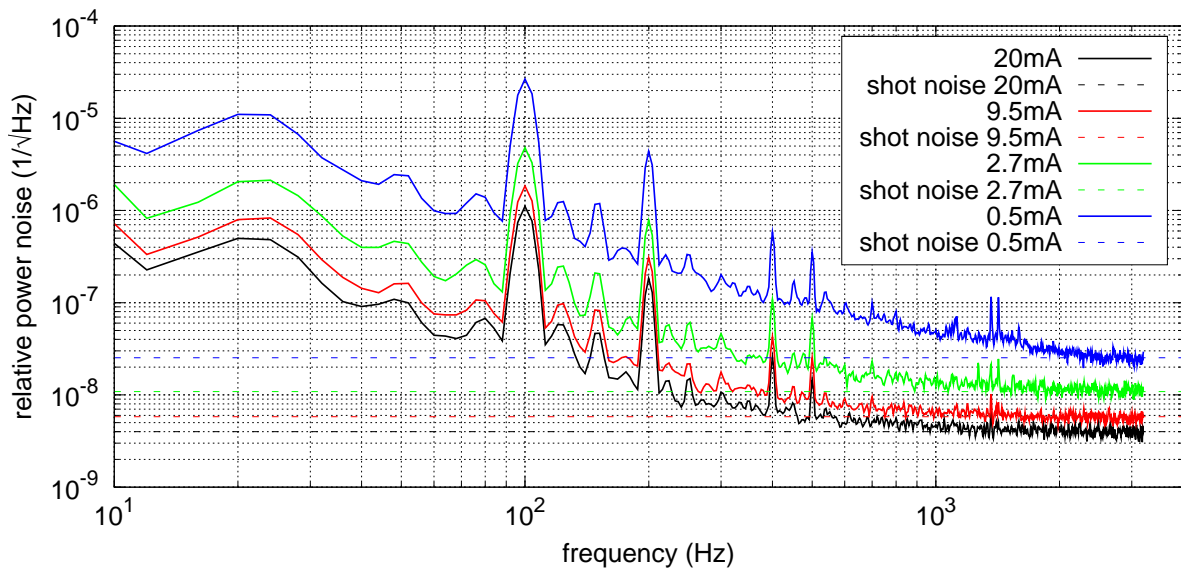
Figure 4.14: Results of the balanced-detection scheme with fiber-optical components.

bridge excited by one or more alternating currents. These include, amongst others the double frequency ac method [149], the 0°/90° subtraction method [137] and the 45° cross correlation technique [111, 122, 165, 167]. The advantage of these techniques is the separation or elimination of background noise (e.g. Johnson noise) from the excess noise to be measured. On the other hand, with low-noise amplifiers available today, the simple DC-measurement technique is also very powerful [16, 86].

There are several commonly used types of resistors: carbon, thin film, thick film, metal foil or wirewound. Each type has specific characteristics suitable for different applications with varying requirements. Thick-film resistors are made of a mixture of conductive particles (metallic grains) with a glassy binder and an organic fluid. This "ink" is printed on a ceramic substrate and heated in an oven. During this firing process the conductive particles within the glassy matrix are fused to the substrate and form the resistor. Thin film resistors are fabricated by sputtering a metal or alloy on an isolating substrate. Wirewound or foil-resistors are made from foils and wires of different metal alloys attached to an isolating substrate. All of them have in common that the total noise can be divided into thermal noise and excess noise. Excess current noise is the bunching and releasing of electrons associated with current flow, e.g. due to fluctuating conductivity based on imperfect contacts within the resistive material. The amount of current-noise depends largely on the resistor technology employed.

Current noise in materials is directly proportional to the current flowing through the device. The noise power density varies with the reciprocal of the frequency $(1/f)$, rounding off at the point where it equals thermal noise. Current-noise of resistors is measurable and is expressed as a function of the voltage drop across a resistor. The amount of noise is expressed as a resistor-noise quality index. This index, the "microvolts-per-volt" index, is an expression for the rms noise voltage, in microvolts, per volt of applied DC voltage, in volts, transmitted in a

single frequency decade [29]. The noise index NI is expressed in decibels, and the equation converting µV/V to dB is

$$NI = 20 \log_{10} \left(\frac{v_{\mathrm{rms}}}{V_{\mathrm{DC}}} \right) \qquad \text{[dB] in a decade} \tag{4.6}$$

with v_{rms} the root mean square noise voltage (in microvolts) and V_{DC} the voltage drop across the resistor. Therefore a noise index of $0\,\mathrm{dB}$ equates to $1\,\mathrm{µV/V}$. It should be noted that the same amount of noise power is transmitted in a frequency decade regardless of the absolute frequency, if the noise has a true $1/f$ spectrum. In general, the mean-square noise voltage is given by

$$\overline{v^2} = \int\limits_{f_1}^{f_2} S(f) df = \int\limits_{f_1}^{f_2} \frac{\overline{e^2(f)}}{\Delta f} df \tag{4.7}$$

where $S(f)$ is the PSD of the measured resistor current-noise in the frequency band f_1 to f_2 and $\frac{\overline{e^2(f)}}{\Delta f}$ is the mean-square noise voltage spectral density at frequency f. The power spectral density of current noise is commonly assumed to be proportional to $1/f$. Then the product of the PSD and frequency is constant and Equation 4.7 can be rewritten as

$$\overline{v^2} = \frac{\overline{e^2(f)}}{\Delta f} f \int\limits_{f_1}^{f_2} \frac{df}{f} \tag{4.8}$$

$$= \frac{\overline{e^2(f)}}{\Delta f} f \ln \frac{f_2}{f_1} \tag{4.9}$$

$$= \frac{\overline{e^2(f)}}{\Delta f} f \ln 10 \qquad \text{for one decade} \, (f_2 = 10 f_1) \tag{4.10}$$

The root mean square noise voltage can now be expressed using the noise index as

$$v_{\mathrm{rms}} = \sqrt{\overline{v^2}} = V_{\mathrm{DC}} \cdot 10^{NI/20} \sqrt{\log_{10} \frac{f_2}{f_1}} \qquad \text{[µ}V_{\mathrm{rms}}\text{] in frequency band } f_1 \text{ to } f_2 \tag{4.11}$$

$$= V_{DC} \cdot 10^{NI/20} \qquad \text{[µ}V_{\mathrm{rms}}\text{] in one decade} \tag{4.12}$$

Based on the IEC recommendation [75] and MIL-STD-202, Method 308 [162] for measuring the current noise generated in fixed resistors, a low-noise measurement setup for excess noise measurements of several commercial available resistors was built and a large quantity of resistors was characterized.

4.2.1 Measurement setup

Although the DC-measurement technique has several limitations, it has been used to measure the excess noise of commercial available resistors used in our institute. The disadvantage of this technique is, that the overall performance is limited by the background noise (Johnson noise of the resistors and amplifier input noise). Nevertheless this technique is sufficient, because the main interest for this thesis was to find the excess noise which limits the overall performance of the power stabilization setup. The measurement setup is illustrated in Figure 4.15.
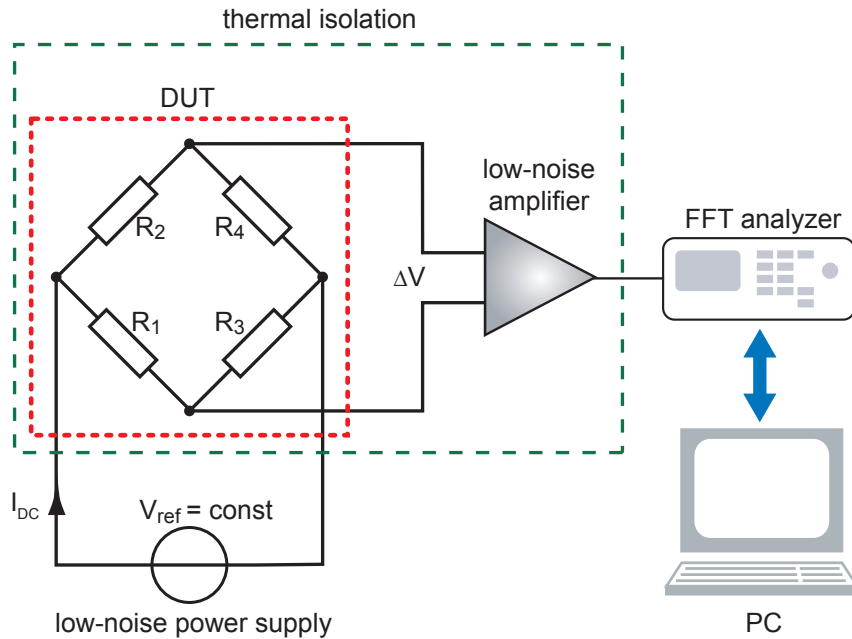
Figure 4.15: Resistor current noise measurement setup using a full Wheatstone bridge configuration.

The tested resistors (DUT) are connected in a voltage-driven full Wheatstone bridge configuration. Traditionally, the voltage-driven Wheatstone bridge configuration is used for precise measurement of small resistance changes, but can be also used for resistor current noise measurements. The excitation voltage V_{ref} is applied across one diagonal of the bridge and a constant current $I_{\text{DC}}/2$ flows through all four resistors of the bridge. The output voltage of the bridge ΔV is measured differentially across the other diagonal.

For resistor current noise measurements, the bridge current I_{DC} through the resistors under test was supplied by an adjustable, low-noise, high current voltage source. In order to avoid disturbances coming from the power supply and other common mode interference, the use of differential configurations is mandatory. The noise voltage across the bridge was amplified by an ultra low-noise differential amplifier optimized for the impedance of the DUT. The amplifier output is fed into an FFT analyzer, which was remotely controlled by a personal computer running a LabVIEW® program for automated noise measurements. To obtain a high resolution spectrum over the entire frequency range accessible by the analyzer, the noise measurements were repeated a few times with different parameters in order to combine different bandwidth-frequency resolutions. The entire bridge and the differential amplifier are mounted in a aluminum box for thermal shielding against air currents and electromagnetic interferences and was supplied using batteries to reduce disturbances from line harmonics.

The nominal values of the four resistors of the full bridge R_1 to R_4 are chosen to be equal (R_0). Thus the impedance of the bridge seen by the amplifier is R_0. By means of careful selection of modern integrated circuits, the equivalent input noise of a voltage amplifier can be reduced to a minimum, close to the thermal noise limit of the setup. For a resistance R_0 up to $1\,\text{k}\Omega$, a low-noise instrumentation amplifier INA103 (Texas Instruments) with a gain $G = 60\,\text{dB}$

was used, for higher values of R_0 the AD620 (Analog Devices) with a gain $G = 40\,\mathrm{dB}$ was used. The performance characteristics of the amplifiers are listed in Table 4.1.

	INA103, 60 dB gain	AD620, 40dB gain
input current-noise density i_n	$0.7\,\mathrm{pA}/\sqrt{\mathrm{Hz}}$	$6.3\,\mathrm{fA}/\sqrt{\mathrm{Hz}}$
noise corner frequency for i_n	$223\,\mathrm{Hz}$	$20\,\mathrm{Hz}$
input voltage noise density v_n	$1.15\,\mathrm{nV}/\sqrt{\mathrm{Hz}}$	$9.9\,\mathrm{nV}/\sqrt{\mathrm{Hz}}$
noise corner frequency for v_n	$6\,\mathrm{Hz}$	$4.5\,\mathrm{Hz}$
bandwidth	$100\,\mathrm{kHz}$	$65\,\mathrm{kHz}$

Table 4.1: Measured differential amplifier data for the resistor current-noise measurement setup.

In order to evaluate the influence of the bridge excitation voltage to the noise performance on the noise measurement setup, the common-mode rejection ratio (CMRR) of the full bridge has to be estimated. The largest differential signal ΔV and hence imbalance of the bridge is achieved when opposite resistors in the bridge change resistance as shown by $\pm \Delta R$

$$R_1 \;=\; R_4 = R_0 \pm \Delta R \tag{4.13}$$
$$R_2 \;=\; R_3 = R_0 \mp \Delta R \tag{4.14}$$

The differential voltage ΔV across the bridge is given by

$$\Delta V = \pm \frac{\Delta R}{R_0} \cdot V_\mathrm{ref} \tag{4.15}$$

Since the bridge sensitivity $\Delta V / (\Delta R / R_0)$ is proportional to V_ref, also the noise signal obtained from the bridge is sensitive to the noise of the excitation voltage. Thus, for the current-noise measurement, the resistors are matched in a way that the differential voltage across the bridge is as small as possible and hence the voltage noise of the excitation voltage is suppressed by a large factor.

The maximum output for the differential amplifier is $\approx 10\,\mathrm{V}$. Therefore, for a minimum gain of $40\,\mathrm{dB}$, the maximum input voltage of the amplifier can be $100\,\mathrm{mV}$. Thus, as a worst case for a $10\,\mathrm{V}$ bridge supply, the mismatch of resistance can be 1%, which corresponds to a common-mode reduction for the excitation noise of $40\,\mathrm{dB}$. For higher gains of the amplifier the bridge mismatch allowed that does not saturate the amplifier is even lower and therefore the common-mode reduction even higher.

In order to estimate the limitations due to the bridge excitation voltage, the output voltage noise of the voltage source for several DC output levels was measured. The noise induced by the voltage source must be well below the thermal noise of the bridge impedance. As derived above, the CMRR of the bridge for the excitation noise equals the gain as a minimum. Thus the influence of a noisy excitation voltage on the measurement can be estimated. The noise projection of the excitation for different voltage levels of V_ref $(1, 2, 5, 10\,\mathrm{V})$ assuming a minimum CMRR of $40\,\mathrm{dB}$ of the balanced bridge is shown in Figure 4.16.

Using the low-noise power supply, the noise reduction is sufficient so as not be the limiting factor. With the lowest gain of $40\,\mathrm{dB}$, the noise level is comfortably below the minimum thermal noise limit of the bridge ($1\,\mathrm{k\Omega}$ impedance). For resistor values below $1\,\mathrm{k\Omega}$, the gain was $60\,\mathrm{dB}$
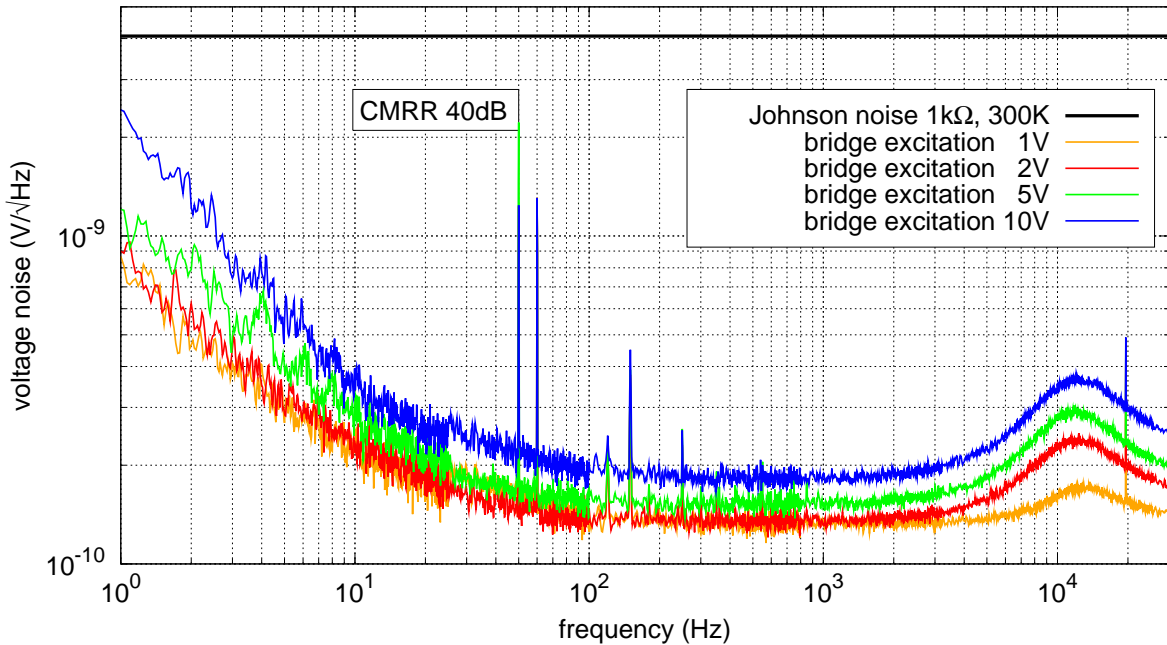
Figure 4.16: Noise projection of the high current voltage source for different voltage levels assuming a minimum CMRR of 40 dB of the balanced bridge.

and so the noise of the excitation voltage at least one order of magnitude below the plotted spectra. The intended minimum resistance value to be measured is $100\,\Omega$ ($\approx 1.3\,\mathrm{nV}/\sqrt{\mathrm{Hz}}$ thermal noise), which is large compared to the maximum excitation noise expected for $60\,\mathrm{dB}$ of gain.

In practice, the overall sensitivity is limited by the thermal noise of the bridge itself and the differential amplifier input voltage and current-noise, especially at low frequencies. Since the input voltage and current noise spectral densities of the differential amplifiers can be assumed to be constant, these noise sources can be characterized carefully and subtracted from the noise measurements of the DUT. The input noise of the two differential amplifiers used was measured for several different bridge impedances distributed over the entire measurement range. For low impedances the total noise is dominated by the input voltage noise of the amplifier, for high impedances by the current noise. From the data obtained, the noise contribution of the voltage and current noise of the input was calculated and a model for each amplifier was generated. Later, these models were used to subtract the amplifier input noise for the impedance of the DUT. This enables measurements down to the thermal noise equivalent to the input noise of the amplifiers or even below.

As the current noise of resistors scales with the voltage drop across it, the bridge supply was chosen to be $10\,\mathrm{V}$ for all noise measurements. The voltage across one resistor is then half the excitation voltage. Since the current noise of the resistors is uncorrelated, the noise contribution of all four resistors of the bridge sum up to a factor of two. Thus the measured noise of a complete bridge can be interpreted as an estimate for the noise of one of its resistors driven by the full $10\,\mathrm{V}$. The noise index and thus the product quality is estimated from measurements on a group of nominally "identical" resistors. All resistors are tested at the same excitation

voltage, $V_{\text{ref}} = 10\,\text{V}$. Hence the differences in the measured noise can be attributed to excess current noise of the tested devices.

4.2.2 Results

As reported in the literature, the current noise of resistors is linear with the voltage drop across it. An experiment for some typical resistors used in our institute was conducted to evaluate the amount of current noise as a function of applied excitation voltage. A typical plot of noise spectra for several voltage drops from $0\,\text{V}$ to $10\,\text{V}$ is shown in Figure 4.17.
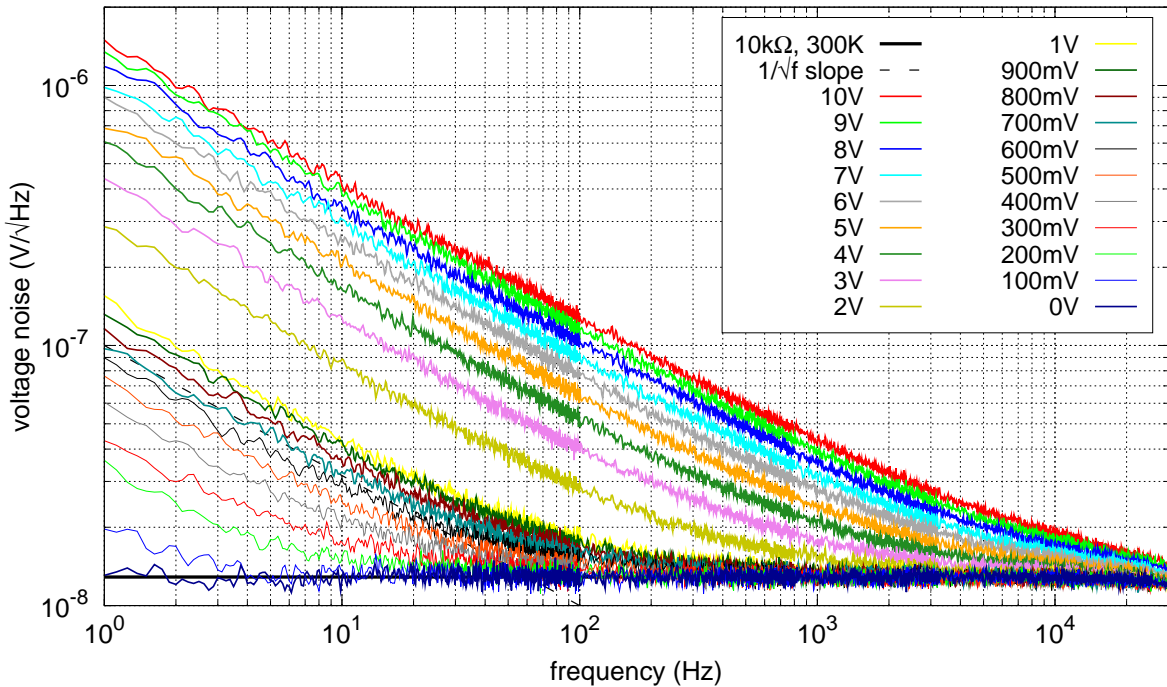
Figure 4.17: Resistor current noise spectra for different excitation voltages (in units of the corresponding voltage drop fluctuations).

As expected, the noise level increases with rising voltage drop at low frequencies. In order to demonstrate the linearity, the noise level of each graph at Fourier frequencies $1\,\text{Hz}$, $10\,\text{Hz}$ and $100\,\text{Hz}$ has been taken and plotted against the voltage drop. The result is shown in Figure 4.18. The measurement points obtained from the individual spectra were fitted using a linear regression. The increasing noise spectra is linear over the entire range from $0\,\text{V}$ to $10\,\text{V}$ of the excitation voltage, which is in agreement with the literature.

Tests on a large number of different manufacturers' products were performed. All measurements were performed at room temperature within a frequency range of between $1\,\text{Hz}$ and $30\,\text{kHz}$ for three groups of resistors having nominal values of $100\,\Omega$, $1\,\text{k}\Omega$ and $10\,\text{k}\Omega$. Each group consisted of 4 identical samples (one full bridge). Higher and lower values are often not needed and it is expected that devices with higher resistivity values of the same type of resistor have even higher excess noise. This expectation is supported by datasheets where the manufacturers give typical values for the noise index of their products. Representative of all measurements performed, the results for devices with a nominal value of $100\,\Omega$ measured for a voltage drop of $10\,\text{V}$ are summarized in Figure 4.19. All the results can be found in [140].
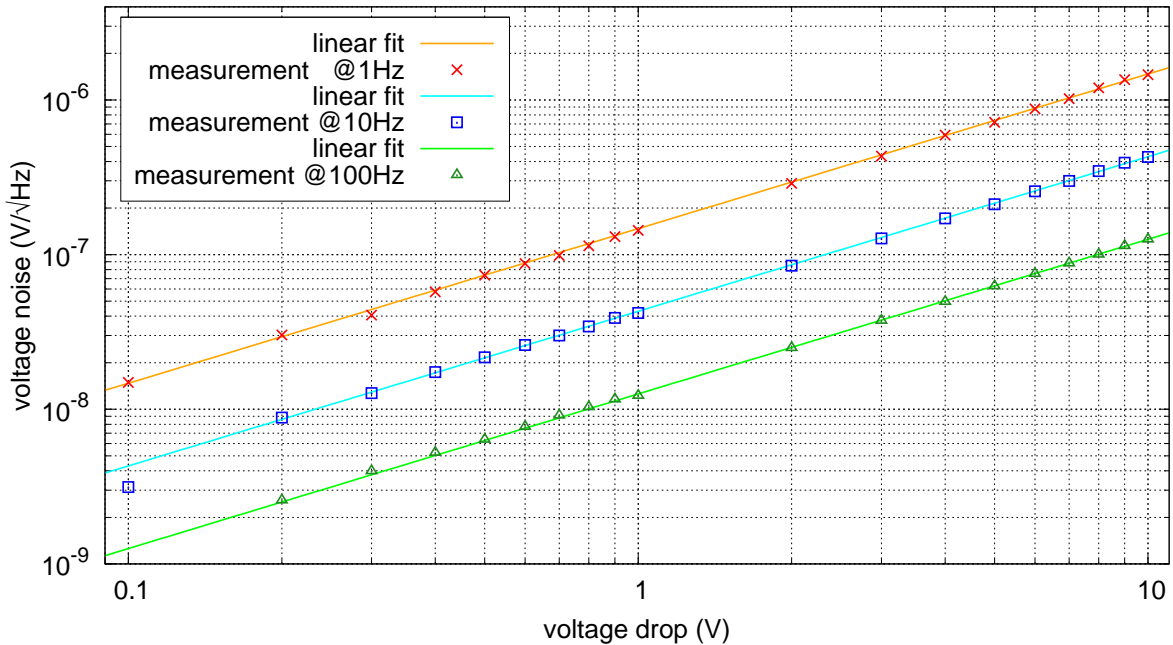
Figure 4.18: Resistor current noise as a function of voltage drop (in units of the corresponding voltage drop fluctuations).

This study has pointed out that excess noise can be observed in all kind of resistors tested and used in our designs. The observed level varies over almost three orders of magnitude and depends on several parameters like type, size, wattage, process, manufacturer, etc. Because of this it is very hard to find the ideal resistor for every day usage in the lab. For comparison, the calculated noise spectra for resistors having a noise index of -20 dB, -40 dB and -60 dB are plotted as well.

For frequencies above 1 Hz, the very expensive ultra high precision Bulk Metal® Z-Foil and classical wirewound resistors appear to have very little or no excess noise. Wirewound resistors however, do have inductance that may affect the circuit operation. Metal film or thin film resistors have little excess noise in these tests and thick film resistors show large excess noise [169, 170]. It could be observed that the noise decreases with increasing mechanical size or volume of the same type of resistor, which is in agreement with experiments reported in the literature [32, 99, 106, 127]. For the same resistance value and current, a higher power resistor of the same style will generate less noise. Furthermore, the excess noise has a linear voltage dependence as reported in the literature [64]. The temperature dependence of the low-frequency noise has not been measured, but it can be found in the literature that the $1/f$-noise in resistors can be temperature dependent [27, 44, 107]. These papers suggest that a change in temperature changes the distribution of relaxation times of the noise process due to changes of the microstructure. This is only important for large changes in temperature, not for operating conditions around room temperature.

The data presented in this work offers a background for evaluating noise in electronic designs which to date is not implemented in standard simulation software. Even though the noise level largely depends on the voltage drop, an upper limit can be set by assuming an potential difference equal to the supply voltage. Furthermore sample-to-sample variations have to be
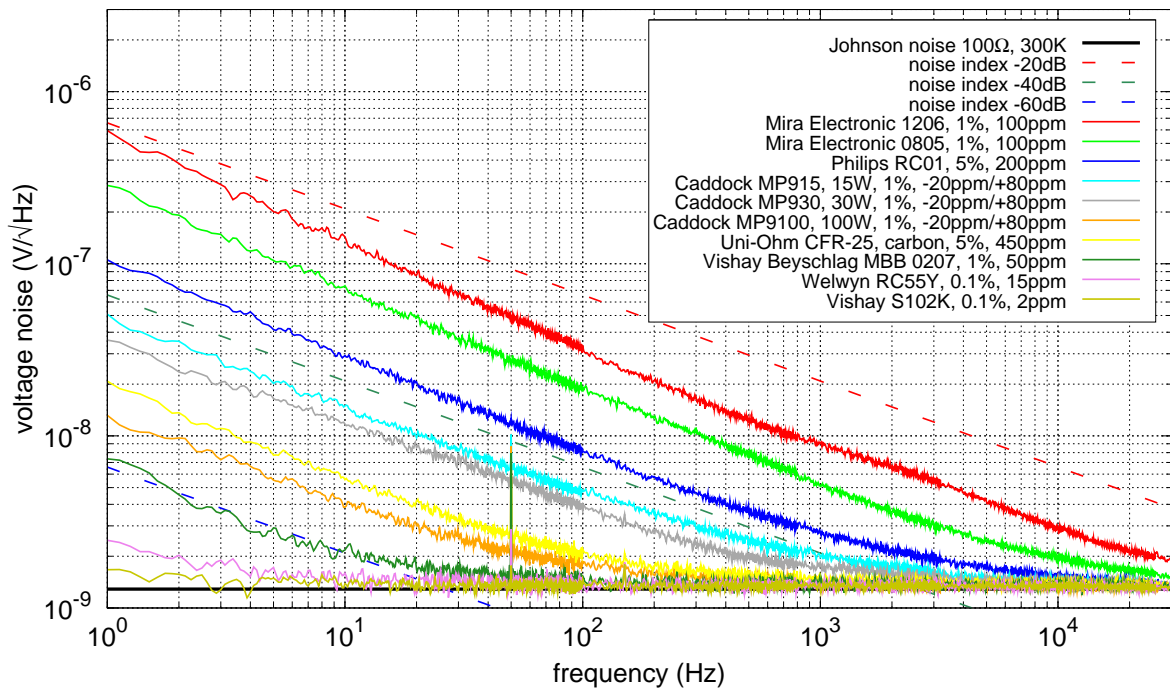
Figure 4.19: Selected results of measured resistor current-noise for $10\,\text{V}$ voltage drop.

taken into account. Hence a pre-selection of critical components is suggested before their use in a circuit. The results given here are well suited for an estimation of the amount of excess noise for existing electronics, which can then be easily optimized.

A more detailed noise study for lower frequencies will be performed in the near future to get similar data for devices used in the LISA and LISA-Pathfinder electronics. Because measurements at lower frequencies are very sensitive to thermal disturbances, these measurements will be performed with one of the phase sensitive readout schemes. Furthermore only a few publications on low-frequency noise in capacitors are available [88, 143]. Hence a careful noise characterization of capacitors should be considered as well.

The excess noise measured for the metal film resistors and the high-power thick film resistors used in the power stabilization scheme can explain some of the excess noise which limits the overall performance of the stabilization loop. The resistors used in the transimpedance amplifier and in the input stage of the power stabilization servo were tested independently from the generic measurements. The results are shown in Figure 4.20.

The shot noise contribution was converted into an equivalent voltage noise at the output of the photodetector with a transimpedance resistance of 100Ω. The individual noise contributions of the resistors were summed and added to the shot noise of about $80\,\text{mA}$ for each photodetector as used for the best power stabilization results obtained (see Section 3.2.4). The estimated total amount of excess noise from the resistors in the power stabilization electronics together with the calculated shot noise contribution on both detectors is very close the best stability achieved. Thus current noise in resistors is an important factor in the low-frequency noise of power stabilization experiments and future experiments have to be carefully designed with regard to this effect. At sufficiently high frequencies the excess noise contribution is smaller and negligible compared with other noise sources such as thermal or shot noise.
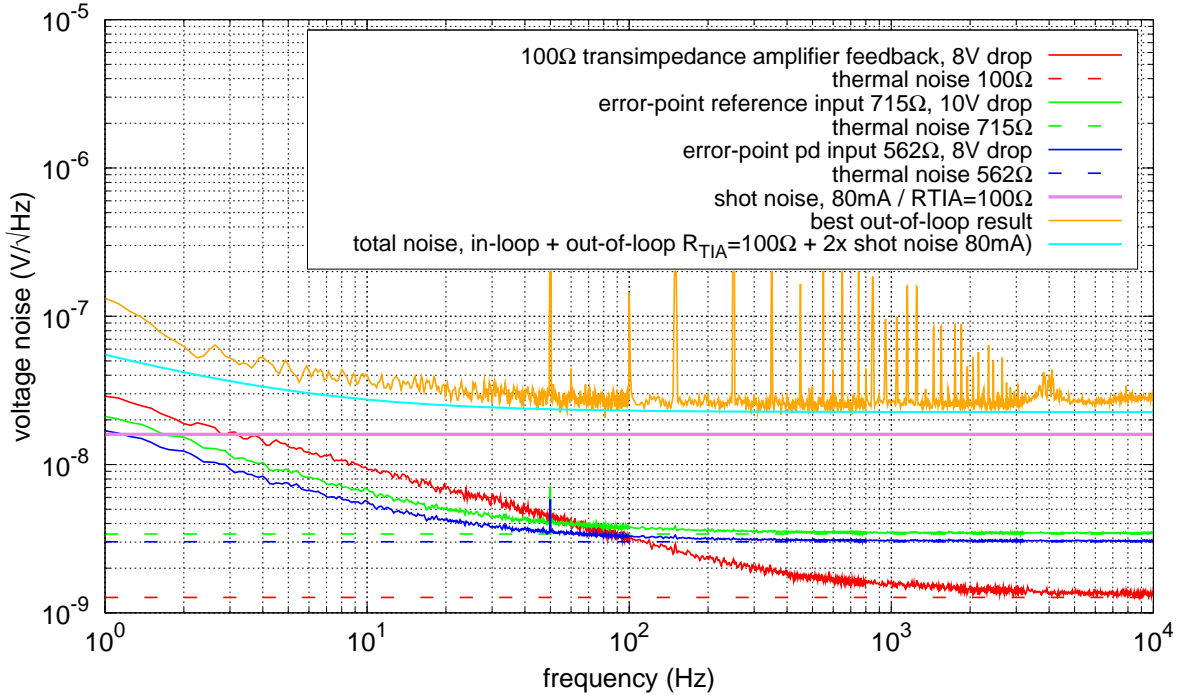
Figure 4.20: Resistor current noise projection for the power stabilization experiment described in Section 3.2.

4.3 Position-dependent photodiode efficiencies

From the previous chapter we know that the pointing of the laser beam in conjunction with position-dependent responsivity of the photodiode can have a large impact on the achievable power stability. Previous measurements made on Si, GaN, Ge and InGaAs photodiodes have shown that the rms variation of the responsivity across a diode can range from less than 0.1% to greater than 2% [13, 26, 40, 41, 52, 63, 96, 97, 148, 160, 174]. This could be a result of imperfections in the manufacturing process of the photodiodes [151], as well as from dust particles on the diode surface [94].

The uniformity of the response across the sensitive area of a photodetector can be determined by scanning a small circular spot of radiation of a selected diameter across the surface and measuring the responsivity $\mathcal{R}$ as a function of the position of the probe beam. The diameter of the probe beam determines the resolution of uniformity measured. Previous measurements have shown that the responsivity of photodiodes largely depends on the selected wavelength [40, 96, 97]. Hence measurements have to be performed at the wavelength of interest (here 1064 nm). Thus λ will be assumed to be constant in the following discussion.

As only relative variations of the responsivity are of interest, the local responsivity $\mathcal{R}(x, y)$ will be normalized to the maximum responsivity measured as

$$\sigma(x, y) = \frac{\mathcal{R}(x, y)}{\max \mathcal{R}} \tag{4.16}$$

Larger beams will see an average of the local responsivity, depending on the beam size and position on the active area. Hence typical surface or layer defects or fine dust particles on the

detector surface which partially block the photo-sensitive area have only small consequences on the sensitivity if large beam diameters are used.

The relative local responsivity $\sigma(x, y)$ can be used to calculate the integrated responsivity S for larger Gaussian beams as used in the power stabilization experiment with a dimensionless optical power distribution of

$$p(x, y) = \frac{P(x, y)}{P_0} = \exp\left[-\frac{2}{\omega^2}\left(x^2 + y^2\right)\right] \tag{4.17}$$

where ω is the beam radius and (x, y) is the position within the beam. The position-dependent sensitivity $S(x, y)$ can then be calculated to be

$$S(x, y) = \int \sigma(x', y') \cdot p(x' - x, y' - y)\, dx'\, dy' \tag{4.18}$$

with (x, y) now being the position of the center of the beam on the photodiode. The sensitivity $S(x, y)$ can also be measured directly for a given beam diameter by measuring the changes in response of the detector while scanning the active area of the device with the probe beam.

To determine the susceptibility of the photodetector signal to small changes of the beam position on the photodiode, changes in the sensitivity when moving the beam have to be determined. The gradient of the sensitivity $S(x, y)$ is the linear coupling coefficient $K_S(x, y)$ between small fluctuations in the position of the beam (beam pointing) and a signal of the photodiode as

$$K_S(x, y) = \left|\frac{\nabla S(x, y)}{S_0}\right| \qquad [1/\text{m}], \tag{4.19}$$

with the relative sensitivity $S(x, y)/S_0$ normalized to the operating point (x_0, y_0) of the photodiode with $S_0 = S(x_0, y_0)$. The coupling coefficient $K_S(x, y)$ can also be directly measured by using a large beam with appropriate size and then applying a defined pointing to the beam while scanning the surface.

On the assumption that fluctuations in the position of the beam are small and uncorrelated for different directions, the linear coupling coefficient $K_S(x, y)$ can be used to make an estimation of the relative power fluctuations for a beam with constant power P_0 as

$$\frac{\delta P}{P_0}(f) \approx K_S \cdot a(f) \qquad [1/\sqrt{\text{Hz}}], \tag{4.20}$$

where $a(f)$ is the PSD of the beam pointing at the detector surface (units m/$\sqrt{\text{Hz}}$).

4.3.1 Experimental setup

As explained above, three different methods can be used to evaluate the coupling coefficient $K_S(x, y)$ of pointing on the photodiode to measured power fluctuations. A high resolution responsivity scan has the advantage that the sensitivity and hence the coupling coefficient can be calculated for any beam size larger than the resolution whilst a direct scan with a large beam does not gather any information about small local changes. The coupling coefficient of an InGaAs photodiode (Perkin Elmer, C30642, sn:A4302) has been determined experimentally using these three methods and the results have been compared. Details can be found in [94]. The generic setup is illustrated in Figure 4.21.

The photodiode to be measured was placed on a computer controllable x-y translation stage (Physik Instrumente, M-405.CG) in a plane perpendicular to the beam propagation (along the
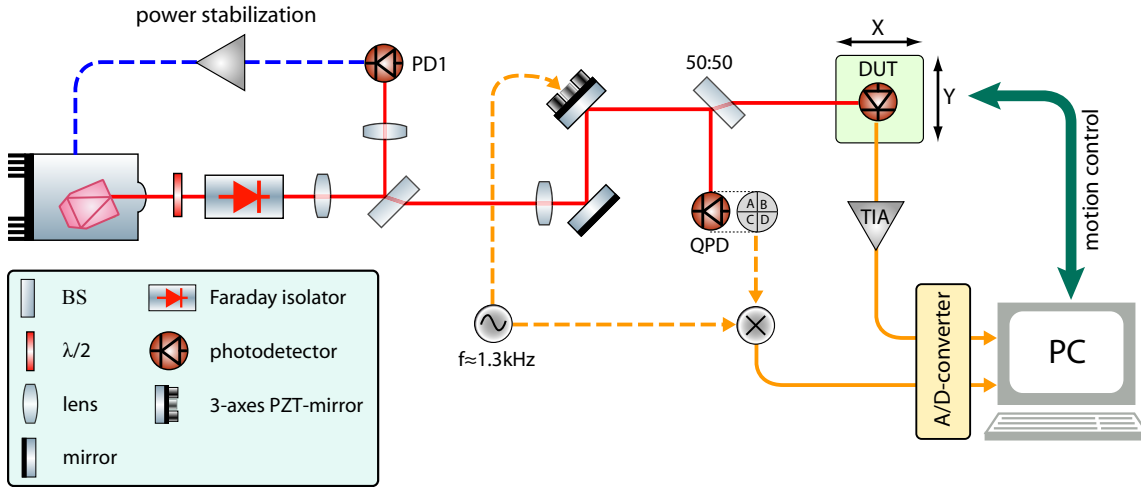
Figure 4.21: Photodiode responsivity measurement setup.

z-axis). The translation stages had a design resolution of about $0.1\,\mu$m and a bidirectional repeatability of about $2\,\mu$m. All measurements were performed in a rectangular grid with 10μm resolution for both axes. As power fluctuations of the probe beam can distort the measurements, the power was stabilized in advance using an additional photodetector (PD1). Details of the individual experiments for the three different techniques will be described below. The results are summarized in Figure 4.22.

Local responsivity scan

The local spatial variations of the responsivity $\sigma(x, y)$ can be measured by scanning the active area of the device with a small beam and then calculating the coefficient $K_S(x, y)$ for a specified beam within two steps. The beam radius at the photodiode surface was about $\omega_{\mathrm{PD}} = 25\mu$m ($1/e^2$). As a small spot is intended to obtain high resolution scans, the optical power has to kept small in order to operate the device in the linear region. The linearity of the detector can be determined by comparing the output of a detector when changing the incident optical flux. The optical power chosen was about $1\,$mW. The measurements of the local sensitivity were then used to calculate the sensitivity $S(x, y)$ for a beam with the radius of $\omega = 420\mu$m, the beam size about $220\,$mm behind the PMC where the photodiodes were placed in the power stabilization setup. Finally, the coupling coefficient $K_S(x, y)$ was calculated from $S(x, y)$.

Sensitivity scan using a large beam

The sensitivity $S(x, y)$ can also be measured directly using a large probe beam instead of a tiny beam. The beam radius was chosen to about $\omega = 420\mu$m, the same size as for the calculations described above. Due to the increased beam size, the power could be also increased to about $50\,$mW. Finally the local gradient $K_S(x, y)$ was calculated from this measurement.

Direct measurement of the coupling coefficient $K_S(x, y)$

The coupling coefficient $K_S(x, y)$ can be directly measured by using a large beam with an appropriate size (here $\omega = 420\mu$m) and then applying a known pointing to the beam while scanning the surface. The pointing was applied by using a multi-axis PZT mirror mount (Physik Instrumente, S-311.10) as the turning mirror in front of the photodiode. The modulation frequency was chosen to $1.3\,$kHz and the amplitude of the beam pointing at the detector surface

was adjusted to about 1–2 µm. The signal obtained from the DUT was demodulated and sampled while scanning the complete surface. A beam splitter and a quadrant photodiode in front of the DUT was used to calibrate and monitor the amount of pointing applied to the beam. The procedure was repeated for a modulation in either x or y-direction and combined to calculate $K_S(x, y)$.

4.3.2 Results

The comparison of the three different methods to evaluate the coupling coefficient $K_S(x, y)$ of pointing on the photodiode into measured power fluctuations is shown in Figure 4.22.

The 2-dimensional data for the normalized local responsivity scan is presented in the upper left plot. The range of the amplitude shown was limited to the upper 2% for better contrast of local features in the main sector. Equipotential lines for 0.1% and 1% deviation from the maximum value are given. The mean responsivity changes from left to right by about 2%, which was independent of the power of the probe beam and the scanning direction. Small local minima in the responsivity are caused by small dust particles on the detector surface.

The result of the responsivity scan using a larger probe beam is in very good agreement with the calculated sensitivity for a larger beam using the data from the local responsivity scan. It validates the calculated result, that the maximum sensitivity is located on the right of the geometric center of the photodiode and that small local variations in the responsivity are negligible when detecting large beams.

The direct measurement of the coupling coefficient $K_S(x, y)$ of pointing on the photodiode is in very good agreement with the calculated ones from both sensitivity scans using a small or a large probe beam. The minimum of the coupling coefficient $K_S(x, y)$ and hence the lowest sensitivity to beam pointing is not located in the geometric center of the active area. The lowest sensitivity is located on the right of the geometric center, close to the edge of the active area. The maximum measured coupling coefficient K_S for the device shown in Figure 4.22 versus beam position relative to the optimal position on the photodiode is illustrated in Figure 4.23.

The coupling changes about one order of magnitude within 70 µm distance from the optimal operation point on the photodiode. Hence precise alignment of the incoming beam on the photodiode is required to minimize the influence of beam pointing.

The measured coupling coefficient was used to estimate the amount of power fluctuations induced by beam pointing on the photodetector within the power stabilization setup. The pointing of the beam was measured using the quadrant photodetector placed behind the PMC operated in high-finesse mode ($\mathcal{F}$=4100), at the same distance as the detectors used for the stabilization (see Figure 3.23). For the power stabilization, the beam was adjusted to maximum sensitivity on the photodetectors using a multimeter, with an assumed relative accuracy of about 0.1%. The corresponding area of the beam position is marked in the sensitivity plots in Figure 4.22 (green colored contour plot). For the same area the maximum coupling coefficient was measured to be K_S=22 /m. Figure 4.24 shows the estimated power fluctuations due to beam pointing behind the PMC.

The best power stability achieved with the power stabilization setup is shown for comparison. Assuming the same pointing sensitivity for the devices used in the power stabilization as measured for the device from Perkin Elmer, position-dependent photodiode efficiencies are not limiting the power stabilization so far, but are within a factor of 4–5 of the design requirements. Hence accurate spatial information for different photodiodes gained by the measurements outlined above could help to optimize future experiments. The maximum acceptable beam-pointing noise and/or the maximum deviation of the beam center from optimal alignment

Figure 4.22: Photodiode sensitivity measurements: Three different methods have been used to evaluate the coupling of pointing on the photodiode into measured power fluctuations; a high-resolution local responsivity scan (upper left graph), a sensitivity scan using a large beam (mid-left graph) and the direct measurement of the coupling (bottom). Calculated graphs are indicated by red arrows. All measurements were performed in a rectangular grid with 10µm resolution for both axes.

Picture of the photodiode which was used to measure the coupling between beam pointing and the signal of the photodiode.
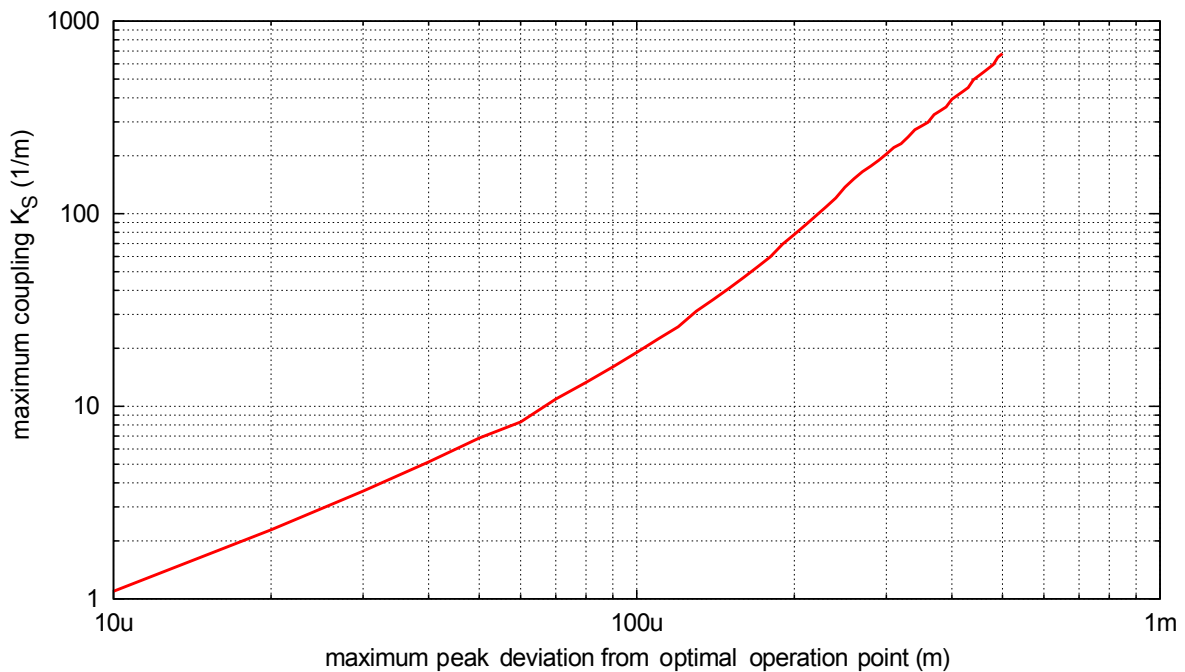
Figure 4.23: Maximum pointing to PD-signal coupling versus beam position relative to the optimal position on the PD (2 mm InGaAs-photodiode from Perkin Elmer (C30642), without window, 420 μm beam radius).

(small K_S) can be calculated to reach a desired power stability level. Results of the calculation for three different power stability levels are shown in Figure 4.25.

As the information about spatial responsivity is important for future stabilization experiments, the measurement setup described above has been optimized and a self-contained measurement setup including temperature stabilization of the photodiode under test has been built. The description of which can be found in [139].

4.4 Temperature fluctuations

Temperature fluctuations within the setup can greatly effect the power stabilization due to several mechanisms. Three major parts of a typical stabilization setup are very sensitive to temperature fluctuations: The beam splitter, the photodiodes including the readout electronics and the optical path between beam splitter and photodiodes.

If the setup is located in air, changes of the refractive index of air lead to beam pointing. The impact of beam pointing was already discussed in the previous section. A sealed acoustic enclosure (e.g. a vacuum tank at atmospheric pressure) greatly reduces these fluctuations. The power stabilization experiments were also performed in vacuum with only a small improvement in stability that was attributed to less acoustics. Because the experiment was performed in vacuum, temperature fluctuations of the air could be ruled out as the dominant cause of excess noise at low frequencies.

Thermoelectric noise, also known as thermoelectric EMF or thermal EMF, can be observed whenever different parts of a circuit are at different temperatures or two different materials are joined together forming a thermocouple, as in an ordinary solder joint. For example, the thermoelectric EMF of lead-tin solder with respect to copper is 3 μV/K and a temperature
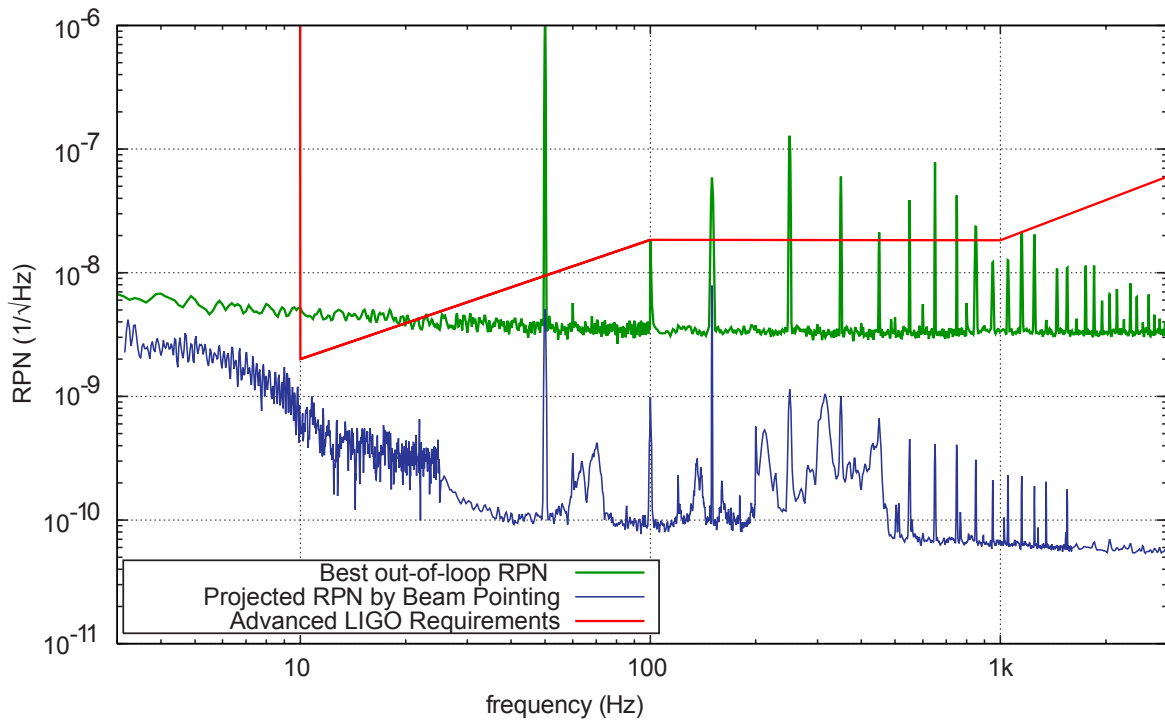
Figure 4.24: Projection of apparent power fluctuations induced by beam pointing on the photodetector of the power stabilization setup.
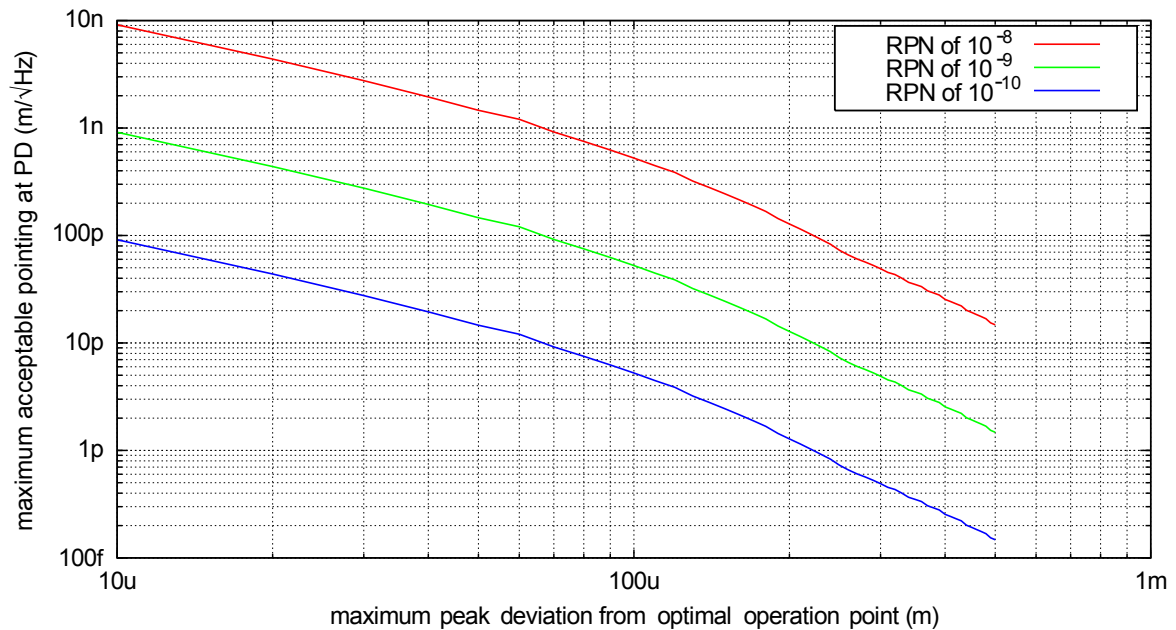
Figure 4.25: Maximum acceptable pointing versus photodiode operation point.

fluctuation of only 1 mK would produce the same noise as the total input noise of the input stage! Therefore the minimization of temperature gradients within the circuit is absolutely

essential to reduce thermoelectric EMFs. Good thermal coupling of individual components as well as proper thermal shielding against air currents is necessary. This was done for the photodetectors, the input stage of the controller and the voltage reference as explained in previous sections. In addition, allowing the stabilization electronics and measurement equipment to warm up and reach thermal equilibrium to a constant ambient temperature also minimizes thermoelectric EMF effects.

Temperature dependencies of the photodiode efficiency (Section 4.4.1) and the temperature dependency of splitting ratio (Section 4.4.2) of the beam splitter used to sample a fraction of the beam for the in-loop and out-of-loop detectors are of utmost concern and need to be measured.

Temperature fluctuations of the active area of the photodiode and the beam splitter volume traversed by the beam cannot be measured directly. Hence temperature fluctuations of the ambient air in the laboratory, in an enclosed metal housing and a sensor glued on top of a beam splitter isolated against the environment were measured for an estimation. Changes in absorbed power of the laser beam itself should have no impact on the stability as power fluctuations and hence its impact on temperature fluctuation are suppressed with an active power stabilization loop.

Temperature fluctuation measurements were obtained using a $100\,\mathrm{k\Omega}$-NTC (Hygrosens Instruments, SEMI833ET) in a full Wheatstone-bridge configuration. Figure 4.26 shows the measured temperature fluctuations.
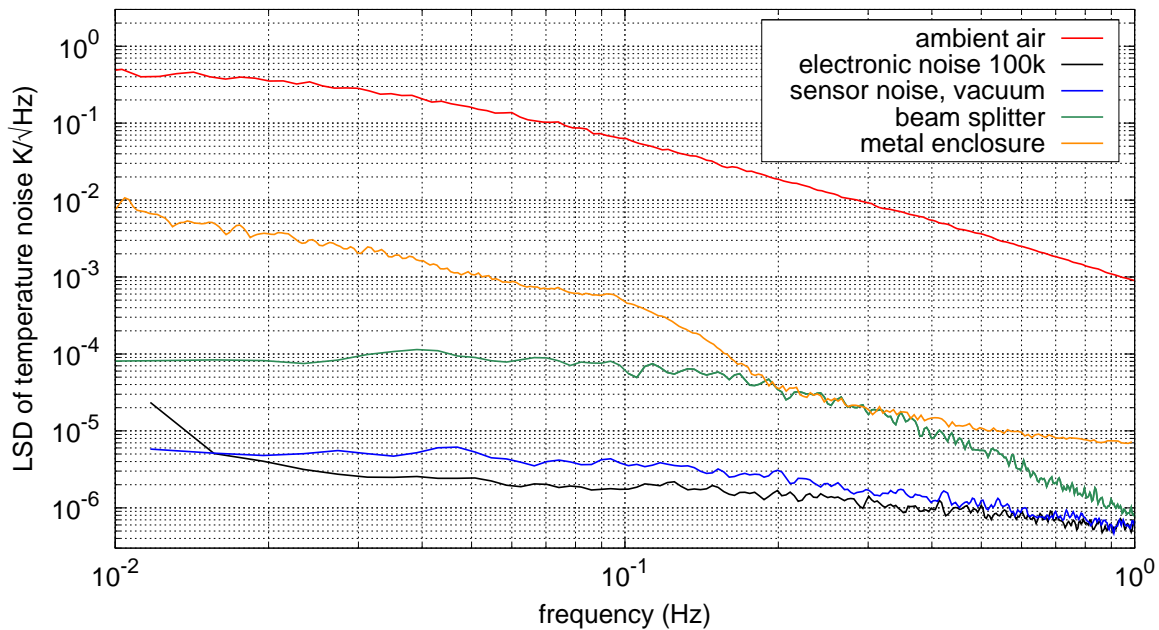
Figure 4.26: Measured temperature fluctuations of ambient air, in an enclosed metal housing and with a sensor in vacuum. Also shown temperature sensor readout noise.

The response time of the temperature sensor (in water) was measured to be $700\,\mathrm{ms}$. To determine the measurement sensitivity and the noise due to self heating of the sensor, a measurement using a sensor placed in vacuum was performed.

The electronic noise of the readout electronics was estimated by using a $100\,\mathrm{k\Omega}$ precision resistor instead of the temperature sensor. As the measurement using the sensor placed in vacuum almost equals the electronic noise, we deduce that the measurement sensitivity is limited by electronic noise or thermal noise of the sensor. At $1\,\mathrm{Hz}$, temperature fluctuations of ambient air are about $10^{-3}\,K/\sqrt{\mathrm{Hz}}$, decreasing with a slope of about f^2. A metal enclosure reduced the temperature fluctuations of the ambient air about two orders of magnitude to a level smaller than $10^{-5}\,K/\sqrt{\mathrm{Hz}}$ at $1\,\mathrm{Hz}$. The measurement using a sensor glued on top of the fused silica beam splitter shows even less temperature noise. Temperature fluctuations of the beam splitter have been measured to about $10^{-6}\,K/\sqrt{\mathrm{Hz}}$ at $1\,\mathrm{Hz}$. For a photodiode mounted to a solid metal mount, fluctuations are expected to be in the same order as measured for the beam splitter.

As derived in Section 4.1.1, the measured junction to case thermal resistance of typical photodiodes used is about $15\,\mathrm{K/W}$. The dissipated electrical power in the photodiode changes with fluctuations in optical power and bias voltage. With the power stabilization loop turned on, the optical power fluctuations on the photodiodes are about $1\,\mathrm{nW}$ or less. Bias fluctuations of the used photodetector designs are about $100\,\mathrm{nV}/\sqrt{\mathrm{Hz}}$ (see Figure 4.29). Hence typical fluctuations in dissipated electrical power are about 10^{-8}. This causes fluctuations in chip temperature of about 10^{-7}. Hence both contributions to temperature fluctuations are very small compared to ambient fluctuations.

4.4.1 Photodiode temperature coefficients

The dependency of the photodiode efficiency on temperature fluctuations is mainly caused by the temperature dependent light absorption coefficient. The spectral efficiency curve of semiconductor photodiodes shifts as temperature changes [37]. Since $1064\,\mathrm{nm}$ is on the steep falling slope near the edge of the spectral response curve for Si photodiodes, the variation of the temperature coefficient is greater than that of InGaAs and Ge. Therefore Si photodiodes should not be used for experiments in the near infrared region where high stability is required. As temperature coefficients also vary for different manufacturers of the same material [160], all InGaAs photodiodes used in this work have been characterized.

The temperature dependency of photodiodes was measured by illuminating the photodiode with a collimated beam of a few mW of light generated by a fiber-bragg-grating wavelength-stabilized single-mode fiber-coupled laser diode (QPhotonics, QFBGLD-1060-10, $10\,\mathrm{mW}\,/\,1060\,\mathrm{nm}$) and measuring the transfer function from temperature modulation around room temperature to change in photodiode response using a network analyzer (Stanford Research, SR785). The modulation was obtained using a digital temperature controller (Team Wavelength, LFI 3751) with an analog programming input. The response was measured for slow changes in temperature, from $1\,\mathrm{mHz}$ to $3\,\mathrm{mHz}$, and the average value of the amplitude response was calculated. To keep the measurement errors due to drifts of the measurement equipment small, a low-noise, chopper-stabilized transimpedance amplifier was used. In addition, the laser diode was stabilized in power using a classical DC-coupled power stabilization loop detecting a small fraction of the main beam with an independent InGaAs photodiode and feeding back to the pump current of the laser diode. The obtained signal from the photodiode under test as well as the temperature signal and power stabilization monitoring signals were recorded using a PC-based data acquisition system.

The experimental setup used was part of a new spatial responsivity measurement setup built during the course of this work. It is explained more in detail in [139]. Table 4.2 shows the magnitudes of the measured photodiode temperature coefficients and the specifications

given by the photodiode manufacturers for these devices. In addition, examples of temperature coefficients of photodiodes sensitivity at 1064 nm for a variety of photodiodes types which can be found in literature are given.

material	device / manufacturer	temperature coefficient
InGaAs	C30641,C30642,C30665 / Perkin Elmer	0.039 %/K [119]
	C30642 sn:936	0.042 %/K (measured)
	C30642 sn:604	0.02 %/K (measured)
	C30642 sn:942	0.046 %/K (measured)
	C30642 sn:942	0.21 %/K (measured, with window)
InGaAs	GAP2000 sn:1 / Germanium Power Devices	-0.141 %/K (measured, with window)
	GAP2000 sn:3	-0.066 %/K (measured, with window)
InGaAs	EPD-1300-0-3.0 / EPIGAP (optimized for 1300 nm)	-0.165 %/K (measured)
InGaAs	G8370-02 / Hamamatsu	<±0.1 %/K [57]
	G8370-02 sn:1	0.244 %/K (measured, with window)
InGaAs	G8605-15 / Hamamatsu	0.2 %/K [160]
		<±0.1 %/K [56]
Germanium	J16TE2-8A6-R05M-SC / Judson Technologies	0.2 %/K [160]
		<0.1 %/K [82]
Germanium	GEP600 / Germanium Power Devices	0.59 %/K (measured, with window)
Silicon	IPL10050 / IPL photonics	1 %/K [160]
Silicon	PC50-7 / Silicon Sensor	2.66 %/K (measured)
Silicon	S1223 / Hamamatsu	0.8 %/K [58]

Table 4.2: Measured photodiode temperature coefficients at 1064 nm and the specifications given by the manufacturers for these devices. Also given temperature coefficients for several devices at 1064 nm found in literature.

The measured coefficients for the photodiodes from Perkin Elmer (C30642), which have been used in most of the photodetectors built for this thesis, were slightly larger than the specified value. The largest coefficient measured for InGaAs photodiodes without a window was found to be -0.165%/K relative efficiency change for an InGaAs photodiode optimized for 1300 nm (EPIGAP, EPD-1300). The measured InGaAs photodiodes showed temperature efficiency coefficients with opposite signs, which is in agreement with the specifications given by different manufacturers [57]. The same photodiode measured with and without the glass window showed different temperature coefficients. These results indicate that an etalon formed by the glass window or between the semiconductor material and the window influences the photodiode efficiency. As a consequence the windows should be removed whenever possible.

Measured temperature fluctuations of ambient air in a typical lab environment are about 10^{-3}/K at 1 Hz, decreasing with a slope of about f^2. If one assumes that the temperature of the chip is directly effected by these fluctuations (no window assumed and tiny mass of the chip), this would cause power fluctuations of about $5 \cdot 10^{-9}/\sqrt{\text{Hz}}$. This is about the same stability level as achieved in the power stabilization experiment in Section 3.2.4). As the experiments performed in vacuum did not increase the stability much at low frequencies, the influence is smaller in reality. If assuming the same temperature stability for the diode chip as for the beam splitter, the contribution to the power stability is at least two orders of magnitude below the requirements.

4.4.2 Beam splitter temperature coefficients

Not only the detection efficiency of photodiodes depends on temperature, also the splitting ratio of a beam splitter can depend on temperature. Usually dielectric coated beam splitters are used. Dielectric coatings, also called thin-film coatings, consist of thin layers of dielectric materials which are deposited on a substrate. The aggregation of thin layers of the coating depends strongly on the kinetic energy of the particles impinging on the substrate surface. Deposition techniques strongly influence the physical properties of the coating. Several deposition techniques can be used: thermal evaporation methods (e-beam and boat evaporation), ion-assisted deposition (IAD) and ion-beam sputter deposition (IBS).

The main physical effect for changes in reflectivity is given by the inclusion of water in the dielectric layers. With varying temperature, the water contents varies, thus altering the layer thickness and hence the reflectivity of the coating. In contrast to other coatings techniques, IBS generates non-porous coatings with very low surface roughness and is well reproducible. The high quality level of IBS-coatings had been confirmed in many applications. Hence all beam splitters used in the stabilization experiments in this work were IBS-coated.

Temperature coefficients have been investigated experimentally for different IBS-coated 50:50 beam splitters. The experimental setup is shown in Figure 4.27.
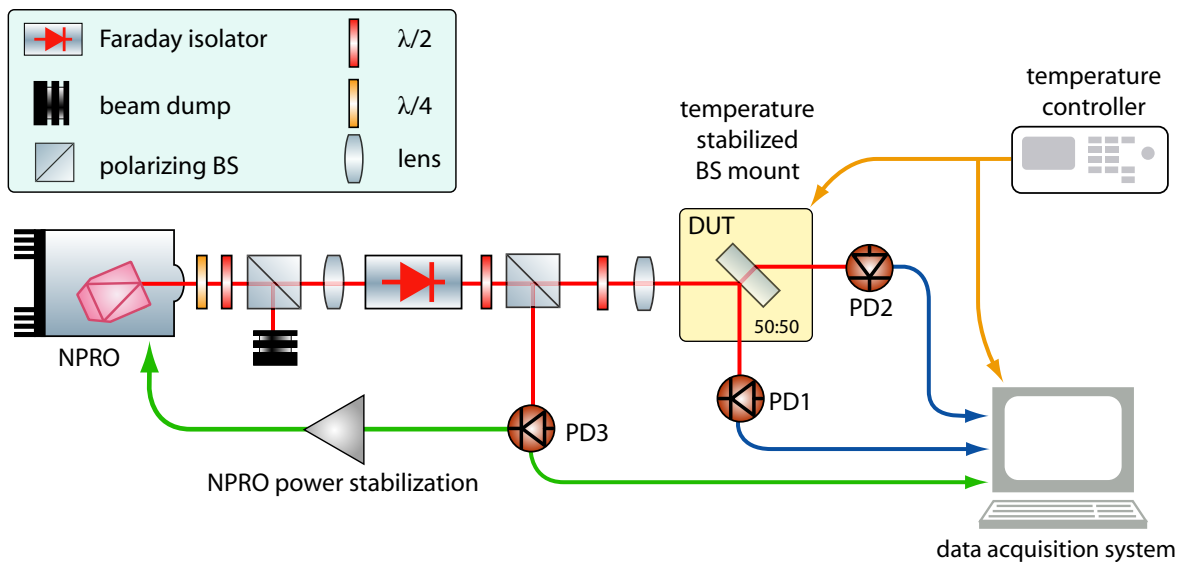
Figure 4.27: Experimental setup for beam splitter temperature coefficient measurements.

The beam of the laser (InnoLight Mephisto 800) was split into two parts. The light from one beam is directly measured by an InGaAs photodetector (PD3) for power stabilization of the laser. The second beam is passed through the beam splitter to be characterized (DUT) which divides the beam into two beams that are very close to being equal in power. To increase the measurement resolution and to reduce the disturbance from power fluctuations of the probe beam, two special low drift InGaAs photodetectors (PD1 and PD2) in a balanced configuration, one in reflection and the other in transmission of the beam splitter were used.

The beam splitter was mounted in temperature controlled mount made of an aluminum alloy, thermally isolated against the environment. To determine the temperature sensitivity of the beam splitter, the temperature was periodically modulated over a range of $30\,\mathrm{K}$ using a

digital temperature controller (LFI 3751, Team Wavelength) and changes in reflectivity were measured. This process was repeated multiple times over an observation time of 2 hours and an average of the peak-to-peak change in splitting ratio was obtained.

The coating for the beam splitters were optimized for either p-polarization or s-polarization. The polarization of the probe beam was adjusted accordingly. The results are listed in Table 4.3.

device	temperature coefficient 1/K
beam splitter 1 / s-pol	$3 \cdot 10^{-6}$
beam splitter 2 / s-pol	$6 \cdot 10^{-6}$
beam splitter 3 / s-pol	$3.8 \cdot 10^{-6}$
beam splitter 4 / p-pol	$8.7 \cdot 10^{-6}$
beam splitter 5 / p-pol	$1 \cdot 10^{-5}$
beam splitter 6 / p-pol	$8.6 \cdot 10^{-6}$

Table 4.3: Measured non-polarizing beam splitter temperature coefficients.

An upper limit for the temperature dependency of the reflectivity was found to $1 \cdot 10^{-5}$/K. The beam splitters optimized for s-polarization tend to be marginally better than the devices optimized for p-polarization. For comparison, for an e-beam coated beam splitter a relative temperature coefficient of $3 \cdot 10^{-3}$/K has been found [147] and the temperature dependency of the reflection coefficient of uncoated fused-silica glass plates has been calculated by Tröbs [160] to be $4.8 \cdot 10^{-5}$/K.

In order to limit the power stabilization experiment at the 10^{-9} level, temperature fluctuations in the order of 10^{-4} K at 10 Hz would be necessary. Figure 4.26 shows that even temperature fluctuations of ambient air in a typical lab environment are about 10^{-3}/K at 1 Hz, decreasing with a slope of about f^2. Without taking the thermal pole of the beam splitter into account, this contribution to the power stabilization experiment is at least one order of magnitude below the requirements.

4.5 Photodiode bias voltage

Changes in the bias voltage greatly affect photodiode parameters like series resistance, junction capacitance, quantum efficiency and the shunt resistance and thus the dark current. The impact on the photodetector output can be separated into two different mechanisms: 1) the gain for the optical signal is changed; 2) bias voltage fluctuations couple directly into the output signal. Since all the independent processes are hard to separate, the response of the output to changes of the bias voltage were investigated.

The design of the detector was chosen to be the one used for the power stabilization experiments, a transimpedance stage with a buffer in the feedback. The photodiode was a 2 mm InGaAs device (Perkin Elmer, C30642G) using a bias voltage of 10 V. The transimpedance gain has been set to $R_{TIA}=100\,\Omega$. An additional high current buffer (Texas Instruments, BUF634T) was added into the bias voltage path to provide an input for bias modulation with high current capability for the high photocurrent. The detector was illuminated using light from an NPRO and the response from the bias voltage modulation input to the detector output signal was measured. Figure 4.28 shows the results obtained for different photocurrents I_{ph}.
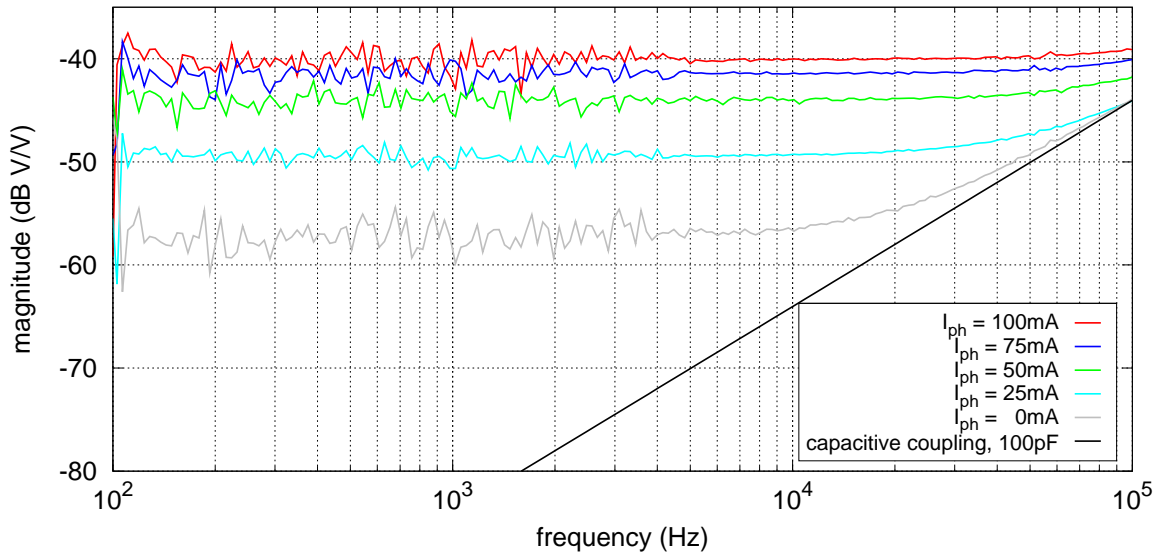
Figure 4.28: Measured and calculated amplitude response of photodetector output for changes in bias voltage.

Large changes in the measured transfer function for different optical power levels were observed. At low frequencies the signal-to-noise ratio of all measurements was dominated by power fluctuations of the laser. With no detected light, the coupling was measured to be independent of frequency up to 10 kHz, for higher frequencies the coupling increases with about 20 dB/decade with increasing frequency. This can be explained by a capacitive coupling, via the junction capacitance of the photodiode, into the transimpedance stage and could be verified by simulation of the circuit with the measured value for the photodiode shunt capacitance (108 pF) and experimentally by adding a small, well known capacitance in parallel. The coupling nonlinearly increases with increasing photocurrent. For the dark condition of the photodetector, the contribution of bias voltage fluctuations to the photodetector output signal was measured to be about 20 dB smaller than the maximum illuminated situation. For 100 mA the coupling could be measured to be almost independent of frequency up to 100 kHz. The frequency independent coupling at low frequencies as well the increased coupling with photocurrent cannot be explained so far, but might be due to a reduction in shunt capacitance or cross coupling within the photodetector circuit. Here further investigations are necessary.

As the noise contribution of the photodiode bias increases with increasing light power, the real measurement limit from the electronic noise of the photodetector depends on its operating point. The typical dark noise measurement of the photodetector output signal might be too small and the impact of bias voltage fluctuations to the photodetector output could dominate the noise performance of the detector when illuminated. Thus the impact of bias voltage fluctuations on the photodetector output has been estimated for two scenarios. In the best case the coupling was assumed to be equal to the one without any detected light, as for the classical dark noise measurement of the detector. The worst case of the coupling was assumed to be -40 dB for all frequencies, as was measured for 100 mA of photocurrent.

The voltage noise of the photodiode bias voltage was measured for photodetectors used for the power stabilization. In those designs, a voltage reference (Analog Devices, AD587) was

used to generate the bias voltage. Since the maximum output current of the voltage references is only about $10\,\mathrm{mA}$, a high current operational amplifier (OPA547) delivering up to $250\,\mathrm{mA}$ was used to buffer the reference output. To further reduce the noise exhibited by the reference, the buffer was configured as an active, 2nd-order low-pass filter with a corner frequency of $0.33\,\mathrm{Hz}$. The results of the calculated noise contribution of the bias voltage to the detector output noise are shown in Figure 4.29.
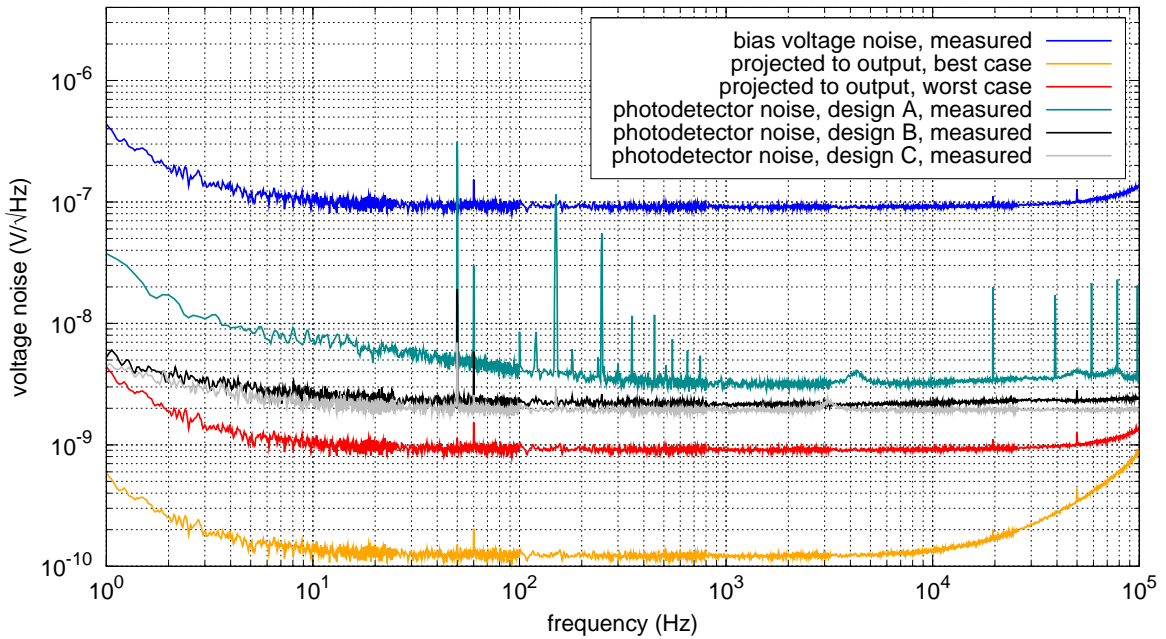
Figure 4.29: Estimated coupling of bias voltage fluctuations to photodetector output signal.

The total output noise measured for three different photodetectors (A to C) used in this work is given for comparison. In the best case, the coupling of noise from the bias voltage into the photodetector output is negligible for these detectors. For high photocurrents the attenuation at low frequencies is not very high and hence the coupling into the photodetector output is close to the electronic dark noise. For higher bias fluctuations, e.g. when using more noisy voltage regulators, or even higher photocurrents this contribution to the total detector noise should be kept in mind and considered for every new photodetector.

4.6 Out-of-band noise

Another challenge is reducing the effect that noise outside the servo bandwidth has on noise in the control bandwidth. The presence of signals with a frequency greater than the specified bandwidth of the control loop can have a profound effect on the performance of the stabilization. Out-of-band frequency components often do not distort the in-band performance directly, but large out-of-band noise tends to generate in-band intermodulation components and limit the dynamic range of the system. The electromagnetic interference (EMI) may be an interfering signal generated internally or externally to the electronic equipment. Recently, great attention was devoted to failures and distortion induced in different types of operational amplifiers from spurious signals conveyed to their inputs [51, 55, 105, 120, 157].

The most common cause of this down conversion of high-frequency noise to lower frequencies is non-linearity (such as slew-rate limiting) in the electronics (often input stages of opamps) in the presence of large, high-frequency signals. The slew-rate of an amplifier is defined as how fast the output can change in response to its input. The higher an opamp's slew rate, the more accurately the device's output signal will conform to its input signal. Signals that require changes faster than allowed by the amplifier slew rate will be distorted. These non-linearities can lead to rectification, which may result in offsets or cause broadband noise at frequencies significantly below those of the slew-rate limited signals. This means the slew rate has to be fast enough to reduce non-linearities.

Typically, reduction of electromagnetic interference in control loops of our laser systems is attempted via passive technology (filtering and shielding) for signals far above the loop bandwidth, e.g. at the radio frequencies used for sideband modulation. In case of power stabilization, often nobody cares about signals close to the upper frequency of the loop, e.g relaxation oscillations of the laser. In case of the NPROs used in this work, the relaxation oscillation frequency is between $700\,\mathrm{kHz}$ and $1.3\,\mathrm{MHz}$ (depending on the pump power) and only about one order of magnitude higher than the wide band noise. A simple experiment using a low-noise differential amplifier with a small ($10\,\mathrm{mV_{pp}}$) excitation signal at $1\,\mathrm{MHz}$ at the input showed that the noise performance of the device is degraded by about one order of magnitude. This could be also demonstrated for the input stage of the FFT analyzer used in our lab (Stanford Research, SR785).

A second experiment was performed using two commercial differential amplifiers (INA103, SSM2143) to receive the signal obtained from a broadband photodetector measuring the power noise of a $2\,\mathrm{W}$ NPRO with a relaxation oscillation frequency of $1.2\,\mathrm{MHz}$. These lasers are delivered with a so-called noise eater which is a control system that reduces the amplitude of the relaxation oscillation. Without any filtering, the noise performance of the amplifier could be changed by switching the noise eater loop on and off. By adding a simple low-pass filter between the photodetector and the receiver this could be eliminated. Since noise due to slew-rate limits is only present if there are very fast signals, this noise would not show up in dark noise measurements of the detector or measurements of the electronics noise of the control loop electronics without at least parts of the loop closed. Consequently, extensive low-pass filtering is required to significantly attenuate these out-of-band signals. If the spurious signal is close to unity gain of the control loop, significant low-pass filtering can be problematic due to additional phase shifts caused by the filter.

4.7 Scattered light

Scattered light, already mentioned as a noise source in GWDs, could cause interference on the photodetectors. Noise associated with scattered light could be observable at characteristic mechanical eigenfrequencies of mirror mounts and other macroscopic objects in the vacuum tank or as a broad spectral feature if the light phase of the interfering beam varies substantially more than 2π. Proper reduction of scattered light by means of iris diaphragms, black anodized aluminum shields and filter glasses with high absorption reduced the scattering but had no influence on the broadband rise of the power noise level at low frequencies. However intentionally generated scattered light directed onto the photodetectors could degrade the performance.

4.8 Polarization fluctuations

Polarization jitter of the incoming laser beam in combination with the polarization dependent beam splitting in the detection setup could cause differential power variations at the in-loop and out-of-loop photodetectors. Also different responsivities of both photodetectors would lead to unequal detected power fluctuations due to fluctuations in the polarization. Further purification of the polarization of the incoming laser beam by means of adding additional high extinction-ratio polarizing beam splitters at the input and output of the PMC did not lead to higher stability. Thus this contribution is neglectable at the current noise level.

4.9 Frequency noise

Laser frequency noise can be converted to power noise, e.g. due to the wavelength-dependent response of the photodiodes or the splitting ratio of the beam splitters behind the PMC or any kind of spurious parasitic interferometers in one of the photodetector paths. If frequency noise from the free running NPRO would be converted into differential power fluctuations at the photodetectors, a reduction of the frequency noise by a frequency stabilization to the reference cavity should yield better results in the power stabilization experiments. This was not the case. An estimate of the noise using the free-running frequency noise of the NPRO, the wavelength-dependent splitting ratios and detection efficiencies of the photodetectors showed that the contribution is much smaller. Furthermore no transfer function could be measured from the error-point of the length control loop of the PMC to the power stabilization loop and a coherence measurement showed no correlation between frequency noise and power fluctuations in the frequency band of interest.

4.10 Conclusions

This Chapter described in detail the identification and characterization of noise sources affecting the performance of a laser power stabilization control loop, especially at low frequencies. After reaching previously unattained lower limit in power stability with the optimized power stabilization experiment presented in Section 3.2, low-frequency sensing noise was considered to be one of the dominating effects limiting the out-of-loop noise performance.

The origin and dependency of low-frequency noise of photodiodes was addressed in Section 4.1. The characteristics of low-frequency noise exhibited by several large area InGaAs photodiodes due to the dark current was investigated. Two general forms of the excess noise could be observed: an $1/f$-shape and a noise shape that can described by the superposition of Lorentzian spectra. The absolute level of the dark noise exhibited by the characterized devices varied by more than four orders of magnitude. In general, it was observed that photodiodes with low dark current and a low bias voltage dependence of the dark current also exhibit low $1/f$-noise. All devices used for current power stabilization experiments showed very low dark current. However, a moderate increase in dark noise for those devices, e.g. due to a temperature change, cannot explain the limit observed in the power stabilization experiments.

The balanced-detection measurements presented in Section 4.1.3 showed that the low-frequency noise of junction photodiodes depends on the photocurrent drawn and is hence different from the dark noise of the photodetector. It could be demonstrated that low-frequency excess noise already limits the performance when using two bare photodiodes without noisy readout electronics. All measurements showed that the low-frequency excess noise observed at high photocurrents in the devices studied in this work does not depend on environmental influences. As the relative noise level seems to level off for high photocurrents, both intrinsic

noise in the photodiode and scattered light may explain the performance. As an intrinsic noise source would be uncorrelated for multiple devices, operating several devices in parallel would lower this limitation by the square-root of the number of devices used. The observed level at 10 Hz for the devices made from InGaAs can explain the limit of the best results of the power stabilization experiment described in this work in Section 3.2.4.

Apart from the photodiodes, tests on a large number of different resistors were performed as shown in Section 4.2. This study has pointed out that excess noise can be observed in all kind of resistors tested and used in our implemented designs. The observed noise level varies over almost three orders of magnitude and depends on several parameters like type, size, wattage, process, manufacturer, etc. It could be observed that the noise decreases with increasing mechanical size or volume of the same type of resistor and has a linear voltage dependence, which is in agreement with experiments reported in the literature. It could be demonstrated that current noise in resistors was one of the major noise sources in previous power stabilization schemes.

To quantify the effect of beam pointing, Section 4.3 dealt with the measurement of the spatial uniformity of photodiodes. Three different methods have been used to evaluate the coupling of pointing on the photodiode into measured power fluctuations. The individual results are in very good agreement with each other. The experiment with a spatial resolution of 10 µm for a typical photodiode used in our stabilization experiments gave a relative sensitivity gradient as large as $2.2 \cdot 10^{-5}$/µm [94]. Assuming the same pointing sensitivity for the devices used in the power stabilization performed in Section 3.2, position-dependent photodiode efficiencies are not limiting the power stabilization so far, but are within a factor of 4–5 of the design requirements. Hence accurate spatial information for photodiodes is essential optimizing future experiments.

As fluctuations in temperature within the setup can greatly affect the power stability of the stabilized laser system, detailed investigations of the effect of temperature fluctuations were performed in Section 4.4. Here, temperature dependencies of the photodiode efficiency (Section 4.4.1) and the temperature dependency of splitting ratio (Section 4.4.2) of beam splitters were of utmost concern. Measured temperature fluctuations of the ambient air in the laboratory and in the setup were used for an estimation of this contribution and temperature fluctuations of the air could be estimated to be at least one order of magnitude below the requirements.

As presented in Section 4.5, changes in the bias voltage of a photodiode greatly affect their electrical and optical parameters. Since the individual processes are hard to separate, the response of the output to changes of the bias voltage were investigated and the impact of bias voltage fluctuations could be determined to be very close to the electronic dark noise of the tested photodetector. This contribution to the total detector noise should be kept in mind and considered for new photodetectors.

As carried out in Section 4.6, the presence of signals with a frequency greater than the specified bandwidth of an electronic component can easily degrade the noise performance of the device by about one order of magnitude. Consequently, extensive filtering is required to attenuate these out-of-band signals in order to prevent the system from failures and distortion.

Scattered light, as already mentioned is a noise source in GWDs, could be identified to be a contributor to the low-frequency excess noise (see Section 4.7). Hence suitable reduction of ghost beams and scattered light are essential for sensitive measurements.

Lastly polarization fluctuations (Section 4.8) and laser frequency noise (Section 4.9) were examined. However, further purification of the polarization and the reduction of the laser

frequency noise by means of active stabilization could not lower the out-of-loop noise level of the power stabilization loop.

A selection of the most important noise sources contributing to the sensing noise of the power stabilization experiment are shown in Figure 4.30.
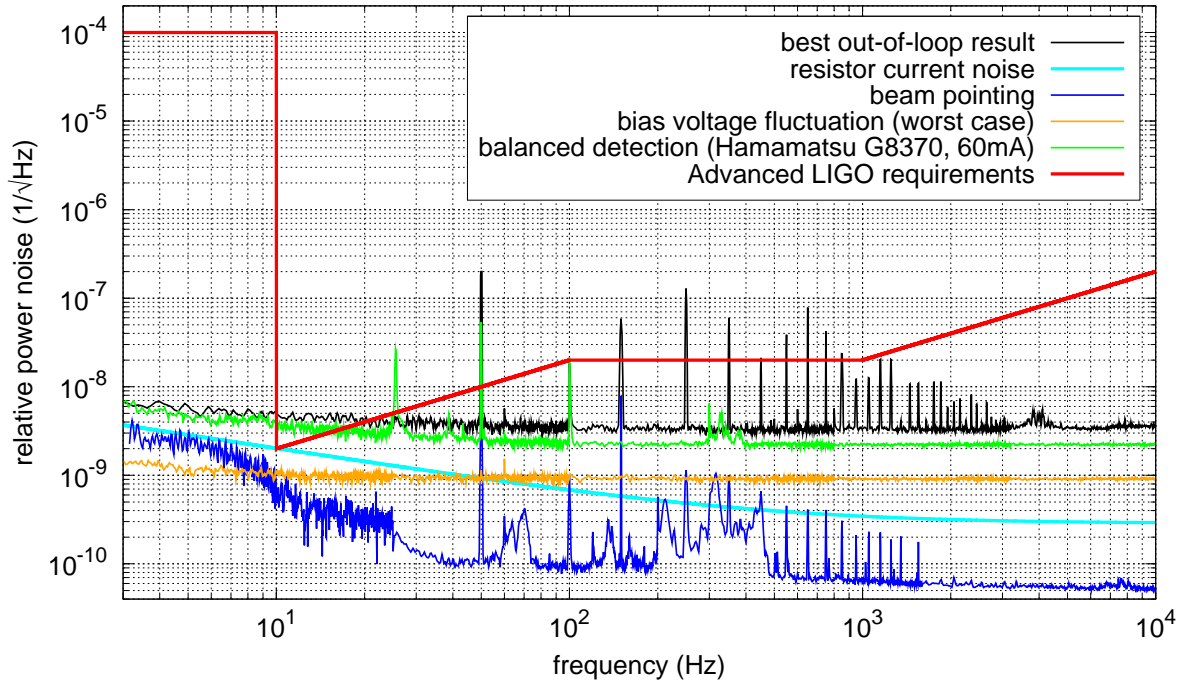

Figure 4.30: Contribution of the most important noise sources to the sensing noise of the power stabilization experiment.

The contribution from the low-frequency excess noise in photodiodes as measured with the balanced detection scheme is most dominant. The other sources are below but not negligible.

Stabilization of the Advanced LIGO laser system

Current plans for the Advanced LIGO gravitational wave detector call for the use of a 200 W laser system [6] and a laser with a power level close to 200 W is already under development [178]. The strongest coupling of laser power fluctuations is expected to be caused by radiation pressure effects in the interferometer arms. This leads to the most demanding requirement for Advanced LIGO for the relative power noise (RPN) of $2 \times 10^{-9} / \sqrt{\mathrm{Hz}}$ at 10 Hz (see Figure 3.1). In order to achieve excellent power noise performance of a stabilized laser system, the fluctuations of the unstabilized system have to be reduced by several orders of magnitude. Hence several noise sources which were already discussed in Chapters 3 and 4 have to be reduced to a minimum.

The following sections deal with the description and stabilization of the Advanced LIGO 200 W laser system. Furthermore a 200 W prototype laser was characterized in order to gain the essential system information for the design of the control loops and their topology. The proposed stabilization scheme will be discussed with special emphasis on the power stabilization of the laser system. A description of the 200 W high-power laser system designed for use in the Advanced LIGO GWDs with detailed descriptions of the individual parts can be found in Section 5.1. In order to develop the power stabilization, a detailed characterization of a prototype laser system is necessary, which will be given in Section 5.2. Subsequently Section 5.3 addresses the concept of the power stabilization feedback loop for the 200 W laser system. As the laser system is still under development and stabilization of the full system is not possible so far, parts of the proposed stabilization concept were conducted on the so-called *front-end* of the 200 W laser system, a 35 W master-oscillator power-amplifier (MOPA) system. The stabilization and its results are presented in Section 5.4.

5.1 Advanced LIGO laser system overview

The standard single-frequency, single-mode non-planar ring oscillator (NPRO) master laser is available with a maximum output power of 2 W. For initial gravitational wave detectors this was increased by injection-locking or amplification to power levels of 10 W–20 W [175, 184].

The Advanced LIGO 200 W laser is based on an injection-locked oscillator concept using a 35 W master-oscillator power-amplifier [46] and a high-power injection-locked oscillator stage [47], developed and fabricated by the Laser Zentrum Hannover (LZH). This high-power laser system will be described in the following section. To achieve the stability level of the laser system required by the gravitational wave detector, several active and passive stabilization techniques are required. The laser system including these stabilizations is called the *pre-stabilized laser system* (PSL). The complete PSL will be described in Section 5.1.2 in more detail.

5.1.1 Layout of the Advanced LIGO laser system

Figure 5.1 shows a schematic of the Advanced LIGO 200 W laser system. The MOPA is made up of a commercial, monolithic non-planar Nd:YAG ring laser (Mephisto 2000NE LIGO, InnoLight GmbH) with 2 W output power which is amplified by a four-stage laser amplifier to a power level of 35 W. The NPRO used is a custom made version with additional diagnostic outputs. The NPRO is equipped with a commercial "noise eater" (amplitude stabilization system) to reduce the effect of the relaxation oscillation (around 1 MHz). A broadband electro-optic modulator (New Focus, model 4001) is used to create phase-modulation sidebands for injection-locking of the high-power stage. The same EOM is used as a fast frequency actuator for the laser system. A sideband frequency f_{LO}=35.5 MHz has been chosen, which is a good compromise between being larger than the injection-locking range and small compared to the FSR of the slave laser cavity.
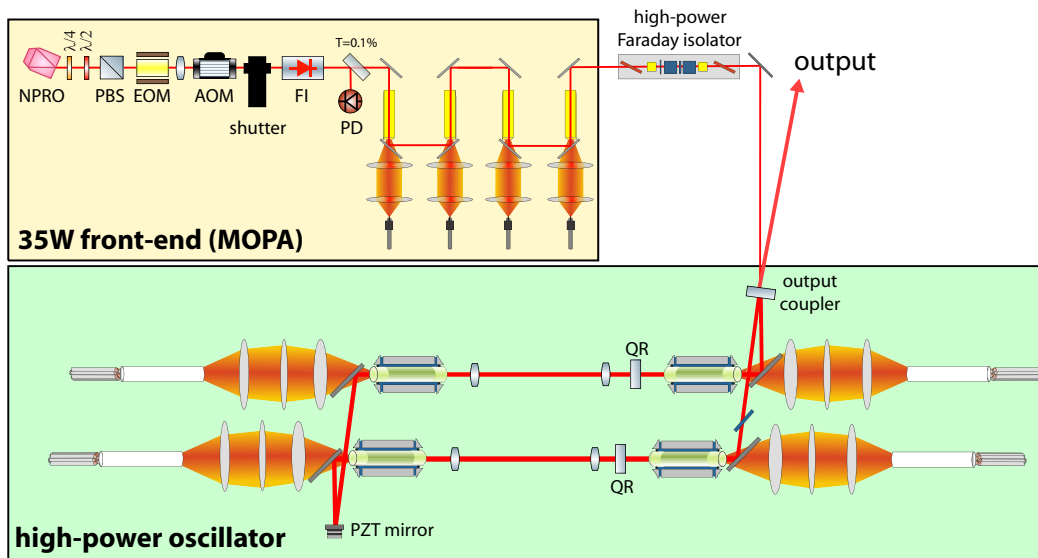

Figure 5.1: Schematic of the Advanced LIGO 200 W laser system.

Due to cross coupling to the laser frequency, the pump current of the NPRO can not be used as a power actuator. As previous power stabilization experiments showed that acousto-optic modulators are well suitable for power modulation, an AOM (Crystal Technology, model 3080-194) operated at a center frequency of 80 MHz was installed in front of the amplifier. A safety shutter behind the AOM is used to block the entire seed beam with the effect of shutting down the output of the complete MOPA. A single stage Faraday isolator (FI)(OFR, IO-5-1064-HP) placed between the shutter and the amplifier input ensures stable single-frequency laser operation and protects the AOM, EOM and the NPRO from laser light traveling in the backward direction. Even a small amount of light reflected back from components downstream of the MOPA could be amplified to the watt level and would damage these components.

The light from the NPRO then passes through a series of four diode-pumped Nd:YVO$_4$ power-amplification stages. The MOPA is an end-pumped design. Good mode control and an highly efficient amplification with excellent beam quality are achieved as a result. The four amplifier stages of the MOPA are pumped using four fiber-coupled laser diodes (Jenoptik, JOLD-45-CPXF-1L, Design 215415624) delivering a maximum output power of 45 W at a

wavelength around 808 nm. Efficient cooling of the laser crystal was realized by mounting the crystal in water-cooled copper blocks. A diagnostic photodetector was placed behind a turning mirror in front of the amplifier to monitor the power entering the amplifier stages and to check the functional status of the noise eater.

The high-power oscillator is based on a ring-resonator design with four end-pumped Nd:YAG laser heads. Thermally induced mechanical stress in the laser crystals results in stress induced birefringence and causes depolarization. The birefringence can be compensated by using two identically heads, a relay optic system consisting of two identical lenses and a 90° quartz rotator (QR). The high-power stage uses two of these birefringence compensated pairs in a ring resonator [47].

Each of the four laser heads is pumped by seven fiber-coupled laser diodes (identical to those used in the amplifier stage) delivering a maximum output power of 45 W each at a wavelength around 808 nm. The laser diodes are individually temperature stabilized to narrow the emission spectrum of the whole fiber bundle for each head and to reduce power fluctuations of the 200 W system due to changes in the pump wavelength. A fused-silica rod placed between the fiber and the laser head is used as a homogenizer for the transverse pump light distribution of the pump light of the seven incoming fibers. This ensures a nearly unchanged pump light profile in case of a pump diode degradation or failure. The laser crystals are Nd:YAG rods with a diameter of 3 mm. They have a doped center segment and undoped segments at both ends to reduce the thermally induced mechanical stress on the end surfaces. The laser crystals in the heads are directly cooled with water.

The MOPA serves as the master laser for the injection-locking scheme of the high-power oscillator. A Pound-Drever-Hall scheme is used to generate the error signal for the injection-locking control loop. A 35.5 MHz resonant InGaAs photodetector at the output of the high-power stage serves as the locking photodetector. The control signal of the injection-locking servo is fed back to a piezo-electrical transducer (PZT) which keeps the length of the high-power oscillator cavity within the injection-locking range. This control loop has a unity gain frequency of around 6 kHz. Due to its ring-resonator geometry, the high-power oscillator changes the direction of lasing if not locked to the MOPA. A special Faraday isolator is used to attenuate any beam from the high-power oscillator back towards the MOPA.

5.1.2 Stabilization of the Advanced LIGO laser system

To achieve the stability level of the laser system required by the gravitational wave detector, several active and passive stabilization techniques are required. Figure 5.2 shows the schematic of the PSL and the major stabilization loops.

The PSL can be divided into four major subsystems: The 200 W laser system, a pre-modecleaner as a spatial filter, a frequency stabilization to a rigid reference cavity and a so-called *diagnostic breadboard*, which enables the online measurement of the beam parameters and the noise, either of the 35 W stage or the 200 W output beam.

Control loops are required for the injection-locking of the high-power oscillator, the length control of the PMC, the laser frequency and for the power stabilization. The control-loops for laser frequency and power noise reduction are divided into two parts each, a so-called *inner loop* and an *outer loop*. The inner loops include all control-loops which are independent of the interferometer and are used to pre-stabilize the laser system as close to the final specifications as possible. Outer loops are used to further improve the stability of laser system to meet the final specifications using additional references and sensors which are part of the gravitational wave detector.
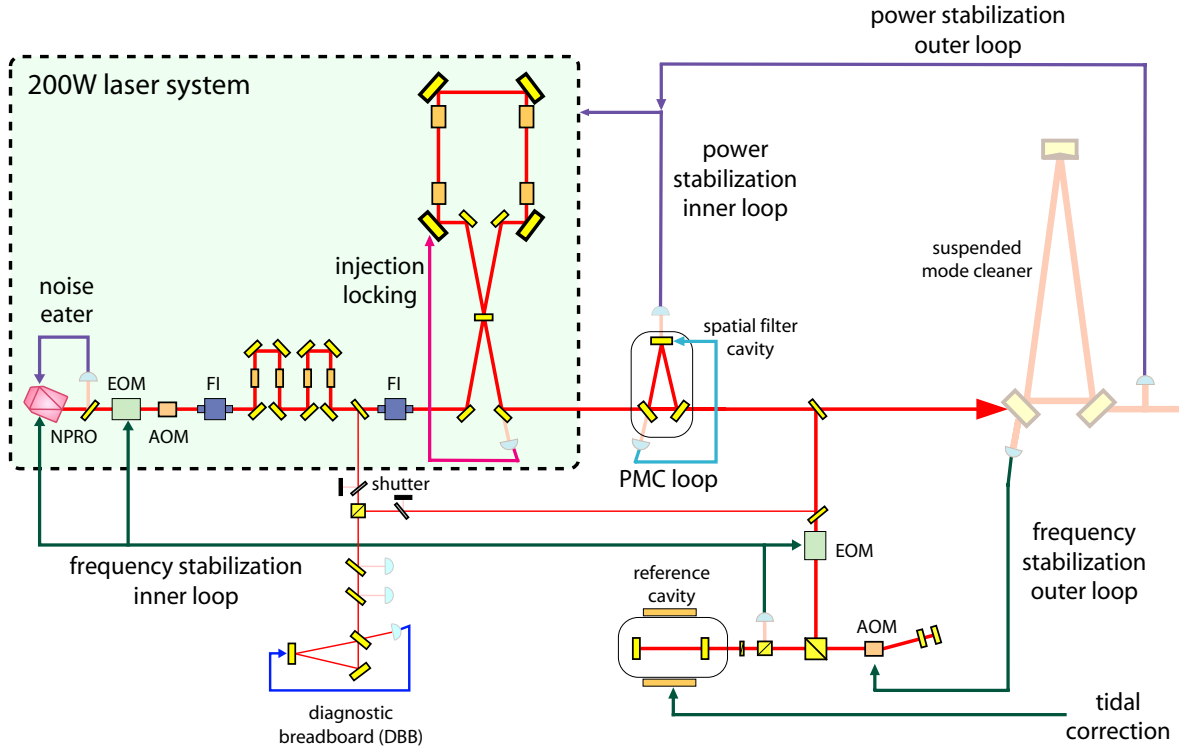
Figure 5.2: Stabilization scheme of the Advanced LIGO PSL.

Spatial filtering:

To improve the spatial profile of the main laser beam sent to the interferometer, the 200 W beam is mode matched into a rigid-spacer three mirror ring-cavity called the high-power pre-modecleaner (HP-PMC) that is very similar to the one already described in Section 3.1.2 [161]. In order to handle the higher incoming power of up to 200 W, the circulating power of the HP-PMC has been designed to have a Finesse $\mathcal{F}$ of 50 for p-polarized light and around 380 for s-polarized light. The HP-PMC is locked to the laser frequency with the HP-PMC length control loop. The Pound-Drever-Hall technique is used to generate an error signal by means of the same phase-modulation sidebands at 35.5 MHz which are already used for the injection-locking of the high-power oscillator. To control the length of the HP-PMC and thereby change the resonance frequency, a piezoelectric transducer (PZT) is glued between the curved mirror and the spacer. The HP-PMC will be housed in a small sealed enclosure to avoid acoustic coupling to the resonator which could lead either to beam-pointing or frequency fluctuations of the transmitted beam and minimizes the chances of contamination of the optical surfaces.

As the PZT is limited to a range of only a few FSRs of the HP-PMC, a second length-actuator with greater range is necessary in order to ensure long term stable operation of the HP-PMC. The spacer is made from aluminum which has a high thermal expansion coefficient. The HP-PMC length can be changed by means of a Kapton® isolated heater. A platinum temperature sensor (PT100) was glued on the spacer to monitor the actual temperature of the spacer.

Frequency stabilization:

The frequency stabilization will be very similar to that used for the initial LIGO detectors.

For the frequency stabilization of the PSL, a small fraction of the beam is split off after the HP-PMC. This beam passes an EOM (New Focus, model 4003) resonant at 21.5 MHz to provide phase modulation sidebands for the locking of the laser system to a suspended, linear, high-finesse reference cavity in a thermally isolated and stabilized ultra-high-vacuum tank. The phase-modulated beam double passes an AOM in the first diffraction order in a retro-reflective configuration. This AOM shifts the laser frequency by a value equal to twice the AOM driving frequency. The beam is then mode matched into the suspended reference cavity. A control loop stabilizes the laser frequency to this cavity by feeding back to the frequency actuators of the NPRO (PZT and temperature) and to the broadband EOM. As the HP-PMC acts as a spatial filter, the light for the frequency stabilization is close to a Gaussian TEM_{00} mode and spurious noise effects due to fluctuations of higher order modes are reduced.

The large suspended modecleaner of the laser interferometer (the shaded cavity on the right side of Figure 5.2) is a more stable frequency reference than the reference cavity for frequencies above a few Hertz. Hence the AOM frequency shifter will be used as an actuator for an outer frequency stabilization loop to stabilize the laser to the suspended modecleaner.

Finally a so-called tidal actuator controls the temperature of the reference cavity to lock the laser to slow drifts of the interferometer arm cavities caused by the earth tides.

Power stabilization:
The power stabilization of the PSL can be split into three control-loops: the internal power stabilization of the NPRO, the pre-stabilization of the high-power laser behind the HP-PMC (inner loop) and finally the outer loop, which senses the power noise behind the suspended modecleaner.

The internal power stabilization of the NPRO called "noise eater" mainly reduces the laser relaxation oscillation of approximately 1 MHz. The inner loop senses the power noise of the high-power laser behind the HP-PMC. This control loop feeds back to different power actuators in the laser system, e.g. the AOM placed between the NPRO and the MOPA and to the current of the pump diodes of the high-power oscillator.

As the suspended modecleaner induces power fluctuations and thus raises the power noise at the input of the interferometer, power fluctuations are sensed by an additional photodetector downstream of the suspended modecleaner. The control signal of that loop will be added into the error point of the inner power stabilization loop in order to achieve the power stability requirements at the interferometer input. The concept for the power stabilization loop of the PSL will be discussed in Section 5.3 in greater detail.

Laser diagnostics:
Spatial, frequency and power fluctuations of the laser are important noise sources in gravitational wave detectors. Consequently a new developed diagnostic tool was included in the laser system which allows analysis of the free-running and stabilized performance of the laser system. A fraction (120 mW to 150 mW) of the 35 W front-end output as well as a fraction of the high-power oscillator output downstream of the HP-PMC can be directed into this so-called *diagnostic breadboard* (DBB). The DBB is a compact diagnostic unit for laser beams. A detailed description of the DBB can be found in [95]. It consists of a rigid spacer Fabry-Perot ring cavity using its eigenmode as a spatial reference. The cavity is placed in a tank for acoustic shielding. The DBB can be controlled manually or in a fully automated mode by a computer. As the DBB is independent from the laser it can be operated whenever necessary. The alignment as well as the mode matching to the ring cavity can be adjusted remotely.

The DBB can be operated in two different modes: a *locked mode* and a *scanning mode*. In the locked mode the cavity is locked to the incoming beam using a slightly modified Pound-Drever-Hall technique. The sidebands for the Pound-Drever-Hall error signal are generated by modulation of the PZT of the ring cavity at 1 MHz. A length control servo is used to keep the cavity on resonance. Four alignment loops are used to automatically align the incoming beam to the resonator using the differential wavefront-sensing (DWS) technique [112]. The DWS signals are generated using two quadrant photodiodes. The length control loop of the cavity provides information about the laser frequency noise and the error. The control signal of the alignment control loop can be used to deduce the beam pointing of the incoming beam relative to the eigenmode of the ring cavity. Frequency noise of the laser and beam pointing can be measured between 1 Hz and 100 kHz. Half of the power of the incoming beam is split off and detected by an InGaAs photodetector. This detector can be used to measure the relative power noise up to 50 mA photocurrent and a 3-dB bandwidth of 50 MHz. The electronic noise is below the shot noise of 50 mA. The relative power noise can be measured between 1 Hz and 100 kHz and between 1 MHz and 70 MHz.

In the scanning mode, the length and alignment control is switched off and the length of the cavity can be scanned over several free spectral ranges, while the light power transmitted by the cavity is detected with a low-offset photodetector and recorded by the computer. This so-called *modescan* can be used to measure the fundamental and the higher order mode content of the incoming laser beam. An analysis program identifies the modes and determines their relative strength.

5.2 System characterization

The characterized high-power laser system is the so-called "*functional prototype*". This laser was fabricated during the preliminary design phase of the Advanced LIGO PSL program which is followed by another prototype, the "*engineering prototype*". After this phase the final construction manual will be written and a so-called "*reference system*" will be built before the system goes into full production. Detailed investigations of the laser performance have been carried out to demonstrate the suitability of the laser design for use in gravitational wave detectors. An overall output power of the injection-locked laser system of 180 W has been measured during a long-term test. The laser spatial beam-quality, relative power noise and beam-pointing fluctuations as well as transfer functions of the individual actuators of the laser system have been characterized in order to develop the stabilization scheme. The main topic of this thesis is the power stabilization of laser systems, so the system characterization will focus mainly on the information necessary to develop the power stabilization scheme of the laser.

First, power fluctuations of the complete laser system have been measured: peak-to-peak fluctuations over a time period of 10 minutes and the relative power noise spectral density in the frequency-band from 1 Hz to 100 kHz. The time series of the output power of the 200 W laser system is shown in Figure 5.3. The noise spectra of the 35 W front-end and the complete Advanced LIGO laser system in front of and behind the HP-PMC are illustrated in Figure 5.4.

The long-term peak-to-peak power fluctuations are higher than expected and are approximately 15%. The free-running noise of the total laser system is dominated by the fluctuations of the high-power oscillator. Starting from a free-running RPN of approximately $5 \times 10^{-3}/\sqrt{\text{Hz}}$ at 10 Hz, the noise level drops to about $10^{-7}/\sqrt{\text{Hz}}$ at 100 kHz. Power fluctuations of a laser system at low frequencies are generally caused by mechanical vibration of optical components, fluctuations in the pump light and modulation of the refractive index of the air inside the laser
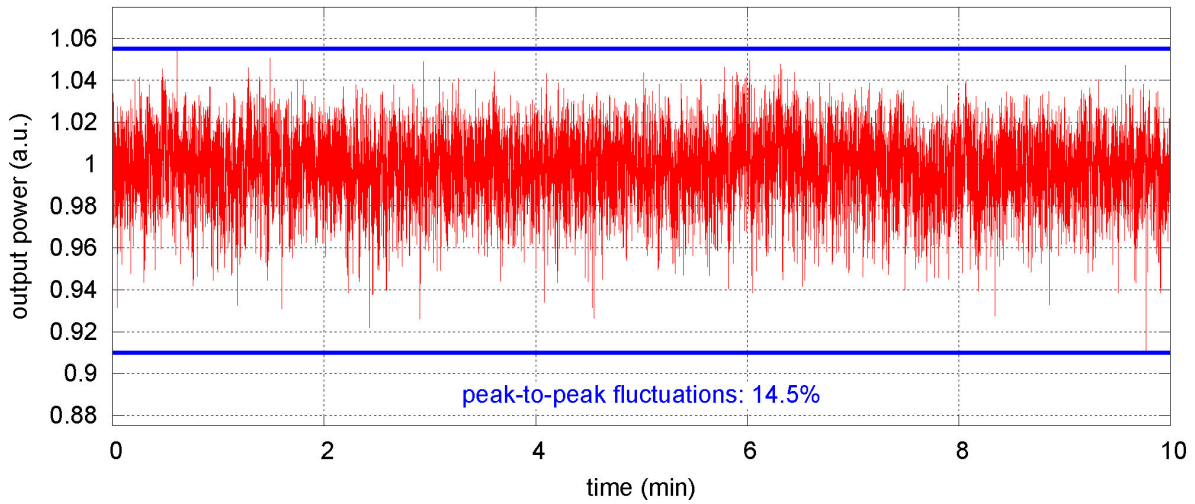
Figure 5.3: Time series of the output power of the 200 W laser system.
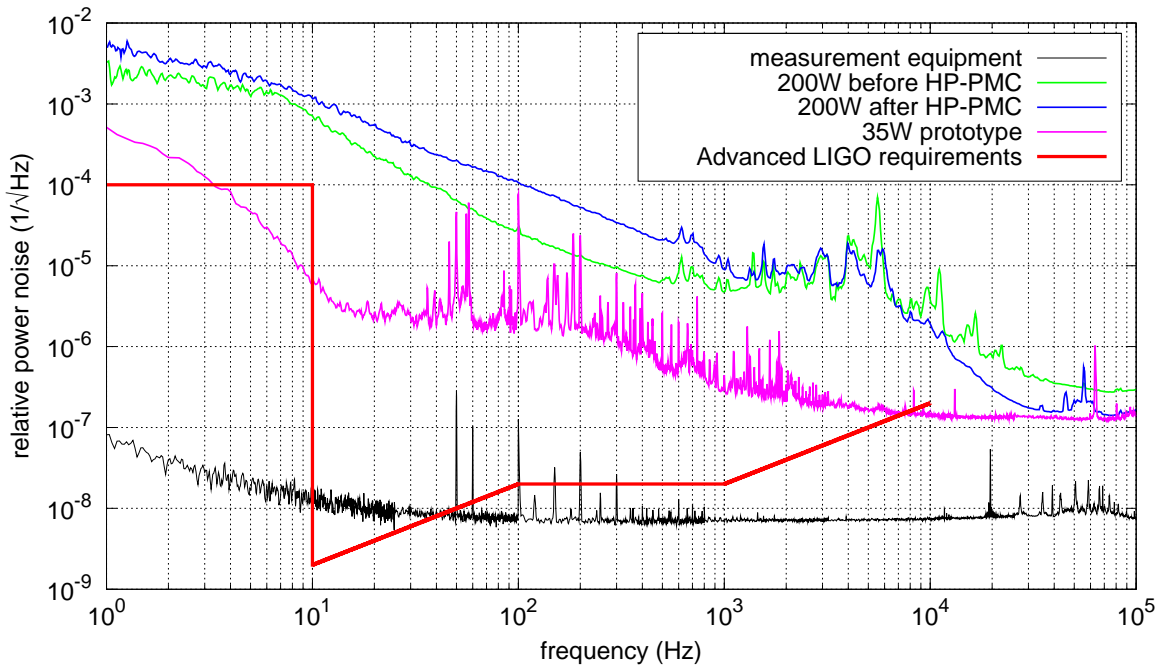
Figure 5.4: Relative power noise of the 35 W MOPA system and the 200 W laser system.

cavity. Mechanical vibrations are mostly generated by turbulences of the cooling water and by acoustics or air pressure fluctuations on the optical table. For the characterized system, power fluctuations of the pump light of the high-power oscillator as well as cooling water driven vibrations of the four oscillator laser heads were ruled out as the dominant noise contributions. Noise from the cooling water can be observed in the kHz region but a change in water flow does not change the overall noise level. So far possible candidates for the dominant noise source are alignment fluctuations of the oscillator eigenmode or some polarization dynamics due to fluctuations in the depolarization of the Nd:YAG laser crystals. A more detailed study

of the source of the high power-noise is ongoing to determine the dominant noise sources of the laser system.

In order to be able to stabilize the system, adequate control actuators have to be part of the high-power laser design. In the following these power actuators will be characterized. Starting with the 35 W MOPA front-end, two power actuators are available. These are the modulation of the NPRO seed-laser power via the AOM included in the front-end and the pump power of the four amplifier stages. The seed power can be controlled via the RF power level applied to the AOM. Figure 5.5 illustrates the power modulation of the MOPA via seed power modulation.
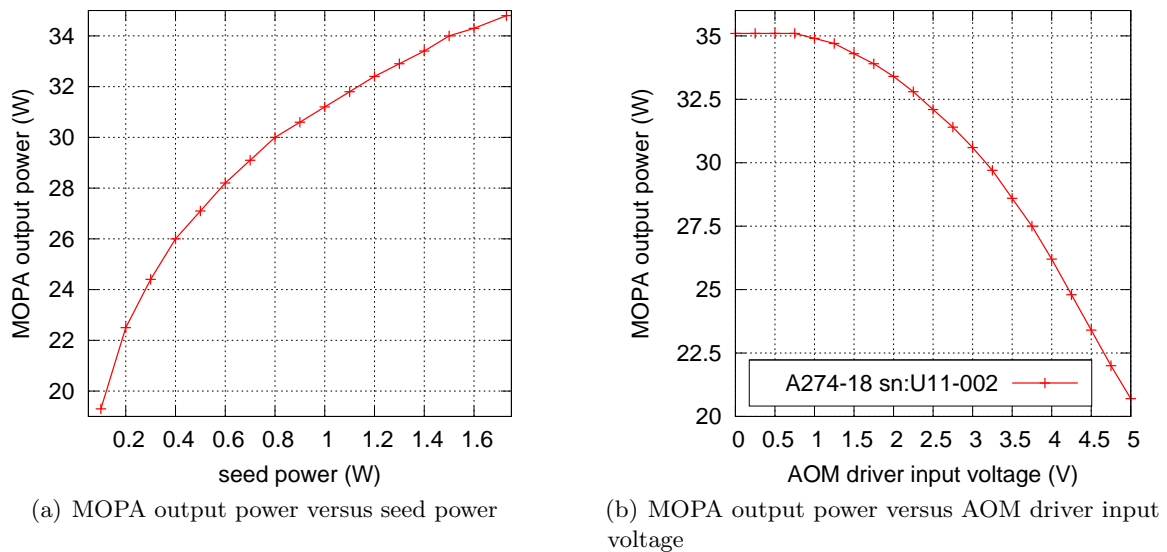

(a) MOPA output power versus seed power

(b) MOPA output power versus AOM driver input voltage

Figure 5.5: Power modulation of the MOPA output power via seed power modulation: (a) full slope of the MOPA power versus seed power; (a) MOPA output power versus input voltage of the used AOM driver.

The minimum output power even with very small input seed power is approximately 19 W. This is due to the fact that the amplifier stages have a large small-signal gain and even a very small input signal is amplified to high power-levels within the first two stages such that almost the full power of the last two stages can be extracted. The maximum diffraction efficiency of the AOM at maximum RF power (5 V AOM driver input voltage) is approximately 88% corresponding to a minimum seed power of 180 mW and a minimum output power of approximately 21 W. Hence a peak-to-peak power modulation of 14 W (40% of the MOPA power) is possible. This corresponds to a peak-to-peak power modulation of the complete high-power laser system of approximately 7%.

The design of an optimized inner control loop for the power stabilization requires the knowledge of the dynamic behavior of the MOPA system. Therefore, the transfer function from seed-laser pump power and amplifier pump power to the output power was measured. Figure 5.6 shows the measured transfer function from relative seed laser power variations to relative amplifier output power variations. It has been obtained by modulating the seed laser power with the AOM, measuring the seed laser output power and the amplifier output power.
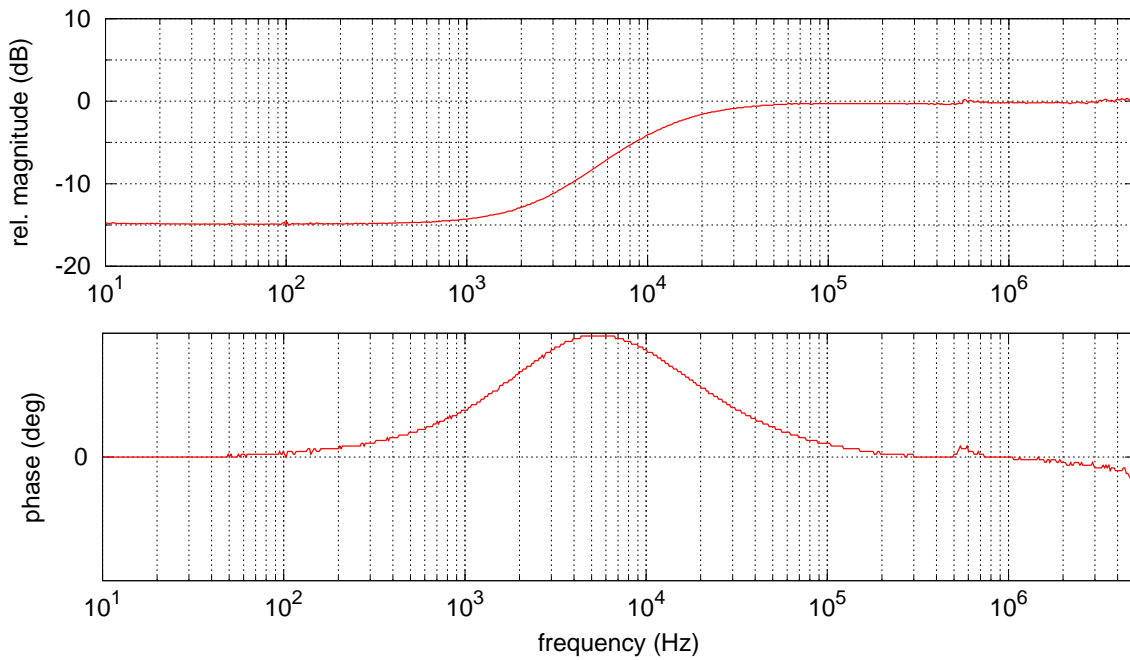
Figure 5.6: Measured transfer function from relative seed laser power variations to relative amplifier output power variations.

The transfer function has the shape of a DT_1-filter. In a saturated amplifier, slow seed laser power variations translate to output power variations of the same amount, since an increase in seed power reduces the inversion in the gain medium and hence the gain in the amplifier [159]. As the first two stages of the amplifier are not fully saturated a small gain can be observed which varies with the absolute power of the seed laser. For modulation frequencies above the inverse effective lifetime of the upper laser level, the inversion cannot follow the seed power changes. Consequently the amplifier acts as a linear amplifier for high modulation frequencies. The transfer function from relative seed-power variations to relative output-power variations equals 1. The useful bandwidth for the built-in AOM is limited by the delay of the acoustic wave inside the AOM crystal to about 450 kHz as already explained in Section 3.2.2.

The modulation input for the laser diode current and hence the pump power of the MOPA is provided at the MOPA control box. The measured transfer function from the current modulation input to the MOPA output power is shown in Figure 5.7.

As the current modulation is conducted via the digital control system of the laser itself (Beckhoff system), the bandwidth is limited to about 1 Hz. A variation of the pump power also changes the beam profile of the MOPA output beam via thermal effects inside the laser crystal, which limits the range of power modulation by pump current variation to a few percent. Nevertheless it can be used for long-term power corrections of the MOPA system, e.g. if the pump power degrades over time. A modulation of the seed power would be preferable because is does not change the beam profile of the output beam.

The high-power oscillator stage provides the pump power of the four laser heads as a power actuator. The pump power can be controlled via the pump diode current. The current is provided by four power supplies, each having an analog programming input (0–5 V) to adjust the current independently from each other. Figure 5.8 shows the measured transfer functions
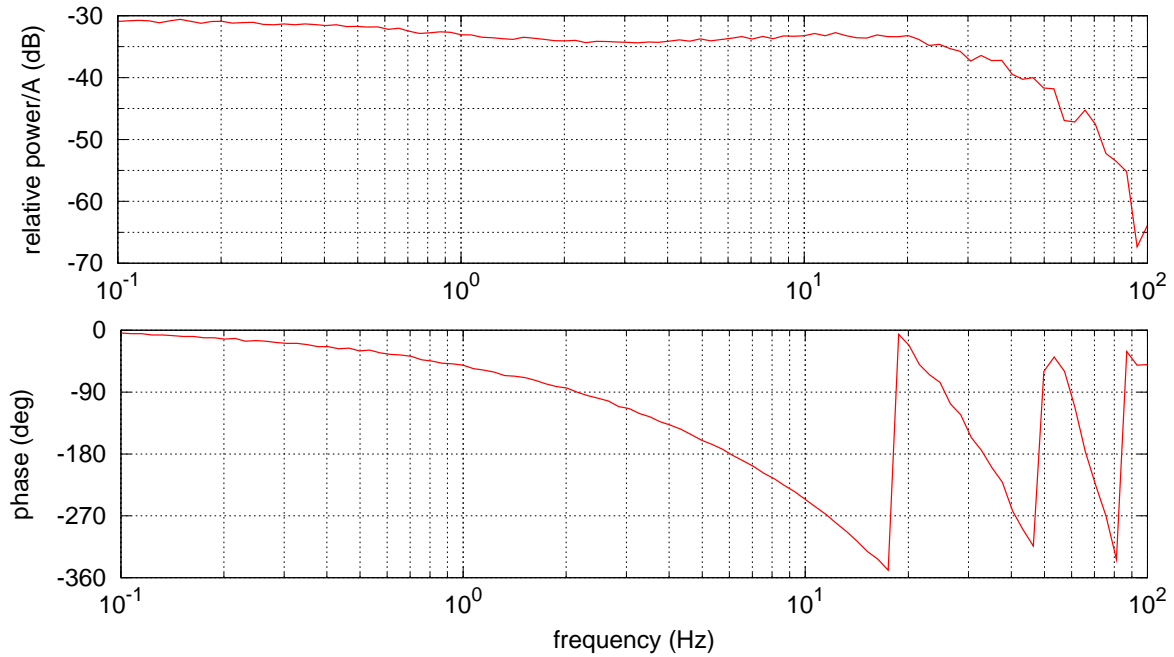
Figure 5.7: Measured transfer function from current modulation of the MOPA pump diode current to the MOPA output power (via Beckhoff).

from this programming input of the pump diode power supply to the output power of the 200 W laser before and after the HP-PMC.

As the finesse of the HP-PMC is only about 50, the corresponding pole frequency is greater than 7 MHz and is thus negligible for the power stabilization control-loop design. The useful response is limited by the power supply input delay to a couple of hundreds of hertz. As one can see the magnitude response downstream of the HP-PMC is higher than without it. This is due to the fact that a change in pump current, and hence pump power, also changes the eigenmode of the laser resonator or pointing of the beam which in turn also changes the coupling efficiency to the cavity.

The stability range of the laser resonator is defined by the thermal lenses inside the laser crystals. Changes in pump power also change the thermal lenses, and hence the resonator eigenmode also changes. Increasing or decreasing the pump current from its optimal point of operation causes the size and the shape of the resonator eigenmode to change to a non-Gaussian mode. Figure 5.9 shows the output power in the fundamental mode of the high-power oscillator versus change in pump current of each head. The change in mode shape for increased and decreased pump current is also shown.

The output beam quality, which plays an important role in the overall performance of the 200 W laser system, limits the amount by which the pump current can be varied. Small amounts of changes in the beam profile can be tolerated because of the filtering by the HP-PMC, where changes in beam profile will be mostly converted into power fluctuations. Changes in pump power also change the resonator length and thus the frequency, which has to be compensated by the injection-locking control loop. As the changes of the thermal lens are not necessarily radially symmetric it could also introduce beam pointing. Hence the total stability of the
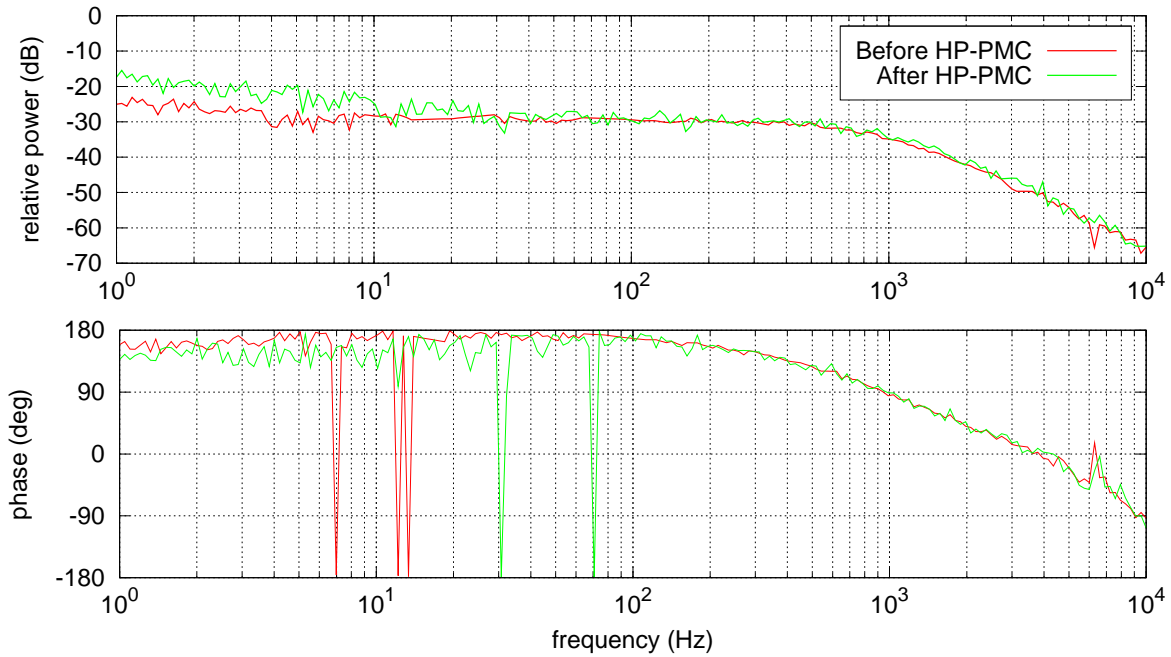
Figure 5.8: Measured transfer function from modulation input of the pump diode power supply to the 200 W laser output power.
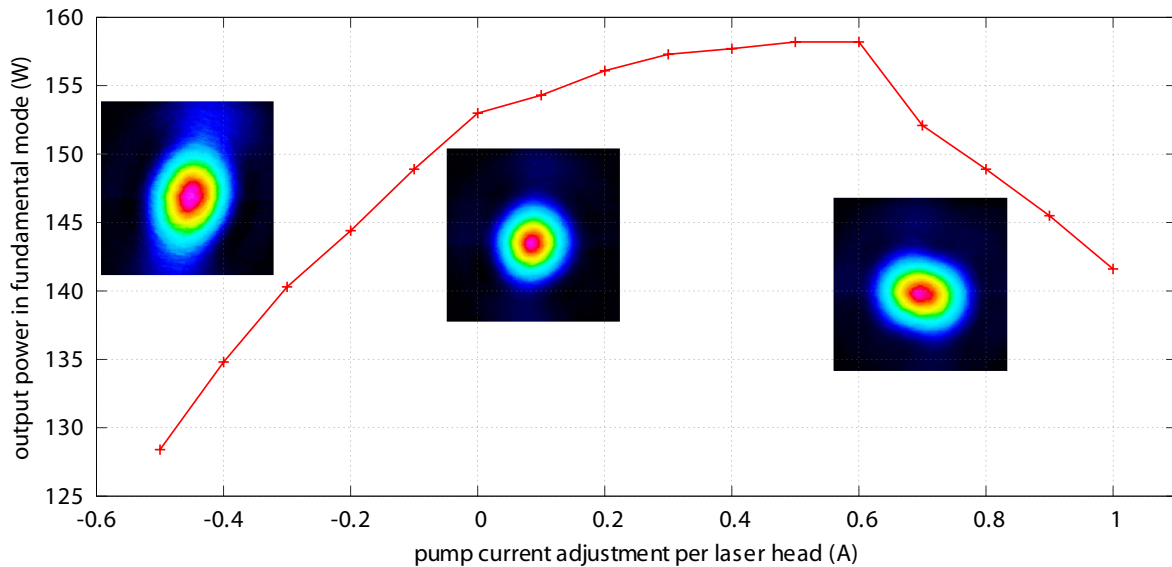
Figure 5.9: Output power of the high-power oscillator resonator versus pump current change: The shape of resonator eigenmode changes to a non-Gaussian eigenmode when changing the pump power.

high-power laser resonator is highly sensitive to changes in pump power and one has to be very careful when modulating the current of the pump diodes of the high-power oscillator.

A second measurement to determine the dynamic range of this actuator was performed. The pump power was modulated with a slow sine wave using the control input of all power supplies simultaneously. The modulation was applied around the optimal operation point (0 A in Figure 5.9) and the output power of the laser system behind the PMC was measured. The result is plotted in Figure 5.10. For large pump power modulations the sign even changes. This
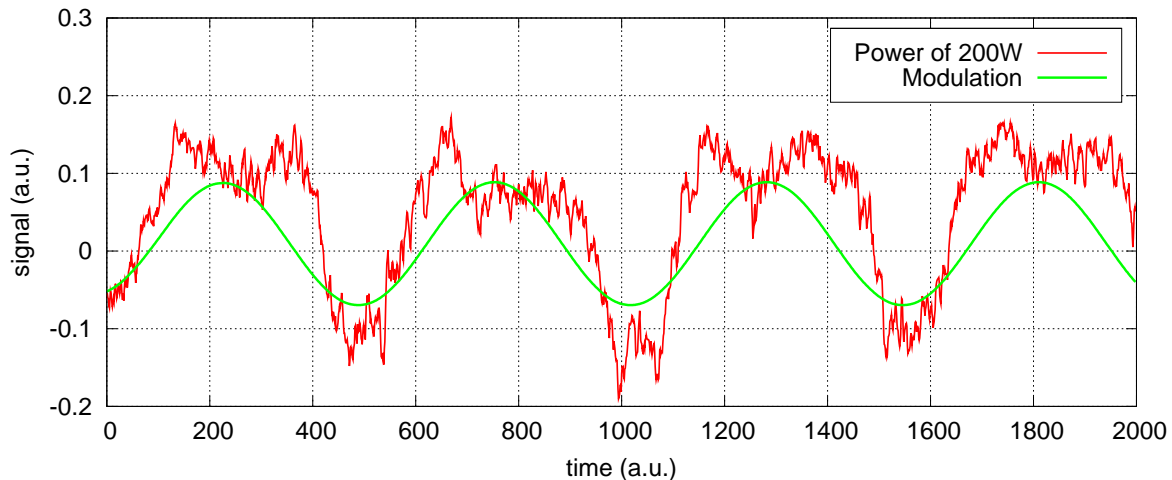

Figure 5.10: Nonlinearity of the 200 W laser system for pump power modulation.

is consistent with the sign change of the slope of the curve in Figure 5.9. Hence the range for pump power modulation around the optimal operation point is limited to a maximum change in output power of about 10%.

5.3 Power stabilization concept

In order to achieve the laser power noise requirements, several control-loops and power actuators are needed to suppress the free-running noise of the laser system to this very demanding level. Starting from a free-running RPN of approximately $5 \times 10^{-3} / \sqrt{\text{Hz}}$ a nested control loop with more than 120 dB loop gain is needed to reach the RPN of $2 \times 10^{-9} / \sqrt{\text{Hz}}$ at 10 Hz. The available power actuators have already been described and characterized in the previous section. The proposed power stabilization scheme of the Advanced LIGO PSL is shown in Figure 5.11.

It is planned to use analog control-loops as well as two independent digital control systems. The first digital system is a modular industrial control system on based real-time Ethernet technology (EtherCAT) from Beckhoff Automation. The complete laser system is controlled via Beckhoff. The bandwidth of the components (ADC, DAC, ...) used is limited to a couple of hertz and hence this system can only be used for slow control loops like temperature controllers or for a long-term drift compensation. For higher-speed applications, PC-based hardware is used that runs real-time Linux (RTLinux) and employs EPICS (**E**xperimental **P**hysics and **I**ndustrial **C**ontrol **S**ystem), a software environment used to develop and implement distributed control systems for devices such as particle accelerators, telescopes and other large experiments. The EPICS/RTLinux environment is also used for data acquisition. Using the existing hardware, digital control-loops with bandwidths up to a kilohertz can be set up. This is too slow to do the complete power stabilization digitally but can be used to control and adjust loop parameters of the analog control-loops like the gain and offsets etc.
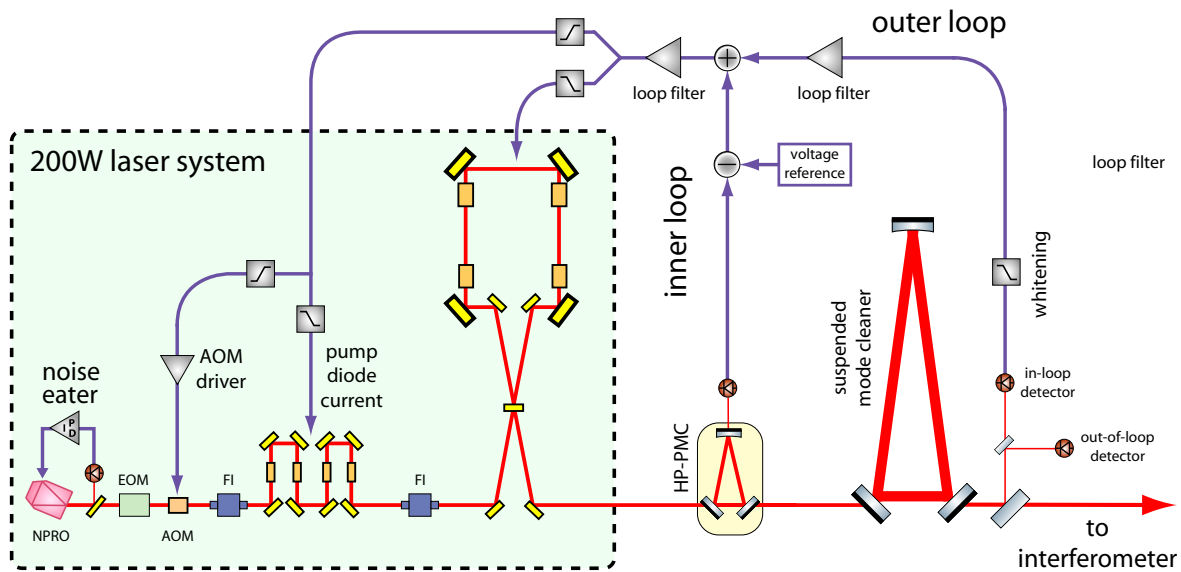
Figure 5.11: Detailed power stabilization scheme of the Advanced LIGO PSL.

A first control loop comes with the NPRO and is used to reduce the relaxation oscillation of the laser at about 1 MHz. As the free-running noise of the high-power laser is dominated by the fluctuations of the high-power oscillator, the next sensing point must be behind the injection-locked oscillator. Several other photodetectors will be available up to this point for system characterization and monitoring, but will not be used for power stabilization of the system. In order to reduce the risk of damaged components in the laser system, especially in the high-power beam, the number of pick-off mirrors should be reduced to a minimum. Therefore the first sensing point is planned to be placed behind the curved mirror of the HP-PMC. This also allows additional power fluctuations caused by beam pointing on the HP-PMC to be detected within the first control loop.

In general it would be best to compensate for fluctuations at the origin of the noise. As long as the detailed study of the source of the high power noise at low frequencies is under investigation, the high peak-to-peak fluctuations will be ignored for the current stabilization concept as it is expected that these will be reduced by an improved laser design in the next design phase. Nevertheless, alternative power modulation techniques are currently under investigation.

Except for the high power fluctuations at very low frequencies the feedback signal could be sent to the AOM placed between the NPRO and the amplifier stage of the MOPA. The AOM has a high bandwidth of up to several hundred kHz. The actuation has a reduced range at low frequencies as the transfer function from the seed power to the MOPA output power is -15 dB up to around 1 kHz due to properties of the amplifier stage (Figure 5.6).

As the injection locking bandwidth of the high-power stage depends of the seed power, a change in the MOPA output power also effects the injection-locking control loop and thus the frequency stability of the laser system. Therefore the maximum acceptable power modulation depth of the MOPA system is roughly estimated to be 10% (3.5 W), which is roughly 2% of the total output power the high-power laser system.

When using the digital Beckhoff interface the bandwidth is limited to around 1 Hz. Instead a direct modulation of the power supply via the analog programming input could be used

which results in a modulation bandwidth up to a couple of hundred hertz (see Figure 5.8). This could be increased by using a current shunt as already used in initial LIGO [1] or the 12 W GEO-laser system (Section 3.1.3). The laser dynamics however determines the useful bandwidth of this actuator to a couple of kilohertz due to a transfer function pole at the frequency that corresponds to the inverse of the effective lifetime of the upper laser level.

The inner control loop will be a DC-coupled design in order to meet the requirements for very-low frequencies. The total power fluctuations should be less than 5% peak-to-peak over any 24-hour period. The requirements for Fourier frequencies up to 10 Hz, the so-called *control band*, are summarized in Table 5.1.

frequency	relative power noise $\delta P/P$
0.1 Hz–0.4 Hz	$< 10^{-3}/\sqrt{\text{Hz}}$
0.4 Hz–10 Hz	$< 10^{-4}/\sqrt{\text{Hz}}$

Table 5.1: Relative power noise requirements for the control band (0.1 Hz to 10 Hz).

After the pre-stabilization using the inner control loop, the laser beam is injected into the Advanced LIGO IO subsystem of the interferometer [6]. The functions of the IO subsystem are to provide the necessary phase modulation of the input light, filter the light spatially and temporally with the suspended modecleaner, provide optical isolation and distribution of various interferometer diagnostic signals. The IO reduces the frequency and beam-jitter noise of the laser, but beam jitter (pointing fluctuations) or beam geometry fluctuations appear as power fluctuations behind it. Hence the so-called outer power stabilization loop will be used to reduce the power fluctuations of the light which enters the interferometer. An additional pair of identical photodetectors (an in-loop and an out-of-loop detector) downstream of the suspended modecleaner will be used to sense power fluctuations of the beam before it is injected into the main interferometer. This also reduces any noise introduced into the inner loop caused by dust passing the sensing beam or by pointing on the inner loop PD. The control signal of the outer loop will be added into the error point of the inner power stabilization loop.

In the previous chapters it has been shown that the detection of power fluctuations at the $2\times10^{-9}/\sqrt{\text{Hz}}$ level is problematic. Thereby the main challenge lies in the sensing and not in the control loop design or the total loop gain as demonstrated with the optimized power stabilization experiment using the NPRO (Section 3.2).

The main interferometer optics including the suspended modecleaner will be mounted on actively stabilized optical tables inside the main vacuum system. The propagation axis of the light leaving the suspended modecleaner might fluctuate relative to the optical table where the sensing photodiodes will be mounted. As pointing of the beam on the photodiode in combination with photodiode non-uniformities has a large influence on the noise performance, the beam on the photodetectors has to stay within a few microns of the sweet spot of the photodiode (see Section 4.3). If it is larger, a beam steering system will be needed and the photodetectors may also have to be suspended. According to the current design, the expected motion of the modecleaner's eigenmode with respect to the isolated table is small enough to stay within this range and the photodiode does not need to be suspended.

The new investigations presented in Chapter 4 indicate that $1/f$ electronic noise is responsible for the excess noise observed at low frequencies. By taking extreme care in the design of the electronics, this noise can be reduced further and we are confident that this can lead to a

stability better than the demonstrated $5\times10^{-9}/\sqrt{\text{Hz}}$ at 10 Hz [141]. As the dark current of photodiodes and the $1/f$-noise are due to imperfections of the device, devices with extremely low dark current are expected to have low $1/f$ noise too, which has to be demonstrated. The thermal resistance between the photodiode substrate and the case of the photodiodes has to be low, because the photodiode has to handle a minimum of 100 mA of photocurrent. As the photodetectors has to be placed inside the ultra-high vacuum system, it may have to be cooled via radiation only, especially if suspended.

Based on the characterization conducted, 3 mm InGaAs photodiodes manufactured by Gtran (formerly Anadigics, PD3M, Class A (shunt resistance >1 MΩ)) will be used for a first prototype of the power stabilization of the PSL. The Gtran devices offer a large active area with low dark current along with very low thermal resistance, as already shown in Section 4.1.1.

Measurements of the low-frequency current noise of a number of resistors suggest that the current noise of the resistors is one of the limiting factors of the photodetector noise performance at low frequencies. This noise increases as the current through the resistor is increased and may limit the performance of the photodetector at high photocurrents. In the Advanced LIGO power stabilization electronics bulk metal foil resistors will be used because these resistors offer the lowest current noise.

Two modes of operation for the laser system are planned: Normal operation at full laser power and an intermediate or low power level, with about 10% of the maximum power. The full power level corresponds to a photocurrent of $I > 100$ mA. If the power is reduced below a certain level, the electronic noise of the high-power photodetector becomes dominant and will limit the stabilization performance. Hence a low-power mode of the photodetector circuit will be necessary with a switchable gain in the main photodetector stage, e.g. two transimpedance gains if the classic transimpedance design is used. Several designs have been evaluated which will be further compared during the development of the in-vacuum photodetector.

Since only very low outgassing is permissible, it is planned to put the electronics in small vacuum-tight containers that are sealed by welding. The first prototypes of these photodetectors are currently under investigation. To reduce the amount of electronics which has to be in the vacuum environment, the detector will be reduced to the basic components and additional electronics like power regulation, whitening and control-loop filters will be outside the high vacuum system.

5.4 Stabilization of the 35 W front-end laser

As the high-power laser system is still under development, parts of the stabilization concept for the complete laser system have been tested using one of the 35 W laser amplifier systems in order to verify the basic concept as much as possible. The 35 W laser system used is the so-called *reference system* for the front-end laser of the Advanced LIGO laser system. This reference system has been set up at the AEI in Hannover and is running around the clock in order to demonstrate the reliability of the system. Figure 5.12 gives an overview of the components of the laser system.

The MOPA system can be separated into five functional parts. The first part is the *MOPA laser head*, a sealed box including the NPRO and the four head amplifier and all intermediate optical components like EOM and AOM. The second part is the *NPRO power supply* which can be located as far as 13 m away from the MOPA head. The third part is the *MOPA Control Box*. The Control Box is connected to the MOPA head and to the NPRO power supply. The Control Box includes an embedded computer with a touch screen which gives the user access
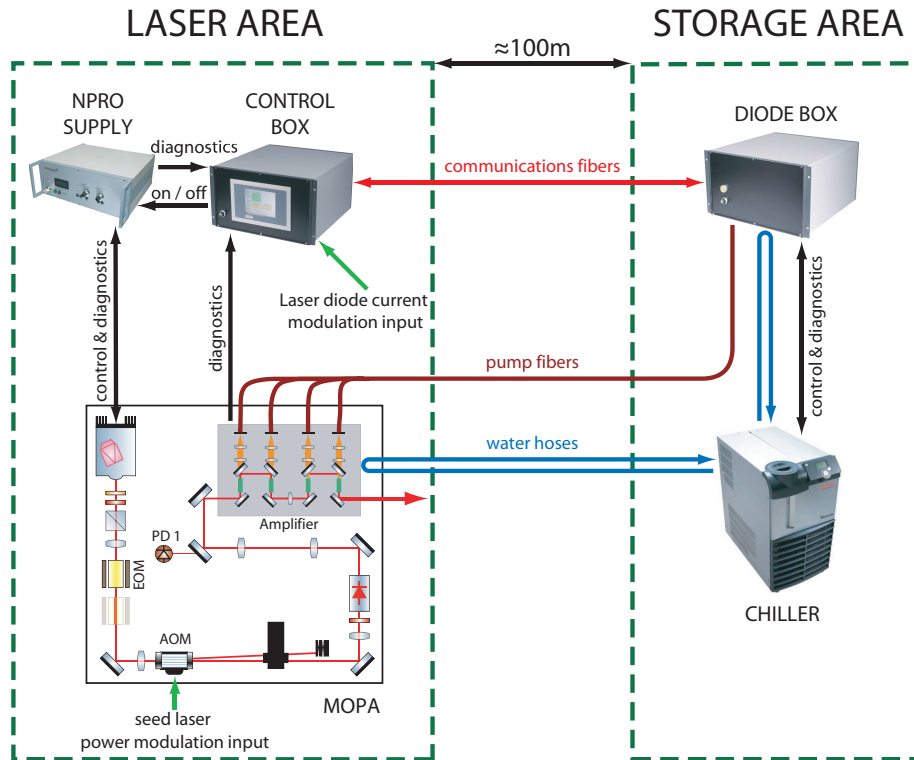
Figure 5.12: Wiring diagram of the 35 W MOPA system and its subsystems.

to all parameters of the amplifier system and additional diagnostics for the NPRO. With this Control Box the complete laser system including the NPRO can be activated.

As acoustics, vibrations and RF interference are a large issue in Advanced LIGO, the other two parts, the laser diodes and the chiller for the cooling water are located separately from the rest of the system. The laser diodes and their power supplies are mounted in the so-called *Diode Box*. The four laser diodes are connected via 100 m long optical fibers to the MOPA head. In order to avoid ground loops, communication connections among the parts next to the laser and the ones far away are done via optical fibers. The chiller can be also controlled and monitored and is directly connected to the Diode Box. Both the MOPA head and the Diode Box have to be water cooled.

5.4.1 Optical setup of the reference system

Figure 5.13 shows the optical setup of the 35 reference system. The system can be split into five parts: The MOPA, the HP-PMC, a power and a frequency stabilization loop using a rigid cavity and the diagnostic breadboard.

Starting with the output beam of the MOPA, the beam is first mode matched into the HP-PMC. To demonstrate the reliability of the HP-PMC over a long period of time, the polarization of the input beam was adjusted to the high-finesse orientation (s-pol, $\mathcal{F}$=383) which means that the circulating power in the HP-PMC is even greater than that expected during operation in Advanced LIGO. For the Advanced LIGO laser and the low-finesse mode of the HP-PMC (p-pol, $\mathcal{F}$=50) the circulating power will be ≈2.8 kW. For the reference system using the other polarization but with less input power, the circulating power is approximately
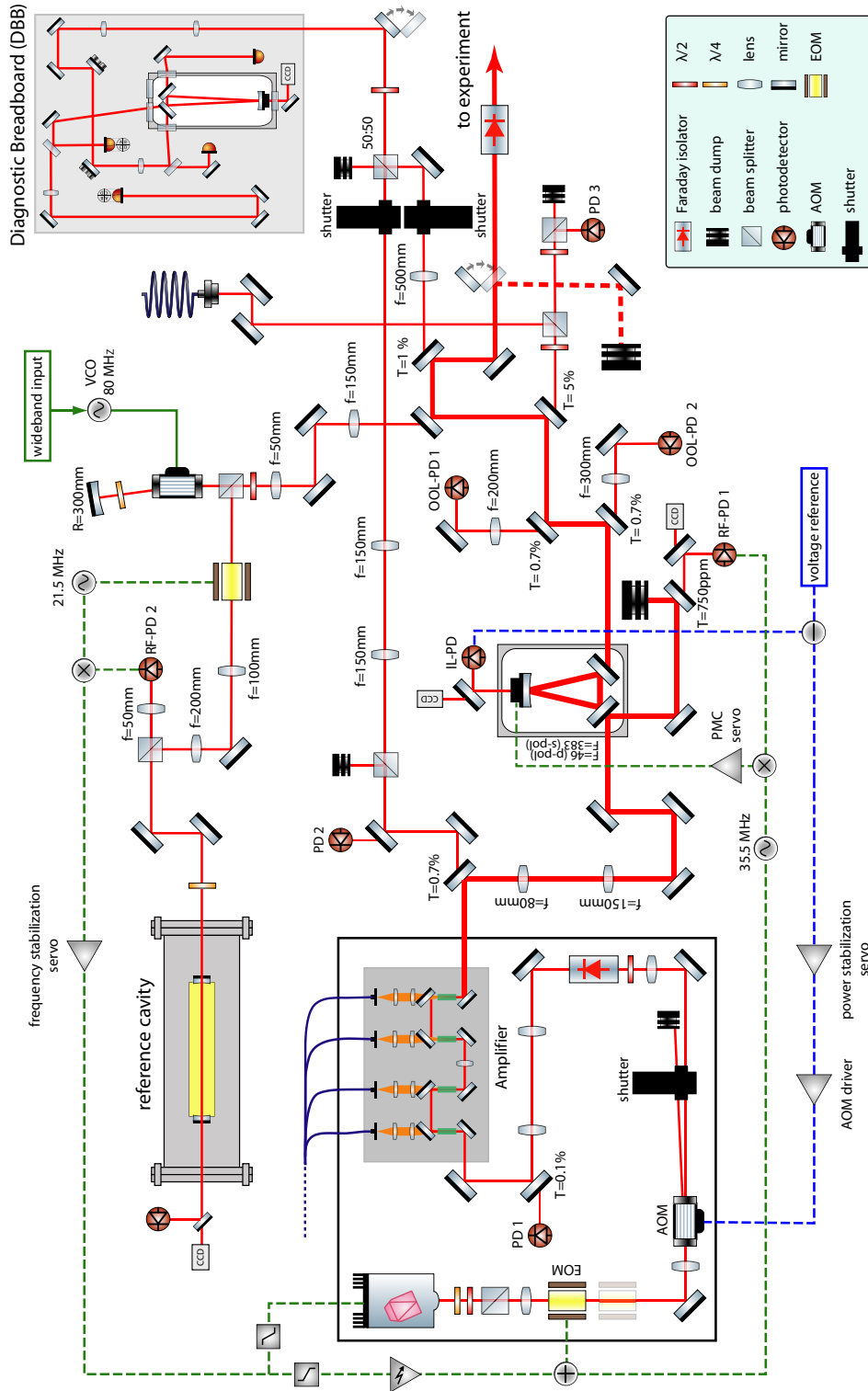
Figure 5.13: Optical layout of the 35 W reference system: The system can be split into five subsystems: The MOPA, the high-power pre-modecleaner for spatial filtering, the power and the frequency stabilization using a rigid cavity and the diagnostic breadboard.

4 kW. The throughput was stable over several months of almost continuous operation, and no thermal loading effects were seen so far. The length of the HP-PMC was controlled via a Pound-Drever-Hall scheme to make the HP-PMC eigenfrequency follow the frequency of the incident beam from the MOPA. The length control was realized by an analog controller with manual lock-acquisition and a high-voltage amplifier similar to the ones used in the other experiments. For the reference system, only the PZT was used as the length actuator. The thermal actuator will be used later to increase the overall actuation range and to allow for a PZT with higher frequencies of the internal resonances but less range. In the future, the analog controller will be controlled and monitored by the EPICS/RTLinux control and data acquisition system. To avoid acoustically driven length changes of the HP-PMC and to keep it clean, the HP-PMC was mounted into a sealed vessel.

Downstream of the HP-PMC several partially-reflective mirrors were used to split off some light for the power and frequency stabilization, and additional beam diagnostics using the DBB. The in-loop detector for the power stabilization loop was located behind the curved mirror of the HP-PMC. The transmission of the curved mirror was measured to be about 20 ppm. So the transmitted power is approximately 78 mW. Two out-of-loop detectors for independent measurements of the loop performance were placed downstream of the HP-PMC behind super-polished low-loss mirrors with a transmission of 0.7%. This corresponds to an out-of-loop detected power of about 230 mW. The detailed power stabilization loop scheme will be explained later in Section 5.4.2.

In order to characterize the spatial, frequency and power fluctuations of the laser system and to characterize the HP-PMC, a DBB was integrated into the system. A fraction (300 mW) of the 35 W beam directly behind the MOPA output could be directed into the DBB, as well as a fraction of the beam downstream of the HP-PMC. These two beam paths were combined using a 50:50 beam splitter and fed into the DBB. The mode matching for both beams was implemented before the beam splitter after which they share a common path. This permits convenient switching between both beams by using two shutters without adjustment of the DBB. The DBB could be controlled manually or remotely via EPICS/RTLinux.

Finally, up to 5% of the full laser power was provided via a single-mode polarization maintaning fiber for other experiments, e.g. the photodiode linearity measurement setup. Figure 5.14 shows a photograph of the 35 W reference system setup.

5.4.2 System characterization and power stabilization loop design

The RPN of the *reference system* is slightly different from the one implemented in the functional prototype of the Advanced LIGO laser system (see Figure 5.15).

This is mainly caused by the exchange of the type of power supplies used for the pump laser diodes. The output noise of the MOPA is dominated by noise of the pump power due to current noise of the power supplies. The new power supplies have higher current noise in the kilohertz region. This is not critical for the 200 W laser design as the MOPA noise level at low frequencies is far below the noise level of the high-power oscillator.

The complete power stabilization scheme of the 35 W reference system is illustrated in Figure 5.16. The in-loop detector was based on the transimpedance amplifier with high-current buffer in the feedback. The feedback resistance was 100 Ω. Downstream of the HP-PMC, two partly reflective mirrors were used to split off some light for two out-of-loop detectors. These detectors were also based on the transimpedance amplifier with high current buffer in the feedback but with a feedback resistance of 50 Ω.
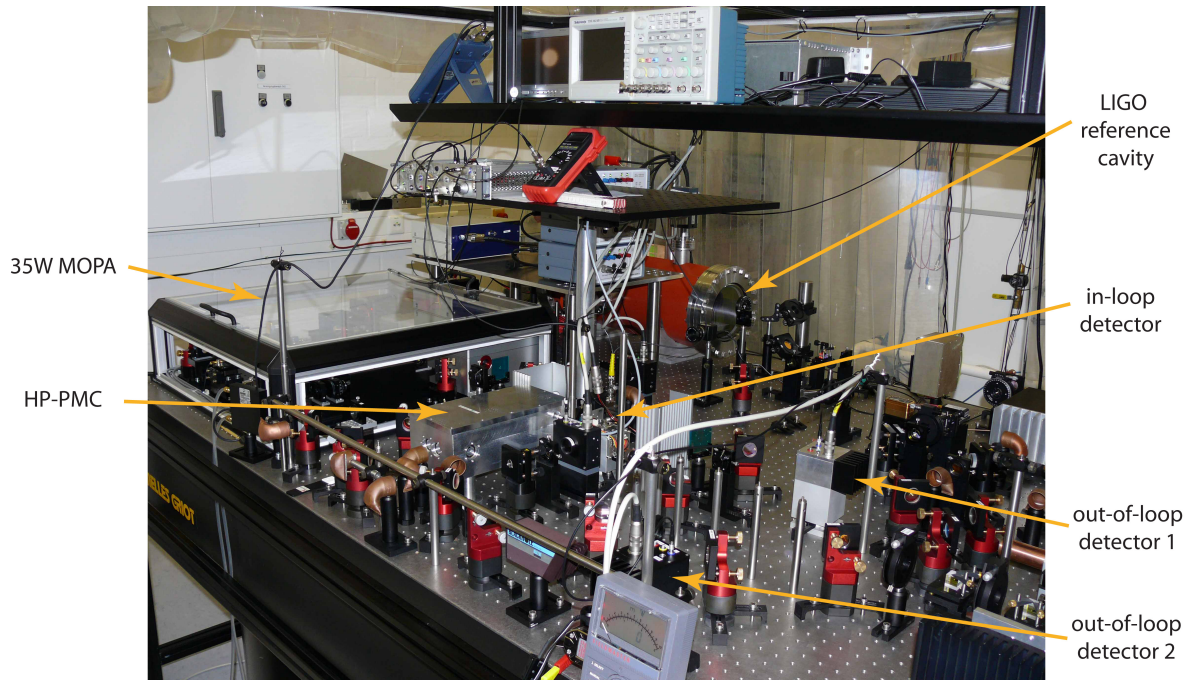
Figure 5.14: Photograph of the 35 W reference system. On the left the MOPA, behind it the LIGO reference-cavity in the vacuum tank.
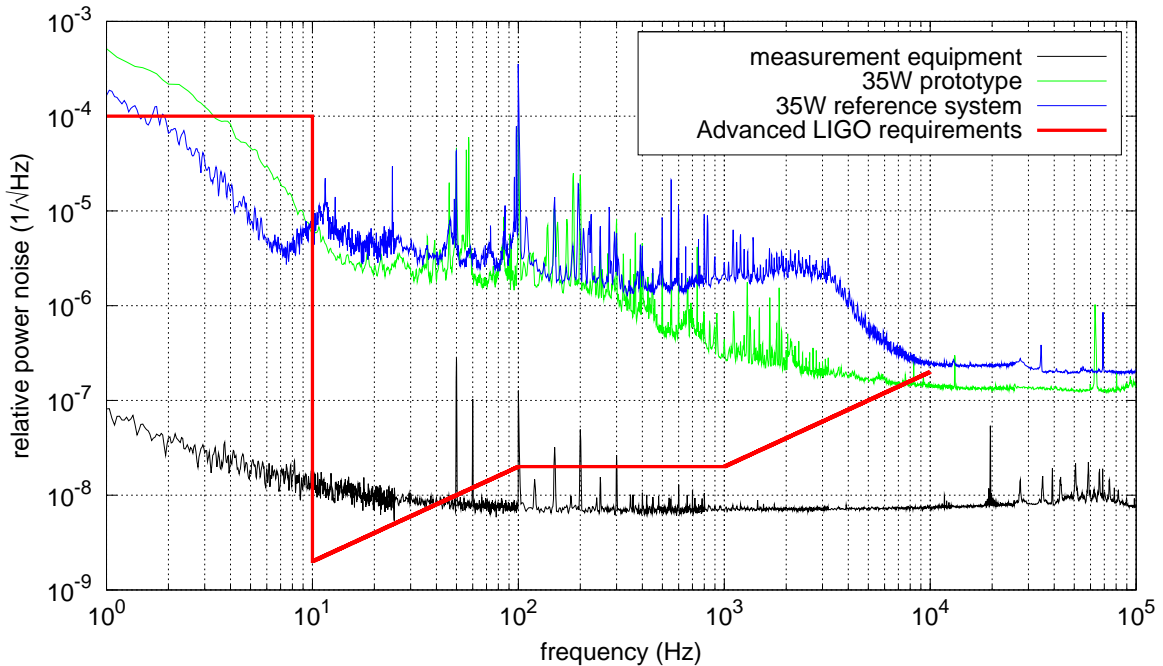
Figure 5.15: Relative power noise of the free-running MOPA system.

The signal obtained from the in-loop detector behind the curved mirror (20 ppm transmission) of the HP-PMC was compared to the reference voltage. The servo electronics is equivalent to the one used in the optimized power stabilization experiment, described in Section 3.2.2.

Figure 5.16: Power stabilization scheme of the 35 W reference system.

For driving the AOM, a fixed-frequency RF oscillator (80 MHz) with an amplitude-controlled power-amplifier (Landwehr Electronic, Q-Switch Driver A 274-18) and a high amplit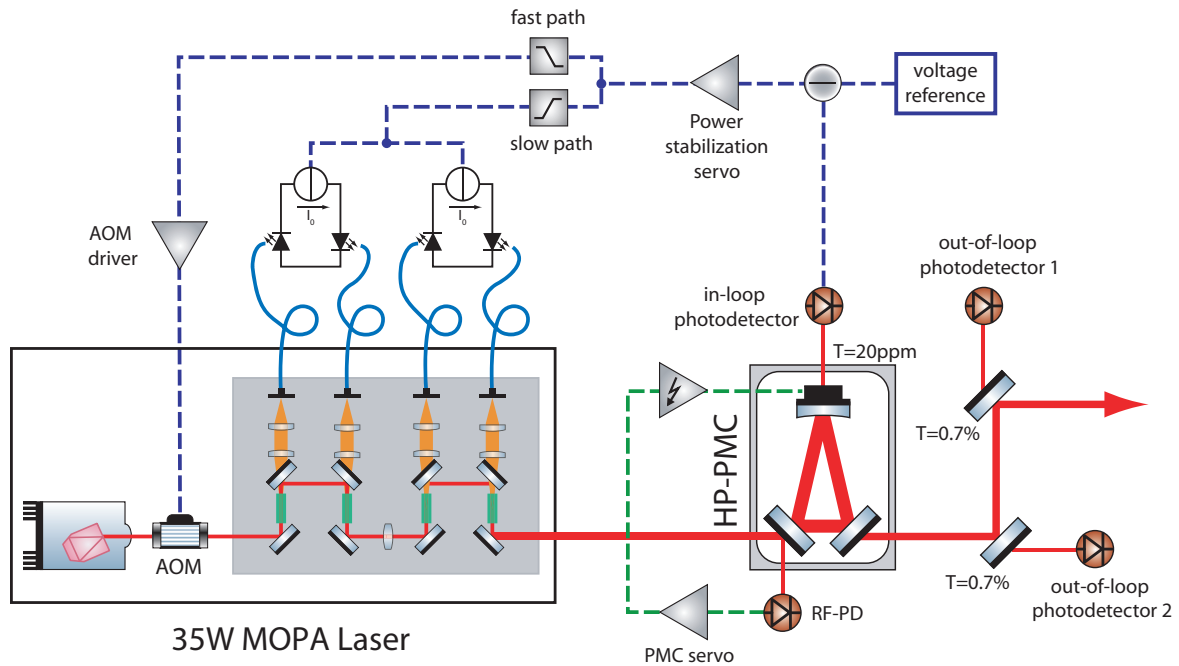ude modulation bandwidth was used. Figure 5.17 shows the measured overall transfer function from the analog input of the driver to the output of the MOPA. The delay of the internal AOM including the AOM driver introduces some additional phase shift at high frequencies as already explained in Section 3.2.2.

The frequency response measurement of the the HP-PMC in high-finesse mode is shown in Figure 5.18. The pole frequency of the HP-PMC has been measured to be 930 kHz and is thus well outside the intended bandwidth of the power stabilization loop. The nonlinear slope of the MOPA output power versus seed power can be assumed to be linear for seed powers larger than 1 W. This corresponds to an output power of the MOPA larger than 31 W. As the RF power is a quadratic function of the input voltage supplied to the modulation input, the diffracted power by the AOM, and hence the reduction in output power, is a quadratic function from input voltage of the RF-driver, too. Therefore the proportional gain of the AOM as an actuator changes with the RF offset power. This is important for loop stability when using a DC-coupled loop design. If the power level of the laser system changes and subsequently the RF-power-level, the loop gain can change by one order of magnitude or more. This has been taken into consideration and yields a high gain-margin requirement for the control loop which in turn reduces the effective bandwidth. The offset for the AOM driver input was set to 1.5 V, a compromise between the dynamic range of the modulator and the MOPA output power loss due to the reduction of the seed power. This corresponds to a MOPA power reduction of 1% and a NPRO power reduction of 13%.

To keep the operating point of the AOM constant and hence the loop bandwidth high, DC power fluctuations were compensated for with a slow feedback loop to the current of the pump diodes of the MOPA. The measured slopes and transfer functions for the reference system are
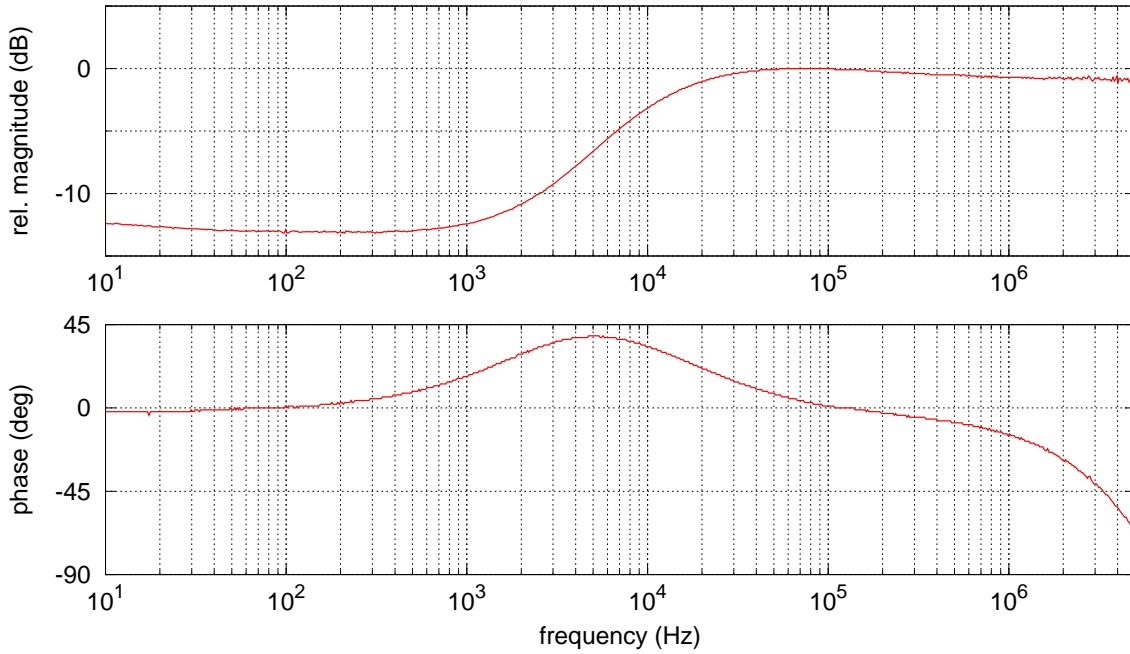
Figure 5.17: Measured relative transfer function from AOM driver input to amplifier output power variations.
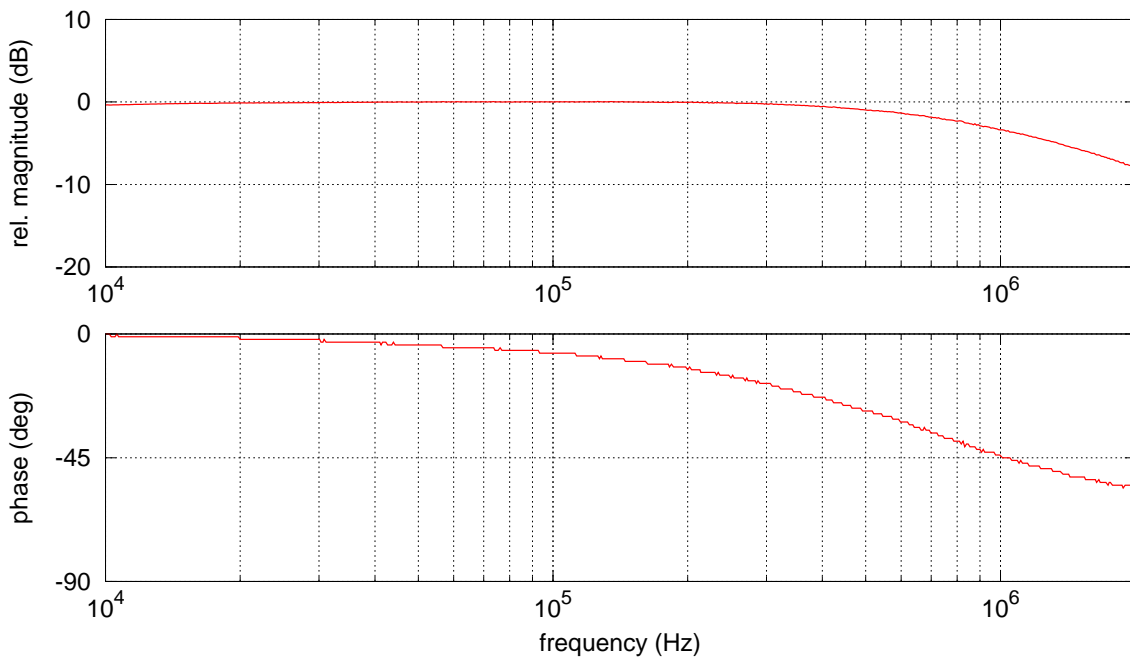

Figure 5.18: Measured transfer function of the HP-PMC in high-finesse mode.

similar to the one of the front-end of the functional prototype of the Advanced LIGO laser already shown in Section 5.2. The bandwidth of these inputs is about 1 Hz and is limited by

the time delay of the slow digital control system. Figure 5.19 shows a block diagram of the power stabilization servo.
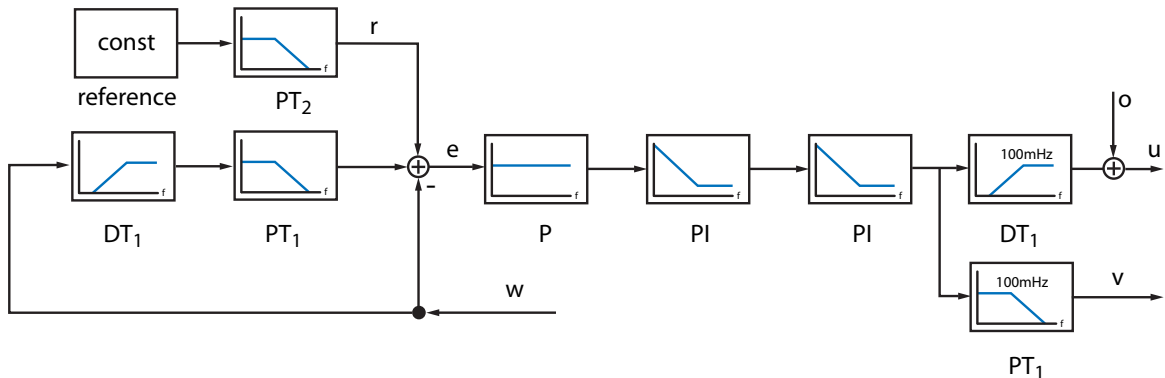

Figure 5.19: Block diagram of the power stabilization servo for the stabilization of the 35 W reference system.

The error-signal (e) was obtained by subtracting the in-loop photodetector signal (w) from the reference (r) with the additional AC-path (see Section 2.2.1). The error signal was then first amplified by an adjustable proportional gain stage, followed by two integrator stages which increased the amplification at low frequencies by more than 100 dB. Both integrators could be switched on or off independently from each other by using analog switches to investigate the noise performance as a function of loop gain (especially at low frequencies). As the cut-off frequency of the filter cavity is 930 kHz no differentiator is needed.

Lastly, a cross-over network consisting of two filter stages was used to split the output signal of the servo to the two different actuators, the current modulation input and the AOM. The cross-over frequency was set to 100 mHz. The low-pass filtered path (v) was connected to both current modulation inputs of the MOPA control boxes to modulate all four laser diodes keeping the changes in pump power for each head to a minimum. To set the AOM at its operating point, an offset (o) has to be applied to the driver to modulate around the nominal power value. This offset (1.5 V) was added inside the servo electronics box. The output signal (u) was injected into the RF-driver for the AOM to adjust the output power of the laser system.

5.4.3 Experimental results

Figure 5.20 shows the results for the power stabilization of the 35 W reference system. In contrast to the experiment discussed in Chapter 3 the power stabilization of the 35 W *reference system* was performed in air. A flow-box with HEPA-filters (High Efficiency Particulate Air) running at minimum speed was used to keep the complete setup on the optical table clean. The small airflow was a compromise between the need to reduce acoustic coupling to the system and a high particle count on the optical table. This is very important as even a single dust particle entering the beam can degrade the performance of the power stabilization.

The detection noise is again dominated by the combined dark noise of the photodetector and the input noise of the FFT analyzer (Stanford Research, SR785). To reduce the input noise of the FFT analyzer the same custom-made battery powered pre-amplifiers were used as before (see Chapter 3). The detection noise is comfortably far below the measured out-of-loop power noise level.
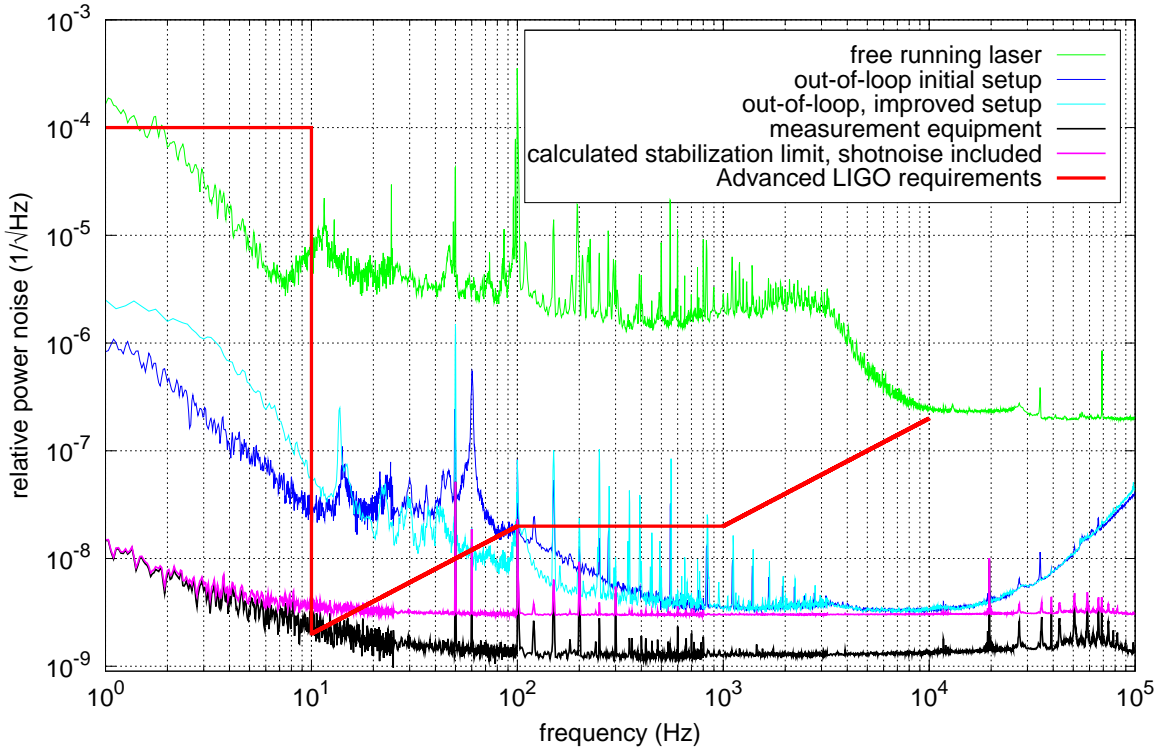
Figure 5.20: Relative power noise of the 35 W MOPA system. Two out-of-loop measurements are shown, one for the initial setup and one after reduction of scattered light without any other changes (see text).

As both out-of-loop detectors have shown equal performance of the system, only detector PD1 will be used in the following. The photocurrent of the in-loop detector was $i_{\mathrm{ph,IL}}$=58 mA and $i_{\mathrm{ph,OOL}}$=164 mA for the out-of-loop detector respectively. The in-loop power is limited to 78 mW by the transmission of the curved mirror of the HP-PMC, which will be even less in the final Advanced LIGO setup with the 200 W laser and the HP-PMC operating in p-polarization mode. As this detector is only to pre-stabilize the laser system close to the final requirements, this is acceptable.

Two out-of-loop measurements are shown, one for the initial setup and one after some improvements of the optical layout. For both measurements, above $\approx$1 kHz the out-of-loop performance is fundamentally limited by the uncorrelated sum of the shot noise on the in-loop and out-of-loop detector or by the loop gain. The independent shot noise for each photodetector is $\approx 2.35 \times 10^{-9}/\sqrt{\mathrm{Hz}}$ for the in-loop and $\approx 1.4 \times 10^{-9}/\sqrt{\mathrm{Hz}}$ for the out-of-loop detector respectively. Summing the shot noise from both photodetectors in quadrature gives a minimum out-of-loop measurement noise of $2.7 \times 10^{-9}/\sqrt{\mathrm{Hz}}$, which is dominated by the detected in-loop power. Additionally the electronic noise of the in-loop detector is imprinted on the light with the loop closed. The several sharp peaks that contaminate the spectra are due to line harmonics or switching power supplies. Further reduction of these peaks by better electronic design, wiring and better shielding is expected in the next design phase.

At low frequencies the out-of-loop noise performance deteriorates. The shape of the noise spectrum below 10 Hz can be explained by particles crossing the laser beam, even with HEPA-filtered air. Small peaks in the time signal due to particles crossing the beam path generate these

typical "shoulders", like a single Lorentzian spectrum, as it can be seen in the measurement for the improved setup below 10 Hz. The likelihood of such an event is further increased by the fact that a large number of averages, and hence long observation times, are required especially for the low-frequency region. The total measurement time is typically 20 min. For the final loop design one has to take care that the power drop for such an event can be compensated by the actuators of the inner loop. The rate of such events can be largely reduced when using beam tubes for the main beam path. This reduces the rate caused by particles falling through the beam but can increases the risk of particles inside the tube which soar up. This has to be tested during the next design phase.

For the high-power laser system, scattered light appears to be one of the largest contributors to the excess noise in the power stabilization. Extensive tests on scattered light showed that this is a major contributor to the out-of-loop performance below 1 kHz. Due to the high laser power, mirrors and windows scattered a large amount of light. By removing these windows and replacing all mirrors in the main, high-power beam path by super-polished low-loss mirrors, the out-of-loop performance of the system could be improved without any further additional changes (see "improved setup" in the graph). This shows that only highest quality optical components should be used for future experimentss in order to minimize these effects. Additional absorbing filters and blackened surfaces should be used to absorb stray beams wherever possible. As the complete detection took place in air, also a coupling of beam pointing into power noise could be observed. As the sensing for the outer stabilization loop for the Advanced LIGO laser will be in vacuum, this effect will be reduced.

The prototype of the "inner loop" for the 35 W reference system is within the specification for the Advanced LIGO laser system except for Fourier frequencies from 10 Hz to 60 Hz. As for the other experiments previously presented, the discrepancy between the theoretical and the observed out-of-loop performance could be reduced, but is still observable at low frequencies.

5.5 Conclusion

The functional prototype of the Advanced LIGO high-power laser consisting of a high-power oscillator stage phase-locked to a master oscillator power amplifier has demonstrated stable single-frequency operation with an output power of 180 W [178]. To achieve the high stability level of the laser system required by the gravitational wave detector, several active and passive stabilization techniques are required. The system has been characterized in detail and a concept for the stabilization in terms of spatial mode, frequency and power has been presented.

The control loops for laser frequency and power noise reduction will be divided into two parts, a so-called inner and outer stabilization loop. The inner loops include all control loops which are independent from the interferometer and are used to pre-stabilize the laser system close to the final specifications. The laser system including these stabilization loops is called the pre-stabilized laser system (PSL). The outer loops are then used to further improve the stability of laser system and to reduce noise introduced on the light on its path from the laser table to the main interferometer to the final specifications by means of additional references and sensors which are part of the gravitational wave detector.

A first prototype of a high-power pre-modecleaner for spatial filtering has been installed in the functional prototype of the Advanced LIGO high-power laser. After spatial filtering, more than 150 W of output power in TEM_{00}-mode could be measured. A second, identical pre-modecleaner has been installed in the so-called reference system of the 35 W front-end laser. This has been operated in the high-finesse where the circulating power in greater than that expected in the final configuration with a 200 W laser beam. The throughput was stable

over more than half a year of almost continuous operation and no thermal loading effects were observed.

To achieve the demanding power stability level required, low-noise techniques and several feedback control-loops are required. Several power actuators will be part of the high-power laser design, e.g. an AOM placed between the NPRO and the MOPA and an electronic summation point to change the current of the pump diodes of the high-power oscillator. So far, the peak-to-peak power fluctuations of the prototype of the high-power laser system over a time period of 10 minutes are approximately 14.5%. The noise of the NPRO as well as the noise of the 35 W amplifier stage is dominated by the fluctuations of the laser diode current. Both are well below the noise of the high-power oscillator stage. The sources for the additional noise of the high-power oscillator are not yet identified and are the subject of further investigations.

The internal power stabilization of the NPRO mainly reduces the laser relaxation oscillation. The photodetector for the inner power stabilization loop is planned to be located behind the HP-PMC. This control loop will feed back to different power actuators in the laser system. As the suspended modecleaner induces power fluctuations and thus raises the power noise at the input of the interferometer, power fluctuations are sensed by an additional photodetector downstream of the suspended modecleaner. The control signal of that loop will be added into the error point of the inner power stabilization loop in order to achieve the demanding power stability requirements.

Parts of the stabilization concept for the complete laser system have been tested using one of the 35 W laser amplifier systems, in order to verify as much of the Advanced LIGO power stabilization as possible before the 200 W laser becomes available. Comparing the overall out-of-loop performance of the power stabilization for the 35 W reference system with the requirements for the Advanced LIGO laser system, the prototype of the "inner loop" is within the specification except for Fourier frequencies from 10 Hz to 60 Hz. For the high-power laser system, scattered light appears to be one of the largest contributors to the excess noise in the power stabilization. This effect was smaller in the experiment in Chapter 3 where the control loop sensing was performed in a sealed environment. Based on these experiments conducted on the 35 W reference system, a first prototype power stabilization of the complete high-power laser system will be installed in the near future.

Conclusion

Next generation interferometric GWDs such as Advanced LIGO will have a much greater sensitivity and hence the effect of laser power fluctuations will be stronger than in currently operating GWDs. In this thesis, experimental investigation of the power stabilization of Nd:YAG laser systems to the power stability required for the Advanced LIGO GWD were carried out. Special attention was paid to identify and quantify different sources of technical noise which has limited the sensitivity of power stabilization experiments so far.

Chapter 3 dealt with the power stabilization of two different Nd:YAG laser systems, a GEO600-type high-power laser system [184] and a simpler system using an NPRO and a different power actuator with reduced cross-coupling into other laser observables. With extreme care in the design of the electronics and the simplified optical setup we were able to achieve a RPN level of better than $4 \cdot 10^{-9}/\sqrt{\text{Hz}}$ between $50\,\text{Hz}$ and $1.5\,\text{kHz}$ [141]. The Advanced LIGO requirements (see Figure 3.1) were met within the complete frequency band of interest, except for Fourier frequencies between $10\,\text{Hz}$ and $20\,\text{Hz}$. The results shown in Figure 3.33 represent, to the best of our knowledge, the lowest RPN levels published so far in this field. This measurement utilizing an independent photodiode not included in the control loop path, shows that the achieved noise level especially at low frequencies is worse than the in-loop measurement would suggest.

After reaching the previously unattained power stability with the optimized power stabilization experiment presented in Section 3.2, extensive investigations on noise sources affecting the performance of a laser power stabilization control loop, especially at low frequencies were performed. Chapter 4 described in detail the identification and characterization of noise sources affecting the power stabilization loop. Here noise sources like temperature fluctuations, the impact of scattered light and low-frequency excess noise in the electronics, as well as different laser observables within the stabilized laser system like the laser frequency frequency, the polarization or pointing of the laser beam were analyzed.

Sources like beam pointing in combination with photodiode non-uniformities or temperature fluctuations are not limiting the power stabilization so far, but are within a factor of 4–5 of the design requirements. However, low-frequency excess noise in commercial available large area InGaAs photodiodes and current noise in resistors could be identified to be the major contributors to the out-of-loop noise performance of the stabilization experiments conducted in this thesis. Both types of noise depend on the current drawn. This is a very important result of this thesis as the noise contribution of photodetectors to precision optical experiments was so far always estimated by measurements of the noise without light on the photodetector. Experiments are underway to test more, preselected resistors and large area InGaAs photodiodes for their $1/f$ noise to design photodetector with even less intrinsic noise than the ones used in this thesis.

Chapter 5 addressed the description, characterization and stabilization of a 200 W laser system designed for use in the Advanced LIGO GWDs. The laser system for Advanced LIGO

consists of two diode-pumped Nd:YAG lasers in a master-slave configuration with an output power of 200 W built by the Laser Zentrum Hannover [178]. The design of the 200 W high-power laser system was described in detail. In order to develop the power stabilization, a detailed characterization of the laser system was done and a concept for the power stabilization of the Advanced LIGO 200 W laser system was introduced. As the 200 W laser system is still under fabrication a stabilization of the full system was not possible. Hence parts of the proposed stabilization concept were conducted on a 35 W master-oscillator power-amplifier (MOPA) system. The stabilization of the MOPA and its results were presented.

In conclusion, the power stabilization experiments on a Nd:YAG laser system carried out in this thesis have achieved a superior stability and the requirements for the Advanced LIGO laser system were met except for Fourier frequencies between 10 Hz and 20 Hz. Detailed investigations of a number of effects that can be the source of additional noise in the sensing of the laser power fluctuations have been performed and the major noise contributions to the stabilization experiments performed in this thesis could be identified. A new power stabilization experiment which is currently conducted in our group shows that careful consideration of the major sources identified in this thesis lowers the excess noise at low frequencies such that even lower relative power noise levels than measured in this thesis should be achievable in the near future.

Low-frequency noise

Noise in the present context is the random and unpredictable fluctuation of a deterministic signal inherent to the process which is under investigation. The wanted signal becomes difficult to distinguish from the background noise when the noise power is significant in relation to the signal power.

But noise is not always unwanted. Also, noise is a measurable effect of several physical phenomena and thus can carry information about them. Because of this property, investigations on noise can be a very powerful tool for the characterization of electronic devices particularly in reliability and diagnostic fields [166].

The total measured noise is made up of contributions from several individual noise mechanisms like thermal noise, shot-noise and others. If the noise measurements are above that predicted by thermal noise and shot-noise, then the additional noise contribution is called excess noise. Excess noise has been theorized to come from different mechanisms. It comes in many forms including generation-recombination (G-R) noise, random-telegraph signal (RTS) noise or flicker noise ($1/f$ or $1/f$-like), which are the most important noise sources in the low frequency region and discussed in the following.

A.1 Generation-recombination noise

Generation-recombination (G-R) fluctuations are due to the random generation and recombination of free charge-carriers in semiconductors. Free carriers, donors or acceptors, occasionally trap a passing carrier. The thermal energy of the crystal lattice will free the trapped carrier again after a short time. Each event causes fluctuation in the number of free carriers thereby causing fluctuations in the number of carriers available for current transport and hence leading to a fluctuation in the material resistance. If a DC-current is passing through a material, a fluctuating voltage related to the fluctuating resistance will appear across the device. Therefore generation-recombination noise is a function of current. G-R noise does not show discrete detectable pulse signals in the time domain.

The characteristics of G-R noise is defined by parameters of the semiconductors, e.g. carrier concentration, capture cross sections for electrons and holes, relaxation times and energy differences of different energy levels and so the G-R process is a natural part of all semiconductor behavior. Because of this, investigations on G-R noise make it possible to analyze these parameters and to use it as a diagnostic tool to detect defects in semiconductor materials and devices [72, 90, 166].

The spectrum of a G-R event with a single time constant τ can be expressed in the form of

$$S_{\mathrm{L}}(f) = A \frac{\tau}{1 + ((2\pi f)^2 \tau^2)} \tag{A.1}$$

where A is a factor for the DC-term that depends on the particular system modeled [104]. This spectral density has a single time constant τ and is called a Lorentzian characteristic.

The frequency response is constant at low frequencies with a corner at a frequency $f_c = 1/2\pi\tau$. Above this corner frequency the slope is proportional to $1/f^2$.

A.2 Random-telegraph signal noise

A special case of G-R noise is random-telegraph signal (RTS) noise, often also called popcorn noise or burst noise. RTS-noise appears as discrete amplitude pulses of randomly varying width and repetition rate in a time series. RTS-noise can be described by a random switch model developed by Machlup [104]. It is often observable in semiconductors and caused by metallic impurities during fabrication process of the semiconductor or a doping process. The rate of the pulses can vary from some pulses per hour to several per second. The RTS-noise process is characterized by the mean values of the pulse height and the time durations (time constants). The power spectral densities (PSD) for the RTS-noise and the G-R noise are both of the Lorentzian type.

A.3 $1/f$-noise

$1/f$-noise, also known as flicker noise or pink noise, has been found in many systems. The observed power spectra are ordinarily of the form $S(f) = constant \times f^{-\alpha}$ ($0.5 < \alpha < 1.5$). Often noise spectra are plotted as linear spectral densities (LSD) instead of power spectral densities and thus $1/f$-noise appears as $1/\sqrt{f}$. Low-frequency fluctuation phenomena are not unique to electronic systems and devices. It is also observed in physics, biology, astrophysics, geophysics, etc., such as in angular velocity of the earth rotation, flow rate of the Nile over the past 2000 years, highway traffic or human heart beat [59]. Its exact physical origins are still unclear.

$1/f$-noise in physical or electronic systems is very important because the noise directly effects the device and system performance. Hence low-frequency noise has become a hot research topic and it was believed that there exists a common origin of different systems. For electronic devices, it is much easier to produce a large number of samples with different noise behaviors via different fabrication processes or measurement conditions achieved by e.g. different stress, bias or temperature. A large number of experiments on electronic devices were completed over the last decades, but no common-origin of the $1/f$-noise was found.

Various mathematical models exist on the generation of the flicker noise spectrum. Even the most promising models like the ones by Hooge [69], McWhorter [108], Voss and Clarke [171] and Handel [59] can only be applied to specific systems or devices [181]. There is neither a theoretical nor experimental reason why a universal equation should exist.

A.3.1 Hooge's phenomenological equation

Hooge carried out a number of experiments in metal films and found that the noise in metal film conductors can be characterized by the empirical formula

$$\frac{S(f)}{V^2} = \frac{\alpha_H}{N f} \tag{A.2}$$

where V is the voltage applied to the device under test, α_H a dimensionless constant with a value of about 2×10^{-3} and N the number of charge carriers in the conductor [69]. Since Equation A.2 is independent of material parameters or environmental parameters like temperature, it is a universal equation. Today it is clear that α_H is not constant. Its value varies from 10^{-2}

to 10^{-9}. Soon it was found that this model is very restrictive and so the relation was modified in order to be applicable to more experiments.

In 1981 Hooge *et al.* discovered that $1/f$-noise is often caused by mobility fluctuations rather than by fluctuations of the number of charge carriers [71]. As a result the formula was modified to

$$\frac{S(f)}{V^2} = \frac{\mu}{\mu_{\mathrm{ph}}} \frac{\alpha_{\mathrm{H}}}{N f} \tag{A.3}$$

where now μ is the total mobility and μ_{ph} is the mobility due to lattice-scattering only (electron-phonon scattering).

Still Hooge's relation is an empirical formula not based on real physical mechanisms and parameters. In addition, the spectral slope is directly proportional to $1/f$ for all frequencies and so the noise power will be infinite at low frequencies. Nevertheless, the Hooge model has been successful in explaining the $1/f$-noise in metals and bulk semiconductors.

A.3.2 McWhorter's number fluctuations model

$1/f$-noise has been considered to be connected mainly with G-R processes (Section A.1) at the surface. If several G-R traps are sufficiently close in energy, they resemble a $1/f$-spectrum. McWhorter developed a low-frequency noise model based on the carriers' number fluctuation due to trapping and detrapping of charge carriers. It has remained the most acceptable basis for $1/f$-noise in silicon-oxide interfaces so far (MOS technology). Each trapping process has a characteristic time constant τ_{i} which results in a Lorentzian spectrum [104]. According to McWhorter [108], a $1/f$-spectrum is given by the superposition of Lorentzian spectra with time constant τ as

$$S(f) = \int_{\tau_1}^{\tau_2} \frac{1}{\tau} \frac{\tau}{1 + (\omega\tau)^2} \, d\tau \tag{A.4}$$

$$= \frac{1}{\omega} \left[\tan^{-1}(\omega\tau_2) - \tan^{-1}(\omega\tau_1) \right] \tag{A.5}$$

which is proportional to $1/f$ within the frequency range $1/\tau_1 < \omega < 1/\tau_2$ and with τ_1 and τ_2 the smallest and largest time constants of the system. Equation A.5 produces a $1/f$-spectrum for an infinite number of independent Lorentzian spectra with a continuous distribution of the time constant τ between τ_1 and τ_2. McWhorter's model has a different noise spectrum compared with Hooge's one, as given in Equations A.2 or A.3. At extremely low frequencies, the noise level is equal to a constant and does not depend on the frequency, which is a problem using Hooge's relation. Figure A.1 illustrates the difference between Hooge's relation and McWhorter's relation.
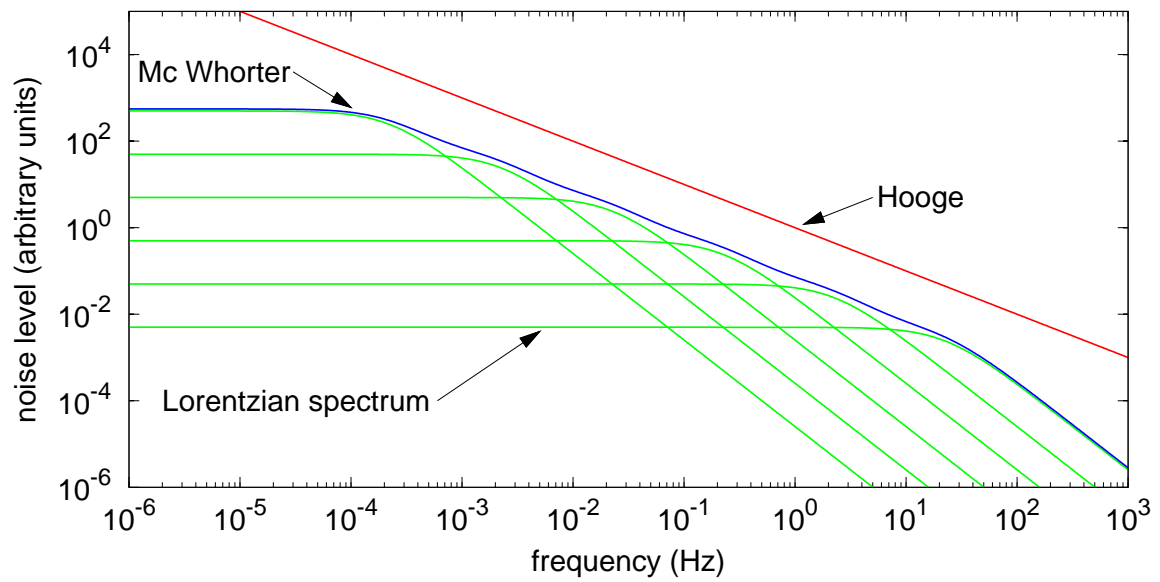
Figure A.1: Comparison of Hooge's relation and McWhorter's model for $1/f$-noise.

Photodiode thermal resistance

The experimental setup to measure the increase in photodiode temperature under illumination via the diode forward voltage has already been explained in Section 4.1.1. In order to calibrate the measured change in forward voltage of the individual devices, the temperature coefficient of the diode forward voltage $K = \frac{\delta V_J}{dT}$ has been determined. The device under test (DUT) is operated with a low constant current in forward direction I_F using a current regulating diode (J505, $1\,\mathrm{mA}$). At low values of forward current I_F, the junction voltage V_J is nearly linear to the junction temperature T_J. The forward voltage drop of the DUT was measured while slowly changing its temperature δT_J from 15° to 40°. The results are summarized in Table B.1.

manufacturer	model	V_J (20°C)	δV_J
Perkin Elmer	C30642G sn:0934	$413\,\mathrm{mV}$	$-1.636\,\mathrm{mV/K}$
Perkin Elmer	C30655G sn:4040	$403\,\mathrm{mV}$	$-1.679\,\mathrm{mV/K}$
FCI	InGaAs-3000 sn:1	$486\,\mathrm{mV}$	$-3.949\,\mathrm{mV/K}$
Judson	J22-5I-R02M-1.7 lot:99599	$402\,\mathrm{mV}$	$-1.665\,\mathrm{mV/K}$
Anadigics	PD2M sn:1	$434\,\mathrm{mV}$	$-1.597\,\mathrm{mV/K}$
Anadigics	PD3M sn:52	$378\,\mathrm{mV}$	$-1.747\,\mathrm{mV/K}$
Germanium Power Devices (GPD)	GAP2000 sn:1	$407\,\mathrm{mV}$	$-1.61\,\mathrm{mV/K}$
Epigap	EPC-1300-3.0 sn:1	$529\,\mathrm{mV}$	$-2.355\,\mathrm{mV/K}$
Epitaxx	ETX2000 sn:0635F6306	$423\,\mathrm{mV}$	$-1.524\,\mathrm{mV/K}$
Epitaxx	ETX3000 sn:0620F5798	$485\,\mathrm{mV}$	$-2.022\,\mathrm{mV/K}$
Hamamatsu	G8370-02 sn:1	$529\,\mathrm{mV}$	$-4.708\,\mathrm{mV/K}$
Hamamatsu	G8370-03 sn:1	$384\,\mathrm{mV}$	$-1.789\,\mathrm{mV/K}$

Table B.1: Temperature coefficient of photodiode forward junction voltage V_J.

The time resolved temperature increase of the chip was measured for 13 different types of large area InGaAs photodiodes. The results are illustrated in Figure B.1.

The junction-to-case thermal resistance of the photodiodes have been calculated from the temperature increase and the total power dissipated in the device. The results for the measured junction-to-case thermal resistance are summarized in Table B.2.
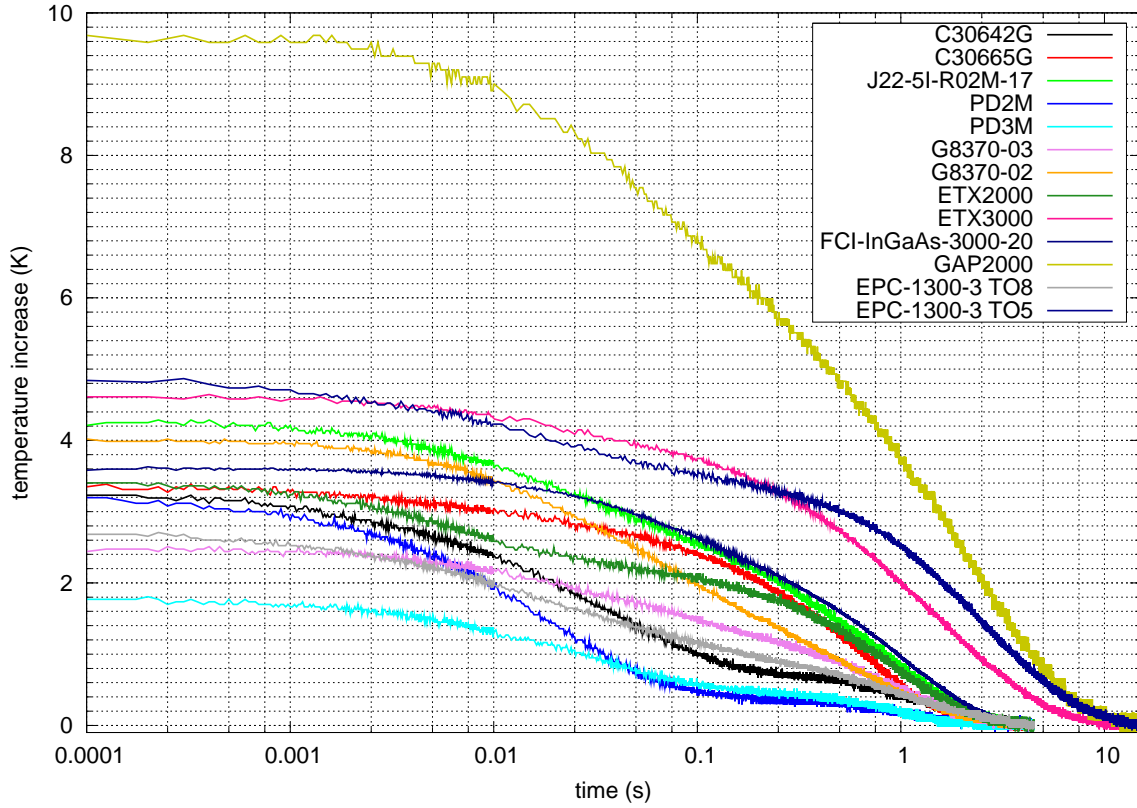
Figure B.1: Measured time resolved photodiode junction-temperatures.

manufacturer	model	R_{th}
Perkin Elmer	C30642G	10.1 K/W
Perkin Elmer	C30655G	10.5 K/W
FCI	InGaAs-3000	10.9 K/W
Judson	J22-5I-R02M-1.7	13.4 K/W
Anadigics	PD2M	8.3 K/W
Anadigics	PD3M	4.5 K/W
Germanium Power Devices (GPD)	GAP2000	30.4 K/W
Epigap	EPC-1300-3.0 TO5	14.2 K/W
Epigap	EPC-1300-3.0 TO8	7.9 K/W
Epitaxx	ETX2000	10.4 K/W
Epitaxx	ETX3000	14.2 K/W
Hamamatsu	G8370-02	12.3 K/W
Hamamatsu	G8370-03	7.7 K/W

Table B.2: Measured junction-to-case thermal resistance for different photodiodes.

Bibliography

[1] R. S. Abbott and P. J. King. Diode-pumped Nd:YAG laser intensity noise suppression using a current shunt. *Review of Scientific Instruments*, 72(2):1346–1349, 2001.

[2] A. Abramovici, W. E. Althouse, R. W. P. Drever, Y. Gursel, S. Kawamura, F. J. Raab, D. Shoemaker, L. Sievers, R. E. Spero, K. S. Thorne, R. E. Vogt, R. Weiss, S. E. Whitcomb, and M. E. Zucker. LIGO: The Laser Interferometer Gravitational-Wave Observatory. *Science*, 256(5055):325–333, 1992.

[3] R. Adhikari. *Sensitivity and noise analysis of 4 km laser interfermetric gravitational wave antennae*. PhD thesis, Massachusetts Institute of Technology, 2004.

[4] R. Adhikari. Enhanced LIGO. In *AAS/High Energy Astrophysics Division*, volume 9 of *AAS/High Energy Astrophysics Division*, pages 21.03–+, September 2006.

[5] R. Adhikari, P. Fritschel, and S. Waldman. Enhanced LIGO. Technical Report LIGO-T060156-01-I, LIGO Laboratory / LIGO Scientific Collaboration, 2006.

[6] Advanced LIGO Team. Advanced LIGO Reference Design - LIGO-M060056-10-M. Technical report, LIGO Laboratory / LIGO Scientific Collaboration, 2007.

[7] M. Ando, K. Arai, R. Takahashi, G. Heinzel, S. Kawamura, D. Tatsumi, N. Kanda, H. Tagoshi, A. Araya, H. Asada, Y. Aso, M. A. Barton, M.-K. Fujimoto, M. Fukushima, T. Futamase, K. Hayama, G. Horikoshi, H. Ishizuka, N. Kamikubota, K. Kawabe, N. Kawashima, Y. Kobayashi, Y. Kojima, K. Kondo, Y. Kozai, K. Kuroda, and N. Matsuda. Stable Operation of a 300-m Laser Interferometer with Sufficient Sensitivity to Detect Gravitational-Wave Events within Our Galaxy. *Phys. Rev. Lett.*, 86(18):3950–3954, April 2001.

[8] P. Aufmuth and K. Danzmann. Gravitational wave detectors. *New Journal of Physics*, 7:202–+, September 2005.

[9] B. Willke and the GEO 600 Team. The GEO 600 gravitational wave detector. *Classical and Quantum Gravity*, 19(7):1377–1387, 2002.

[10] B. Willke and the GEO 600 Team. The GEO-HF project. *Classical and Quantum Gravity*, 23(8):S207–S214, 2006.

[11] B. W. Barr, K. A. Strain, and C. J. Killow. Laser amplitude stabilization for advanced interferometric gravitational wave detectors. *Classical and Quantum Gravity*, 22(20):4279–4283, 2005.

[12] H. Billing, K. Maischberger, A. Rüdiger, R. Schilling, L. Schnupp, and W. Winkler. The Munich Gravitational Wave Detector Using Laser Interferometry. In P. Meystre and M. O. Scully, editors, *Quantum Optics, Experimental Gravity, and Measurement Theory*, volume 94 of *NATO Advanced Study Institute, Series B: Physics*, pages 525–566. Plenum Press, 1983. In *Bad Windsheim 1981, Proceedings, Quantum Optics, Experimental Gravity and Measurement Theory*, 525-566.

[13] A. Bittar and M. G. White. High-resolution spatial uniformity of surface reflectance and response of silicon photodiodes. volume 1712, pages 121–131. SPIE, 1993.

[14] E. D. Black. An introduction to Pound-Drever-Hall laser frequency stabilization. *American Journal of Physics*, 69:79–87, January 2001.

[15] E. D. Black, A. Villar, K. Barbary, A. Bushmaker, J. Heefner, S. Kawamura, F. Kawazoe, L. Matone, S. Meidt, S. R. Rao, K. Schulz, M. Zhang, and K. G. Libbrecht. Direct observation of broadband coating thermal noise in a suspended interferometer. *Physics Letters A*, 328(1):1–5, July 2004.

[16] A. Blaum, O. Pilloud, G. Scalea, J. Victory, and F. Sischka. A new robust on-wafer $1/f$ noise measurement and characterization system. *Microelectronic Test Structures, 2001. ICMTS 2001. Proceedings of the 2001 International Conference on*, pages 125–130, 2001.

[17] V. B. Braginsky, M. L. Gorodetsky, and S. P. Vyatchanin. Thermo-refractive noise in gravitational wave antennae. *Physics Letters A*, 271(5-6):303–307, July 2000.

[18] V. B. Braginsky and S. P. Vyatchanin. Thermodynamical fluctuations in optical mirror coatings. *Physics Letters A*, 312(3-4):244–255, June 2003.

[19] G. Breitenbach, S. Schiller, and J. Mlynek. Measurement of the quantum states of squeezed light. *Nature*, 387(6632):471–475, May 1997.

[20] James J. Brophy and Robert J. Robinson. Fluctuations in CdS due to shallow traps. *Phys. Rev.*, 117(3):738–739, February 1960.

[21] O. S. Brozek. *Frequenzstabilisierung eines Nd:YAG-Hochleistungs-Laser-Systems für den Gravitationswellendetektor GEO600*. PhD thesis, University of Hannover, 1999.

[22] F. Buchali, R. Behrendt, and G. Heymann. InGaAs/InP-photodiodes with dark current limited by generation-recombination. *Electronics Letters*, 27(3):235–237, January 1991.

[23] B. C. Buchler, E. H. Huntington, C. C. Harb, and T. C. Ralph. Feedback control of laser intensity noise. *Phys. Rev. A*, 57:1286–1294, February 1998.

[24] C. J. Buczek, R. J. Freiberg, and M. L. Skolnick. Laser injection locking. *Proceedings of the IEEE*, 61(10):1411–1431, October 1973.

[25] R. E. Burgess. RESEARCH NOTES: Low Frequency Noise in Illuminated Germanium Diodes. *Proceedings of the Physical Society B*, 68:569–571, August 1955.

[26] J. Campos, A. Corrons, and A. Pons. Response uniformity of silicon photodiodes. *Applied Optics*, 27:5154–5156, December 1988.

[27] T. M. Chen, S. F. Su, and D. Smith. $1/f$ Noise in Ru-Based Thick-Film Resistors. *Solid-State Electronics*, 25(8):821–827, 1982.

[28] Eugenio Coccia. Cryogenic gravitational wave detectors. *Physica B: Condensed Matter*, 280(1-4):525–531, May 2000.

[29] Jr. Conrad, G., N. Newman, and A. Stansbury. A Recommended Standard Resistor-Noise Test System. *Component Parts, IRE Transactions on*, 7(3):71–88, September 1960.

[30] D. C. Coyne. The laser interferometer gravitational-wave observatory (LIGO) project. *Aerospace Applications Conference, 1996. Proceedings., 1996 IEEE*, 4:31–61 vol.4, February 1996.

[31] D. R. M. Crooks, G. Cagnoli, M. M. Fejer, A. Gretarsson, G. Harry, J. Hough, N. Nakagawa, S. Penn, R. Route, S. Rowan, and P. H. Sneddon. Experimental measurements of coating mechanical loss factors. *Classical and Quantum Gravity*, 21(5):S1059–S1065, 2004.

[32] G. De Mey. Comments on "An exact formula for the effects of resistor geometry on current noise". *Electron Devices, IEEE Transactions on*, 34(8):1838–1838, August 1987.

[33] A. de Waard, L. Gottardi, J. van Houwelingen, A. Shumack, and G. Frossati. Minigrail, the first spherical detector. *Classical and Quantum Gravity*, 20(10):S143–S151, 2003.

[34] S. Demolder, A. Vancalster, and M. Vandendriessche. The measuring of $1/f$ noise of thick and thin-film resistors. *Journal Of Physics E-Scientific Instruments*, 13(12):1323–1327, 1980.

[35] R. J. Deri and R. Welter. Effect of capacitative imbalance on common-mode rejection of balanced photodetector pairs. *Electronics Letters*, 29(1):75–77, 1993.

[36] L. Dobrzanski and W. Strupinski. On charge transport and low-frequency noise in the GaN p-i-n diode. *Quantum Electronics, IEEE Journal of*, 43(2):188–195, February 2007.

[37] Silvano Donati. *Photodetectors*. Prentice Hall, 2000.

[38] R. Drever. Gravitational radiation. page 321, Amsterdam, Netherlands; New York, U.S.A., 1983. North-Holland; Elsevier.

[39] R. W. P. Drever, J. L. Hall, F. V. Kowalski, J. Hough, G. M. Ford, A. J. Munley, and H. Ward. Laser phase and frequency stabilization using an optical resonator. *Applied Physics B: Lasers and Optics*, 31(2):97–105, June 1983.

[40] M. Durak. Spatial non-uniformity analyses of radiometric detectors to identify suited transfer standards for optical radiometry. *European Physical Journal Applied Physics*, 32:193–197, December 2005.

[41] M. Durak, F. Samadov, and A. K. Türkolu. Spatial Non-uniformity Measurements of Large Area Silicon Photodiodes. *Turkish Journal of Physics*, 26:375–380, September 2002.

[42] A. Einstein. Die Grundlage der allgemeinen Relativitätstheorie. *Annalen der Physik*, 49:769–822, 1916.

[43] F. Acernese et al. The present status of the VIRGO Central Interferometer. *Classical and Quantum Gravity*, 19(7):1421–1428, 2002.

[44] D. M. Fleetwood, T. Postel, and N. Giordano. Temperature dependence of the $1/f$ noise of carbon resistors. *Journal of Applied Physics*, 56(11):3256–3260, 1984.

[45] S. R. Forrest, R. F. Leheny, R. E. Nahory, and M. A. Pollack. In$_{0.53}$Ga$_{0.47}$As photodiodes with dark current limited by generation-recombination and tunneling. *Applied Physics Letters*, 37:322–+, August 1980.

[46] M. Frede, B. Schulz, R. Wilhelm, P. Kwee, F. Seifert, B. Willke, and D. Kracht. Fundamental mode, single-frequency laser amplifier for gravitational wave detectors. *Optics Express*, 15(2):459–465, January 2007.

[47] M. Frede, R. Wilheim, M. Brendel, C. Fallnich, F. Seifert, B. Willke, and K. Danzmann. High power fundamental mode Nd:YAG laser with efficient birefringence compensation. *Optics Express*, 12(15):3581–3589, 2004.

[48] I. Freitag. *Entwicklung und Charakterisierung einer Laserstrahlquelle für den inter-ferometrischen Nachweis von Gravitationswellen.* PhD thesis, University of Hannover, 1994.

[49] P. Fritschel. The Second Generation LIGO Interferometers. In J. M. Centrella, editor, *Astrophysical Sources for Ground-Based Gravitational Wave Detectors*, volume 575 of *American Institute of Physics Conference Series*, pages 15–+, 2001.

[50] B. Fröhlich, T. Lahaye, B. Kaltenhäuser, H. Kübler, S. Müller, T. Koch, M. Fattori, and T. Pfau. Two-frequency acousto-optic modulator driver to improve the beam pointing stability during intensity ramps. *Review of Scientific Instruments*, 78(4):043101–+, April 2007.

[51] H. Ghadamabadi, J.J. Whalen, R. Coslick, C. Hung, T. Johnson, W. Sitzman, and J. Stevens. Comparison of demodulation RFI in inverting operational amplifier circuits of the same gain with different input and feedback resistor values. *Electromagnetic Compatibility, 1990. Symposium Record., 1990 IEEE International Symposium on*, pages 145–152, August 1990.

[52] H. Gong, L. M. Hanssen, and G. P. Eppeldauer. Spatial and angular responsivity measurements of photoconductive HgCdTe LWIR radiometers. *Metrologia*, 41(3):161–166, 2004.

[53] GPD Optoelectronics Corp. Large Area InGaAs Photodiodes, April 2003.

[54] GPD Optoelectronics Corp. Germanium Photodetectors, February 2005.

[55] S. Graffi, G. Masetti, and A. Piovaccari. Criteria to reduce failures induced from conveyed electromagnetic interferences on CMOS operational amplifiers. *Microelectronics and Reliability*, 37(1):95–113, January 1997.

[56] Hamamatsu Photonics K.K. InGaAs PIN photodiode G8605 series – Datasheet, 2001.

[57] Hamamatsu Photonics K.K. InGaAs PIN photodiode G8370 series – Datasheet, 2006.

[58] Hamamatsu Photonics K.K. Si PIN photodiode S1223 series – Datasheet, 2006.

[59] Peter H. Handel. Quantum approach to $1/f$ noise. *Phys. Rev. A*, 22(2):745–757, August 1980.

[60] Charles C. Harb, Timothy C. Ralph, Elanor H. Huntington, Ingo Freitag, David E. McClelland, and Hans-A. Bachor. Intensity-noise properties of injection-locked lasers. *Phys. Rev. A*, 54(5):4370–4382, Nov 1996.

[61] Charles C. Harb, Timothy C. Ralph, Elanor H. Huntington, David E. McClelland, Hans-A. Bachor, and Ingo Freitag. Intensity-noise dependence of Nd:YAG lasers on their diode-laser pump source. *Journal of the Optical Society of America B Optical Physics*, 14(11):2936–2945, 1997.

[62] Gregory M. Harry, Helena Armandula, Eric Black, D. R. M. Crooks, Gianpietro Cagnoli, Jim Hough, Peter Murray, Stuart Reid, Sheila Rowan, Peter Sneddon, Martin M. Fejer, Roger Route, and Steven D. Penn. Thermal noise from optical coatings in gravitational wave detectors. *Applied Optics*, 45(7):1569–1574, 2006.

[63] S. Hava. Comparisons of vacuum surface effects on commercial photodiodes: spatial response uniformity via a computerized laser scanning system. *Applied Optics*, 26:121–126, January 1987.

[64] R. J. Hawkins and G. G. Bloodworth. Measurements of low-frequency noise in thick film resistors. *Thin Solid Films*, 8(3):193–197, September 1971.

[65] L. He, Y. Lin, A. D. van Rheenen, A. van der Ziel, A. Young, and J. P. van der Ziel. Low-frequency noise in small InGaAs/InP p-i-n diodes under different bias and illumination conditions. *Journal of Applied Physics*, 68:5200–5204, November 1990.

[66] P. Hello and J. Y. Vinet. Noise induced by laser power fluctuations via absorption asymmetry in gravitational-wave interferometric detectors. *Physics Letters A*, 230(1-2):12–18, June 1997.

[67] M. Heurs, V. M. Quetschke, B. Willke, K. Danzmann, and I. Freitag. Simultaneously suppressing frequency and intensity noise in a Nd:YAG nonplanar ring oscillator by means of the current-lock technique. *Optics Letters*, 29:2148–2150, September 2004.

[68] M. Hinnrichs, R. DeWames, J. Bajaj, and G. Williams. Light-induced persistence of leakage current and low frequency noise in reverse biased backside-illuminated $Hg_{1-x}Cd_xTe$ photodiodes. *Electron Devices Meeting, 1985 International*, 31:125–128, 1985.

[69] F. N. Hooge. $1/f$ noise is no surface effect. *Physics Letters A*, 29(3):139–140, April 1969.

[70] F. N. Hooge. $1/f$ noise sources. *Electron Devices, IEEE Transactions on*, 41(11):1926–1935, November 1994.

[71] F. N. Hooge, T. G. M. Kleinpenning, and L. K. J. Vandamme. Experimental studies on $1/f$ noise. *Reports on Progress in Physics*, 44(5):479–532, 1981.

[72] Guijun Hu, Yadong Sun, Hongmei Zhang, Jing Li, Yingxue Shi, and Jiawei Shi. Correlation between the g-r noise in semiconductor lasers and device reliability. *Materials, Active Devices, and Optical Amplifiers*, 5280(1):229–232, 2004.

[73] Scott A. Hughes, Szabolcs Marka, Peter L. Bender, and Craig J. Hogan. New physics and astronomy with the new gravitational-wave observatories. *ECONF C*, 010630:402, 2001.

[74] Scott A. Hughes and Kip S. Thorne. Seismic gravity-gradient noise in interferometric gravitational-wave detectors. *Phys. Rev. D*, 58(12):122002, November 1998.

[75] IEC. Method of measurement of current noise generated in fixed resistors, 1965.

[76] M. S. Islam, A. Nespola, M. Yeahia, M. C. Wu, D. L. Sivco, and A. Y. Cho. Correlation between the failure mechanism and dark currents of high power photodetectors. *Lasers and Electro-Optics Society 2000 Annual Meeting. LEOS 2000. 13th Annual Meeting. IEEE*, 1:82–83, 2000.

[77] P. V. V. Jayaweera, P. K. D. D. P. Pitigala, M. K. I. Seneviratne, A. G. U. Perera, and K. Tennakone. $1/f$ Noise in dye-sensitized solar cells and NIR photon detectors. *Infrared Physics & Technology*, 50(2-3):270–273, April 2007.

[78] O. Jennrich, G. Newton, K. D. Skeldon, and J. Hough. A high power photodetection system for use with laser interferometric gravitational wave detectors. *Optics Communications*, 205(4-6):405–413, May 2002.

[79] Robert E. Johanson, D. Scansen, and S. O. Kasap. Effect of light exposure on $1/f$ noise in α-Si:H. *Journal of Vacuum Science & Technology B: Microelectronics and Nanometer Structures*, 17(1):73–76, 1999.

[80] B. K. Jones and D. A. Kozlowski. Low frequency noise and reliability analysis of avalanche photodiodes. *Quality and Reliability Engineering International*, 9(4):359–362, 1993.

[81] A. M. Joshi, G. H. Olsen, V. S. Ban, Sr. Mykietyn, E., M. J. Lange, and D. T. Mohr. Reduction of $1/f$ noise in multiplexed linear $In_{0.53}Ga_{0.47}As$ detector arrays via epitaxial doping. *Electron Devices, IEEE Transactions on*, 40(2):303–308, February 1993.

[82] Judson Technologies LLC. Germanium Detectors and Position Sensors – Short Form Catalog, August 2004.

[83] T. J. Kane and R. L. Byer. Monolithic, unidirectional single-mode Nd:YAG ring laser. *Optics Letters*, 10:65–67, February 1985.

[84] T. J. Kane and E. A. P. Cheng. Fast frequency tuning and phase locking of diode-pumped Nd:YAG ring lasers. *Optics Letters*, 13:970–972, November 1988.

[85] T. J. Kane, A. C. Nilsson, and R. L. Byer. Frequency stability and offset locking of a laser-diode-pumped Nd:YAG monolithic nonplanar ring oscillator. *Optics Letters*, 12:175–177, March 1987.

[86] A. Kerlain and V. Mosser. Robust, versatile, direct low-frequency noise characterization method for material/process quality control using cross-shaped 4-terminal devices. *Microelectronics and Reliability*, 45(9-11):1327–1330, 2005.

[87] J. Kimmerle, W. Kuebart, E. Kuehn, O. Hildebrand, K. Loesch, and G. Seitz. Low frequency noise in InGaAs/InP-Photodiodes. Noise in Physical Systems and 1/f noise, pages 249–252. Elsevier Science Publ. B.V., Amsterdam, 1983.

[88] Alicja Konczakowska. $1/f$ noise of electrolytic capacitors as a reliability indicator. *Quality and Reliability Engineering International*, 14(2):83–85, 1998.

[89] D. A. Kozlowski and B. K. Jones. Excess noise and currents as a predictor of reliability in PIN photodiodes. *Optical Detectors, IEE Colloquium on*, pages 13/1–13/7, January 1990.

[90] I. Krishnan. G-R noise and microscopic defects in irradiated junction field effect transistors. *Solid State Electronics*, 20:897–906, November 1977.

[91] D. V. Kuksenkov, H. Temkin, A. Osinsky, R. Gaska, and M. A. Khan. Low-frequency noise and performance of GaN p-n junction photodetectors. *Journal of Applied Physics*, 83(4):2142–2146, 1998.

[92] D. V. Kuksenkov, H. Temkin, A. Osinsky, R. Gaska, and M. A. Khan. Origin of conductivity and low-frequency noise in reverse-biased GaN p-n junction. *Applied Physics Letters*, 72:1365–+, March 1998.

[93] K. Kuroda, M. Ohashi, S. Miyoki, T. Uchiyama, H. Ishitsuka, K. Yamamoto, K. Kasahara, M.-K. Fujimoto, S. Kawamura, R. Takahashi, T. Yamazaki, K. Arai, D. Tatsumi, A. Ueda, M. Fukushima, S. Sato, S. Nagano, Y. Tsunesada, Z.-H. Zhu, T. Shintomi, A. Yamamoto, T. Suzuki, Y. Saito, T. Haruyama, N. Sato, Y. Higashi, T. Tomaru, K. Tsubono, M. Ando, A. Takamori, K. Numata, Y. Aso, K.-I. Ueda, H. Yoneda, K. Nakagawa, M. Musha, N. Mio, S. Moriwaki, K. Somiya, A. Araya, N. Kanda, S. Telada, H. Tagoshi, T. Nakamura, M. Sasaki, T. Tanaka, K. Oohara, H. Takahashi, O. Miyakawa, and M. E. Tobar. Current status of large-scale cryogenic gravitational wave telescope. *Classical and Quantum Gravity*, 20(17):S871–S884, 2003.

[94] P. Kwee. Charakterisierung von Lasersystemen für Gravitationswellendetektoren. Diploma thesis, University of Hannover, Germany, 2005.

[95] P. Kwee, F. Seifert, B. Willke, and K. Danzmann. Laser beam quality and pointing measurement with an optical resonator. *Review Of Scientific Instruments*, July 2007.

[96] A Lamminpää, M Noorma, T Hyyppä, F Manoocheri, P Kärhä, and E Ikonen. Characterization of germanium photodiodes and trap detector. *Measurement Science and Technology*, 17(4):908–912, 2006.

[97] T. C. Larason and S. S. Bruce. Spatial uniformity of responsivity for silicon, gallium nitride, germanium, and indium gallium arsenide photodiodes. *Metrologia*, 35:491–496, August 1998.

[98] Yu. Levin. Internal thermal noise in the LIGO test masses: A direct approach. *Phys. Rev. D*, 57(2):659–663, January 1998.

[99] D. P. Levinson and A. D. Snider. An exact formula for the effects of resistor geometry on current noise. *Electron Devices, IEEE Transactions on*, 33(1):58–60, January 1986.

[100] LISA Mission Science Office. LISA: Probing the Universe with Gravitational Waves. LISA-LIST-RP-436, January 2007.

[101] Yuk Tung Liu and Kip S. Thorne. Thermoelastic noise and homogeneous thermal noise in finite sized gravitational-wave test masses. *Phys. Rev.*, D62:122002, 2000.

[102] G. Losurdo. Interferometric detectors of gravitational waves on earth: the next genera-tions. *Journal of Physics: Conference Series*, 110(6):062016 (4pp), 2008.

[103] N. Lukyanchikova. Effect of illumination on noise and some other characteristics of p-n junctions in InSb. *Solid State Electronics*, 16:1473–1480, December 1973.

[104] Stefan Machlup. Noise in semiconductors: Spectrum of a two-parameter random signal. *Journal of Applied Physics*, 25(3):341–343, 1954.

[105] G. Masetti, S. Graffi, D. Golzio, and Zs. M. Kovács-V. Failures induced on analog integrated circuits by conveyed electromagnetic interferences: A review. *Microelectronics and Reliability*, 36(7-8):955–972, 1996.

[106] A. Masoero, B. Morten, M. Tamborin, and Prudenziati M. Excess noise in thick film resistors: Volume dependence. *Microelectronics International*, 12(3):5–8, 1995.

[107] A. Masoero, A. M. Rietto, B. Morten, and M. Prudenziati. Excess noise and its temperature dependence in thick-film (cermet) resistors. *Journal of Physics D: Applied Physics*, 16(4):669–674, 1983.

[108] A. L. McWhorter. $1/f$ *noise and related surface effects in germanium*. PhD thesis, Massachusetts Institute of Technology, 1955.

[109] Brian J. Meers. Recycling in laser-interferometric gravitational-wave detectors. *Phys. Rev. D*, 38(8):2317–2326, October 1988.

[110] N. Mio, T. Ozeki, K. Machida, and S. Moriwaki. Laser Intensity Stabilization System Using Laser-Diode-Pumped Nd:YAG Rod-Laser Amplifier. *Japanese Journal of Applied Physics*, 46:5338–+, August 2007.

[111] J. S. Moon, A. F. Mohamedulla, and N. O. Birge. Digital measurement of resistance fluctuations. *Review Of Scientific Instruments*, 63(10):4327–4332, October 1992.

[112] Euan Morrison, Brian J. Meers, David I. Robertson, and Henry Ward. Experimental demonstration of an automatic alignment system for optical interferometers. *Applied Optics*, 33(22):5037–5040, 1994.

[113] A. C. Nilsson, E. K. Gustafson, and R. L. Byer. Eigenpolarization theory of monolithic nonplanar ring oscillators. *Quantum Electronics, IEEE Journal of*, 25(4):767–790, April 1989.

[114] F. Nocera. LIGO laser intensity noise suppression. *Classical and Quantum Gravity*, 21(5):S481–S485, 2004.

[115] R. Nowicki. Output power stabilization of a helium-neon laser. *Journal of Physics E: Scientific Instruments*, 4(4):274–276, 1971.

[116] M. Ohashi. Status of LCGT and CLIO. *Journal of Physics: Conference Series*, 120(3):032008 (3pp), 2008.

[117] D. J. Ottaway, P. J. Veitch, C. Hollitt, D. Mudge, M. W. Hamilton, and J. Munch. Frequency and intensity noise of an injection-locked Nd:YAG ring laser. *Applied Physics B: Lasers and Optics*, 71(2):163–168, August 2000.

[118] R. H. Pantell and J. Warszawski. Laser Power Stabilization by Means of Nonlinear Absorption. *Applied Physics Letters*, 11:213–215, October 1967.

[119] PerkinElmer Optoelectronics. Large-area InGaAs photodiodes - datasheet, 2000.

[120] A. S. Poulton. Effect of conducted EMI on the DC performance of operational amplifiers. *Electronics Letters*, 30(4):282–284, 1994.

[121] Volker M. Quetschke. *Korrelationen von Rauschquellen bei Nd:YAG-Lasersystemen*. PhD thesis, Universität Hannover, 2003.

[122] A. Raab, C. Jung, and P. Dullenkopf. Current noise of trimmed thick-film resistors: measurement and simulation. *Microelectronics International*, 15(1):15–22, 1998.

[123] Timothy C. Ralph, Charles C. Harb, and Hans-A. Bachor. Intensity noise of injection-locked lasers: Quantum theory using a linearized input-output method. *Phys. Rev. A*, 54(5):4359–4369, November 1996.

[124] M. Rimini-Döring. *Korrelationseffekte im Generations-Rekombinations-Rauschen*. PhD thesis, University of Stuttgart, 1991.

[125] M. Rimini-Döring, A. Hangleiter, S. Winkler, and N. Klötzer. Non-equilibrium generation-recombination noise in InGaAs/InP photodiodes. *Applied Physics A: Materials Science & Processing*, 54:120–123, February 1992.

[126] N. A. Robertson, S. Hoggan, J. B. Mangan, and J. Hough. Intensity stabilisation of an argon laser using an electro-optic modulator —performance and limitations. *Applied Physics B: Lasers and Optics*, 39:149–153, March 1986.

[127] D. Rocak, D. Belavic, M. Hrovat, J. Sikula, P. Koktavy, J. Pavelka, and V. Sedlakova. Low-frequency noise of thick-film resistors as quality and reliability indicator. *Microelectronics Reliability*, 41(4):531–542, April 2001.

[128] J. Rollins, D. Ottaway, M. Zucker, R. Weiss, and R. Abbott. Solid-state laser intensity stabilization at the 10^{-8} level. *Optics Letters*, 29:1876–1878, August 2004.

[129] S. Rowan, A.M. Campbell, K. Skeldon, and J. Hough. Broadband Intensity Stabilization of a Diode-pumped Monolithic Miniature Nd:YAG Ring Laser. *Journal of Modern Optics*, 41:1263–1269, June 1994.

[130] S. Rowan and J. Hough. Gravitational wave detection by interferometry (ground and space). *http://www.livingreviews.org/lrr-2000-3*, 2000.

[131] E. Rubiola, E. Salik, Nan Yu, and L. Maleki. Flicker noise in high-speed p-i-n photodiodes. *Microwave Theory and Techniques, IEEE Transactions on*, 54(2):816–820, February 2006.

[132] S. L. Rumyantsev, N. Pala, M. S. Shur, R. Gaska, M. E. Levinshtein, V. Adivarahan, J. Yang, G. Simin, and M. Asif Khan. Low-frequency noise in $Al_{0.4}Ga_{0.6}N$-based Schottky barrier photodetectors. *Applied Physics Letters*, 79(6):866–868, 2001.

[133] S. L. Rumyantsev, C. Wetzel, and M. S. Shur. Current and optical low-frequency noise of GaInN/GaN green light emitting diodes. In *Society of Photo-Optical Instrumentation Engineers (SPIE) Conference Series*, volume 6600 of *Presented at the Society of Photo-Optical Instrumentation Engineers (SPIE) Conference*, July 2007.

[134] S. Sakata, V. Leonhardt, S. Kawamura, K. Numata, O. Miyakawa, S. Sato, A. Nishizawa, T. Yamazaki, M. Fukushima, A. Furusawa, and A. Sugamoto. A study for reduction of radiation pressure noise in gravitational wave detectors. *Journal of Physics: Conference Series*, 122:012020 (7pp), 2008.

[135] S. Saraf, R. L. Byer, and P. J. King. High-extinction-ratio resonant cavity polarizer for quantum-optics measurements. *Applied Optics*, 46(18):3850–3855, 2007.

[136] P. R. Saulson. *Fundamentals of interferometric gravitational wave detectors*. World Scientific Pub Co Inc, 1994.

[137] J. H. Scofield. AC Method For Measuring Low-Frequency Resistance Fluctuation Spectra. *Review Of Scientific Instruments*, 58(6):985–993, June 1987.

[138] F. Seifert. Entwicklung einer quantenrauschbegrenzten Leistungsstabilisierung für ein Präzisionslasersystem. Master's thesis, University of Hannover, 2002.

[139] F. Seifert. Additional documents, schematics, drawings, etc. *http://www.aei.mpg.de/∼frs/* , 2009.

[140] F. Seifert. Resistor Current Noise Measurements - LIGO-T0900200-v1. Technical report, LIGO Laboratory / LIGO Scientific Collaboration, 2009.

[141] F. Seifert, P. Kwee, M. Heurs, B. Willke, and K. Danzmann. Laser power stabilization for second-generation gravitational wave detectors. *Optics Letters*, 31(13):2000–2002, July 2006.

[142] A.E. Siegmann. *Lasers*. University Science Books, 1986.

[143] D. T. Smith. Low frequency noise in tantalum capacitors. *Active and Passive Electronic Components*, 12(4):215–221, 1987.

[144] J. R. Smith, J. Degallaix, A. Freise, H. Grote, M. Hewitson, S. Hild, H. Lück, K. A. Strain, and B. Willke. Measurement and simulation of laser power noise in GEO600. *Classical and Quantum Gravity*, 25(3):035003 (12pp), 2008.

[145] K. Somiya, Y. Chen, S. Kawamura, and N. Mio. Frequency noise and intensity noise of next-generation gravitational-wave detectors with RF/DC readout schemes. *Phys. Rev. D*, 73(12):122005–+, June 2006.

[146] K. Somiya, Y. Chen, S. Kawamura, and N. Mio. Erratum: Frequency noise and intensity noise of next-generation gravitational-wave detectors with RF/DC readout schemes [Phys. Rev. D 73, 122005 (2006)]. *Phys. Rev. D*, 75(4):049905–+, February 2007.

[147] Frank Steier. Methoden zur thermo-optischen Charakterisierung optischer Komponenten. Master's thesis, University of Hannover, 2004.

[148] K. D. Stock, R. Heine, and H. Hofer. Influence of inhomogeneity of NIR-Photodiodes on calibrations at 1047nm. *Metrologia*, 28(3):207–210, 1991.

[149] H. Stoll. Analysis of resistance fluctuations independent of thermal voltage noise. *Applied Physics*, 22(2):185–187, 1980.

[150] H. L. Stover and W. H. Steier. Locking of laser oscillators by light injection. *Applied Physics Letters*, 8(4):91–93, 1966.

[151] H. K. Taylor, H. Sun, T. F. Hill, A. Farahanchi, and D. S. Boning. Characterizing and Predicting Spatial Nonuniformity in the Deep Reactive Ion Etching of Silicon. *Journal of The Electrochemical Society*, 153(8):C575–C585, 2006.

[152] J. A. J. Tejada, A. Godoy, A. Palma, and P. Cartujo. Temperature dependence of generation-recombination noise in p-n junctions. *Low Temperature Electronics, 2002. Proceedings of the 5th European Workshop on*, pages 71–74, 2002.

[153] The Virgo Collaboration. Advanced Virgo White Paper - VIR-NOT-DIR-1390-304. Technical Report VIR-NOT-DIR-1390-304, 2005.

[154] The Virgo Collaboration. Advanced Virgo Conceptual Design - VIR-042A-07. Technical Report VIR-042A-07, 2007.

[155] The Virgo Collaboration. Report for the EGO council virgo+ review team - VIR-001A-08, January 2008. VIR-001A-08.

[156] Kip S. Thorne and Carolee J. Winstein. Human gravity-gradient noise in interferometric gravitational-wave detectors. *Phys. Rev. D*, 60(8):082001, September 1999.

[157] E. D. Totev and C. J. M. Verhoeven. Out of band interference measurement of negative feedback amplifiers. *ASIC, 2005. ASICON 2005. 6th International Conference On*, 2:676–680, October 2005.

[158] C. D. Tran and R. J. Furlan. Indirect amplitude stabilization of a tunable laser through control of the intensity of a pump laser by an electrooptic modulator. *Applied Spectroscopy*, 47(2):235–238, February 1993.

[159] M. Tröbs, P. Weßels, and C. Fallnich. Power- and frequency-noise characteristics of an Yb-doped fiber amplifier and actuators for stabilization. *Optics Express*, 13(6):2224–2235, 2005.

[160] Michael Tröbs. *Laser development and stabilization for the spaceborne interferometric gravitational wave detector*. PhD thesis, University of Hannover, 2005.

[161] N. Uehara, E. K. Gustafson, M. M. Fejer, and R. L. Byer. Modeling of efficient mode-matching and thermal-lensing effect on a laser-beam coupling into a mode-cleaner cavity. volume 2989, pages 57–68. SPIE, 1997.

[162] U.S. Department of Defense. MIL-STD-202G, METHOD 308 - Current-Noise test for fixed resistors, November 1961.

[163] A. van der Ziel. Noise in solid-state devices and lasers. *Proceedings of the IEEE*, 58(8):1178–1206, August 1970.

[164] A. van der Ziel. Unified presentation of $1/f$ noise in electron devices: fundamental $1/f$ noise sources. *Proceedings of the IEEE*, 76(3):233–258, March 1988.

[165] Aldert van der Ziel. *Noise. Sources, characterization, measurement.* Prentice-Hall Information and System Sciences Series, Englewood Cliffs: Prentice-Hall, 1970, 1970.

[166] L. K. J. Vandamme. Noise as a diagnostic tool for quality and reliability of electronic devices. *Electron Devices, IEEE Transactions on*, 41(11):2176–2187, November 1994.

[167] A. H. Verbruggen, H. Stoll, K. Heeck, and R. H. Koch. A novel technique for measuring resistance fluctuations independently of background-noise. *Applied Physics A-Materials Science & Processing*, 48(3):233–236, March 1989.

[168] Jean-Yves Vinet, Violette Brisson, and Stefano Braccini. Scattered light noise in gravitational wave interferometric detectors: Coherent effects. *Phys. Rev. D*, 54(2):1276–1286, July 1996.

[169] Vishay. Audio noise reduction through the use of bulk metal foil resistors - "hear the difference". Technical report, Vishay, July 2005.

[170] Vishay. High-precision bulk metal foil resistors for military and aerospace applications. Technical report, Vishay, September 2005.

[171] Richard F. Voss and John Clarke. Flicker $(1/f)$ noise: Equilibrium temperature and resistance fluctuations. *Phys. Rev. B*, 13(2):556–573, January 1976.

[172] D. F. Walls. Squeezed states of light. *Nature*, 306(5939):141–146, November 1983.

[173] J. Weber. Detection and generation of gravitational waves. *Phys. Rev.*, 117(1):306–313, January 1960.

[174] M. G. White and A. Bittar. Uniformity of quantum efficiency of single and trap-configured silicon photodiodes. *Metrologia*, 30(4):361–364, 1993.

[175] W. Wiechmann, T. J. Kane, D. Haserot, F. Adams, G. Truong, and J. D. Kmetec. 20-W diode-pumped single-frequency Nd:YAG MOPA for the Laser Interferometer Gravitational Wave Observatory. *Lasers and Electro-Optics, 1998. CLEO 98. Technical Digest. Summaries of papers presented at the Conference on*, pages 432–433, May 1998.

[176] G. M. Williams, R. E. de Wames, J. Bajaj, and E. R. Blazejewski. Photo-induced excess low frequency noise in HgCdTe photodiodes. *Journal of Electronic Materials*, 22:931–941, August 1993.

[177] B. Willke, S. Brozek, K. Danzmann, V. Quetschke, and S. Gossler. Frequency stabilization of a monolithic Nd:YAG ring laser by controlling the power of the laser-diode pump source. *Optics Letters*, 25(14):1019–1021, 2000.

[178] B. Willke, K. Danzmann, M. Frede, P. King, D. Kracht, P. Kwee, O. Puncken, R. L. Savage, Jr., B. Schulz, F. Seifert, C. Veltkamp, S. Wagner, P. Wessels, and L. Winkelmann. Stabilized lasers for advanced gravitational wave detectors. *Classical and Quantum Gravity*, 25(11), June 2008.

[179] B. Willke, N. Uehara, E. K. Gustafson, R. L. Byer, P. J. King, S. U. Seel, and Jr. R. L. Savage. Spatial and temporal filtering of a 10W Nd:YAG laser with a fabry-perot ring-cavity premode cleaner. *Optics Letters*, 23(21):1704–1706, 1998.

[180] Willke, B. *et al.* Pre-stabilized laser design requirements - LIGO-T000035-00-W. Technical report, LIGO Laboratory / LIGO Scientific Collaboration, 2004.

[181] Hei Wong. Low-frequency noise study in electron devices: review and update. *Microelectronics Reliability*, 43(4):585–599, April 2003.

[182] Toshihiko Yoshino and Kiyoshi Kurosawa. A New Method for the Intensity Stabilization of He-Ne Lasers. *Japanese journal of applied physics. Pt. 1, Regular papers & short notes*, 21(3):555–556, 1982.

[183] Toshihiko Yoshino, Shinsuke Umegaki, Hiroaki Inoue, and Kiyoshi Kurosawa. Light intensity stabilization using highly-efficient faraday rotator. *Japanese journal of applied physics. Pt. 1, Regular papers & short notes*, 21(4):612–616, April 1982.

[184] Ivo Zawischa. *Injektionsgekoppelte diodengepumpte Nd:YAG- und Nd:YVO$_4$-Laser für terrestrische interferometrische Gravitationswellendetektoren*. PhD thesis, University of Hannover, 2003.

[185] Jing Zhang, Hongliang Ma, Changde Xie, and Kunchi Peng. Suppression of intensity noise of a laser-diode-pumped single-frequency Nd:YVO4 laser by optoelectronic control. *Applied Optics*, 42(6):1068–1074, 2003.

Acknowledgements

Curriculum vitæ

Personal data

Name:	Frank Seifert
Address:	Am Stöckener Bach 20A 30419 Hannover, Germany
Date of birth:	19. June 1977
Place of birth:	Berlin, Germany
Nationality:	German

University studies

2003–present	Scientific assistant (wissenschaftlicher Mitarbeiter) at the University of Hannover / Max Planck Institute for Gravitational Physics (Albert Einstein Institute)
2002	Electrical engineering diploma, *"Entwicklung einer quantenrauschbegrenzten Leistungsstabilisierung für ein Präzisionslasersystem"*
1997–2002	Diploma studies in electrical engineering at the University of Hannover

Military service

1996–1997	Basic military service, Holzminden

Education

1996	University-entrance exam, German certificate of maturity (Abitur), Gymnasium Alfeld(Leine)
1989–1996	High School (Gymnasium) Alfeld (Leine)
1984–1989	Primary School (Grundschule, Orientierungsstufe) Grünenplan/Duingen.